Measurement of jet fragmentation functions and of their moments in pp collisions at Vs = 2.76 TeV with ALICE at the LHC

Mengliang Wang

UNIVERSITE BRETAGNE LOIRE

UNIVERSITÉ DE NANTES

Thèse de Doctorat

Mengliang WANG

Mémoire présenté en vue de l'obtention du
grade de Docteur de l'Université de Nantes
et de Central China Normal University (CCNU)
sous le sceau de l'Université Bretagne Loire

École doctorale : Matière, Molécules Matériaux en Pays de la Loire

Discipline : Constituants élémentaires et physique théorique
Spécialité : *Physique des ions lourds*
Unité de recherche : *SUBATECH Nantes – CNRS/IN2P3*

Soutenue le :10 Decembre 2016
Thèse N° :

Mesure des fonctions de fragmentation des jets et de leurs moments dans les collisions pp à $\sqrt{s}$ = 2.76 TeV ave ALICE au LHC

JURY

Rapporteurs :	**Matteo CACCIARI**, Professeur, Universite Paris 7 & LPTHE Paris **Arnaud LUCOTTE**, Directeur de recherche CNRS, LPSC Grenoble
Président / Examinateur :	**Pengfei ZUHANG**, Professeur, Tsinghua University Beijing Chine.
Invités :	**Zhongbao YIN**, Professeur, Central China Normal University (CCNU) Wuhan Chine **Xiaoming ZHANG**, Docteur, Central China Normal University (CCNU) Wuhan Chine
Encadrants :	**Magali ESTIENNE**, Chargé de recherche CNRS, SUBATECH Nantes **Alexandre SHABETAI**, Chargé de recherche CNRS, SUBATECH Nantes
Directeur de Thèse :	**Sonia KABANA**, Professeur, Université de Nantes
Co-directeur de Thèse :	**Daicui ZHOU,** Professeur, Central China Normal University (CCNU) Wuhan Chine

分类号_____ 密级

UDC _____ 编号_____

华中师范大学

博士学位论文

LHC/ALICE实验上质子-质子碰撞中喷注碎裂函数及碎裂函数矩的测量

学位申请人姓名: 王梦亮

申请学位学生类别: 博 士

申请学位学科专业: 粒子物理与原子核物理

指导教师姓名: 周代翠 教授

Sonia KABANA 教授

博士学位论文

LHC/ALICE 实验上质子-质子碰撞中喷注碎裂函数及碎裂函数矩的测量

论文作者：王梦亮

指导教师：周代翠　教授

Sonia KABANA　教授

学科专业：粒子物理与原子核物理

研究方向：高能重离子碰撞实验

华中师范大学物理科学与技术学院

2016年12月

Dissertation

Measurement of jet fragmentation functions and of their moments in pp collisions at $\sqrt{s}=2.76$ TeV with ALICE at the LHC

By

Mengliang WANG

Supervisors: Prof. Daicui ZHOU

Prof. Sonia KABANA

Specialty: Particle Physics and Nuclear Physics

Research Area: Heavy-Ion Collisions Experiment

College of Physical Science and Technology

Central China Normal University

December 2016

华中师范大学学位论文原创性声明和使用授权说明

原创性声明

本人郑重声明：所呈交的学位论文，是本人在导师指导下，独立进行研究工作所取得的研究成果。除文中已经标明引用的内容外，本论文不包含任何其他个人或集体已经发表或撰写过的研究成果。对本文的研究做出贡献的个人和集体，均已在文中以明确方式标明。本声明的法律结果由本人承担。

作者签名：　　日期：　　年　　月　　日

学位论文版权使用授权书

学位论文作者完全了解华中师范大学有关保留、使用学位论文的规定，即：研究生在校攻读学位期间论文工作的知识产权单位属华中师范大学。学校有权保留并向国家有关部门或机构送交论文的复印件和电子版，允许学位论文被查阅和借阅；学校可以公布学位论文的全部或部分内容，可以允许采用影印、缩印或其它复制手段保存、汇编学位论文。（保密的学位论文在解密后遵守此规定）

保密论文注释：本学位论文属于保密，在____年解密后适用本授权书。

非保密论文注释：本学位论文不属于保密范围，适用本授权书。

作者签名：　　导师签名：

日期：　　年　　月　　日　　日期：　　年　　月　　日

本人已经认真阅读“CALIS 高校学位论文全文数据库发布章程”,同意将本人的学位论文提交“CALIS 高校学位论文全文数据库”中全文发布,并可按“章程”中的规定享受相关权益。同意论文提交后滞后：□半年；□一年；□二年发布。

作者签名：　　导师签名：

日期：　　年　　月　　日　　日期：　　年　　月　　日

摘　　要

格点量子色动力学（lQCD）的预言，在高温和低化学势的极端情况下，夸克及胶子会退“禁闭”，物质会由普通状态过渡为夸克胶子等离子体（QGP）。实验上，我们通过极端相对论重离子碰撞来产生并研究这一热密物质形态。

产生于碰撞早期的高能部分子来自硬散射过程，它会在介质中损失能量后碎裂成一簇强子，这就是喷注（jet）的演化过程。产生的于 QGP 在实验中的极短暂寿命，对它的观测只能基于各类末态“探针”。喷注的结构和碎裂形态，被广泛在质子-质子及重离子碰撞实验中进行研究测量。前者对应于真空环境，而后者环境中会包括产生的高密介质，QGP。在对二者的对比中，可以得到在 QGP 存在情况下的的喷注的碎裂（结构）的变化，这一改变揭示了 QGP 的性质。碎裂函数描述了喷注内部强子的分布情况。在质子-质子碰撞中，它有助于理解喷注碎裂过程，并进而检验微扰量子色动力学（pQCD）。同时它还对质子-核子及核子-核子碰撞提供参考，通过对比，以分别揭示出冷核效应和热密 QGP 的影响。然而，对它在重离子碰撞下的测量受到了喷注背景及其涨落的巨大影响。为了克服这一难题，Cacciari*et.al.*在【1】中提出了一个新的物理量：碎裂函数矩。

在大型强子对撞机（LHC）上的大型离子对撞实验（ALICE）对带电粒子具有独特的分辨能力，精度下限达到 150MeV/c。这一能力使对喷注结构改变及碎裂函数的测量成为可能。ALICE 上的电磁量能器也可以用于早期硬探针的测量，包括喷注、高能光子等。在 2015-2018 的 LHC 的第二阶段运行（Run2）中，ALICE 添加了别一个与 EMCal 相对的量能器（双喷注量能器 DCal）。它们将联合促进双喷注、强子-喷注及光子-喷注事件的关联研究。

本研究工作主要应用 LHC/ALICE 的中心桶部径迹探测系统(central berral tracking system)，利用探测到的带电粒子径迹，重建出带电粒子喷注（以下简称喷注）。对 2.76 TeV 质心系能量的质子一质子对撞数据进行分析，对喷注的碎裂函数矩(fragmentation function moments)进行首次测量。为了加深对新物理量的理解，我们也测量了喷注的碎裂函数(fragmentation function)。这一测量包括了喷

注中的带电强子谱(p_T)，带电强子能量分数的分布(z, ξ)，方位夹角的分布($\Delta\theta$)和喷注内能量的横向延伸/扩展的分布(j_T)几个方面。对于不同的喷注分辨率(R，它圈定了喷注的空间张角大小上限)，上述各个结果都显示出与理论模型(PYTHIA)很好的契合度。作为博士工作一部分，DCal 在官方分析软件 ALIROOT 中代码实现，也将在本文中给予讨论

本论文的章节安排如下：本文第一章将对工作的物理背景作一介简单的介绍，包括重粒子碰撞及演化和 QCD 相图等。第二章会着重介绍与喷注相关的物理，包括喷注研究的近况，遇到的问题，解决方案。第三章将会对 ALICE 实验中所用到的探测器作一个简要介绍。第四章会着重介绍 ALICE 的取样电磁量能器和本人在代码实现上在工作。后者主要包括了二个部分：一、规范了 EMCal 代码，更新了几何结构、各联接之间的映射：电子学通道，clusterization 及触发 trigger 的部分。二、构建了三个版本的 DCal 几何结构，分别对应于：之前投标时的版本，正在 ALICE 上使用的版本和一个将来可能的更新版本。最后，对这一工作结果进行了验证研究和全项兼容性测试。第五章对 ALICE 实验下的分析框架作了简短介绍，同时介绍了本次测量所应用的数据和相应的 MC，并作了数据质量分析，介绍了喷注分析所需要的常见技术。最后对于中心探测区域的径迹（track）作了一系列研究以深入理解。第六章给出了 2.76TeV 质子－质子碰撞在 ALICE 实验下的碎裂函数测量，测量结果与理论 QCD 模型预期一致，并对测量中运用的背景扣除、Bin-by-Bin 修正及次级粒子修正等各项技术进行了讨论。第七章给出了同样实验条件下，新变量碎裂函数矩的测量结果，并进行多种方案的讨论。其结果与碎裂函数相吻合。对于这一新变量的初次测量的经验将会有助于推进其到相应的重离子碰撞中。限于工作量和时间，这一工作尚未完全完结，本文对一部分系统误差工作进行了讨论和展望，并会在近期完成整个系统分析。最后在第八章对本论文工作的总结。

关键词：质子-质子碰撞，超相对论重离子碰撞实验，夸克－胶子等离子体，大型强子对撞机（LHC），大型离子对撞实验（ALICE），喷注，碎裂函数，碎裂函数矩（fragmentaion function moments）

Abstract

A cross-over between ordinary nuclear matter and a state of deconfined quarks and gluons, the Quark Gluon Plasma (QGP), is predicted by lattice QCD calculations at low chemical potential and high temperature in the nuclear phase diagram. Experimentally, ultra-relativistic heavy ion collisions are used to produce and study the hot and dense QGP medium.

Produced in a hard scattering at the early stage of the collision a highly energetic parton is first expected to lose energy in the medium before fragmenting into a hadronic spray of particles called jet. A detailed study of the modification of the jet structure and of its fragmentation pattern in vacuum and in medium should provide insights into the QGP properties. The jet fragmentation functions describe the momentum distribution of hadrons inside a reconstructed jet. In proton-proton (pp) collisions their measurement is important for understanding the mechanisms of parton fragmentation. Such measurements also provide a test of perturbative Quantum Chromo Dynamics (pQCD) as well as a baseline for similar measurements in p-A collisions (revealing potential cold nuclear matter effects) or in A-A collisions (shedding light on the energy loss mechanisms in presence of a hot and dense medium). However, in heavy-ion collisions the presence of a large underlying event and of its event-by-event fluctuations makes the measurement of jet fragmentation functions a challenging task. The use of the fragmentation function moments has been proposed in [1] as a way to overcome this difficulty.

The ALICE detector at the Large Hadron Collider (LHC) has unique tracking capabilities enabling to measure charged particles down to transverse momenta as low as 150 $\sim MeV/c$. This allows assessing possible modifications of the jet structure and helps constraining the jet fragmentation functions. The ALICE Electromagnetic Calorimeter (EMCal) can also be used to measure hard probes of the initial collision, including jets, high p_T photons, neutral mesons (π^0, η, ω), and electrons. For LHC Run 2 (2015-2018) an additional detector was installed on the opposite side of the beam axis, the Di-Jet Calorimeter (DCal). It provides the angular coverage necessary to facilitate jet-jet, hadron-jet, and γ-jet correlations.

In this thesis we will present the our measurements of charged-jet fragmentation functions in pp collisions at $\sqrt{s}$ = 2.76 TeV with ALICE. The first studies of fragmentation function moments will be discussed. Part of this work is also dedicated to the ALICE EMCal and DCal sampling electromagnetic calorimeters. The implementation of the DCal geometry in the ALICE offline software will be pre-

sented.

The document is organized as follows. The first chapter introduces and motivates the study of the QGP in heavy-ion collisions. Chapter 2 presents a few aspects of jet physics and motivates the study of jet fragmentation. Chapter 3 is dedicated to the ALICE experiment at LHC. Its sub-detectors are introduced and described with a main focus on those that are used for jet analyses studies. In Chapter 4, after discussing about the basic principles of electromagnetic calorimeters, the ALICE EMCal and DCal detectors are presented. The DCal geometry together with the its implementation in ALIROOT and the validation tests that we performed in order to validate it are discussed. In Chapter 5, after introducing the tools used in our physics analyses and focuses on the running conditions and quality checks of the data. In Chapter 6 we present our measurement of charged jet fragmentation functions with the ALICE experiment in pp Minimum Bias Collisions at the LHC at $\sqrt{s} = 2.76$ TeV. The measurement covers (mini)-jet momenta from 5 to 60 GeV/c. Details about the underlying event subtraction as well as about the bin-by-bin and secondary particle corrections are given before to discuss the results. Finally in Chapter 7, our measurement of jet fragmentation function moments is presented and discussed.

Keywords: pp collisions, ultra-relativistic heavy-ion collisions, QGP, ALICE, jets, fragmentation functions, fragmentation function moments, electromagnetic calorimeters, EMCal, DCal

Contents

List of Figures

List of Tables

Chapter 1

Physics Introduction

1.1 Theories

In order to explain Nature, physicists search to discover the laws of physics allowing to understand and predict natural phenomena in macroscopic and microscopic level. Physics at the microscopic level, explains the "elementary" structure of the world and the interactions between the elementary constituents. While the idea of the "atom" in philosophy was formulated few hundred years B.C. , the search for atoms and the discovery of the atomic model for matter was possible only at the beginning of 19th century, and from then on the last 100 years we advanced in significant way in our understanding of the sub-atomic level. Nowadays the theory of the fundamental elements and their interactions is summarized in the so called Standard Model.

1.1.1 Standard model

According to the Standard Model (SM), the 3 basic interactions are : the Strong interaction, the Weak interaction and the electromagnetic interaction (the gravity is not included in the SM). In SM, matter is made up by *Fermions* (with half-integer spin) of 6 flavors (types) for both quarks and leptons, classified in 3 generations. As shown in the figure 1.1, the left 3 rows $\times$ 4 columns are the *Fermions*. The first generation (column) of quarks and lepton constitute the everyday matter. For example, nuclear matter is made of charged nuclei and the electrons (e) around. The nuclei contain proton (p) and/or neutron (n) which are made up by 3 quacks (they are baryons, uud/udd for p/n). Neutrino (ν_e) contains no charge and only take part in weak interaction, thus it is hard to be "seen" directly. The forth column

are force particles (carriers) (*Bosons*, with integer spin): gluon (g) carrier of strong interaction, photon (γ) carrier of electromagnetism and intermediate vector bosons (Z, $W^{+/-}$) carrier of weak interaction. The "Higgs" boson was found in 2012 [12][13], and completes the SM with a mass creation mechanism.

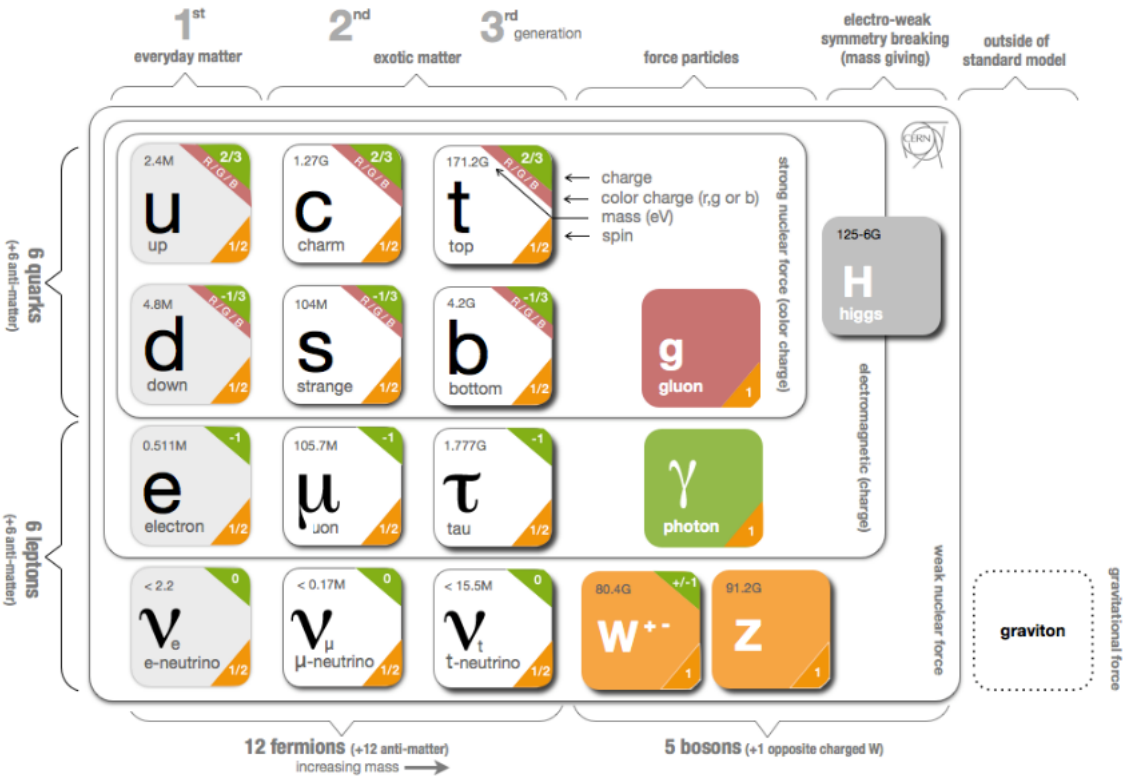

Figure 1.1: **Standard Model**: particles in Standard Model and the external graviton

In fig. 1.2 3 typical interactions in Standard Model are shown. The figure from left to right shows examples of strong interaction mediated by gluons, weak interaction mediated by a W^- and electromagnetic interaction mediated by photons.

1.2 Quantum Chromodynamics

Quantum Chromodynamics (QCD) is the theory describe the strong interaction between particle with color charge, like quarks and gluons. The color charge are labeled as "red", "green", "blue", or short for r, g, b. In the Quantum Electrodynamics (QED), the photon is the mediator of the electromagnetic interaction. The role of gluon in QCD is analogous to that of the photon in QED. But the difference is that the gluon itself has color charge, while photon has no (electric) charge. So the gluon can interact with itself.

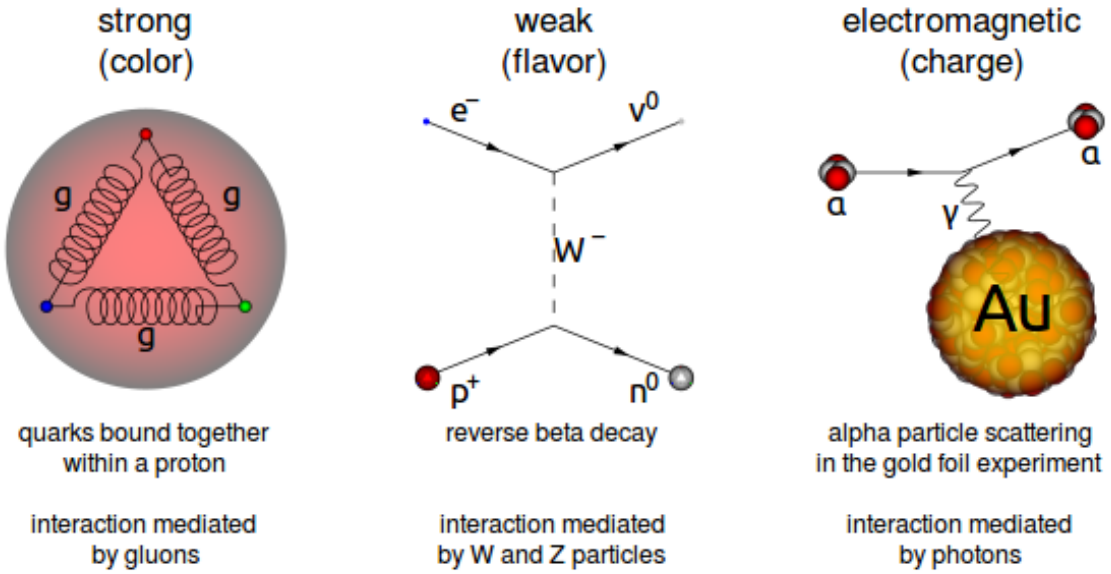

Figure 1.2: Interactions of particles in SM. The left one is the quarks bounded by gluons within a proton; The center one is so-called "reverse beta decay"; The right one is the scattering of an α particle (He^{2+}) on a gold nucleus.

The Lagrangian of QCD is written as [14]:

$$\begin{aligned} \mathcal{L}_{QCD} &= \mathcal{L}_q + \mathcal{L}_g \\ &= \overline{\phi}(i\not{D} - m)\phi - \frac{1}{4}(F^A_{\mu\nu})^2 \\ &= \sum_q \overline{\psi}_{q,a}(i\gamma^\mu \partial_\mu \delta_{ab} - g_s \gamma^\mu t^C_{ab} \mathcal{A}^C_\mu - m_q \delta_{ab})\psi_{q,b} - \frac{1}{4} F^A_{\mu\nu} F^{A,\mu\nu} \end{aligned} \tag{1.1}$$

The first term represent the quark-gluon coupling by strong force, when a quark (q) changes its color by emitting/absorbing a gluon; ψ_q is the quark-field for a special flavor (q). The corresponding gluon-field is $\mathcal{A}^C_\mu$, g_s is the coupling strength, the generators t^C_{ab} of the SU(3) group represent the "color octet" ($N_c^2 - 1 = 8$) of the gluon. The other parameters are: the mass m_q, γ^μ is the Dirac γ-matrix, and the μ is a Lorentz vector index.

The gauge-invariant gluon field strength tensor $F^A_{\mu\nu}$ is expressed as:

$$F^A_{\mu\nu} = \partial_\mu \mathcal{A}^A_\nu - \partial_\nu \mathcal{A}^A_\mu - g_s f_{ABC} \mathcal{A}^B_\mu \mathcal{A}^C_\nu, \tag{1.2}$$

where the f_{ABC} is the SU(3) structure constants. Comparing with QED, the additional $\mathcal{A}^A_\mu$ allows the self-interaction of the gluons. This self-interaction gives rise to important properties of QCD: color confinement, asymptotic freedom, which are discussed in the next section 1.2.1.

1.2.1 Coupling constant α

Analogous to the coupling constant (α) in QED, the coupling constant in QCD, $\alpha_s = \frac{g_s^2}{4\pi}$, describes the strength of strong interaction. It depends on the momentum transfer Q, the typical values as $\alpha_s \sim 0.1$ for 100 GeV–TeVrange. In perturbative QCD (pQCD), α_s can be expressed as a function of an renormalization scale μ_R with [15]:

$$\mu_R^2 \frac{d\alpha_s}{d\mu_R^2} = \beta(\alpha_s) \quad = \quad -b_0\alpha_s^2 - b_1\alpha_s^3 - b_2\alpha_s^4 - \ldots \tag{1.3}$$

where the b_i is used to calculate the $(i+1)$-loop coefficient. E.g. $b_0 = (11C_A - 4n_f T_R)/(12\pi) = (33 - 2n_f)/(12\pi)$ is referred to as the 1-loop beta function coefficient. The fist order of coefficient in Eq. 1.3 is negative ($-b_0 < 0$, as the number of quarks $n_f \leq 6$), shows the fact that the QCD coupling effectively *decreases* with energy, and this phenomenon is called *asymptotic freedom*. One can consider only the b_0 term at an energy range where the number of flavors is constant, under the assumption $\mu_R^2 \simeq Q^2$, written as[16, 17]:

$$\alpha_s(Q^2) = \frac{1}{b_0 \ln(Q^2/\Lambda_{QCD}^2)} \tag{1.4}$$

where Λ_{QCD} corresponds to the non-perturbative scale of QCD ($\Lambda_{QCD} \sim$ a few hundred MeV). The measurements of the QCD coupling presented as a function of the energy scale Q is shown in Fig. 1.3.

From Fig. 1.3, we see that the coupling constant α_s decrease with the momentum transfer increasing (equivalently at short distances), which is a main characteristic feature of QCD. At low momentum transfers, the coupling constant α_s is large and the perturbative approach is not valid. The quarks and gluons are confined in the hadrons (which are colorless), and this is known as color *confinement*. On the contrary, when α_s is approaching zero, the quark interaction becomes weak and can behave as if they are free. This feature of the state is the so-called *asymptotic freedom* as we have discussed.

1.3 Latice QCD and the Quark-Gluon Plasma

Non-perturbative methods have been developed to study the region of large coupling constant, namely the Lattice QCD (LQCD), proposed by K. Wilson in 1974 [18]. In LQCD, the QCD Lagrangian is described in Euclidean space-time

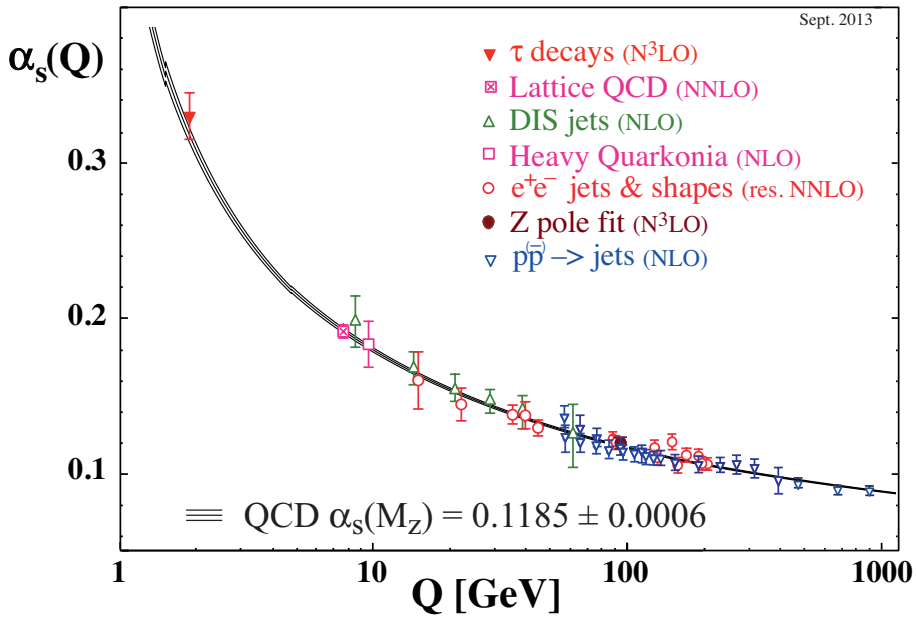

Figure 1.3: Summary of measurements of α_s as a function of the energy scale Q. The α_s extracted from QCD perturbative calculations are shown at next-to-leading order (NLO) (purple squares, green and inverted blue triangles), next-to-next-to leading order (NNLO) (red open circles), next-to-NNLO (N^3LO) (red solid triangle and brown dot). The cross filled square in purple is based on lattice QCD. The plot is taken from [2].

lattice, where quark fields are located on the lattice points and gauge fields are defined as the links between points. The LQCD predicts a transition from the hadron phase to a state of deconfined quarks and gluons with increasing Temperature. Such a deconfined state of quarks and gluons is called Quark-Gluon Plasma (QGP), by analogy with classical plasma [19].

From the calculation, a transition which is in fact a "cross over" at baryonic potential $\mu_B = 0$ for massless quarks is obtained. Historically important results for the field of relativistic heavy ion collision were an estimated phase transition temperature (called critical temperature, T_c) of $T_c \sim 170$ MeV, and corresponding density of energy $\varepsilon = 0.7$ GeV/fm^3 [20]. More recent LQCD results exhibit lower values of T_c of about ~ 155 MeV. The jump of the energy density divided by the temperature at T_c is shown in the left panel of Fig. 1.4.

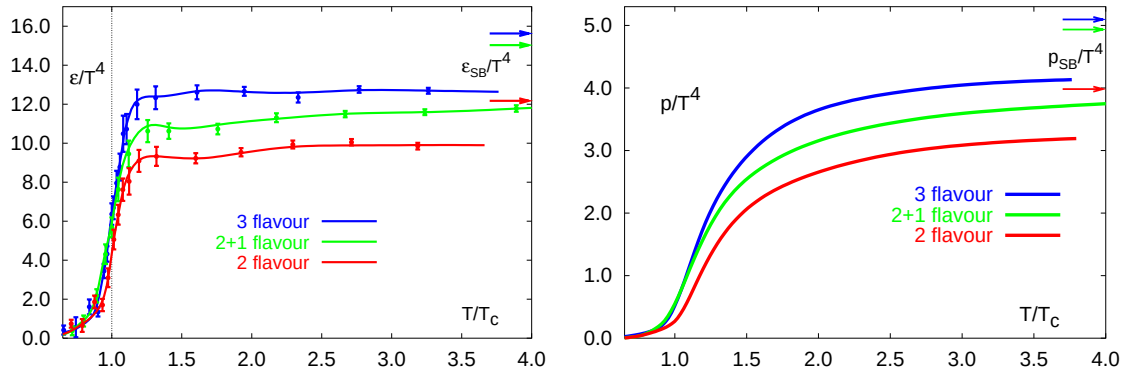

Figure 1.4: **Left:** Scaled energy density ε/T^4 as function of temperature T from lattice calculations. **Right:** Scaled pressure p/T^4 in QCD with different number of degrees of freedom as a function of temperature T. Both calculations are carried out with 2 or 3 light flavors or 2 light and 1 heavy flavor (s-quark). The arrows are the predictions with Stefan-Boltzmann limit corresponding to different number of flavors.

The QCD pressure can approach the ideal QGP phase value at infinite temperature due to the asymptotic freedom of QCD (the coupling strength becomes even weaker at higher temperature). As shown in the right panel of Fig. 1.4, the pressure strongly depends on the number of degrees of freedom [21]. Both of these calculations are based on $16^3 \times 4$ lattice and used the p4-improved staggered quark action with the Symanzik improved gauge [21].

1.3.1 QCD Phase diagram

The QCD phase diagram is shown in Fig. 1.5. The vertical axis shows the temperature while the horizontal axis the baryon chemical potential (μ_B). Under extreme conditions, like high temperature or high baryon chemical potential (or both), a phase transition between hadrons gas to partonic matter (so called quark-gluon plasma) is expected to occur, and in the latter quarks and gluons become free within volumes larger than the volume of the nucleon. At finite μ_B the white line shows the 1st order phase transition believed to separate the hadron state (below the line) from the quark-gluon plasma state (above the line). This line of 1st order ends at a possible critical point [22]. At even larger μ_B one expects to have other states of matter like the color superconductor state [23]. At small μ_B, a cross-over is expected between the first order phase transition from hadron gas to QGP [24][25] and is depicted in the diagram with a dashed line. Some experiment regions also are shown in the phase diagram with yellow and orange marks. In the diagram the

point corresponding to nuclear matter is also shown.

Deconfined partonic matter at large baryon chemical potential is considered to possibly exist in the interior of neutron stars [26], where the density of the nuclear matter is compressed many times more than normal nuclear matter.

The phase transition to the quark gluon plasma state can be achieved experimentally by "heating up" nuclear matter while colliding heavy nuclei at enormous energies, *i.e.* SPS, RHIC and LHC. The first few moments in the small region of the collision, the temperature can achieve larger values than the critical temperature, thus the QGP can be created.

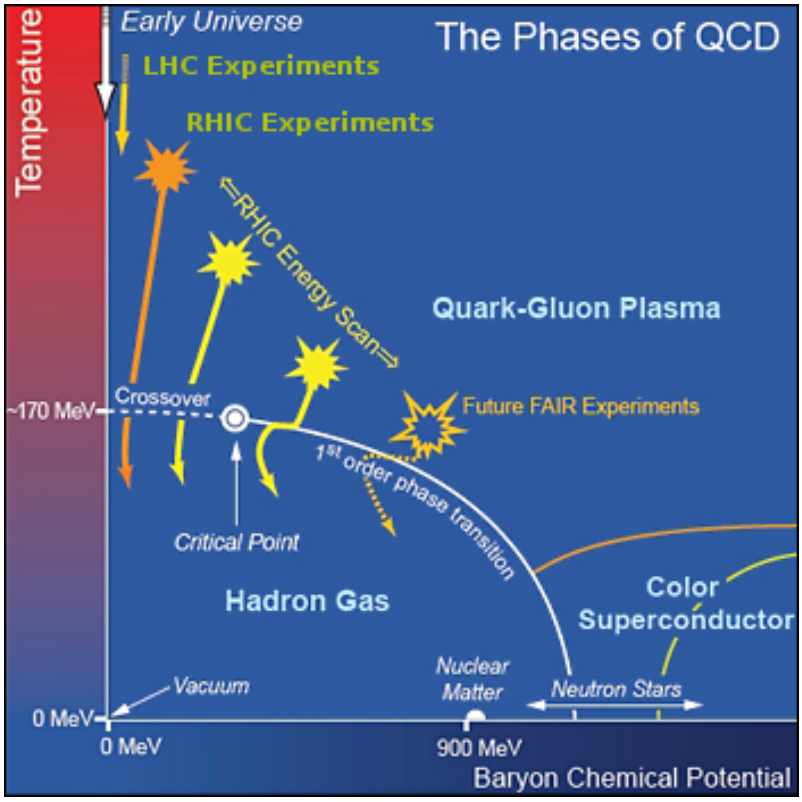

Figure 1.5: Figure of the QCD phase diagram of nuclear matter in terms of the temperature (T) versus baryon chemical potential (μ_B). The solid curve in white shows the phase boundaries for the indicated phases. The big solid circle depicts the critical point. At low μ_B a cross-over between the 2 phases is indicated. Possible trajectories for systems created in the QGP phase at different accelerator facilities are also presented (RHIC, LHC, and for the future FAIR...).

Locating this critical point is a great challenge both experimentally and theoretically. Current theoretical calculations are highly uncertain about the location of the critical point. At RHIC, a running program has started to search for the critical point by an energy scan using Au+Au collisions with energies between 5 GeV and

20 GeV, corresponding to μ_B values from about 100 MeV to 500 MeV.

According to the current cosmological model, it is believed that after the "Big Bang" [27] and after the electro-weak transition ($t \sim 10^{-11}$ s and $E \sim 1$ TeV), the QCD phase transition happened at $t \sim 10^{-6}$ s. Therefore, studying the phase transition to quark-gluon plasma also helps to understand the behavior of matter in the very early universe.

1.3.2 Space time evolution of a Heavy Ion Collision

In collisions of relativistic heavy ions due to the high energy density we expect the formation of QGP. Then this "fireball" will expand and freeze-out to normal state as hadron gases. The whole process would include the following steps: initial state, pre-equilibrium, QGP creation and hydrodynamics expansion, hadronization, hadronic phase (hadron gas) freeze-out. Fig.1.6 shows the comparison of the conditions between the case where there is QGP creation (in A–A collision) and the case where there is no QGP creation (like in pp collision) in two dimensions: time as a function of z coordinate (space).

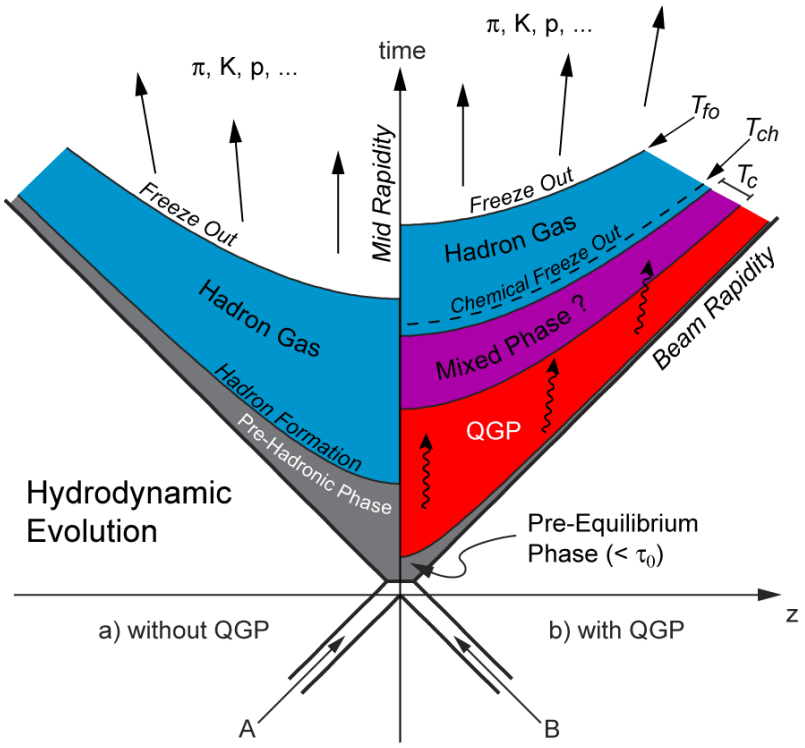

Figure 1.6: Evolution of relativistic heavy ion collisionin light cone. A/B represent the incoming protons or heavy ion. The z axis represent the space dimension. The left side of the time axis represent a collision evolution without QGP formation, while the right side represent the relativistic heavy ion collision evolution with QGP formation.

1.4 Experimental Relativistic Heavy Ion Collision Physics

The de-confined state of quarks and gluons can be achieved by colliding heavy nuclei at enormous energies, which is the only way we can use to study this state (QGP) in experiment. In the collision of high energy heavy nuclei, many nucleons can possibly create a big enough region with high energy density, thus QGP could be formed.

Therefore the experiment requires to have high energy heavy nuclei, which is possible with powerful accelerator. The powerful accelerators (like the Large Hadron Collider, LHC) can accelerate these ions up to several TeV, which means the speed of these ions are quite approaching the speed of light ($\beta = v/c \gtrsim 0.999999 \sim 1$). So this process is also called Relativistic Heavy Ion Collision.

In general, phenomenological effects from nuclear matter can be divided into two aspects: Modification effects in A–A collisions may be due to hot nuclear matter

(QGP) or to cold nuclear matter (CNM, such as shadowing/anti-shadowing[28–30] and intrinsic transverse momentum broadening [31]). As these processes can not be measured directly, the comparison of different collision systems (*pp*, *p*–A, A–A) are need to understand these effects. In *pp* collisions, there is no QGP created, as there will not be enough matter (participants) deposition in the collision region. In *p*–A collisions, there is no QGP created, but it contains an "A" (heavy ion) nuclei and CNM effects have been observed. Thus the CNM effect can be obtain by focusing on the comparison between the *p*–A and *pp* collision.

1.4.1 QGP evolution in A-A collisions

The interaction of participants from the colliding nuclei (the lead nuclei, $^{208}_{82}$Pb, is used in ALICE) will create a large bulk of matter with extremely high energy deposition in the collision region. This fireball will melt into a de-confined state (QGP) while equilibrium is achieved. The system will continues expanding fast and the QGP continue cooling down. The lifetime for QGP is ~ 10 fm/c at LHC. When the temperature falls down below the critical point ($T_c \sim 150$MeV), the de-confinement will break, partons will combine back to mesons and baryons. After the temperature falls to T_{ch} (*chemical freeze-out*), the particle yields are "freezed", but they are subject to elastic collisions, until the so called *kinematic freeze-out*. Later, the final hadrons (or their decay products) will fly over a macro distance, then they can be captured or measured by the detector

1.4.2 Centrality in Pb–Pb collision

As shown in fig. 1.7 the centrality of a collision of two nuclei can be expressed in terms of the impact parameter "*b*" which is inversely proportional to the overlap region of the two nuclei namely as b decreases, the collision of these two nuclei become more central. The spectators are the nuclei which did not take part in the interaction, the participants are those which took part.

In experiment, the direct measurement of parameter b is impossible, we use other measurement which can reflect the value of b. The centrality is defined as a percentage (from $0 \sim 100\%$) of the total nuclear interaction cross section. In general, the smaller b means the more central the collision, which will have more participants and also produce more hadrons. So the number of the (charged) hadron produced in an event can be used to estimate the b in experiment, thus also be used to estimate the centrality.

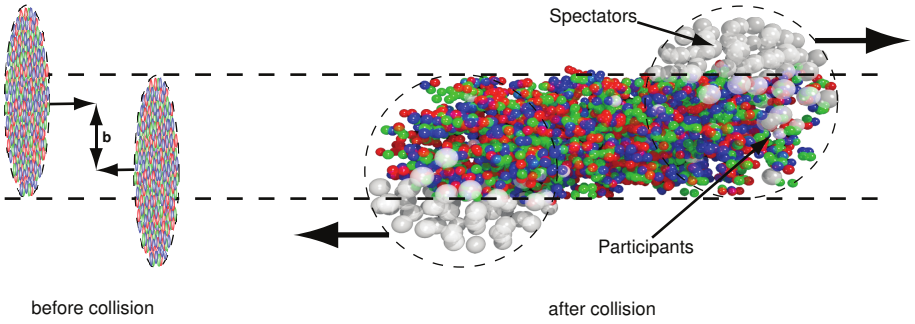

Figure 1.7: Geometry of a Pb-Pb collision, left figure represents the nuclei before collision, right figure represent the situation after collision. The spectators are the nuclei which did not take part in the interaction, the participants are those which did took part.

1.4.3 Physics processes: hard and soft processes

In *pp* collision, hard processes (introduced in details in section 2.1) are more "clean", that is they have less background than in A–A collisions, and the products from hard processes in *pp* collisions are expected to be explained by (p)QCD theory. In Pb–Pb collisions, the products from hard processes (known as "hard probes") can be used to verify the existence of QGP and measure characteristics of QGP. Because they are created in the early stage of the collision, they will interact during the full QGP expansion (see 1.3.2, if QGP exist), and will provide us with some information about the QGP. A lot more details will be given in chapter 2.

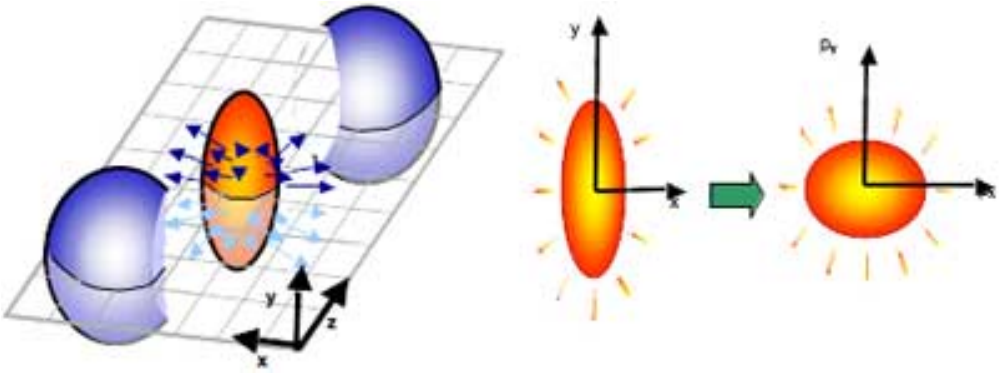

Figure 1.8: Left figure indicates the almond shaped interaction region in semi-peripheral relativistic heavy ion collision, where the gray grid represent the reaction plane which is a plane spanned by the impact parameter (***b***, along axis-x) and the beam axis (axis-z). The right figure shows that the anisotropies in coordinate space give anisotropies in the momentum space.

Different from hard processes, the soft processes, are dominated by non-perturbative QCD effects, which are much less understood. They create the so called "underlying event" to hard probes, like jets. The details on this topic will be introduced in

Section 2.1.3. In relativistic heavy ion collision, these soft processes can also be used to probe the QGP (the corresponding probes are known as "soft probes"). One such soft probe is the so called "flow". Flow refers to a collective expansion of bulk matter, arising from the density gradient from the center to the boundary of the created fireball in nuclear collisions. This so-called collective flow is accumulative over the whole system evolution, and it will be sensitive to the characteristics of the expanding matter, like the shear viscosity. This can be tested with hydrodynamic models, with which we can extract for example the value of the shear viscosity of the system.

The figure 1.8 demonstrates the creation of elliptic flow in mid-central relativistic heavy ion collision. Its definition is the second (largest) component of the Fourier decomposition of azimuthal distribution related to the reaction plane.

$$v_n(RP) =< cos[n(\phi - \Psi_{RP})] > \tag{1.5}$$

The results from RHIC can be explained by theoretical models based on ideal relativistic hydrodynamics with a QGP EoS and small shear viscosity. This result has been considered as one of the key evidences for QGP existence at RHIC. The results from ALICE have been included in Fig. 1.9. The increasing of about 30% compared to the RHIC energy agreed with models of hydrodynamic with viscous correction, see [32]. Detailed elliptic flow measurements of identified particles which clarify the role of radial expansion can be found in Ref. [33].

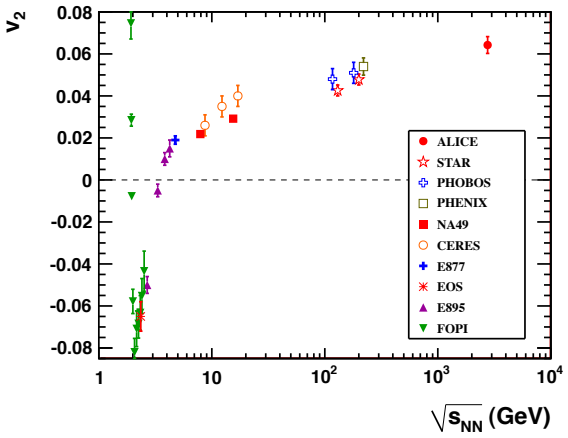

Figure 1.9: The integral v_2 from different experiment and the corresponding energy. Result from ALICE is the integral for $0.5 < p_T < 5$ GeV for the 20–30% centrality (mid-central) Pb–Pb collision at 2.76 TeV [3].

Chapter 2

Probing the Quark Gluon Plasma with Jets

The measurement of jets, introduced in this chapter, in heavy ion collisions is very promising to probe the transport properties of the deconfined QCD medium. Produced in a hard process in the early part of a collision, a hard parton (which initiates a jet at the parton level and then at the hadron one, see section 2.1) while passing through the hot and dense medium sees its physics properties modified giving birth to a modified parton shower with respect to what it should be in the vacuum. Mainly, its energy clears in the medium because of its interactions with the medium components. This phenomenon is known as jet quenching effect. It causes a jet yield suppression with respect to the vacuum reference as discussed in section 2.3.3. But looking at the structure of the produced parton shower itself, in other words at the fragmentation of the produced hard parton, one expects to measure its modification as the gluon radiation is modified all along the shower (see section 2.4.2). Several observable can then be experimentally measured to highlight this second phenomenon: the jet fragmentation functions, their profiles, their shapes, etc.

In this thesis work, we have focused our interest on the measurement of the jet fragmentation functions introduced in Chapter 6. However, this differential measurement is quite sensitive to the fluctuations of the background of heavy ion collisions, as explained in 2.3.2 which make it a challenging measurement. The biases generated by the heavy ion background could be overcome thanks to the study of a new observable: the jet Fragmentation Function Moments (FFM) as proposed in [1] which provide an alternative way to subtract background and deconvolute fluctua-

tions with respect to the traditional jet observables. This point will be introduced at the end of the chapter and motivates the present work. For the first time, the FFM are measured in pp collisions at $\sqrt{s} = 2.76$ TeV in the ALICE experiment. Our results presented in chapter 7 could be used in future as a reference with respect to the same study in $Pb-Pb$ collisions. In parallel, we also performed the corresponding FF measurement in pp collisions at $\sqrt{s} = 2.76$ TeV. The corresponding analysis is presented in chapter 6.

2.1 Jet production in binary nucleon–nucleon collisions

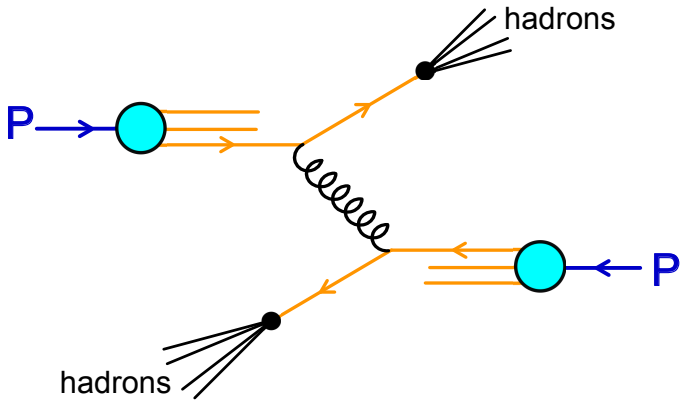

Figure 2.1: **$2 \to 2$ process**: schematic of hard process in p–p collision. Two quarks (q and q') from different proton interact, exchanging a gluon with large momentum. initial/final state radiation are marked in green/red. The collimated final hardons from the out-going partons are also showed.

2.1.1 Towards jet definition

Figure 2.1 maps the production of jets in a typical $2 \to 2$ pQCD hard process. In such process, two ingoing partons from the incident nucleons interact with each other via a hard scattering with gluon exchange and form two outgoing hard partons. These two highly energetic partons first radiate gluons giving birth to two parton showers (not shown in Fig. 2.1) before the hadronization occurs. Experimentally, the whole process results in the production of two sprays of hadrons. Three definitions of a jet can be given at that stage. The jet can be either defined as the outgoing hard parton produced, either defined as the parton shower itself (jet of partons), but also at the hadron level as the shower of hadrons (jet of hadrons).

Whatever the level of definition, energy should be conserved. Moreover, the parton radiation in the shower is by no means arbitrary. Color coherence effects of QCD imply an angular ordering in the way the partons are produced and emitted in the shower [34]. Because of the presence of colored objects in the shower, each new gluon radiated in the parton shower has an emission constrained in a given angle with respect to the previous emission. Moreover, the parton emission is stopped at some point in the shower or can not occur below a given emission angle. Both aspects directly impact the global structure of the jet produced both at the parton and hadron levels. It will be discussed later on in the chapter (see section 2.4.2).

The jet definition can be a bit "modified" by pQCD higher order effects such as the initial and final state gluon radiations as shown in the figure. Both aspects correspond to the emission of a gluon (not necessarily soft) by the incoming partons before the hard process occurs or by the outgoing hard partons just after the hard process. This parton emission can modify the kinematics and the shapes of the jets produced.

2.1.2 Factorization theorem

The production cross section of the outgoing hard partons illustrated in Fig. 2.1 is safely predicted by pQCD calculations. The factorization theorem allows to express the jet production cross-section as the product of independent terms dissociating the hard process from processes occuring before or after at different energy scales. The whole production cross-section of jets from two incoming nuclei A and B is illustrated by the simple diagram in Fig. 2.2 and can be expressed as the convolution of three different terms as in equation 2.1 dissociating perturbative and non-perturbative terms.

$$E_h \frac{d\sigma}{d^3 p_h} = \sum_{abcd} \int f_{a/A}(x_a, Q^2) f_{b/B}(x_b Q^2) D_{i\to h}(z, Q^2) \frac{d\sigma_{ab\to cd}}{d\hat{t}}(x_a, x_b, Q^2) \qquad (2.1)$$

In equation 2.1, the two non-perturbative terms are :

- $f_i, I(x_i, Q^2)$ (i=a or b and I=A or B): the parton distribution functions (PDF). A PDF describes for example in the case of the nucleus A, the probability to find a parton of flavor a and of momemtum fraction x=$p_{parton}/p_{nucleus}$ in this nucleus. Several researches by different groups on PDF exist, like Martin-Stirling-Thorne-Watt (MSTW) [35], the Coordinated Theoretical-Experimental

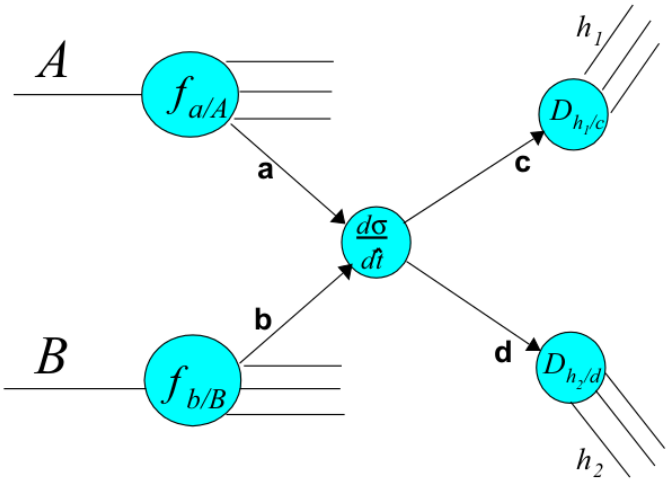

Figure 2.2: Illustration of a dijet production in the formalism of the factorization theorem in hadronic collisions. $f_{a,b}$ are the parton distribution functions and $D_{i\to h}$ the fragmentation functions.

project on QCD (CTEQ) [36], Neural Network Parton Distribution Functions (NNPDF) [37], ...). In this thesis, the CTEQ PDF has been used in MC simulations.

- $D_{i\to h}(z, Q^2)$ (i=c or d): the fragmentation function. It describes the probability that the outgoing parton i hadronizes in a final hadron h with a momentum fraction z=p_{hadron}/p_{parton}. It includes the gluon radiation described by the DGLAP[1] equation until Q reaches $Q_0 \sim 1$ GeV and the final hadronization of low p_T partons extracted from the combined fits of DIS experiment data.

The perturbative term $d\sigma_{ab\to cd}/d\hat{t}$ represents the production cross-section of the 2 to 2 hard process. It can be pQCD calculated, Q being defined as the momentum transferred between the partons a and b.

2.1.3 Underlying event

In a pp collision, besides the hard process and the following hadronization, the remaining fragments of 2 protons (like A and B in fig. 2.2) will also hadronize and dominate in the forward/backward regions at large pseudo-rapidity. They contribute to the underlying event (UE) of the collisions, as soft processes, multiple interactions between the remaining partons, beam-beam remnants, etc. Note that in the case of

[1] Dokshitzer, Gribov, Lipatov, Altarelli, Parisi [38] [22] [39]

heavy ion collisions, the background to take into account is even more complicated. It will be discussed in more details in the section 2.3.2 below.

2.2 Jets in experiment

Experimentally, jets can't be directly measured at the parton level as only hadrons are confined objects. A jet can be seen as the detector response to a collimated shower of particles. Several experimental definitions of what is effectively a jet were translated in jet reconstruction algorithms over the years starting in 1977 by Sterman and Weinberg [40]. The different algorithms have progressed a lot since then [41–45] as well as the criteria defining what should be a "good jet". Among the different expected criteria defining a good jet, we would like to emphasize 3 points: i) the reconstruction algorithm should be applicable both at the experimental and theoretical levels ; it should be insensitive to both ii) collinear and iii) infrared divergences [44] . In case of points ii) and iii), it means that the algorithm should not change the reconstructed jets (in number and hardness) as a function of the order considered.

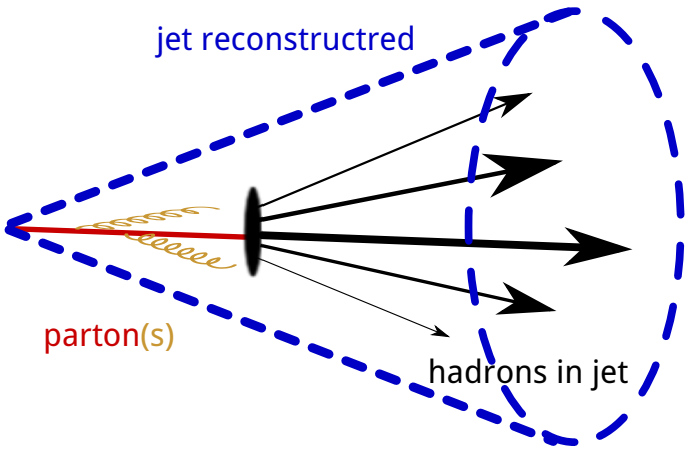

Figure 2.3: jet after reconstruction

The jet reconstruction algorithms can be classified in two categories: the cone based and the sequential based algorithms. Both of them depends on the jet resolution parameter $R = \sqrt{(\Delta\eta)^2 + (\Delta\phi)^2}$ ($R = \sqrt{(\Delta y)^2 + (\Delta\phi)^2}$ in modern algorithms) which defines the region of the reconstructed jet in the $\eta - \phi$ plane as illustrated in Fig. 2.3.

Cone based algorithms gather particles within specific conical angular regions (using R as the jet radius). The cone axis is obtained by summing of momenta of its

constituents in the cone. Since the radiation and hadronization of hard parton do not change the direction of its energy flows, a stable cone is physically close to the direction (jet axis) and energy (sum of energy in the cone) of the original parton. The various cone algorithms distinguish mainly by two criteria: the strategy used for searching stable cones and the procedures used to split/merge particles.

Sequential recombination algorithms start with combining particles with some given conditions until no particle in the considered phase space satisfy the selection criterion. Different sequential recombination algorithms are identified by their criteria. In this thesis, the anti-k_T algorithm is used for jet reconstruction [46], and the k_T algorithm is used for the background estimation as suggested in [47]. Both algorithms are included in the FASTJET package [48].

2.2.1 jet production cross-section

In hard processes, the energy transferred between the 2 incoming parton projected in the transverse plane (E_T) directly comes from the hard interaction, therefore, it is commonly experimentally used to express the jet production cross-section as in equation 2.2 where $\mathcal{L}^{int}$ is the integrated luminosity, ΔN_{jets} is the number of jets in the region ΔE_T, $\Delta\eta$, η being the pseudo-rapidity.

$$\frac{Ed^3\sigma}{dp^3} \equiv \frac{d^3\sigma}{dp_T^2 dy} = \frac{1}{2\pi E_T}\frac{d^2\sigma}{dE_T d\eta} = \frac{1}{2\pi E_T}\cdot\frac{1}{\mathcal{L}^{int}}\frac{\Delta N_{jets}}{\Delta E_T \Delta\eta} \tag{2.2}$$

Usually, the mass of the parton is neglected so that $E_T = p_T$ and the measurement is performed in the central pseudo-rapidity interval $|\eta| < 1$ and the results are integrated on the interval.

Figure 2.4 shows the invariant production cross section of inclusive jets as a function of transverse energy (E_T) measured in proton-anti-proton $\sqrt{s}$ =1.8 TeV collisions at Tevatron [49]. The Jet Clustering algorithm (JetClu) has been used to reconstruct the jets with $R = 0.7$. The R_{sep} is used to merge/separate the jet candidates. The cross section spans more than seven orders of magnitude from low E_T jets of 50 GeV to $\sim$ 400 GeV jets. The solid line is the EKS NLO pQCD calculation with CTEQ4M parton distribution function [49]. A good agreement with the theory is observed over the full E_T range within the error bars apart from the extremely higher E_T region, where the theory lightly underestimates the measurement considering only the statistical errors.

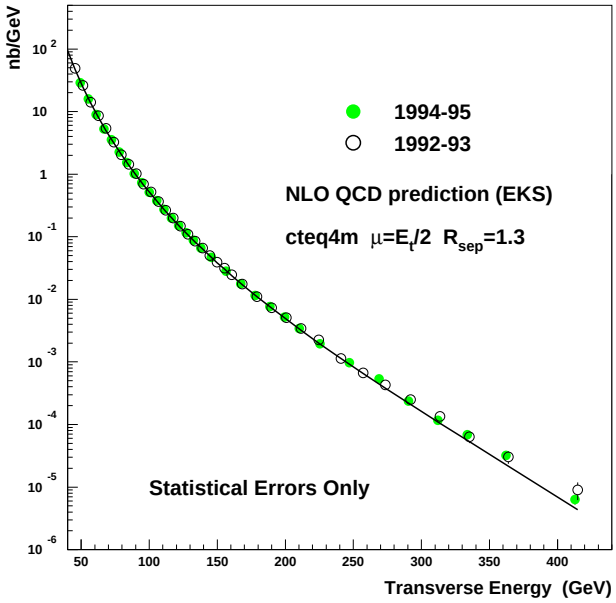

Figure 2.4: Inclusive jet cross section from the Run 1B data (94-95) compared to a QCD prediction and to the published Run 1A data (92-93) ($0.1 < |\eta| < 0.7$).

2.3 Jet measurements with the ALICE detector and background issues

2.3.1 Out-of-cone and charged-to-neutral fluctuations

In ALICE, two types of jets can be reconstructed: i) charged jets from the combination of the momenta of the charged particles measured in the Central Tracking System (see chapter 3.4) and ii) full jets from the combination of the charged jets with the electromagnetic components measured by ALICE electromagnetic calorimeters (see section 3.4 and chapter 4). In both cases, the reconstruction is first limited by the detector acceptance which prevents to reconstruct the jets with a large R parameter which implies out-of-cone fluctuations [50]. In the case of charged jets, charged to neutral fluctuations tarnish even more the reconstruction procedure whereas in the case of full jet reconstruction, part of the neutral component can't be measured ($\sim$ 10%). In any case, both the mean reconstructed energy and the reconstruction resolution are biased and smear the reconstructed jet spectrum which is steeply falling with the jet p_T. See [51] [52] or more details. Unfolding technics are usually used to correct the data with different methods [53–56].

2.3.2 Jet contamination by the collision background

Contamination in pp collisions

The background contamination of jets in pp collisions is mainly due to particles which are not originating from the hard process and is not a big issue for jet analyses. Taking into account the event multiplicity in pp collisions which is really small compared to nucleus-nucleus collisions ($dN_{ch}/d\eta \simeq 6$ in pp collisions of this analysis against $dN_{ch}/d\eta \simeq 1600$ (35) in most central (peripheral) $Pb-Pb$ collisions at 2.76 TeV [57]), the UE contribution to the jet reconstruction is really small compared to the detector effects discussed in the previous section. However, we can estimate its contribution event-by-event for instance by opening a cone perpendicularly (keeping the same η) to the di-jets axis produced in the collision and summing the track momenta located in the corresponding cone. This method is also used to subtract the (track) background from fragmentation distributions.

$$p_{\mathrm{T,jet}} = p_{\mathrm{T,rec}} - \sum_{\mathrm{Area}} p_{\mathrm{T,track}},$$

An alternative background subtraction approach is based on MC models [58].

Today a ρ based background subtraction method proposed in [47] and presented section 2.3.2 is commonly used to subtract the UE from a jet spectra.

The corresponding contribution of the background in transverse momentum density is between 0 and 2 GeV/c per unit area (η–ϕ space), which is small compared to the reconstructed jet energy. The associated "fluctuation" can be considered in the pp case as uncertainties of the UE. For $R = 0.2$, the uncertainties to the energy fraction is 0.2% for low p_{T} jets ($p_T^{jet} = 25$ GeV/c) and negligible for high p_{T} jets ($p_T^{jet} = 100$ GeV/c); for $R = 0.4$, the uncertainties to the energy fraction of the order of 1.0% for low p_{T} jets and 0.3% for high p_{T} jets[59]. In most of the cases, it can be neglected compared with the detector effects listed in the previous paragraph which are one order higher.

For the more differential observables such as the one listed in section 2.4 which are studied in ALICE in bins of jet p_T, the background correction is applied to each $p_{\mathrm{T}}^{\mathrm{jet}}$ bin. From the study of charged jets, the background uncertainties for these variables (σ_{jet}, $< N_{ch} >$, R_{80}, $< dp_T^{sum}/dr >$, z, ξ, etc.) are much smaller than the one associated to the track efficiency and to the p_{T} resolution [5].Another contribution to the background comes from the secondary particles in pp collisions, like photon conversion, interaction in material (detector), decays from charged pion

and strange particle. But the contribution is also small, comparing to the detector effects [5].

The UE background and its fluctuations in AA collisions

One of the main experimental difficulties of measuring jets in heavy-ion collisions is the estimation and the subtraction of the fluctuating background (contribution from the underlying event). In ALICE, the background energy density is estimated by clustering the whole event with the k_T–algorithm and calculating the density $\rho = \text{median}(p_T^{jet,i}/A^{jet,i})$ (where A is the area of a given jet, i calculated with the active ghost area method) for every (background) jets except the two leading ones which are more likely to be the signal jets, as proposed in [47].

The average background density is then subtracted from the p_T of signal jets (found using anti-k_T algorithm) as:

$$p_T^{jet\,sub} = p_T^{raw} - \rho \cdot A, \tag{2.3}$$

where p_T^{raw} is the uncorrected jet p_T, A is the area of the anti-k_T jet and ρ is estimated for charged only (using 2010 data [60]) and full (charged + neutral) jets (using 2011 data [61]). The left panel of Fig. 2.5 illustrates how the charged background density measured by the ALICE collaboration in $Pb-Pb$ collisions at $\sqrt{s_{NN}} = 2.76$ TeV scales with the charged particle multiplicity ($\rho \sim$ N $\times <$ p_T $>$). The right panel of the figure shows its evolution with the collision centrality as well as the "scaled" ρ extrapolated from the charged one (1.5 times $\rho_{charged}$) to estimate the full background density. Naturally, $\rho_{charged}$ increases linearly with the number of tracks in the event and decreases from most central to most peripheral collisions.

After subtraction, the corrected jet spectrum is still affected by the background fluctuations as shown in Fig. 2.6. The left p_T spectrum is for charged jets reconstructed with R = 0.2 in the most central $Pb-Pb$ collisions at 2.76 TeV at mid-rapidity while the right one is for jets reconstructed with R = 0.3. The spectra reach 100 GeV/c. In the figures, three spectra a systematically compared in both cases applying or not a cut on the leading track p_T inside the jet (no cut: circles, $p_T^{leading\,track} > 5$ GeV/c : cross and $p_T^{leading\,track} > 10$ GeV/c).

Increasing the cut on the leading track p_T reduces the number of combinatorial background jets in the low p_T region from the background fluctuations. Note that this p_T cut helps stabilizing the unfolding procedure. We observe that above a given jet p_T, the cut has no effect anymore showing that this p_T cut only biases the low jet p_T region.

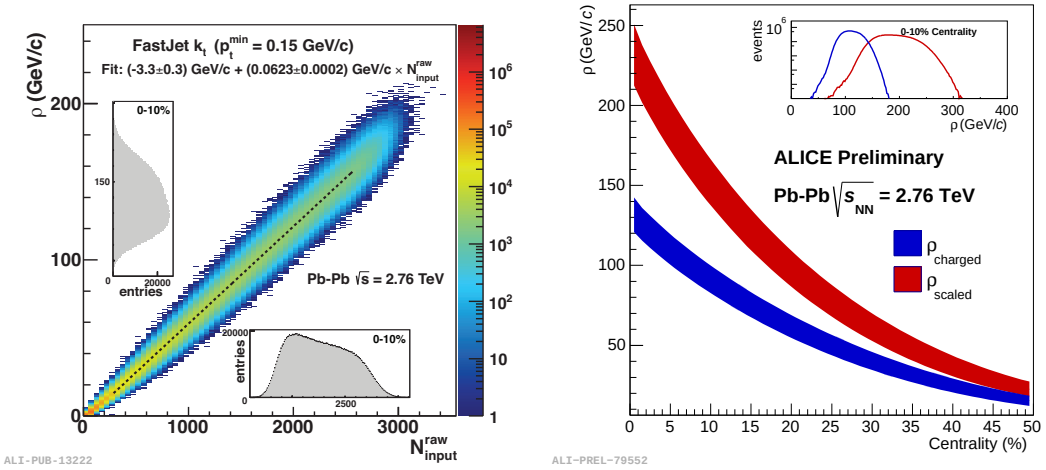

Figure 2.5: **Jet Background**: Background energy density in ALICE for 2.76 Pb–Pb collisions. The left one is ρ v.s. "track (charged particle) multiplicity" for charged particle. The right one is ρ v.s. centrality for charged and the scaled (represent for all particles).

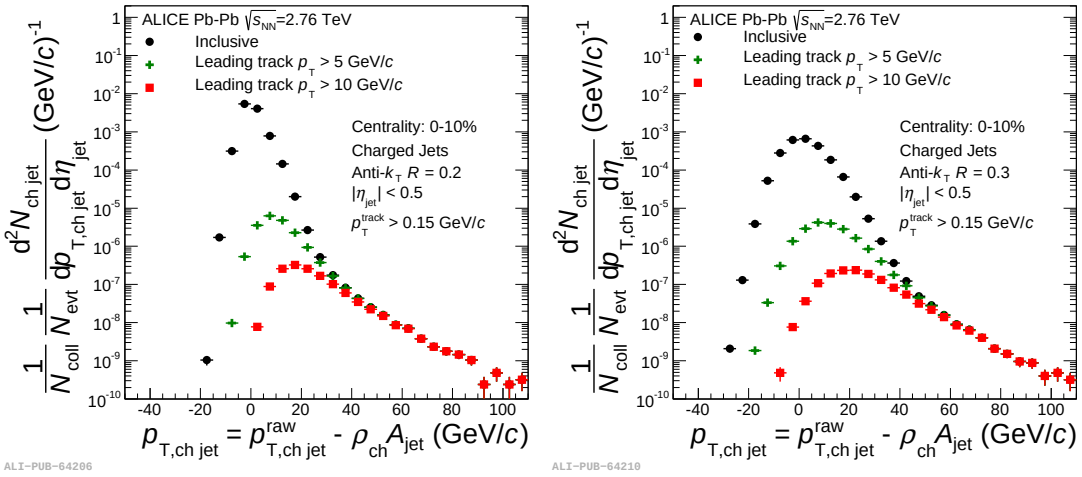

Figure 2.6: **Background Subtracted Spectra**: charged jets spectrum with background subtracted in most central Pb–Pb collision at 2.76 TeV. Left is for $R = 0.2$, right one is for $R = 0.3$

In addition, point-to-point background fluctuations δp_T (as defined by equation 2.4) were estimated by placing random cones in the measured events, or by embedding a known (high p_T) probe in the event and then looking at the collection of jets found by the anti-k_T algorithm and matched to the embedded probe [62, 63].

$$\delta p_T = p_T^{jetsub} - p_T^{probe} = p_T^{raw} - \rho \cdot A - p_T^{probe} \tag{2.4}$$

The δp_T distribution is then fitted with a Gaussian and the width (σ) of the distribution is extracted. The corresponding σ_{ch} and σ_{ch+em} were estimated for a given jet radius from R = 0.2 to R = 0.4 [64] . Results from the standard method, "Random Cones", are shown in the left panel of Fig. 2.7 for R = 0.2 and R = 0.3.

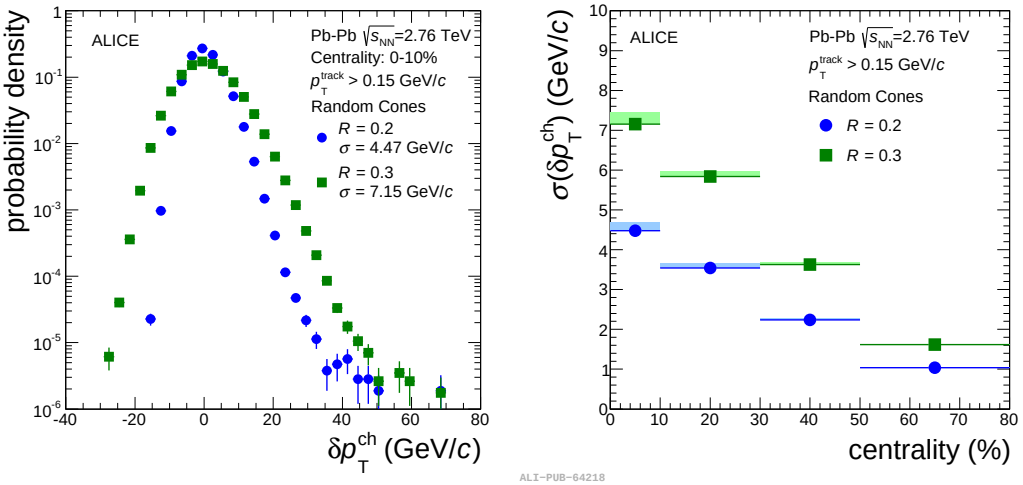

Figure 2.7: **Background Fluctuations**: Left: $\delta p_{\mathrm{T}}^{ch}$ distribution in most 10% central Pb–Pb collision at 2.76 TeVobtained for R = 0.2 (circles) and R = 0.3 (squares). Right: width of the $\delta p_{\mathrm{T}}^{ch}$ distribution as a function of the collision centrality and R.

For smaller reconstructed jets radii, the total energy inside the cone is smaller and consequently, the corresponding background fluctuations are also reduced. $\sigma_{ch} \simeq 7.2$ GeV/c was measured for R = 0.3 compared to $\sigma_{ch} \simeq 4.5$ GeV/c for R = 0.2. When neutral particles are included, the jet energy resolution increases, but the background fluctuations also become larger: $\sigma_{ch+em} > \sigma_{ch}$. For instance, for R = 0.3, $\sigma_{ch+em} \simeq 9$ GeV/c and $\sigma_{ch} \simeq 7$ GeV/c. Eventually, the width of δp_T is larger in the central collisions than in peripheral collisions and is larger for larger values of R as shown in the right panel of the figure as it increases with the track multiplicity. We are thus facing a conflict between increasing the reconstruction parameter R for a better control of the reconstructed jet energy and resolution and the consequences of strongly increasing the background fluctuations contribution in the given R.

We will first focus on the measurements of jet Nuclear Modification factors and on their limitations before to introduce semi-inclusive tools such as "Recoil-jet" [65] developed by ALICE in order to help with the limitations introduced by background effects.

2.3.3 The nuclear modification factor of jets and its limitations

In central heavy-ion collisions, the jets interact with the dense and hot partonic medium formed in these collisions and are expected to lose significant amount of energy, resulting in differences in the p_T dependence of jet production with respect to pp collisions. In the past, several measurements have contributed to highlight this "quenching" phenomenon as for example a hadron nuclear modification factor lower than unity observed by PHENIX experiments [66, 67] or the first away-side jet peak suppression observed by the STAR experiment in 2003 [68].

The nuclear modification factor of hadrons defined according to equation 2.5 is an inclusive measurement which allows to distinguish what are currently called initial and final states effects.

$$R_{\mathrm{pA/AA}} \equiv \frac{\mathrm{d}\sigma_{\mathrm{pA/AA}}/dp_{\mathrm{T}}}{< T_{\mathrm{AA}} > \mathrm{d}\sigma_{\mathrm{pp}}/dp_{\mathrm{T}}} = \frac{dN^{had/jets}_{pA/AA}/dp_T}{< N_{coll} > dN^{had/jets}_{pA/AA}/dp_T} \times \frac{N^{events}_{pp}}{N^{events}_{pA/AA}}, \tag{2.5}$$

In equation 2.5, T_{AA} is the average nuclear overlapping function in a given event activity in A–A or (p–A) collisions and $< N_{coll} >$ is the average number of binary collisions. In the absence of nuclear modifications, hard processes are expected to follow the N_{coll} scaling. The corresponding nuclear modification factor would then be unity ($R_{AA} = 1$). In the contrary, a deviation from unity can sign nuclear modifications due to initial state effects such as Cronin effect for a R_{AA} larger than one, or some final state effects due to the dense medium for a R_{AA} smaller than one. Studying the R_{AA} of hadrons only gives a partial view of the quenching phenomenon as it consists in measuring the "leading" part of a jet. One can go a step further by measuring directly the jet nuclear modification factor also defined at the jet level by equation 2.5.

In order to understand nuclear modification of jets not due to the dense medium produced at the LHC, the ALICE experiment has measured the jet nuclear modification factor in $p-Pb$ collisions: R_{pA} defined as in equation 2.5.

Figure 2.8 shows the R_{pPb} of charged-particle jets reconstructed with $R = 0.2$ (left) and $R = 0.4$ (right) in $p - Pb$ collisions at $\sqrt{s_{\mathrm{NN}}} = 5.02$ TeV measured by ALICE [69]. For this measurement, the pp reference has been obtained by re-scaling the spectrum measured at $\sqrt{s} = 7$ TeV.

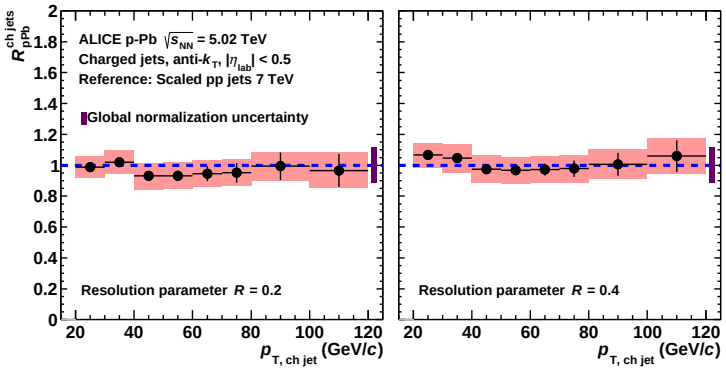

Figure 2.8: R_{pA} **at ALICE**: the two figures represent the R_{pA} of charged jets from $p-A$ collisions in ALICE at 5.02 TeV with different resolution parameters ($R = 0.2/0.4$). The reference is from a scaling of 7 TeV pp collision data.

First of all, in both cases, the R_{pPb} does not show any enhancement in the low jet p_T region. It suggests the absence of strong cold nuclear matter (CNM) (like Cronin effect) effects on jet production at LHC. Comparing this result with lower energy experiments as RHIC, where the Cronin effect is obviously seen [70], at LHC, it seems that the main contribution to the Cronin enhancement from initial-state multiple scattering is compensated by nuclear PDF shadowing in agreement with EPS09 model calculations [30]. Moreover, the R_{pPb} is consistent with unity within uncertainties over the full p_T range covered by the measurement. It shows that no suppression is measured in the high p_T region in favor of the absence of final state effects in $p - Pb$ collisions. It also suggests that if a suppression is measured in $Pb - Pb$ collisions, it should be due to the presence of a QCD medium. This conclusion is consistent with the one obtained for single particle measurement [71].

Using the charged jet spectrum measured in 2 centrality classes from 2011 $Pb-Pb$ data combined with the differential cross-section measured in pp collisions, a jet R_{AA} was obtained in 0-10% central (left panel of Fig. 2.9) and 10-30% more peripheral (right panel of Fig. 2.9) collisions.

A strong jet suppression, similar to the hadron R_{AA} is observed for central events, suppression which is slightly decreasing with increasing jet p_T. For more peripheral events the suppression is a bit less pronounced. This implies that the full jet energy is not captured by jets with R= 0.2 in $Pb - Pb$ collisions. Moreover, as the $p - Pb$

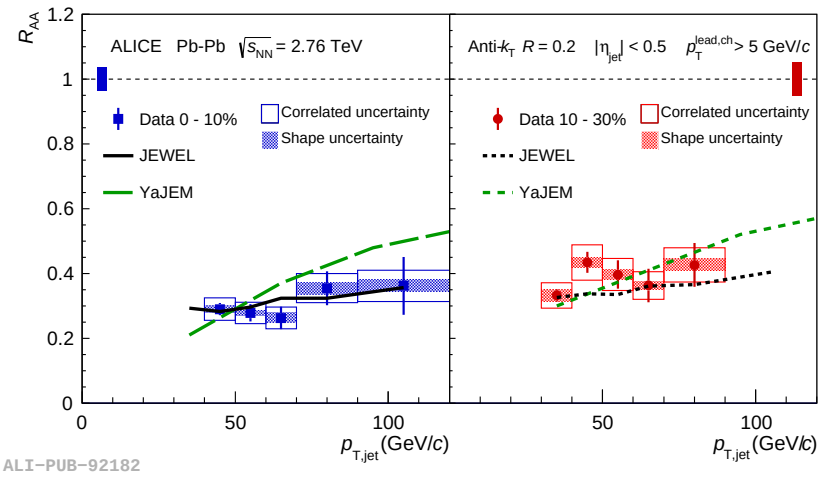

Figure 2.9: R_{AA} **at ALICE**: Nuclear modification factor of fully reconstructed jets, using the Anti-k_T algorithm with $R = 0.2$, in Pb-Pb collisions at 2.76 TeV. Jets are reconstructed in $|\eta| < 0.5$ and are biased requiring a leading charged particle $p_T > 0.5$ GeV/c.

measurement has shown the absence of CNM, it suggests the observed suppression comes from the hot medium produced. The same effect is, within uncertainties, reproduced by JEWEL [72] and YaJEM [73] predictions in which the energy exchange between hard partons and medium components is modeled by path length in medium and the transport coefficient $\hat{q}$ (which reveals the strength of the interaction between the parton and the media). This $\hat{q}$ is proportional to the density of the medium.

Even if this suppression was initially explained by medium induced large angular gluon radiations[2], more differential measurements (introduced later in the chapter) such as jet fragmentation function studies in $Pb-Pb$ collisions have shown that the global structure of the jet close to the jet axis was not modified in medium [74, 75]. Jet R_{AA} measurement suffer from several experimental biases such as leading track p_T cut (which biases the jet fragmentation), out-of-cone fluctuations and surface biases which prevent to give a direct physics interpretation of the suppression. All these aspects are briefly discussed in the next sections. In order to fully quantify the measured jet quenching, additional measurements are ongoing in order to study the radius and the centrality dependence of jet R_{AA} but also, more differential observables have been introduced in order to understand how the fragmentation works in medium.

[2]They imply that part of the initial parton energy redistributes into the direction far away from the jet axis in heavy-ion collisions and results in the observed jet yield suppression with respect to the pp reference

2.4 Jet shape-related observables

Experimentally several jet shape-related observables can be explored to quantify the medium induced small angular gluon radiation inside the jet cone, such as:

- $< N_{\text{constituents}} >$: the average number of constituents in jets.
- $< R_{80} >$: the average radius from jet axis which contains 80% of the jet energy (p_T).
- $< \mathrm{d}p_T^{\text{sum}}/\mathrm{d}r >$: the average energy ($p_{\mathrm{T}}$) density in jets as a function of the distance from the jet axis.
- j_{T}: the transverse profile jet constituents.
- $\delta\theta$: the angular distribution between the jet axis and jet constituents.
- $f(z \text{ or } \xi)$: the transverse momentum fraction distribution of jet constituents, where $z = p_T^{\text{constituents}}/p_T^{\text{jet}}$ and $\xi = -\log(z)$.

however, they can be highly sensitive to the heavy ion background which strongly biases the jet reconstruction as explained in the previous section.

2.4.1 Solution to background fluctuation effects

There are so far few observables which have been proposed to overcome the biases induced by the background fluctuations in jet analyses. We will now discuss "recoil-jet" measurements. Fragmentation function moments were also proposed as a way to overcome the limitations introduced by background fluctuations. They will be introduced in section 2.4.2

Hadron-jet correlation and the physics of "recoil-jets"

Both di-hadron and hadron-jet correlations are sensitive to the di-jet structure expected from hard scattering. Model calculations show that a high p_T hadron trigger induces a geometrical bias towards jets generated close to the surface of the fireball (surface bias) [76, 77]. The jet population recoiling from such a trigger is biased towards larger in-medium path length. Such a scheme is illustrated in Fig. 2.10 where the trigger hadron close to the surface of the fireball and the correlated jet are "back-to-back" in the transverse plane.

To exploit that effect, a jet-hadron measurement was made [65], using 2010 Pb-Pb data, based on the semi-inclusive distribution of reconstructed charged particle jets (using anti-k_T with R = 0.2 and 0.4) recoiling from a high p_T trigger hadron. The distribution of recoil jets is measured by counting the number of jets in the

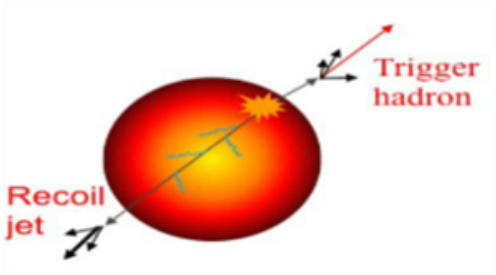

Figure 2.10: **Hadron-jet correlation**: Schematic view of a hadron triggered recoil jet in the QGP. The high p_{T} hadron triggers a biased recoil jet in the opposite direction in azimuth.

event within ϕ(trig) - ϕ(jet) $< \pi$ - 0.6 and normalized to the corresponding number of triggers. Hadron triggers are selected with $p_T > 10$ GeV/c in order to select a single hard process in the collision. The recoil jet distribution (measured in 0–10% central Pb-Pb collisions), plotted as function of the jet $p_T^{jet\,sub}$ defined in equation 2.3 is shown Fig. 2.11. For jet $p_T < 20$ GeV/c the shape of the distribution is identical for all choices of trigger p_T. This p_T region corresponds to combinatorial background jets. For jet $p_T > 20$ GeV/c a clear evolution with the trigger p_T can be seen. This region, dominated by high Q^2 events, corresponds to the "signal" part of the recoil jet spectrum which depends strongly on the trigger p_T (as a consequence of the trigger bias effect: the p_T of selected partons increases while increasing the trigger p_T). To get rid of the combinatorial jets (in a purely data driven way []), the difference called Δ_{recoil} of two measured jet distributions with hadron triggers in different p_T intervals is used:

$$\Delta_{recoil}(p_{T,jet}^{ch}) = Y(p_{T,jet}^{ch}; p_T^{min}, p_T^{max}) - Y(p_{T,jet}^{ch}; p_{T,ref}^{min}, p_{T,ref}^{max}) \tag{2.6}$$

with

$$Y(p_{T,jet}^{ch}; p_T^{min}, p_T^{max}) = \frac{1}{N_{tr}} \frac{dN(p_{T,jet}^{ch}; p_T^{min}, p_T^{max})}{dp_{T,jet}^{ch}} \tag{2.7}$$

In addition, this method does not impose any bias on the fragmentation of the recoil jets. The resulting Δ_{recoil} distribution (which is free of combinatorial jets) is then unfolded using both χ^2 minimization and the Bayes theorem. The difference between the two methods contributes to the anti-correlated shape uncertainty shown in Fig. 2.11. In the same way as for the R_{AA}, the Δ_{recoil} is interesting to better constrain quenching effect by looking at its ratio with the same quantity in pp collisions. This ratio is defined as the $\Delta I_{AA} = \Delta_{recoil}^{Pb-Pb}/\Delta_{recoil}^{PYTHIA}$ using PYTHIA in the denominator because, so far, the statistic in pp collisions is too limited in the high

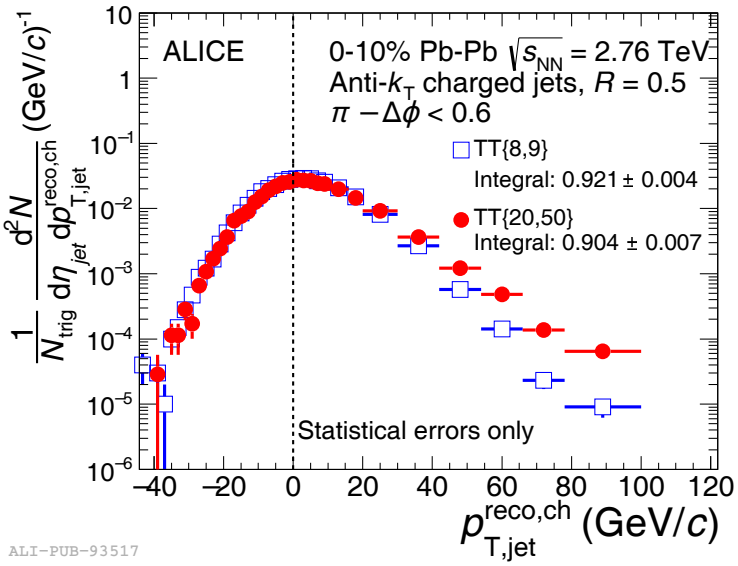

Figure 2.11: **Recoil jet spectrum**: The charged "recoil jet" spectrum in the most 10% central Pb–Pb collision at 2.76 TeVwith anti-k_T algorithm, $R = 0.5$. The recoil jet is selected in $\pi - \Delta\phi < 0.6$ with respect to the trigger hadron. The latter (the reference from the hard process) is selected in the p_T window [8, 9] (GeV/c) (TT{8, 9}), or [20, 50] (GeV/c) (TT{20, 50}).

p_T region. ΔI_{AA} is presented in Fig. 2.12 for three different jet resolution parameters R=0.2 (top left), R=0.4 (top right) and R=0.5 (bottom) with a p_T cut on the jet constituents of 0.15 GeV/c. Overall, $\Delta I_{AA} \simeq 0.6 - 0.7$ with no visible broadening of recoil jets from R = 0.2 to R = 0.5. In addition, the comparison of these distributions (relative to PYTHIA) does not indicate a large energy redistribution towards lower p_T constituents. Note that this observable present no limitation with respect to the value of R in contrary to all the other jet observables studied to characterize the quenching phenomena. It is not at all dependent of the background fluctuations. The ratios of $\Delta_{recoil}(R = 0.2)/\Delta_{recoil}(R = 0.4 or 0.5)$ as shown in Fig. 2.13 compared to the same ratios obtained with PYTHIA distribute similarly versus the jet p_T within the error bars. It suggests no significant medium induced broadening of the intra-jet energy profile.

2.4.2 Jet fragmentation functions and jet fragmentation function moments

Color coherence effect previously introduced (cf. section 2.1.1) which "constrains" the development of a jet directly impacts the way the charged particle momenta

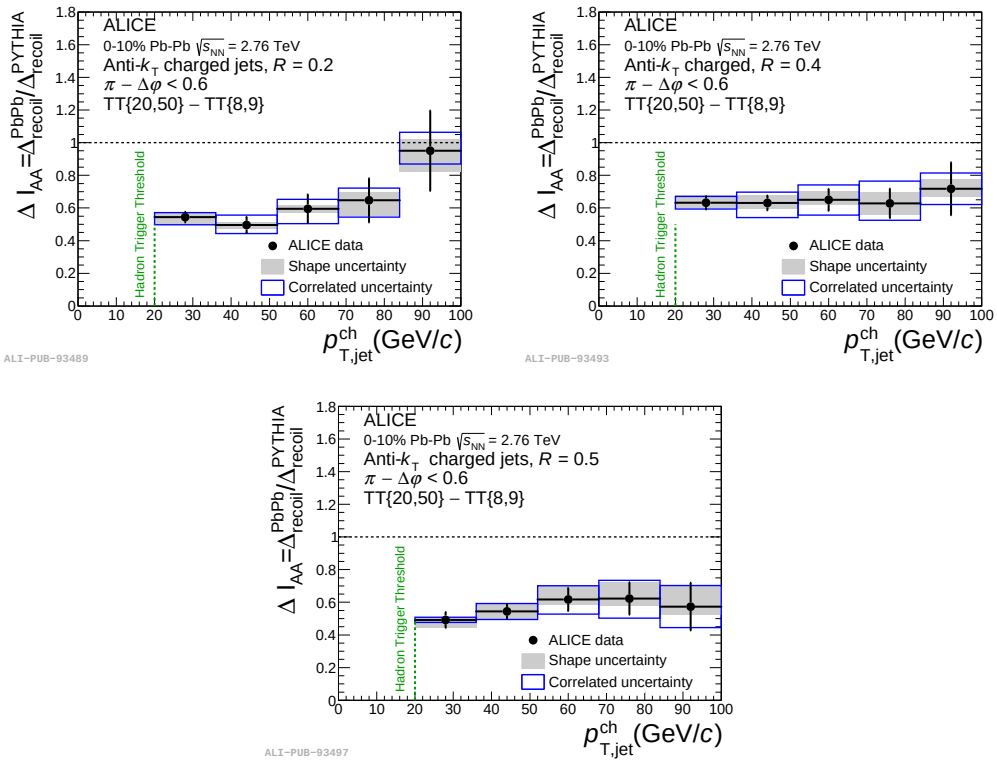

Figure 2.12: ΔI_{AA} of charged jets in the most 10% central Pb–Pb collision at 2.76 TeV for different R.

distribute inside a jet. The fragmentation function $dN/d\xi$, defined as the number of charged particles with respect the $\xi = ln(p_T^{jet}/p_T^{hadron})$ variable exhibits a typical shape, known as hump-backed plateau as illustrated in Fig. 2.14 as predicted in perturbative QCD in the modified leading logarithmic approximation (MLLA) [78].

The plot shows moreover how the distributions evolve with the jet energy in a given θ_c angle: the higher the jet energy, the more significant the soft gluon emission. This representation in bins of ξ allows to highlight how low p_T particles distribute in the jet because of the logarithm present in its definition. In order to have a better view of what is going on at larger particle p_T, the z variable defined as $z = p_T^{hadron}/p_T^{jet}$ is also employed.

In the ALICE experiment, the charged particle momentum distribution defined with respect to the charged jet p_T (instead of the full jet energy) has been measured in pp collisions at $\sqrt{s} = 7$ TeV in both ξ and z variables. This is illustrated in the left and right panels of Fig. 2.15 as a function of ξ and z respectively. Even if the two quantities are not directly comparable, exactly the same behavior as the

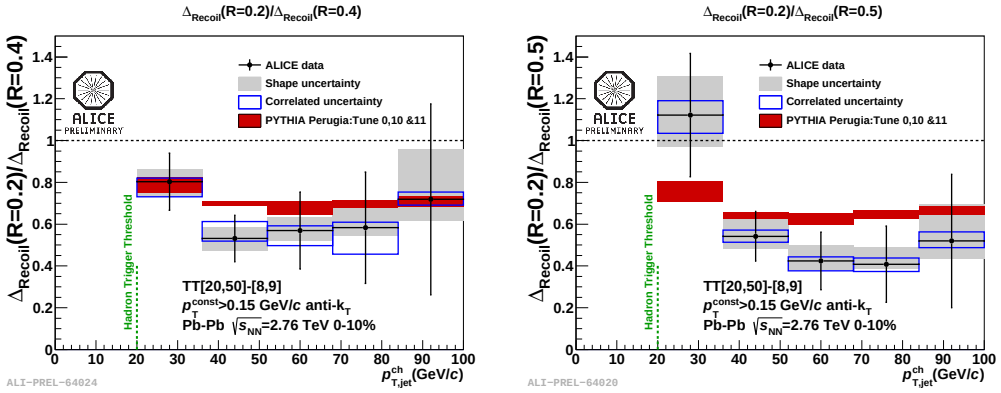

Figure 2.13: **Ratio of Δ_{Recoil} in different R**: These results are the ΔI_{AA} of charged jets in the most 10% central Pb–Pb collision at 2.76 TeV for different R. The left one is $R = 0.2$ and the right one is $R = 0.4$.

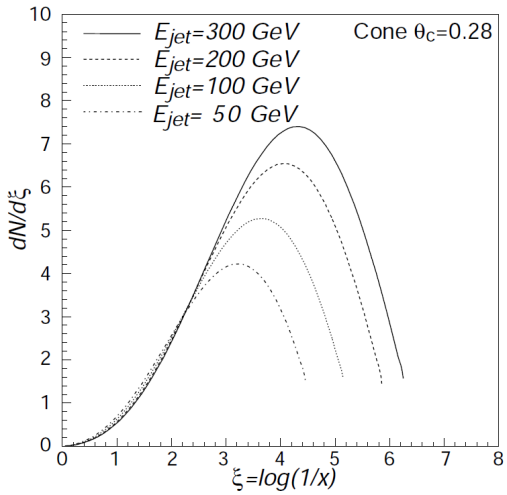

Figure 2.14: Predictions of the hump-backed plateau for 4 jet energies in the MLLA formalism [4].

one predicted by QCD for the fragmentation functions is observed for these particle momentum distributions in jets. In the z representation, and for $z_{ch} > 0.1$ all measured distributions are consistent within uncertainties, which might indicate a scaling behavior of the jet fragmentation.

Even if the fragmentation functions are of great interest to study how quenching effects affect the fragmentation process in jets, they are unfortunately dependent on the jet energy and thus sensitive to the background fluctuations. In order to overcome this issue, a new observable associated to the jet fragmentation has been proposed: the moments of the fragmentation functions. The motivation for such measurement in presented below.

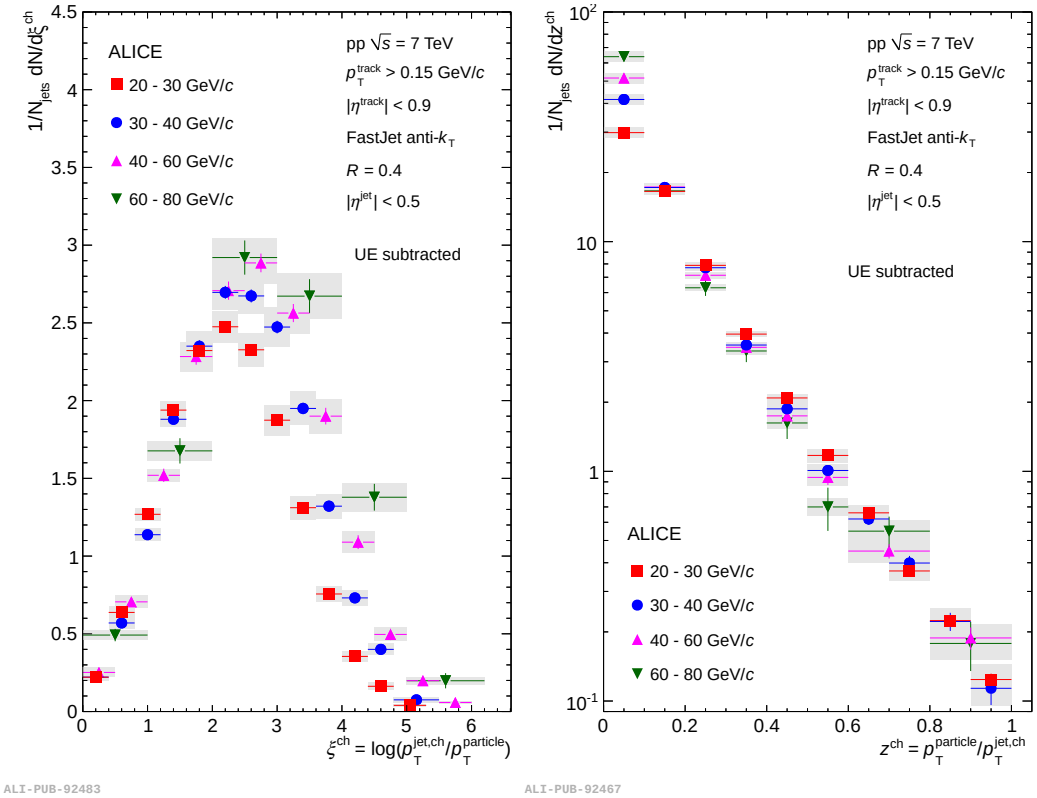

Figure 2.15: Jet fragmentation: Left: charged particle scaled p_T spectra $dN/d\xi^{ch}$ in leading jets for different bins in jet transverse momentum, compared to simulations. Right: same distributions as a function of z [5].

The study of fragmentation functions is heavy ion collisions is limited by the presence of a large fluctuating background due to particles originating from sources other than the hard interaction, predominantly soft interactions deforming the p_T information of the measured jet and its fragmentation function. To overcome this limitation, a new variable, "Fragmentation Function Moments"[1] was proposed and defined as:

$$M_N = \frac{1}{N_{jets}} \int_0^1 z^N \cdot \frac{dN_{jets}^{hadron}}{dz} dz.$$

In practice, the M_N distribution for each jet will be calculated as

$$M_N = \sum\nolimits_{i \in jet} z_i^N = \frac{\sum_{i \in jet} p_{T,i}^N}{p_{T,jet}^N} = \frac{\sum_{i \in jet} p_{T,i}^N}{(\sum_{i \in jet} p_{T,i})^N},$$

The figure 2.16 shows model calculations of fragmentation function moments from simulations in pp collisions via PYTHIA [79]. A heavy-ion central event (10% central Pb–Pb collisions) is simulated via Hydjet. A quenching case is calculated via Pyquen [80, 81]. Two different background subtraction methods are also shown. The

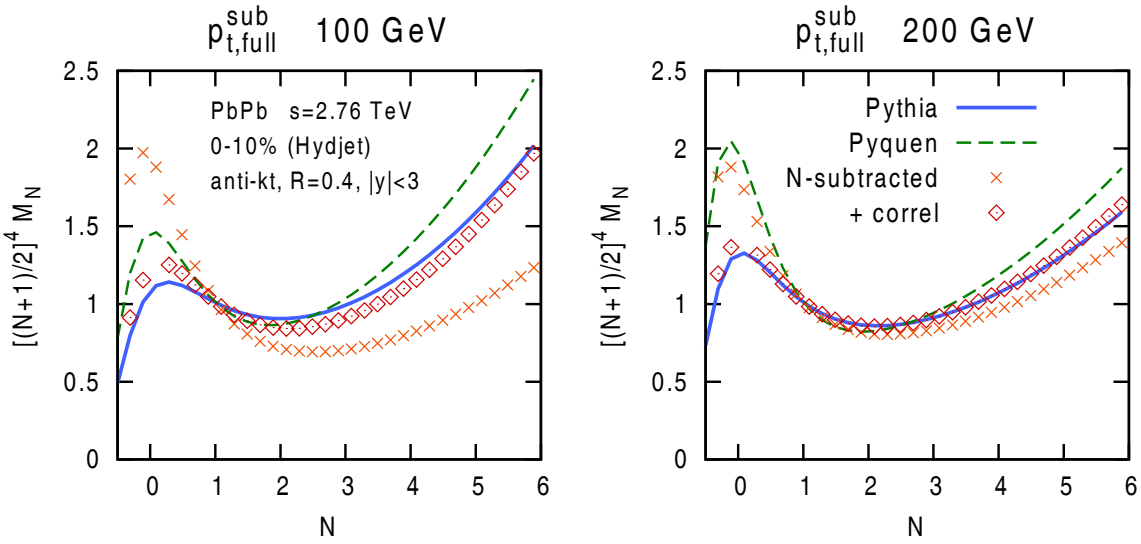

Figure 2.16: **Model calculations of jet Fragmentation function moments (using ATLAS parameters)**: The PYTHIA distribution (blue line) embedded into a Hydjet Pb-Pb event is compared to distributions obtained using Hydjet with 2 different background subtraction methods. The simple "N-subtracted" method, and the "+correl" method, improved to take into account correlations. A quenched cased (from "Pyquen") is also shown. The left one is for jet $p_T \geq 100$GeV, and the right one is for jet $p_T \geq 200$GeV.

red points noted as "N-subtracted" correspond to a rho based method generalized in momentum space. A improved background correction, introduced in [1] and using analytical unfolding of the background fluctuations is plotted with the red points and noted as "+ correl". The improved background subtraction method ("+ correl") allows to recover the input pp distribution (blue curve),

Figure 2.16 shows in addition (with a green dashed curve) the jet fragmentation function moment distribution as it would be expected in a quenched scenario (Pyquen is used). This comparison shows that fragmentation function moments provide an alternative way to subtract background and to deconvolute fluctuations while they also are sensitive to quenching effects.

In the last chapter of this thesis, we will present the first measurement of fragmentation function moments in pp collisions with ALICE at the LHC.

Chapter 3

The ALICE experiment at LHC and its detectors used for jet analyses

As discussed in the previous chapter, two kinds of jets ("charged" or "full") can be reconstructed and studied depending on the type of their constituents (charged or neutral particles) that experimentalists can have access to. Because of its multi-purpose structure, the general ALICE apparatus that will be briefly presented in section 3.2 allows to have access to both types of jets thanks to its central tracking system (CTS) on one side, or thanks to the combination of its CTS with its electromagnetic calorimeters on the other side. Two sections will be devoted to the description of the detectors used for jet reconstruction in ALICE. Section 3.4 which introduces the Central Tracking System (CTS), presents the main detectors used to measure the "charged component" of the jets while section 3.5 explains how the electromagnetic component of the jet can be experimentally achieved. Before to be able to reconstruct jets, it is essential to select the events of interests for the analysis. We have thus chosen to spend some time on the description and principles of the detectors used for the event and collision centrality selections in section 3.3. But first, the Large Hadron Collider (LHC) where ALICE and the three other experiments ATLAS, CMS and LHCb take data since the end of 2009 is introduced in section 3.1.

3.1 The Large Hadron Collider at CERN

Jet physics in heavy ion experiments becomes achievable and useful as long as enough energy is shared between partons during a collision process. With the

increase of the center of mass energy first achieved with fix target experiment at SPS at CERN with respect to the previous synchroton AGS at Brookhaven, and then at RHIC, first collider of heavy ions at ultra-relativistic energies, the physics of jets has first been highlighted for the first time in heavy ion experiments with the observation of several phenomenon related to the now famous jet quenching effect. But the "real" physics of jets (and not anymore of the leading particle of a jet) has exploded at RHIC with the direct measurement a total jet and its modification in the medium. It is in this physics context that the end of the building of the Large Hadron Collider at CERN has been performed and that the first collisions have been analysed with an already large jet physics programmed defined.

3.1.1 International context and first collisions

Not restricting ourselves to heavy ion physics, the LHC which is located at the French/Swiss border close to Geneva is today the world's largest and most powerful particle collider, having overtaken in terms of center of mass energy the Tevatron at Fermilab which ran at $\sqrt{s}$=1.96 TeV for 8 years.
The LHC which is the fruit of the work of more than 10,000 scientists and engineers from more than 100 countries and of more than 10 years of work, has faced several accidents and delays since december 1994 when the project was first approved. The last most important issue that it had to face[1] happened during its inaugural tests in September 2008 and postponed to a year its restarting. Eventually, on 20 November 2009, low-energy beams circulated in the tunnel for the first time since the incident, and shortly after, on 30 November, the LHC achieved 1.18 TeV per beam to become the world's highest-energy particle accelerator.

3.1.2 The LHC machine

The accelerator systems

The LHC uses the synchrotron technology. It has been built to accelerate and collide protons, anti-protons and heavy-ions. For economical reasons, it has been built in the ~3 meters wide tunnel and 27 km long of the previous Large Electron Positron (LEP) and at a depth ranging from 50 to 175 metres underground. Protons or heavy-ions, before to be injected in the LHC are successively produced

[1] A magnet quench in 2 sectors caused the damage of more than 50 superconducting magnets and their mountings and provoke the contamination of the vacuum pipe

and accelerated in a series of systems previously used for the SPS, including the SPS itself. Protons are first produced firing electrons on a hydrogen gas. They are then accelerated with a system of radio-frequence quadripoles before to be injected and accelerated again in the linear accelerator LINAC 2 generating 50-MeV protons, which feeds the Proton Synchrotron Booster (PSB). There the protons are accelerated to 1.4 GeV and injected into the Proton Synchrotron (PS), where they are accelerated to 26 GeV. Finally the Super Proton Synchrotron (SPS) is used to further increase their energy to 450 GeV before they are at last injected (over a period of several minutes and in two opposite directions) into the main ring. Here the proton bunches are accumulated, accelerated (over a period of 20 minutes) to their peak energy, and finally circulated for 5 to 24 hours while collisions occur at four intersection points as shown in Fig. 3.1.

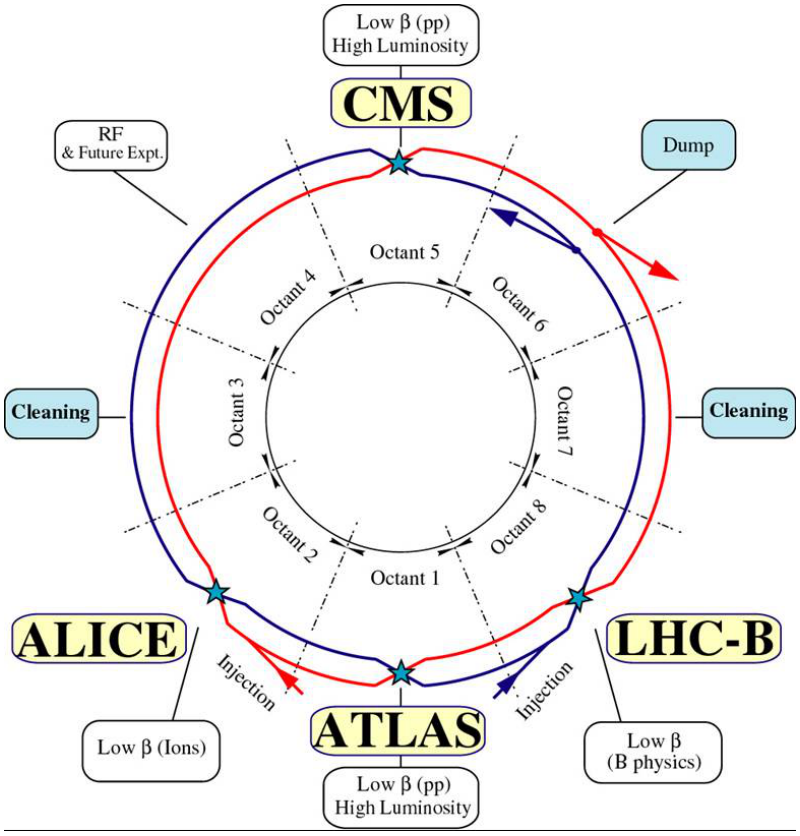

Figure 3.1: Schematic view of the LHC ring. The two beams running in the opposite directions are represented as blue and red lines. They interact in 4 positions corresponding to the 4 main LHC experiments: ATLAS (point 1), ALICE (point 2), CMS (point 5) and LHCb (point 8). More details are given in the text.

Concerning the heavy ions (essentially lead ions - Pb^{82+} - but lighter ions will

be concerned as well in future), they are first produced ... accelerated by the linear accelerator LINAC 3, and the Low-Energy Ion Ring (LEIR) is used as an ion storage and cooler unit. The ions are then further accelerated by the PS and SPS before being injected into the LHC ring, where they reached an energy of 1.58 TeV per nucleon.

The LHC ring

In Fig. 3.1, the injection points are visible on both sides of the ATLAS experiment. The two lines, blue and red, depict the path of the two beams running in opposite directions and colliding in four places (blue stars) where the experiments ATLAS, CMS, LHCb and ALICE are situated. The ATLAS experiment location is in front of the main entrance of CERN close to the French/Swiss border on the Switzerland side. CMS is on the border as well but on the French side at 27 km from ATLAS. ALICE and LHCb are both located in France at $\sim$2 km from the border.

The LHC is not a perfect circle. It is made of 8 arcs containing each 154 dipolar curvature magnets, 8 linear insertions between the arcs, and 2 regions of transition (the dispersion suppressors) at the end of each insertion. The name "sector" at the LHC refers to the part of the machine situated between two insertion points. Each sector is an operational unit of the LHC (i.e. the material is turned on, sector by sector, of the dipole of a given sector are connected in series and are located in a same cryostat, etc.). In Fig. 3.1, the octant term is used as well. It starts from the middle of an arc and stops in the middle of the next arc. It thus includes a complete insertion. The used of this term should be preferred if one is interested by the use of the magnets for focusing the beams to the interaction points. For instance, ALICE is located at point 2 (Octant 2). The final focus in the low-β insertions (Fig. 3.1) is achieved with a inner triplet together with a matching section of four quadrupoles [82]. RF in the figure stands for revolution frequency. It will be briefly commented in section 3.1.3.

3.1.3 Experimental conditions for physics analysis

Four experiments for different physics goals

Among seven experiments built at CERN and exploiting the LHC collisions, four of them, bigger, have been designed for perfecting our knowledge of fundamental physics and for exploring its frontiers. ATLAS and CMS, use general-purpose

and independantly designed detectors for general purpose particle physics to elucidate the nature of electroweak symmetry breaking, to shed light on the theoretical consistancy of the standard model above 1 TeV and to test theories beyond the SM (supersymmetry, extra dimensions, etc.). Thanks to their structures, they allow good charged-particle momentum resolution and reconstruction efficiency, efficient triggering and offline tagging of τ's and b-jets, good electromagnetic energy resolution, good diphoton and dielectron mass resolution, π^0 rejection, and efficient lepton and photon isolation at high luminosities, good muon identification and momentum resolution of low and high momenta and over a wide range angles, and good dimuon mass resolution, good missing tranverse energy, high energy jet reconstruction and good dijet mass resolution. More specific domains in fondamental physics like B physics and nuclear matter properties under extreme conditions (QGP physics) are studied by LHCb and ALICE respectively. LHCb is designed for very detailed and precised spectroscopy of charm and beauty decays. The ALICE experiment has been specifically built to work in the really high multiplicity environment of heavy ions collisions. It is quite a slow detector because of the use of its main detector (the Time Projection Chamber (TPC)) but it allows to reconstruct charged-particle momenta to really low momenta ($\sim$150 MeV) with a good energy resolution. ALICE is also designed to perform particle identification (PID). A more exhaustive view of the ALICE apparatus is given in section 3.2.

Beam and luminosity definitions

The collision products (data) analysed so far at the LHC are dependent on two quantities which are essential in particle colliders: the beam (energy) and the luminosity, L. The luminosity describes the ability of the collider to produce a required number of events. For a given center of mass energy, one can estimate the expected event rate of a physics process of given σ cross section[2] by the product $\sigma \times \mathcal{L}$. The absolute knowledge of the luminosity thus gives access to a measurement of the absolute cross sections in an experiment. In this section, we first explain how the beam is defined[3] in order to explain how the luminosity can be derived from machine parameters.

[2] σ expresses the probability of a given process to occur.

[3] Our aim is to introduce some important terms which are currently used to describe a beam and give a rough explanation on where its structure comes from.

Proton beam characteristics

So far, le LHC is the most powerful particle accelerator in the world and its radius, the strength of the dipole magnetic field as well as its radiofrequency cavities are the main constraints that determine the maximum energy that can be reached per proton (7 TeV). The energy of the collision in case of collider is thus the sum of the 2 beam energies designed to reach 14 TeV at the LHC. The "proton beam" is a well defined and structured object well more complicated than a simple superposition of independent accelerated protons. A beam is made of cylinder-like bunches 7.48 cm long and $\sim$ 1 mm wide far from an interaction point. Each bunch are separated by 7.5 m which makes a time spacing between 2 bunches moving at almost the speed of light of 25 ns. Theoretically, over the 27 km of circumference of the LHC, 3550 bunches should move at the same time and thus define the "proton beam". However, for some technical reasons associated to the injection/extraction of new or non-useful bunches, the effective number of bunched is 2808 which makes a rate of bunches with protons of 0.8. The structure in bunches described above is due to the radiofrequency (RF) cavities used at the LHC (eight cavities per beam) which generate a longitudinal oscillating voltage applied across an isolated gap in the vacuum chamber.

Luminosity definitions

The luminosity is the measurement of the number of collisions that can occur per cm^2 and per second. Its expression can be derived from the beam parameters such as beam width and particle flow rate, and from the target properties (target size and density) [83]. In case of two colliding beams, both beams can be considered as target and "incoming" beam at the same time. In case of two gaussian beams colliding "head-on" (gaussian profiles in all dimensions), assuming equal beams and bunches travelling almost at the speed of light, the luminosity is given by equation 3.1

$$\mathcal{L} = \frac{N_1 N_2 f N_b}{4\pi\sigma_x\sigma_y} \tag{3.1}$$

where N_1 and N_2 are the number of particles per proton bunch, f is the revolution frequency and N_b is the number of bunches in one beam. σ_x and σ_y define the transversal sizes of the bunch at the interaction point in x and y directions. This equation shows how the luminosity depends on the number of particles per bunch and the beam sizes. It can be extended as well in case of two different beam transverse profiles ($\sigma_{1x} \neq \sigma_{2x}$, $\sigma_{1y} \neq \sigma_{2y}$) but still assuming approximately equal bunch lengths

($\sigma_{1z} \sim \sigma_{2z}$) to the formula 3.2

$$\mathcal{L} = \frac{N_1 N_2 f N_b}{4\pi\sqrt{\sigma_{1x}^2 + \sigma_{2x}^2}\sqrt{\sigma_{1y}^2 + \sigma_{2y}^2}} \tag{3.2}$$

These definitions of the luminosities made the assumption of "ideal" head-on collisions of bunches where the particle densities in the three dimensions are uncorrelated. In real machines, additional effects have to be taken into account as the real running conditions are more complicated than the conditions taken to extract the previous formula. Several effects such as crossing angle (to avoid unwanted interactions), collisions offset (beams which do not collide head-on), non-Gaussian beam profiles, non-zero dispersion at collision point, etc. should be considered for a more accurate determination of the luminosity. More details on these different contributions can be found elsewhere [83]. In practice, the luminosity is often measured using the Van Der Meer scan method [84].

Note that these luminosity definitions are time dependent and thus allow to extract an expected value of the "instantaneous" luminosity at the LHC of $\sim 10^{34}$ $\mathrm{cm}^2\mathrm{s}^{-1}$. This quantity is of course really important as it allows to compute how many time a given physical process can occur per second if we multiply the luminosity by the cross section of the corresponding process.

The other important quantity of interest for any physics analysis is the knowledge of the total size of the collected data. In order to obtain it, one first need to extract the integrated luminosity obtained integrating the delivered luminosity over the sensitive time, i.e. excluding possible dead time (formula 3.3).

$$\mathcal{L}_{int} = \int_0^{t_r} \mathcal{L}(t')dt' = \mathcal{L}_0 \times \tau \times (1 - e^{\frac{-t_r}{\tau}}) \tag{3.3}$$

One has to keep in mind that because of the interactions between particles that occur inside the beam with time, the intensity of the beam decreases with time, the transverse emittance grows, the bunch length increases, etc. and thus it shortens the luminosity life time, τ. The decay of the luminosity with time can be modelized exponentially with a given lifetime τ so that the remaining integrated luminosity over the time t_r (length of the luminosity run) is given after integration by the right expression of equation 3.3, $\mathcal{L}_0$ being the initial (nominal) luminosity.

The number of observed events is then given by equation 3.4 knowing the production cross section of the p process σ_p.

$$Number\,of\,events\,of\,interest = \mathcal{L}_{int} \times \sigma_p \tag{3.4}$$

The ALICE case and the run I conditions

Because of its apparatus and especially its main detector, the Time Projection Chamber (TPC) which limits the speed of the acquisition system, ALICE can not run under the nominal LHC luminosity conditions in *pp* collisions unlike ATLAS or CMS. The TPC will be presented in section 3.2. This is illustrated in the top panels of Fig. 3.2, where the evolutions of the peak luminosity (left) and the integrated luminosity for *pp* collisions at $\sqrt{s} = 7$ TeV are shown for the four LHC experiments. In order to be able to read the ALICE integrated luminosity, a log scale is preferred for the representation.

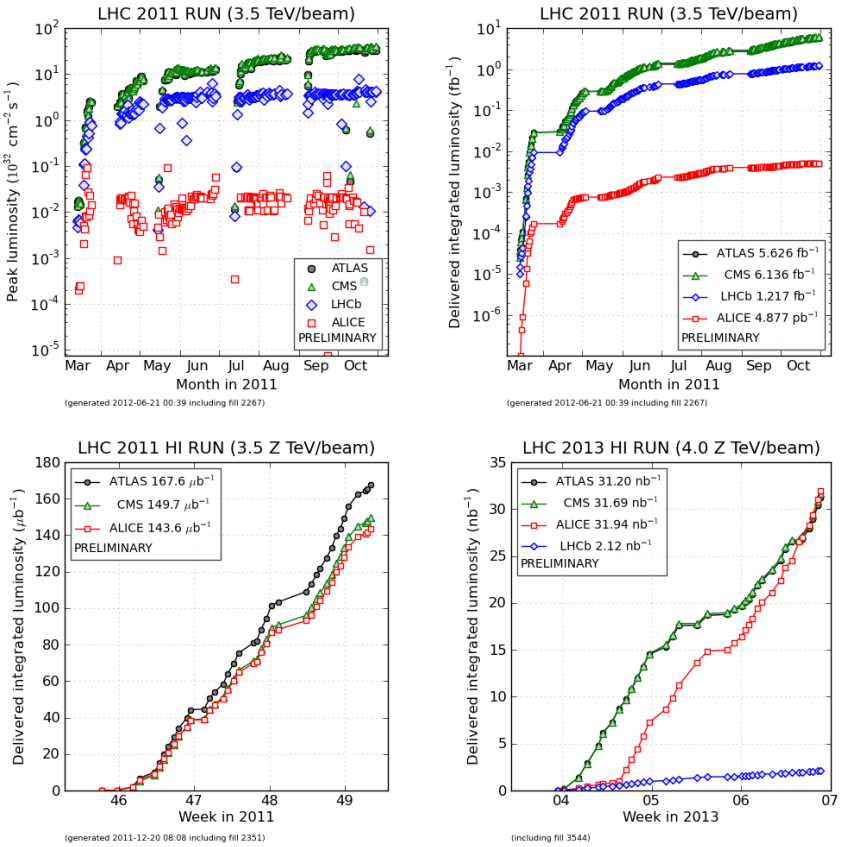

Figure 3.2: Peak luminosity (top left) and delivered integrated luminosity (top right) for the four LHC experiments during 2011 *pp* runs. Bottom left: integrated luminosity for 2011 PbPb collisions for ATLAS, CMS and ALICE experiments. Bottom right: same distributions for the four LHC experiments for 2013 *pPb* runs.

The two bottom plots display the evolution of the integrated luminosity for 2011 PbPb collisions at $\sqrt{s_{NN}} = 2.76$ TeV (bottom left) and for the asymmetric pPb runs in 2013 for the four LHC experiments. These two plots illustrate that ALICE is re-

ally dedicated to heavy ion collision study and is able to register the same amount of luminosity than the two other big experiments ATLAS and CMS.

In table 3.1, we have summarized the run I conditions under which ALICE has operated for about three full years of data taking starting at the end of 2009 (the beginning of the LHC data taking) and ending in February 2013.

Year	System	$\sqrt{s_{NN}}$ (TeV)	Running mode	Peak $\mathcal{L}$	Duration beam (h)	$\mathcal{L}_{int}$	Recorded statistics (10^6 events)	Recorded data (TB)
2009	pp	0.9	MB	5.2×10^{-4}	n.a.	19.6 μb^{-1}	0.5	0.43
	pp	2.36	MB	1.1×10^{-4}	n.a.	0.87 μb^{-1}	0.04	0.01
2010	pp	0.9	MB	1.5×10^{-2}	15.7	0.31 nb^{-1}	8.5	5.97
	pp	7.0	MB+rare (mixed)	1.7*	847	0.5 pb^{-1}	825	773
	PbPb	2.76	MB	2.8×10^{-5}	223	9 μb^{-1}	56	811
2011	**pp**	**2.76**	**rare**	**4.4×10^{-1} (450 kHz)**	**35**	**46 nb^{-1}**	**74**	**101**
	pp	7.0	rare	9	1332	4.9 pb^{-1}	608	1572
	PbPb	2.76	rare	4.6×10^{-4}	203	146 μb^{-1}		908
2012	pp	8	MB	0.2* (10 kHz)	1824	9.7 pb^{-1} (altogether)	38	1286
			rare	20 (1 MHz)			86	
	pPb	5.02	MB (pilot)	9×10^{-5} (180 Hz)	7.6	1.5 μb^{-1}	2.43	3.4
2013	pPb	5.02	MB	5×10^{-3}* (10 kHz)	50.2	0.891 nb^{-1}	134	91
			rare	1×10^{-1} (200 kHz)	70.1	14.0 nb^{-1}	10	97
	Pbp	5.02	rare	1×10^{-1} (200 kHz)	77.1	17.1 nb^{-1}	18	151
	pp	2.76	rare	2.2* (105 kHz)	27.4	129 nb^{-1}	20	16

Table 3.1: ALICE data taking conditions in Run I (2009-2013).

The really good running performances of the LHC over this run I period resulted in a faster increase of the luminosity than expected. The values reached for ALICE are given in table 3.1 for the different systems and center of mass energies considered. The table also summarizes the duration time of the runs, the statistics and the data recorded over the full period. In the column "running mode", one can see which type of trigger (Minimum Bias (MB), or rare) was considered for a given run. In the case of ALICE which is dedicated to the study of the properties of the quark gluon plasma (see the first chapter of this document), it is important to note that two periods at the end of the years 2010 and 2011 which were dedicated to Pb–

Pb collisions at $\sqrt{s_{NN}} = 2.76$ TeV, in which the QGP is expected to be produced. Moreover, p–Pb and Pb–p collisions at $\sqrt{s_{NN}} = 5.02$ TeV are of interest to study among other things the existence of initial state effects, ended the run I period in 2012 and at the beginning of 2013.

Note that the bold lines in the run I condition table summarize the set of data that has been analysed in this thesis. The details of this analysis and the associated results for jet fragmentation functions and fragmentation function moments will be presented in chapters 6 and 7 respectively.

3.1.4 ATLAS, CMS and ALICE: three complementary experiments to study the QGP properties

With the 14 TeV energy of the colliding protons that will be achieved at the LHC, a phase space of roughly 20 units of pseudo-rapidity will be covered. Particle production is peaked at central rapidities while most of the energy is emitted at low angles as shown in the left panel of Fig. 3.3.

The four main LHC experiments mainly cover the central rapidity region where the particle production is at its maximum (Fig. 3.3, right). However, spanning more specifically the η region $\sim \pm 4$, quite some large discrepencies can be seen between them. Whereas ATLAS and CMS have clearly been built to study high transverse momentum physics (and especially jets) over the full rapidity range, the ALICE experiment is focusing on the central rapidity region. In the right panel of Fig. 3.3, one can note that ALICE is the only experiment covering the central rapidity region which is able to probe really low transverse momenta (down to 150 MeV/c).

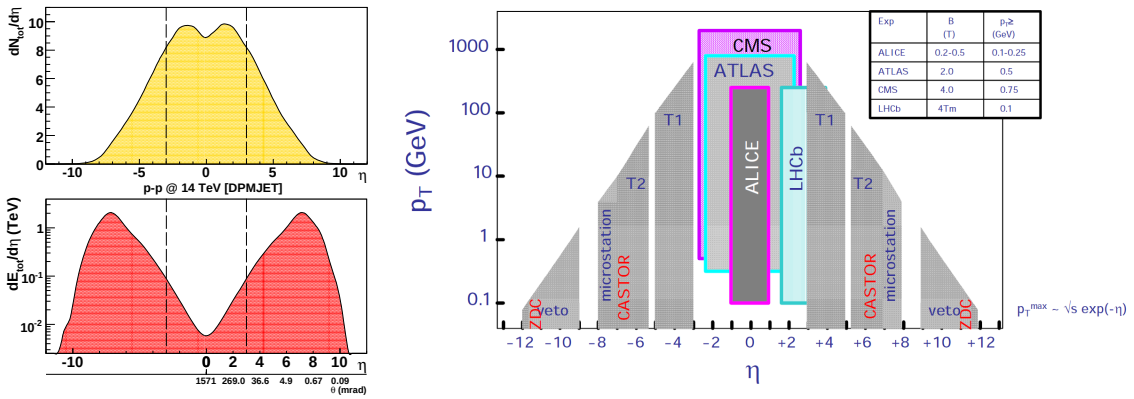

Figure 3.3: Left: Pseudo-rapidity distributions for the total hadron multiplicity (top) and energy (bottom) in p-p at 14 TeV as given by the DPMJET3 model [6]. Right: Schematic representation of the (p_T,η) acceptance covered by the four main LHC experiments.

In heavy ion collisions, these different characteristics between experiments bring complementarities in the study of the QGP properties. The design of the detectors built for particle physics make them particularly efficient to study hard probes of the QGP. The association of the electromagnetic and hadronic calorimeters allow a full reconstruction of the jet energy of hundreds of GeV over a wide rapidity range. It has lead to the first observation of the jet quenching effect at the LHC on an impressive jet p_T range never achieved before in heavy ion experiments [85]. An other example that can be given concerns b jets. Thanks to the tools developed for b tagging for Higgs physics and then adapted to heavy ion collisions, the first isolation of jets from bottom quarks in heavy ion collisions has been achieved in 2012 in CMS and demonstrated that bottom quark jets experience the same quenching effect as light jets at large transverse momentum [86]. Moreover, ATLAS and CMS are also extremely efficient to measure photons, W and Z bosons in pp but also in heavy ion collisions over a wide p_T range bringing insight to the understanding of electromagnetic probes which production is not suppressed by the QGP [74, 75].

Unlike ATLAS and CMS and in a complementary way, ALICE has been first designed to probe really high multiplicity environnement down to low transverse momenta ($\sim$ 150 MeV/c) thanks to its tracking capabilities in its central barrel (section 3.4) or thanks to the muon arm in a higher rapidity region. The other feat of arm of ALICE is its unique capabilities to identify particles from few hundreds of MeV to a hundred of GeV. If ALICE is dedicated to the study of global event and bulk properties, it has also demonstrated its hability to bring great contribution to the physics of hard probes. The experiment has been particularly efficient to characterize the background properties of jets and the impact of its fluctuations on their reconstruction in heavy ion collisions. It is also particularly well designed to precisely characterize the jet composition and its modification inside a medium as already partly presented in chapter 2.

3.2 A Large Ion Collider Experiment, ALICE

3.2.1 General considerations

ALICE (A Large Ion Collider Experiment) [87] is a general-purpose particle detector designed to study heavy-ion collisions. It has been optimized for the very high multiplicity environment that is created in central heavy-ion collisions. The design was developed for $\mathrm{d}N_{ch}/\mathrm{d}\eta = 4\,000$, but tested up to $\mathrm{d}N_{ch}/\mathrm{d}\eta = 8\,000$. With

the multiplicity measured so far in Pb-Pb collisions at $\sqrt{s_{NN}} = 2.76$ TeV of the order of 2000, the collaboration will be fully equipped to work under the multiplicity that will be reached at 5.5 TeV. ALICE has been built and is operated by a collaboration of more than 1 200 members from about 36 countries.

The apparatus illustrated in Fig. 3.4 consists of a central barrel ($|\eta| < 0.9$) contained in a magnetic field of 0.5T used for charged particle reconstruction (tracking), electromagnetic measurement (calorimetry) and particle identification. This central part has been optimized for the detection of hadrons, electrons, and photons. The ALICE detector also includes a muon spectrometer at forward rapidities associated to a dipole magnet of 0.66T as well as additional forward and trigger detectors.

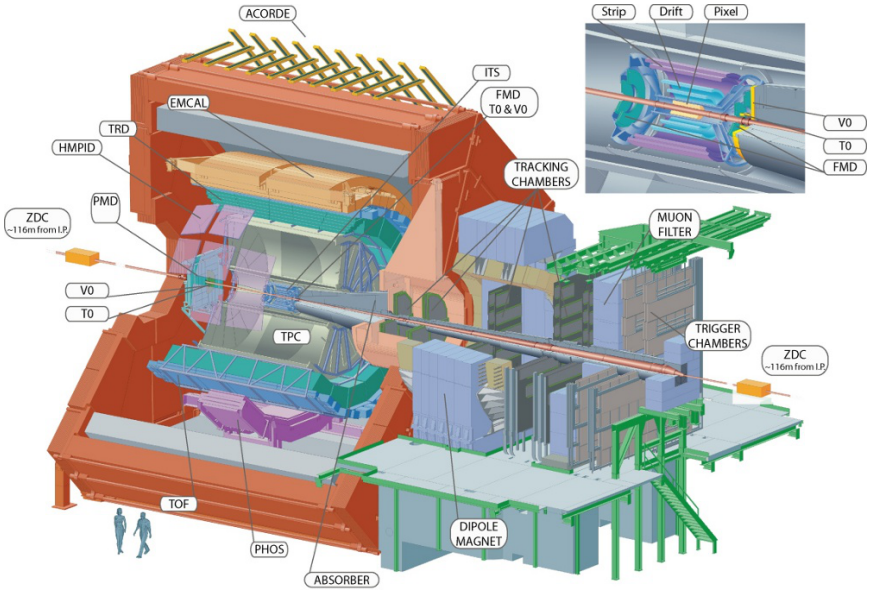

Figure 3.4: ALICE schematic layout

In order to give general survey of the experiment, the principal characteristics of these detectors which pseudo-rapidity curvature is given in Fig. 3.5 (overlaying a $dN_{ch}/d\eta$ distribution predicted by Pythia for pp collisions) will be introduced in this section. In the three following ones, we will focus on the description of three groups of sub-systems that have been used to compute the work presented in this manuscript. Section 3.3 will present the detectors used in ALICE for the selection of event (general triggering) or of the collision centrality. The two other sections, will detail the sub-systems used for charged jet reconstruction (section 3.4) or full jet reconstruction (section 3.4 complemented by section 3.5).

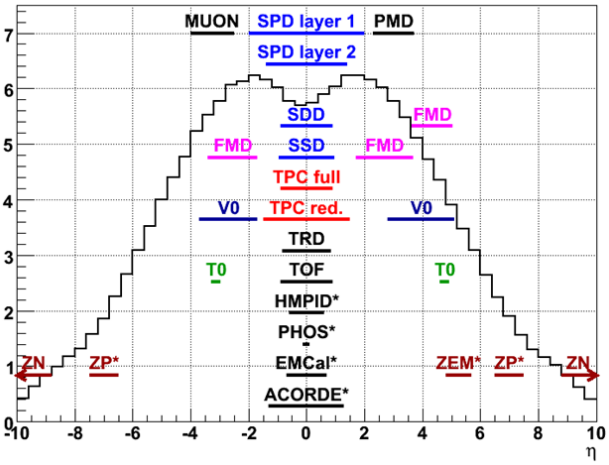

Figure 3.5: Pseudo-rapidity coverage of the different sub-detectors of the ALICE experiment (the * symbol indicates the subsystems which acceptance in ϕ is lower than 2π. The black full line depicts the particle distribution as a function of the pseudo-rapidity [7, 8].

3.2.2 Detectors in the central part of ALICE

In the central region, and in order of increasing radii, one can find the Inner Tracking System (ITS)[88] (the closest sub-system to the interaction point, see section 3.4.1), the Time Projection Chamber (TPC)[89] (the principal detector of ALICE, see section 3.4.2), the Transition-Radiation Detector (TRD), and the Time-Of-Flight (TOF). They cover the full azimuthal acceptance at mid-rapidity (roughly $|\eta| < 0.9$). Their main functions are tracking and particle identification in high-multiplicity environment. Then several detectors of smaller acceptance come after them : the PHOton Spectrometer (PHOS), the ElectroMagnetic Calorimeters (EMCal and DCal (not shown in Fig. 3.4 and 3.5, see next chapter), the High-Momentum Particle Identification Detector (HMPID), and the ALICE Cosmic Ray Detector (ACORDE).

- **The Inner Tracking System**: the ITS is designed to allow the reconstruction of the primary vertex of the collision with a resolution better than 100 μm, as well as the secondary vertexes from the decay of hyperons, or D and B mesons. It is also used to improve (momentum and angle resolution) the particle reconstruction by the TPC (tracking). One of its main tasks is also to track and identify particles with momentum lower than 200 MeV/c with the measurement of the energy loss (dE/dx). This detector which surrounds the beam pipe, consists of six cylindrical layers of silicon detectors of three different technologies: 2 layers of pixels (SPD), 2 layers of drifts (SDD) and 2

layers of strips. More technical details will be given in section 3.4.1.

- **The Time Projection Chamber**: the TPC is the main tracking device of the central barrel. It is optimised to provide with other detectors in the central part of ALICE charged-particle momentum measurements (from $\sim$ 150 MeV/c up to 100 GeV/c with good resolution), particle identification and vertex determination. This detector consists in a large cylindrical field cage filled with a mixture of Ne, CO_2 and N_2 and operated at high voltage gradients ($\sim$ 400 V/cm). With its 90 m^3, it is the biggest TPC in the world. It uses the drift of the primary electrons emitted after the ionization of the gas by a charged particle to reconstruct point by point its trajectory and compute its momentum. More technical details will be given in section 3.4.2.

- **The Transition Radiation Detector**: the main task of the TRD is to provide electron identification in the central region for momentum above 1 GeV/c in conjunction with the TPC which can identify them below this value via energy loss measurement. The association of the measurement of the transition radiation photons from electrons and the dE/dx provide good electron/pion rejection with this detector. The TRD is also designed to provide a fast trigger for charged particles at high p_T of interest for Υ, high-p_T J/Ψ, jet, di-lepton (high-mass region) measurements. The detector, located at radii from 2.9 m to 3.7 m from the interaction point, is composed of 540 individual read-out modules, each of them consisting in the association of a carbon fibre sandwich radiator, a drift section filled with a mixture Xe/CO_2 (85:15) and a multi-wire proportional chamber section with pad read-out.

- **The Time-Of-Flight**: the main purpose of the TOF is Particle Identification in the intermediate momentum range of pions (below 2.5 GeV/c), kaons (below 2.5 GeV/c) and protons (up to 4 GeV/c) with a π/K and K/p separation better than 3σ via the measurement of their respective time of flights: the time between the collision and their arrival in the TOF (time resolution 40 ps). Inscribed in a cylindrical shell (internal and external radii: 3.7 m and 3.99 m respectively), it is a high resolution array consisting of multi-gap resistive plate gas chambers in a high and uniform electric field. It is sensitive to the ionisation produced by a traversing charged particle. It generates a gas avalanche which translates in the observation of signals on the pick-up electrodes.

- **The PHOton Spectrometer**: the PHOS is a high-granularity calorimeter designed to measure low p_T direct photons with excellent energy resolution, and high-p_T π^0 or η via their decay photons. It can also provide L0 and L1 triggers. Each PHOS module (so far 4 modules among 5 have been installed in ALICE) is segmented in 3584 detection cells consisting each in 22×22×180 mm^3 lead-tungstate crystal ($PbWO_4$) coupled to a 5×5 mm^2 Avalanche Photo-Diode (APD) followed by a low-noise preamplifier. One module has been complemented by a Charged-Particle Veto (CPV) in order to improve the discrimination against charged hadrons. More technical details will be given in section 3.5.1.

- **The ElectroMagnetic Calorimeters**: as their names indicate it, the ALICE electromagnetic calorimeters EMCal and DCal are dedicated to the measurement of electromagnetic probes (photons and electrons) at high p_T. Located at a radius of $\sim$ 4.5 m from the interaction point, the quite large acceptance of EMCal[4] ($|\eta| < 0.7$ and $\Delta\Phi = 107°$) offers a cost effective way to have access to the physics of jets. It also provides fast and efficient L0 and L1 triggers for jets and high p_T photons and electrons. EMCal and DCal are layered Pb-scintillator shashlik calorimeters. The detector is segmented in 12288 towers approximately projective in η and ϕ to the interaction point. Scintillation photons produced in each tower are captured by wavelength-shifting (WLS) fibres (36 per tower) that run longitudinally through each tower and finally mate with an APD photo sensor. Chapter 4 will be dedicated to EMCal and DCal.

- **The High-Momentum Particle Identification Detector**: the main purpose of the HMPID is the inclusive measurements of identified hadrons beyond the p_T interval reached through energy loss (with the ITS and the TPC) and time-of-flight measurements (in TOF). The detector was optimised to extend the range for π/K and K/p discrimination up to 3 and 5 GeV/c respectively. The HMPID is a proximity focusing Ring-Imaging Cherenkov (RICH) which acceptance covers 5% of the central region phase space.

- **The ALICE Cosmic Ray Detector**: it has mainly two tasks in ALICE: provide a fast L0 trigger signal for commissioning, calibration and alignment of some ALICE sub-systems and study the high-energy cosmic rays in the energy

[4]For DCal, see chapter 4

region of the knee [8]. The detector is an array of plastic scintillator counters located on the upper surface of the L3 magnet.

3.2.3 Detectors at forward rapidity

At forward rapidity we have other sub-detectors that will be briefly described below among which some are used for specific triggering or event selection: the Photon Multiplicity Detector (PMD), the Forward Multiplicity Detector (FMD), the Zero Degree Calorimeters (ZDC), the VZERO (V0) and the TZERO (T0).

- **The Photon Multiplicity Detector**: photons in the region $2.3 \leq \eta \leq 3.7$ are measured with the PMD. Their multiplicity and spatial distributions can give access to the electromagnetic E_T and to the reaction planes event by event. It consists of two gas proportional chambers (first used as a charged particle veto, second to identify photons) separated by a lead converter. The PMD cannot be used as a trigger because of its slow readout.

- **The Forward Multiplicity Detector**: the FMD provides a charged-particle multiplicity measurement in the ranges -3.4 $< \eta <$ -1.7 and 1.7 $< \eta <$ 5 in addition to the ITS pixels (SPD). On their pseudo-rapidity regions of overlap, both sub-systems provide a good cross-check of the measurement. The FMD consists of silicon strips located in five rings. It cannot be used as a trigger because of its slow readout.

- **The Zero Degree Calorimeters**: the 2 hadronic ZDCs are dedicated to the measurement of the spectator nucleons which can give an indirect access to the geometry of the collision. The centrality information provided by the ZDC is also used for triggering at L1. The position of the ZDCs at high rapidity (location at 116 m on either side of the Interaction Point) allows to use these detectors to estimate the reaction plane of the collision. Each ZDC consists in two detectors: ZN and ZP respectively dedicated to the measurement of spectator neutrons and protons. They are quartz fibres sampling calorimeters [90]. The shower developed by incident particles in a dense absorber produces Cherenkov radiation in quartz fibres interspersed in the absorber. The ZDCs are complemented by two small electromagnetic calorimeters (ZEM) placed opposite to the muon arm at 7 m from the IP on both sides of the beam pipes. More details about the set of ZDCs and how they are used to determine the centrality or for triggering will be given in section 3.3.

- **The VZERO**: the tasks of the V0 detector in ALICE are multiple. First of all, it is used as minimum-bias triggers in *pp* and A-A collisions. It can serve as an indicator of the collision centrality via its measurement of the multiplicity of the event. It is used to reject beam-gas events. The luminosity in *pp* can also be estimated with a 10% resolution with the V0. It is a small angle detector made of two arrays of scintillator counters (the V0A and V0C) located on both sides of the ALICE IP at 3.4 m from the IP opposite to the muon arm for the V0A, and at 0.9 m from the IP in front of the muon absorber for the V0C.

- **The TZERO**: the T0 is the fastest triggering system of the ALICE experiment. As the VZERO, it can also be part of the minimum-bias trigger deffinition. It provides a start time ("time 0") for the TOF detector and allows to determine the vertex position with a precision of 1.5 cm. If the vertex position is within a preset value, the T0 provide the earliest L0 trigger ; if not, a beam-gas rejection signal is generated. The V0 can also provide a "wake-up" signal to the TRD, prior to L0. The detector consists of two arrays of Cherenkov counters (12 per array) which include a photomultiplier tube optically coupled to a quartz radiator. T0-C is placed at 72.7 cm from the nominal vertex on the muon arm side. T0-A, is at the opposite, at about 3.75 m (see also section 3.3).

At forward rapidity, ALICE also counts the muon spectrometer dedicated to the physics of quarkonia.

- **The Muon Spectrometer**: the muon spectrometer is mainly dedicated to the measurement of the complete spectrum of quarkonia (J/Ψ, Ψ',Υ,Υ',Υ'') in the $\mu^+\mu^-$ decay channel with a mass resolution that is good enough to separate these states as well as the ϕ meson. The separation of the Υ states requires a resolution of 100 MeV/c^2 in the 10 GeV/c^2 dimuon invariant-mass region. Located on the C-side of ALICE, it accepts particles in -4 $< \eta <$ -2.5 and has full azimuthal coverage for muons with momentum larger than 4 GeV/c. This cut-off is due to the fact that to reach the spectrometer muons first have to pass through the front absorber (for photon and hadron rejection) made of carbon, concrete, and steel. They can then be measured by five tracking stations with two planes each made of very thin, high-granularity, cathode strip tracking stations. A dipole magnet with an integrated magnetic field of 3Tm is located outside of the L3 magnet to allow the reconstruction of the momenta on the muons. Finally, an iron wall of 1.2 m acts as a further muon

filter after which two trigger stations with two planes each of resistive plate chambers are located.

3.3 Event and centrality selections

In a heavy ion collision, the number of participants Nparticipants or spectators Nspectators is directly linked to its geometry. The more frontal (central collisions), the more Nparticipants icreases. Indeed, when the collision is peripheral, there are few participants and the majority of the nucleons are of large rapidity. The centrality can be determined thourgh the number of spectator nucleons from the measure of their energy in the beam direction. In the ideal case where all spectators are detected, the number of participants can be obtained thanks to the following equations:

$$E_{ZDC}[\text{TeV }] = 2.76 \times \text{Nspectators}$$
$$\text{Nparticipants} = \text{A - Nspectators}$$

where 2.76 TeV is the energy of the Pb ions at LHC and A (= 208) their mass number The spectator protons are separated from the spectator neutrons thanks to the magnetic elements of the LHC beam, and measured by the ZP. The neutrons are measured by the ZN. However in very peripheral collisions, spectators are deviated so smally that they stay along the beam axis and are not detectable by the ZDCs. In order to distinguish these collisions from the central ones in which the number of spectators is small, the measures from the ZDC are correlated with the ZEM ones, which measure the particle energy at very large rapidity (increasing with the collision centrality). From these collisions, 11 centrality classes are extracted. The V0 can also send trigger signals for the determination of the centrality of a heavy ion event. It evaluates the event centrality tranks to the amplitude of the measured signals, proportional to the multiplicity of the event. The V0 can be used alone or associated to the ZDCs.

3.3.1 ZDC

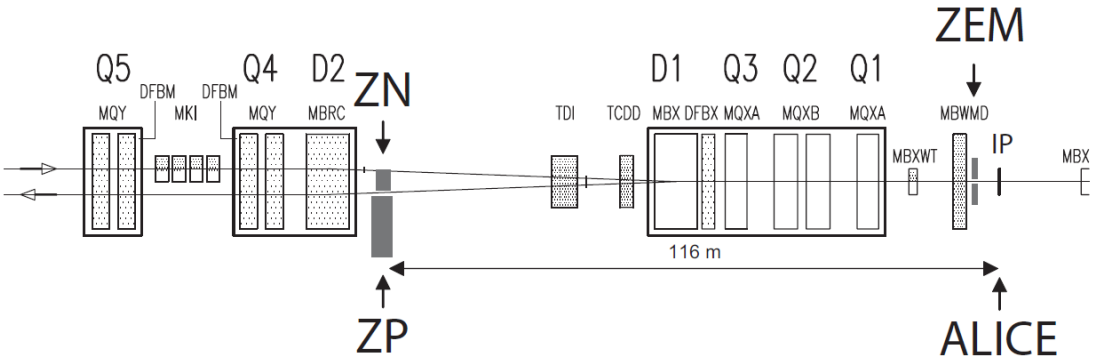

Figure 3.6: ZDC structure

The Zero Degree Calorimeters (ZDC) are composed of neutron calorimeters (ZN) and proton calorimeters (ZP). Two ensembles of ZDC are placed at 116 m around the interaction point and at zero degree w.r.t the beam axis. They are supplemented by two small Forward Electromagnetic Calorimeters (ZEM for Zero degrees Electro-Magnetic calorimeter). The ZEMs are located 7 meters away from the interaction point, on one beam side only, and at ± 45 degrees w.r.t. the beam axis. These detectors are made of slab layers and quartz fibers acting as a Cherenkov detector. The distance to the interaction point makes of these detectors level L1 triggers. The ZDCs measure the energies E_{ZDC} of charged hadrons and neutral spectators, which have not participated to the collision, using the Cherenkov light. They allow determining the event centrality. They can also be used as a trigger.

3.3.2 V0 (A-C)

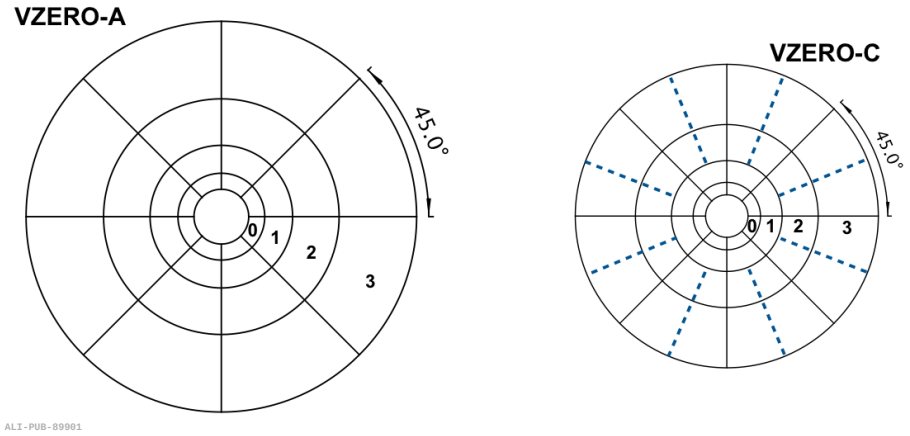

Figure 3.7: V0 structure

The V0 is made of two scintilating grids on both sides of the interaction point. V0A, on the opposite side from the di-muon arm, at 340 cm from the interaction point, and V0C on the other side at 90 cm from the interaction point. They both have a segmented disk shape, in 4 rings and 8 sectors of ±45 degrees in azimuth. They cover the range $2.8 < \eta < 5.2$ and $-3.7 < \eta < -1.7$ in pseudo-rapidity respectively. This detector triggers also the MB signal for central detectors in pp collisions and in heavy ion collisions. It is also used in ALICE to determine the centrality of heavy ion collisions.

3.4 Detectors used for "charged" jet reconstruction

As already introduced in section 2.2, jets can be experimentally defined as sprays of charged and neutral particles. In order to reconstruct them, several algorithms have been developed to combine the momenta of these particles recovering step by step the energy of the initial parton at the origin of this shower of particles. In an ideal world, where all the particles could be accessed, the complete jet energy can be reconstructed (this is called a "full" jet). Unfortunately, experimentally, their reconstruction is limited by the type of particles one can measure, by the efficiency with which particles are reconstructed in a given detector and by the resolution of the kinematic characteristics of the reconstructed particle. In this chapter, we concentrate on the type of particles one can have access to with the ALICE experiment.

A full jet contains charged and neutral particles. In ALICE, the charged particles are measured thanks to the Central Tracking System: they are called tracks. In this section, the CTS and more specifically the detectors which have been used in our thesis are detailed. The basics principles of the tracking (the way a track is reconstructed) are explained in the chapter 5 of [51]. By definition, we will call "charged" jets, jets reconstructed only from the momenta of the charged particles.

Note that in the next section a description of the detectors used in ALICE to measure the neutral component of jets will be given. We will see that in our experiment, the information on the neutral component of jets is partially known.

The CTS consists in three main subsystems: the Inner Tracking System (ITS), the Time Projection Chamber (TPC) and the Transition Radiation Detector (TDR) previously introduced in section 3.2.2. In this thesis, the ITS and the TPC only were used to reconstruct the charged and full jets. They are the only subsystems we have chosen to describe more specifically.

3.4.1 ITS

As introduced briefly above, the Inner Tracking System contributes to practically all physics topics addressed by the ALICE experiment. It surrounds the beam pipe which is an 800μm-thick beryllium cylinder of 6ćm outer diameter, coaxial with the ITS detector layers.

structure

The structure of the ITS is the following [88]: six cylindrical layers of silicon detectors, located at radii between 4 and 43 cm, covering the rapidity range of $|\eta| < 0.9$ for all vertices located within the length of the interaction diamond ($\pm$ 5.3 cm along the beam direction). The number, position and segmentation of the layers were optimized for efficient track finding and high impact-parameter resolution. In particular, the outer radius is determined by the necessity to match tracks with those from the TPC, and the inner radius is the minimum allowed by the radius of the beam pipe. The first layer has a more extended pseudo-rapidity coverage ($|\eta| < 1.98$) to provide, together with the Forward Multiplicity Detectors (FMD), continuous coverage for the measurement of charged particles multiplicity.

The two times three cylinders made of coaxial semi-conductors are assembled as follows:

- The Silicon Pixel Detector (SPD) : it has a pseudo-rapidity coverage larger than the two ITS other layers: $|\eta| < 2$ and $|\eta| < 1.4$ for the internal and external layers respectively. The basis of the SPD is a ladder made of 256×160 detecting cells. Each cell has a 50 μm r dimension and 425 μm in z. The assembly of 4 ladders along the z axis is called a stave. The SPD gives the (x,y) position of the particles. It is also a very fast L0 level trigger. Every 100 ns, 1200 signals called Fast-Or are transmitted. They indicate if at least one pixel gave a signal. These signals contribute to the decision by the ALICE Central Trigger Processor (CTP) to register data or not.

- The Silicon Drift Detector (SDD): is composed of 6 ladders on the internal layer and 8 on the external one. It allows to reconstruct the position and energy of the crossing particles.

- The Silicon Strip Detector (SSD) composed of 34 ladders of 22 modules and 38 ladders of 25 modules on the internal and external layers respectively. As the SDD, the SSD measures the particle position and their energy loss.

The choice of the various layers (SPD, SDD et SSD) has been made as a function of the particle density awaited in each layer: from 80 particles/cm2 at the SPD level, up to 7 particles/cm2 at the SDD level and less than 1 particle/cm2 fpr the SSD. The detector granularity can face at most a multiplicity of 8000 charged particles per rapidity unit, at mid-rapidity, as was simulated for Pb+Pb collisions at $\sqrt{s_{NN}}$ = 5.5 TeV in the ALICE design study.

The resolution in total pT of the ITS for pions from 200 MeV to 1.2 GeV varies from 1.35% to 1.5%.

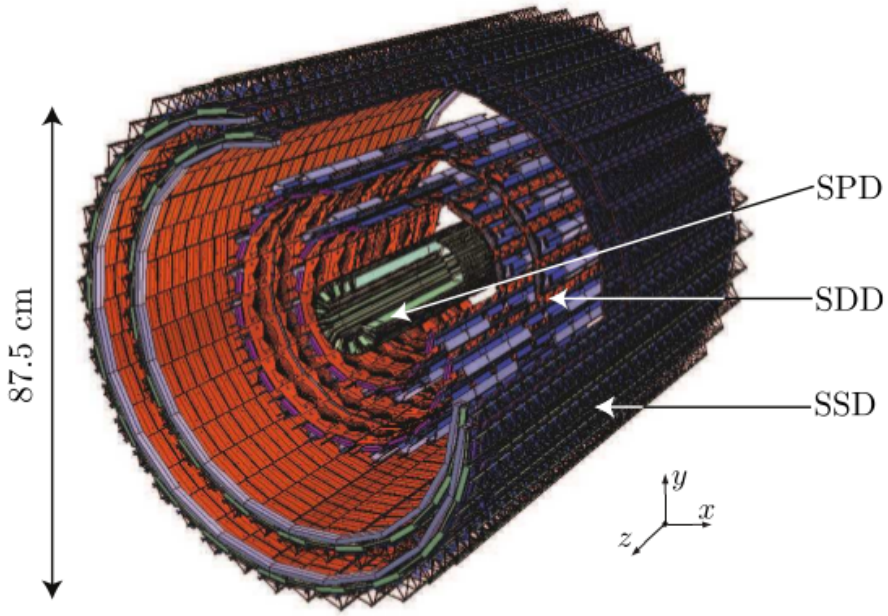

Figure 3.8: ITS structure

parameters

The dimensions of the ITS detectors (active areas) are given in table 3.2.

Layer	Type	r (cm)	±z (cm)	Area (m^2)	Channels
1	pixel	3.9	14.1	0.07	3276800
2	pixel	7.6	14.1	0.14	6553600
3	drift	15.0	22.2	0.42	43008
4	drift	23.9	29.7	0.89	90112
5	strip	38.0	43.1	2.20	1148928
6	strip	43.0	48.9	2.80	1 459 200

Table 3.2: Dimensions of the ITS detectors (active areas).

3.4.2 TPC

The ALICE TPC is the main detector of the central barrel.

Working principle

The ALICE TPC is a 88 m^3 cylinder filled with gas and divided in two drift regions by the central electrode located at its axial centre. The field cage secures the uniform electric field along the z-axis. Charged particles traversing the TPC volume ionise the gas along their path, liberating electrons that drift over a distance of maximum 2.5 m towards the end plates of the cylinder. The necessary signal amplification is provided through an avalanche effect in the vicinity of the anode wires strung in the readout. Moving from the anode wire towards the surrounding electrodes, the positive ions created in the avalanche induce a positive current signal on the pad plane. This current signal, which is characterised by a fast rise time (less than 1 ns) and a long tail with a rather complex shape, carries a charge that, for the minimum ionising particle, is about 4.8 fC. The readout of the signal is done by the 570132 pads that form the cathode plane of the multi-wire proportional chambers located at the TPC end plates.

structure

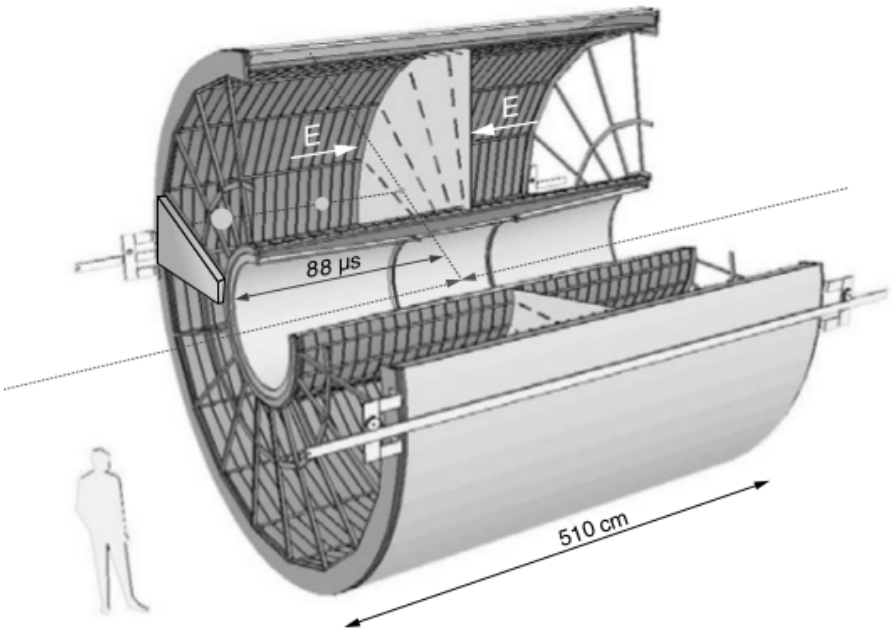

Figure 3.9: TPC structure

The TPC is a cylinder of internal and external radius 84.5 cm and 246.6 cm respectively, for a length of 500 cm. It is closed by two end-plates which support

detecting pads. It has a pseudo-rapidity acceptance of $|\eta| < 0.9$ (and 1.5 for tracks of low momentum and small length) and a full acceptance in ϕ. it undergoes a magnetic field reaching 0.5 T curving the particle trajectory, allowing to differentiate particles of opposite charges et to determine their momentum. The r coordinates of the trajectory are determines thanks to the hit pad position and the z coordinate with the charge drift time. The TPC, allowing to measure charge particles down to transverse momenta as low as 150 MeV, is appropriate for jet measurement because the measurement of the hadron and charged leptons p_{T} and position is mandatory for their reconstruction.

3.5 Detectors used for "full" jet reconstruction

The neutral particles which constitute a full jet with charged particles are of different types. The main ones are photons (bosons), neutral hadrons (neutrons, K_0^L, etc.) and neutral leptons (neutrinos). In ALICE which does not contain any hadronic calorimeter, photons only (and by the way electrons) can be measured thanks to two electromagnetic calorimeters EMCal and DCal (its recent extension) and a photon spectrometer, PHOS[5]. The latter is presented below while the complete chapter 4 is devoted to the electromagnetic calorimeters of the experiment as part of the work of this thesis has been dedicated to these subsystems. Note that PHOS has not been used in this PhD work but it will be combined to DCal in future to improve the reconstruction of jets on a larger acceptance.

3.5.1 PHOton Spectrometer, PHOS

The PHOS is a homogeneous calorimeter of small acceptance(coverage), η in [-0.12, 0.12], ϕ in [260°, 320°]. It can measure the electro-magnetic energy (γ, π^0, et.). Mostly we use it to do correlation studies with jet as a back-to-back trigger in ϕ, like γ-jet correlation or π^0-jet correlations. Because of its narrow acceptance, usually we would not use it alone to measure jets, but it may be used by combined with other calorimeter. See Chapter 4.

[5]One can consider that more or less 10% of the neutral energy of a jet is lost in ALICE in the absence of hadronic calorimeter.

structure

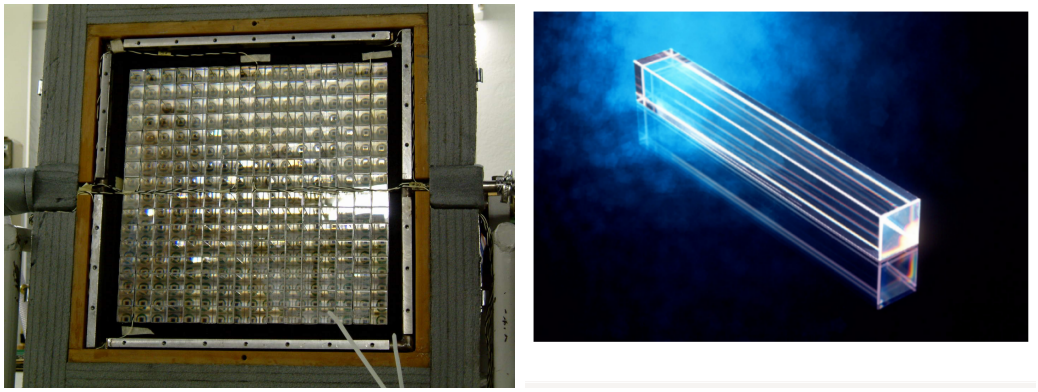

Figure 3.10: Left: one PHOS module = 3584 cells (distributed 56 × 64), 3 modules arranged from ϕ in [260, 320]. Right: one PHOS crystal.

3.5.2 EMCal and DCal

As part of this thesis work has been performed on the electromagnetic calorimeter (EMCal) and the di-jet calorimeter (DCal) which is of same technology than EMCal. They both can be used as trigger detectors (especially for jets and photons). The associated trigger algorithms, combined with PHOS, also aim at estimating the jet background density. Those two detectors are more specifically introduced in the next chapter (chapter 4) before to present the results obtained for their geometry modification and implementation respectively for EMCal and DCal in ALICE.

Chapter 4

The "Di-jet Calorimeter", DCal, and its Geometry Implementation in AliRoot

Electromagnetic calorimeters have been developed and improved for particle physics experiments for the measurement of electrons and photons through their electromagnetic interactions (bremsstrahlung, pair production, etc.). When one of these particles bump into a calorimeter which is usually a big structure of instrumented material, it is partly or totally absorbed (depending on the calorimeter characteristics) via the production of a shower of secondary particles with progressively degraded energy (see section 4.1 for the basic principles). Measuring the energy deposited by the charged particles of the shower in the active part of the calorimeter gives access to the energy of the incident particle. Calorimeters can be mainly classified in two types of construction techniques: sampling and homogeneous calorimeters. The first type consists in the alternative superimposition of layers of a dense material used to degrade the energy of the incident particle and of an active material in which the signal to be measured becomes accessible. The second type of calorimeter uses only one type of material to perform both tasks (degradation of energy et regeneration of the signal).

The ALICE experiment which was originally mainly built to study the properties of the bulk (as far as concerns the central part of the experiment) did not count any calorimeter among its sub-systems in its initial configuration. However, the explosion of hard probes at RHIC around 2006 to highlight and characterize the plasma properties strongly motivated the ALICE experiment to equipped with a

calorimeter. Discussions started among collaborators more or less at the same period and in 2007, the decision to build a calorimeter in ALICE was taken. Two years later, ALICE saw the installation of the first blocks of the EMCal[91] calorimeter in its cavern. In 2012, the complete detector was installed. Moreover, already in 2009, a decision to extend the acceptance of the EMCal calorimeter to allow azimuthal correlations was taken as well. This gives rise to the building and the installation (which ended in November 2014) of the Di-jet calorimeter (DCal). DCal took its first data with the beginning of the LHC run II. It is currently under commissioning and the first data taken are already promising.

The physics motivations for jets for adding a calorimeter to the ALICE apparatus are threefold: to access the electromagnetic component of the jet energy (improves its energy reconstruction and its resolution measurement) [91], to improve the statistics using trigger capabilities [92] and to access (photon/hadron/jet-jet) back-to-back correlations using calorimeter cells located back-to-back in azimuth to reconstruct the energy of the correlated objects [93].

Part of this thesis work has been dedicated to the EMCal and DCal calorimeters with more emphasize given to DCal. This work has been the result of a year of development and it counts as a service work performed for the collaboration. It has consisted in the implementation of the geometry of the full DCal detector in the official software of the ALICE collaboration. At the same time, the EMCal geometry software has been cleaned in order to standardize the package.

In the first section of this chapter, the general principles of calorimeters are explained. The EMCal detector is presented in sections 4.2 and 4.3 before to move on to DCal. The latter is presented in section 4.4 while the work performed for its geometry and the results obtained are detailed in section 4.5. Finally the tests made to validate our results are presented in section 4.6.

4.1 Electromagnetic calorimeter basic principles

4.1.1 Interaction and shower development

The shower development in an electromagnetic calorimeter as briefly described in the introduction of the chapter is mainly based on the way electrons and photons interact with matter via a few well-known QED processes. In Fig. 4.1, one can see in the left panel the average energy lost by electrons in lead, and in the right panel, the photon interaction cross section in the same material as a function of energy.

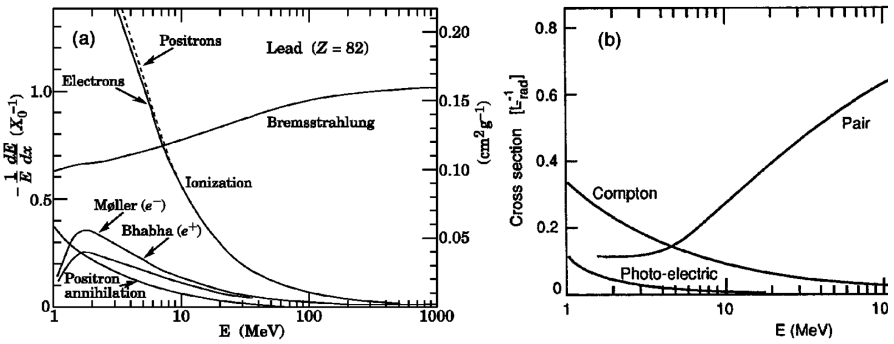

Figure 4.1: a) Energy loss by electrons and positrons in Lead vs energy [9]. b) Photon interaction cross section in Lead vs energy [10].

Mainly two regimes can be identified at "low" and "high" energies. Above 10 MeV, electrons lose their energy via bremsstrahlung while the interactions of photons produce mainly electron-positron pairs[1]. Below 10 MeV, electrons and positrons mainly lose their energy through collisions with atoms of the material giving rise to ionization and thermal excitation. Concerning photon energy loss, it happens via Compton scattering and photoelectric effect.

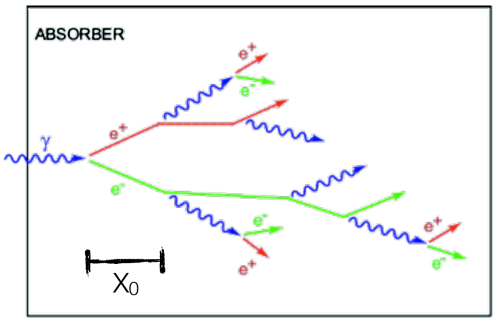

Figure 4.2: Schematic view of an electromagnetic shower developed after the interaction of a photon in a block of material (absorber). The radiation length X_0 of the material is represented as well. The size of the arrows represents the momenta of a produced particle. It is degraded step-by-step in the shower.

The direct consequences of these basic physics principles are the following: at energy above 1 GeV, incident electrons or photons hitting a block of lead produce either secondary photons by bremsstrahlung or secondary pairs of electron/positron which, in turn, produce other particles by the same mechanisms. Step-by-step, an electromagnetic shower is developed as illustrated in Fig. 4.2. Each new particle

[1]Note that above 1 GeV, both processes are more or less energy independent.

produced in the shower carries an energy progressively degraded with respect to the energy of the previous emission. When the energy of the emitted particles becomes lower than a given energy threshold (the critical energy ϵ), the energy is dissipated in ionization or excitation and not in generation of other particles anymore so that the shower development stops.

4.1.2 General features of the produced shower

The longitudinal and lateral sizes of the produced shower can be parametrized with simple empirical functions. They can be described in a given material via one parameter: the radiation length X_0 (dependent on its atomic number, Z, and weight, A [9]). It represents the quickness with which electrons lose energy by bremsstrahlung or photons are absorbed via pair production. For an electron, it is the average distance x needed to be travelled in the material to reduce its energy to $1/e$ of its initial energy. For a photon, its intensity is reduced to $1/e$ of the original intensity after having travelled $x = \frac{9}{7}X_0$.

The physical scale over which a shower develops is then similar for electrons and photons, it is independent of the material type if expressed in terms of X_0. This parameter thus offers a universal way to express the shower characteristics via simple functions of X_0. Equation 4.1 gives the mean longitudinal profile in terms of depth inside the material in radiation lengths (t), and in terms of a and b, parameters related to the nature of the incident particle (γ or $e^{+/-}$) for an incident energy E_0[2].

$$\frac{dE}{dt} = E_0 b \frac{(bt)^{a-1}e^{-bt}}{\Gamma(a)}, t = \frac{x}{X_0} \tag{4.1}$$

Equation 4.2 expresses a measurement of the transverse size[3] of the shower, integrated over the full shower depth: the Molière radius. It represents the average lateral deflection of electrons at the critical energy after traversing one X_0. On average, 90% of the shower energy is contained in a cylinder of one R_M. Note that the transverse size is roughly energy independent.

$$R_M(g/cm^2) \sim 21MeV \frac{X_0}{\epsilon(MeV)} \tag{4.2}$$

[2]Note that the depth at which the maximum number of secondary particles is produced can be derived from equation 4.1 at $t_{max} \sim ln(E_0/\epsilon) + t_0, t_0$ = -0.5 (0.5) for electrons (photons).

[3]It is mainly due to multiple scattering of electrons and positrons away from the shower axis. The bremsstrahlung photons emitted by these electrons and photons also contribute to the transverse size.

4.1.3 Energy resolution

In an ideal electromagnetic calorimeter, the sum of the energy released by ionization and excitation by the charged particles in the shower is proportional to the energy of the incident particle. This is usually expressed via the total track length, T_0, of the shower[4] which is proportional to $X_0 \frac{E_0}{\epsilon}$, $\frac{E_0}{\epsilon}$ being the number of particles in the shower. The energy resolution of such ideal calorimeter is due to the fluctuations of T_0 so to the fluctuations of the number of track segments in the shower. As the shower development is a random process, the intrinsic energy resolution which is thus purely statistical is given by $\sigma(E) \propto \sqrt{T_0}$ which gives the $\frac{1}{\sqrt{E_0}}$ dependence of $\frac{\sigma(E)}{E}$.

However, realistic calorimeters suffer for not being infinite and for having a detector response deteriorated by instrumental effects. These different contributions allow to define the real energy resolution of an imperfect calorimeter as the quadratic sum of three terms:

$$\frac{\sigma(E)}{E} = \frac{a}{\sqrt{E}} \oplus \frac{b}{E} \oplus c \tag{4.3}$$

The first term, the "stochastic term", corresponds to the result of the shower intrinsic fluctuations explained above. The second one is the "noise term" coming from the electronic noise of the readout chain. It depends on the detector technique and on the features of the readout circuit. The last term, the "constant term" includes contributions that do not depend on the energy of the particle ; mainly nonuniformities which can come from the detector geometry, imperfections in the detector mechanical structure and readout system, from radiation damage, from the age of the detector, from the temperature gradient, etc. These nonuniformities can be cure if they present some periodic pattern. If not, they are more difficult to be corrected.

The constants a, b and c are three typical terms defining the quality of the detector resolution. For a sampling electromagnetic calorimeter, a is in the range 5-20%. b is much smaller than 100 MeV per channel for applications in several GeV region. c is usually smaller than 1%.

[4] T_0 is defined as the sum of all ionization tracks due to all charged particles

4.2 The ALICE electromagnetic calorimeter EMCal

In this section, the ALICE electromagnetic calorimeter EMCal will be introduced. As the main work of this thesis related to the calorimeter has been dedicated to the development of the calorimeter extension geometry in the ALICE computing software, the global structure of the calorimeter will be presented in more details.

4.2.1 EMCAL general principle of measurement

In EMCal which is a sampling calorimeter, a large fraction of the energy deposited by the charged particles and by the photons of the shower is collected. Each basic structure (a tower) of the calorimeter made of alternative layers of absorbers and active mediums that will be technically detailed in the sub-section 4.2.3 works the following way. In the absorber, the dense medium (pure Pb in EMCal), the shower is initiated and maintained while in the active part, the scintillator, the energy of the charged particles and photons is collected. Due to the action of the β and γ radiations, the scintillating materials emit light via a fluorescence process. The ionisation is converted in visible scintillation photons (from the deexcitation of the atoms of the scintillator) captured and transported in wavelength-shifting fibres that run longitudinally through the Pb/scintillator stack. The fibre bundle in each tower connects to an APD (Avalanche Photo Diode) photo sensor through a short light guide. In the APD, the signal collected in terms of number of scintillation photons is converted in an electrical signal which can then be experimentally exploited (see sections 4.2.3 and 4.2.4).

4.2.2 Technology and properties

The EMCal is the product of a collaboration of three countries (in alphabetical order): France, Italy and the United-States. It is a large Pb-scintillator sampling calorimeter of shashlish technology with cylindrical geometry located at a radius of $\sim$ 4.5 m from the beam line. Due to the installation of the PHOS below the TPC and the HMPID above the TPC, the full acceptance of EMCal is limited to a barrel section covering 107° in azimuth ($\phi \in$ [80°,187°]) and $\sim$ 1.4 units of pseudo rapidity along the beam direction ($\eta \in$ [-0.67,0.67]) (see Fig. 4.3). Its large acceptance however provides a pathway to jet physics. It is positioned opposite in azimuth to PHOS (see Fig. 3.4) allowing γ-jet correlation studies as well.

The calorimeter design incorporates a moderate detector average active volume density of $\sim$ 5.68 g/cm^3 which results from a 1 : 1.22 Pb to scintillator ratio by volume element. This results in a compact detector, consistent with the EMCal integration volume at the chosen detector thickness of 24.6 cm corresponding to $\sim$ 20 radiation lengths (20 X_0). EMCal is segmented in 12,288 elementary volumes (the towers) approximately projective in η and ϕ to the interaction point. Each of these towers is a basic detection sensor of the detector capable of high-resolution measurements of electromagnetic energy. Its typical transverse size of the order of the Molière radius (95% of effective Molière radius) is summarized in table 4.1. Technical details on the towers will be given in 4.2.3. Table 4.1 summarizes the main characteristics of the calorimeter.

Table 4.1: The EMCal Physical Parameters.

Quantity	Value
Tower Size (at η=0)	$\sim$6.0 $\times$ $\sim$6.0 $\times$ 24.6 cm^3 (active)
Tower Size	$\Delta\phi$ x $\Delta\eta$ = 0.0143 x 0.0143
Sampling Ratio	1.44 mm Pb / 1.76 mm Scintillator
Number of Layers	77/76 layers of Scintillator/Pb
Effective Radiation Length X_o	12.3 mm
Effective Moliere Radius R_M	3.20 cm
Effective Density	5.68 g/cm3
Sampling Fraction	10.5
Number of Radiation Lengths	20.1
Number of Towers	12,288
Number of Modules	3072
Number of Super Modules	10 full size, 2 one-third size
Total Coverage	$\Delta\phi = 110^o$, -0.7 $< \eta <$ 0.7

4.2.3 Mechanical structure of EMCal

General structure

The EMCal is located in the L3 magnet within a cylindrical integration volume sandwiched between the ALICE central barrel and the magnet coils. The EMCal Calframe visible in Fig. 4.3 supports the 100 t weight of the calorimeter between

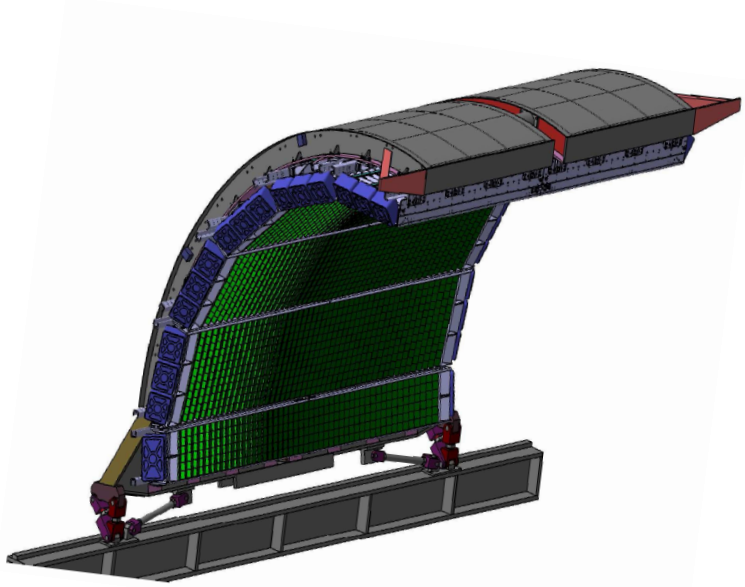

Figure 4.3: The full EMCal is constituted of 10 super modules and 2 one-third SMs. The Calframe and one of the two rails supporting EMCal are also represented.

two rails.EMCal consists of 10 "Super Modules" (SM), covering 20° in ϕ and 0.7 in η each, and distributed as depicted in Fig. 4.3, and 2 small SM of 1/3 of the normal size in the ϕ direction. These two extra SM can be considered as the first extension that has been added to the first designed EMCal geometry. Each SM counts 288 modules, 12 (in ϕ) $\times$ 24 (in η), while the one-third size SM contains 96 modules, 4 (in ϕ) $\times$ 24 (in η). Each module is divided into 4 (2 $\times$ 2) "towers/cells" so that one "normal" SM constains 1,152 towers/cells and the full EMCal counts a total of 12,288 (1,152 $\times$ (10 + 2$\times$1/3)) towers/cells.

Super Modules

A super module is the basic building block of EMCal and is the final unit which is handled for movement into the underground cavern and installation into the ALICE magnet. The 288 modules constituting a SM are arranged in 24 sub-structures called "strip modules" of 12 modules each (4 for the one-third SM) as shown in Fig. 4.4 and 4.5. In order to get the modules to face as much as possible the interaction point, strip modules are positioned in the super module with a small angle in η so that they are approximately projective with an average angle of incidence at the front face of the module of less than 2° in η and less than 10° in ϕ. The first strip module at η

= 0 is vertically positioned so that the 2 super modules in the positive and negative η regions perfectly join together at mid-rapidity (no gap). The blue boxes visible in Fig. 4.4 located at $\eta = \pm 0.67$ contain the SM electronic. The SM crate also visible in the same figure, mostly constituted in non-magnetic aluminum alloys, was designed not as a box holding the individual modules but as an integrated structure in which the individual strip module elements contribute to the overall stiffness.

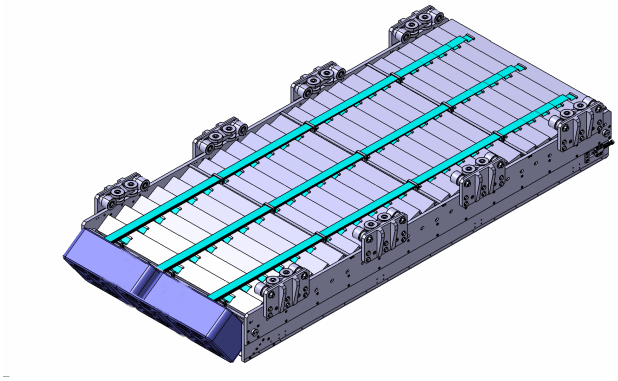

Figure 4.4: One of standard super module in EMCal. The upper surface (with green cables) is the farthest from the interaction point. The 24 strip modules are 1.5° rotated with respect to each others.

strip module

The structure of one strip module introduced in the previous paragraph is illustrated in Fig. 4.5. As for the SM, the strip module is a self-supporting unit. The 12 constituting modules are stacked thanks to a molded one-piece strongback made from sand cast aluminium. A strongback is 1494 mm long, 130 mm wide, and 100 mm thick with a weight of 15 kg. It is designed thick enough to provide sufficient inertia and mechanical stiffness. In addition to mechanical support for modules, a strongback is part of the structural component of the super module crate. It allows to protect the optical fibers which bundle ends in the strongback. It also acts as a structural mount for the light guide, APD, and charge sensitive preamplifier, and a light-tight enclosure for all these elements.

The electronics of one strip module is divided in 3 regions (left, middle and right). The green plates in the Fig. 4.5 illustrate how these regions distribute. The electronic output of the same regions of the strip modules are instrumented by 12 Front End Electronic (FEE) cards connected to the same trigger processor (Trigger Region Unit, TRU), which are used for event selection. So each SM has 36 FEE cards.

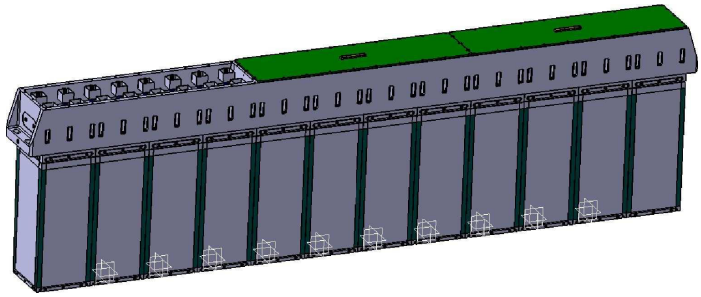

Figure 4.5: Schematic view of a strip module. It is mainly built from the association of 12 (4 in the EMCal extensions) modules stacked thanks to a strongback.

Module

The smallest building blocks of EMCal are the individual modules which contains $2\times2 = 4$ towers [91]. Every 4 towers in one module are bounded together with Aluminium plates (the straps). Each tower is made as a sandwich of 77 layers of 1.76 mm polystyrene base scintillator and 76 layers of 1.44 mm lead. White bond papers serve as a diffuse reflector on the scintillator surfaces and provide friction between layers. The scintillator edges are treated with TiO_2 loaded reflector to improve the transverse optical uniformity within a single tower and to provide tower to tower optical isolation at $> 99\%$. The Pb-scintillator stack is held precisely in place thanks to a compressive force applied first from the action of the front and back aluminium plates aligned and maintained by four straps on the module edges and secondly from the compression aluminium plate and the Belleville washers. A minimum compressive force is thus applied for stability which results in a resultant pressure in the stack is of $\sim 1.1\,\mathrm{kg/cm^2}$. The superposition of these different module pieces can be seen in Fig. 4.6 left (a module during its building) and right (cross sectional view of a module). One can note that each module has a radial slice rectangular cross section in the ϕ direction and a trapezoidal cross section in the η direction with a full taper of 1.5 degrees.

In order to collect the scintillation photons produced by the shower in a module, an array of $6 \times 6 = 36$ WLS fibers (Kuraray Y-11) run longitudinally through the Pb/sintillator sandwich in a given tower. At the top of each module, the fibers are bundled in a few mm diameter disk connected to the APD photo sensor (Hamamatsu S8664-55[5]) via a short light diffuser as can be seen in Fig. 4.7.

[5]The peak spectral response of these APDs is at a wavelength of 585 nm compared to the 476 nm emitted by the fibers Y-11.

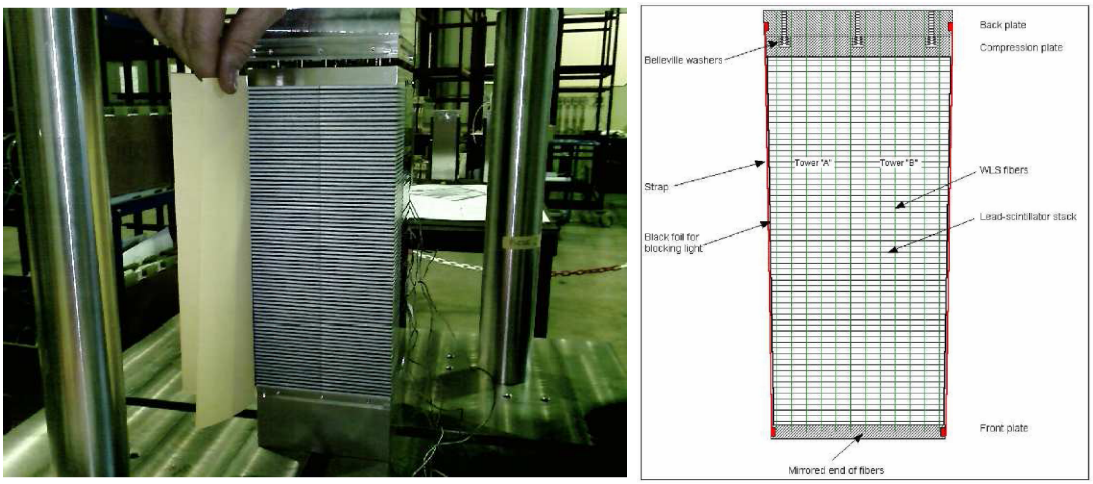

Figure 4.6: Left: A module fully equipped with fibres in its manufacturing process. Right: Cross sectional view of a module. The two towers constituting the module crosswise are clearly visible as in the left picture. Green lines illustrate the fibres crossing the tower (6×6 fibres in each tower, 12 fibres in this 2-tower section view).

Figure 4.7: Prototype EMCal module where the back enclosing structure has been removed in order to show the fibres bundled into the APDs.

4.2.4 Electronic readout, typical response and triggering

Readout

The collected light signal from fibres is converted in electrons in the APDs. Typically, an electromagnetic shower generates ~4.4 primary electrons/MeV. This signal is amplified by a factor 30 in the APDs before to be converted in a step pulse via a Charge Sensitive Preamplifier (CSP). The amplitude of the step is proportional

to the number of electrons integrated from APD and thus proportional to the energy of the incident particles. Note that the APDs can be operated at moderate gain for low noise and high gain stability in order to maximize the energy and timing resolutions. The signal from the CSP is then digitized in the FEE cards[6] (Front End Electronic) located at the large η end of each super modules (see section 4.2.3). In the FEE cards which provide readout of 32 EMCal towers, the electric signal is shaped (semi-gaussian shape) with 100 ns shaping time in dual shaper channels differing by a factor of 16 in gain (2 channels, one for low gain, one for high gain), and then digitized at 10 MHz with the 10-bit ALICE TPC Readout (ALTRO) chip for 14-bit effective dynamic range.

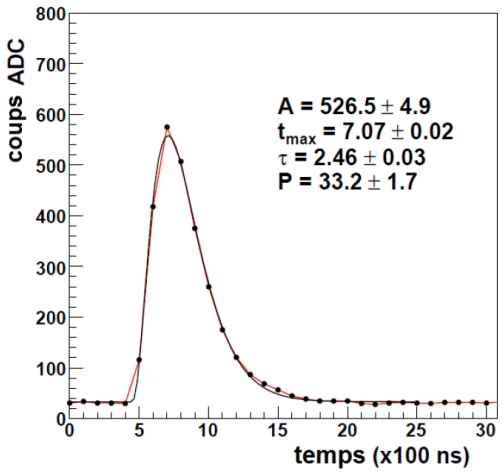

Figure 4.8: Signal reconstruction.

The typical obtained signal sampled in ADC counts is illustrated in Fig. 4.8 and reproducted by a Γ-function in ADC(t) (equation 4.4). It is dependent on the pedestal and the amplitude A.

$$ADC(t) = pedestal + A.e^{-n}.x^{n}.e^{n.(1-x)}, x = (t - t_0)/\tau. \quad (4.4)$$

As the shaper is a Gaussian of second order, n=2 in equation 4.4 and $\tau = n.\tau_0 = 2\tau_0$, τ_0 being the shaper constant. The energy deposited in the tower which corresponds to the charge collected from the APDs, is equal to the value of the parameter A at the time $(t_0 + \tau)$ where the function peaks.

[6]Note that the readout electronics of the PHOS have been adopted for the EMCal with small modifications [94].

Trigger

For a better selection of events, EMCal can be used as a trigger detector. The EMCal L0/L1 trigger for photons is using the same Front End Electronics (FEE) as PHOS. The FEE generates fast signals of a 2×2 tower sums (sliding window algorithm) which are then summed in the Field-Programmable Gate Array (FPGA) of the Trigger Region Unit (TRU) into 4×4 regions for high energy shower trigger decisions at L1. The output will be transmitted to the Summary Trigger Unit (STU) at a decision rate of 40 MHz. Also a L1 jet trigger of typically 8×8 towers region (up to 16×16) can be used to jet analyses.

4.2.5 Resolutions and detector response

The performance of the ALICE EMCal modules constructed according to the final design has been measured at CERN from a test beam in 2007. A 4×4 array of modules equipped with the full electronics chain with shapers and APD gains were tested. A LED calibration system was installed as well to monitor time-dependent gain changes. For more details about the experimental setup, one can refer to [94].

Energy and position resolutions

The energy resolution of the calorimeter obtained for electrons as a function of the incident beam energy on the range 0.5-100 GeV is illustrated in the left panel of Fig. 4.9 and is compared to a GEANT3 MC simulation. These energy scans were performed at different positions in the 4×4 module configuration including edges and the average value is displayed in the figure. A fit to the data following eq. 4.3 gives an energy resolution of $1.7 \oplus 11.1/\sqrt{E(GeV)} \oplus 5.1/E(GeV)$ and is directly compared to the energy resolution obtained from the simulation. We note an increase of the stochastic term (a) in test beam data compared to the simulation mainly due to light attenuation and light collection inefficiencies which were not taken into account in the simulation. The linear term (electronic noise), b, is probably set too high in the simulation. The small difference in the constant term (c) suggests a good tower-by-tower calibration. From the simulation, we also know that this term is dominated by the shower longitudinal leakage.

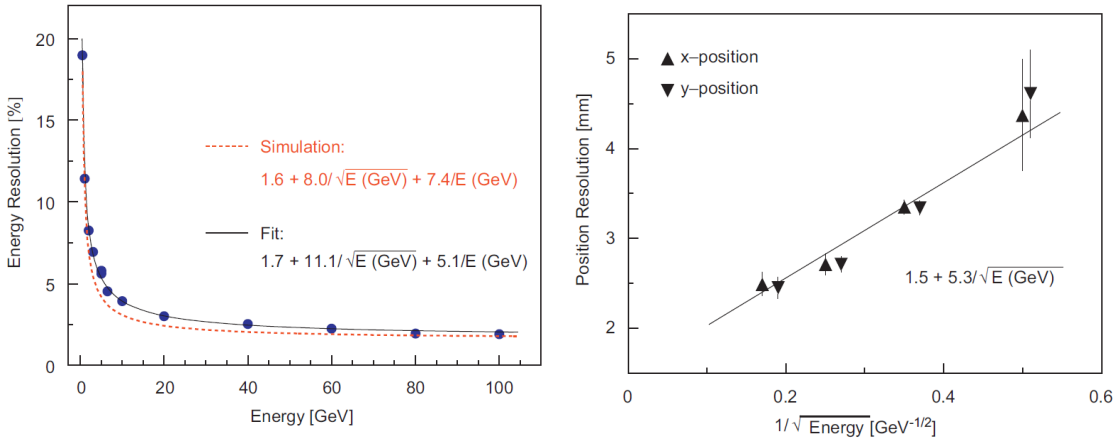

Figure 4.9: Left: Energy resolution for e^- as a function of the incident beam energy. The full line is a fit to the test beam data according to eq. 4.3. The dashed curve represents the resolution obtained from MC simulations. Right: position resolution (triangles for x-position and reversed triangles for y-position shifted to the right for visibility) as a function of the deposited energy for e^-.

The right panel of Fig. 4.9 displays the position resolutions in x and y of the calorimeter as a function of the deposited energy for electrons. No difference in the resolution in x and y is observed. The best fit result gives a shower position resolution of 1.5 mm $\oplus$ 5.3 mm / $\sqrt{E(GeV)}$. The segmentation of the calorimeter allows to obtain the hit position from the energy distribution inside a cluster with a better accuracy than the tower size.

Linearity

In order to study the uniformity of the energy response of the calorimeter, the absolute energy calibration obtained with a 3×3 tower cluster (the reconstructed energy - E_{meas}) is compared to the incident energy (E_{beam}) as shown in Fig. 4.10 as a function of the beam energy (full circles - linear fit to the data).

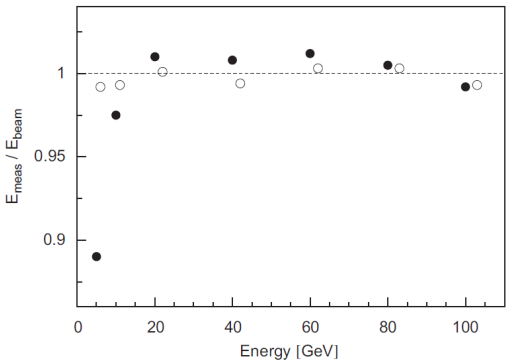

Figure 4.10: EMCal linearity measurement.

First of all, one can note that the linearity of the response is better than 1% above 20 GeV. A small deviation of the ratio from unity is observed however at high energies where longitudinal shower leakage are expected. At low energy, a clear deviation from unity is observed. In this region, threshold effects become non-negligible compared to the deposited energies and a loss of the light transmission should be responsible of the degradation of the reconstructed energy. Fitting the reconstructed energy response with a cubic function, one obtains a ratio close to unity (open circles).

4.3 EMCal in AliRoot

In ALICE, the offline framework called AliRoot is accessible to every users of the collaboration to perform simulation, reconstruction or analysis. It is a computer code built on the ROOT [95] system which uses the Geant3/Geant4 and FLUKA packages to perform the transport of particles through the detector or to simulate their energy deposition in a detector. The framework is based on the Object Oriented programming language C++ except for some libraries such as Pythia or HIJING. AliRoot is in continuous evolution as every user can improve its abilities or functions with his own code development.

Every tools available to perform any physics study in AliRoot are stored in sub-directories called "modules" containing either general tools (which make the foundation of the framework, which allow to steer ... or to handle the inputs/outputs, to generate events or to load analyses (STEER, EVGEN, ANALYSIS, etc.)), either tools to simulate/reproduce the detectors of the ALICE apparatus and their response (EMCAL, TPC, ITS, HMPID, etc.), either tools related to generators (PYTHIA6,

PYTHIA8, TDPMjet, HIJING, etc.) or "on-line" tools (HLT, RAW, MONITOR, etc.).

The work that has been performed for this thesis regarding the implementation of the DCAL geometry as well as the improvement of the EMCAL one has been implemented in the EMCAL module. This module contains mainly 6 sub-directories containing all the tools needed by a user to study the response of the EMCal detector to any input particle either simulated (EMCALsim), reconstructed (EMCALrec), treated on-line or off-line (EMCALraw and EMCALbase). Some general tools including the geometry definition of the calorimeter are stored in the EMCALUtils directory. EMCALTriggerBase has been developed to treat the EMCal trigger response. In this context which contains almost one hundred classes, a bit less than thirty classes and several macros have been modified and improved for this PhD work. This work and its results are presented in this section.

4.3.1 Generalities about the EMCal geometry implementation in AliRoot

Geometry configuration options

Several EMCal geometry definitions have been implemented in AliRoot by several collaborators in order to reproduce the different configurations that have been successively accessible to the collaboration during the installation phases of the calorimeter and hence during the following data taking periods. Presently, the following geometries are implemented in the EMCAL module, the correspondance in terms of Super Modules is given for each of them:

- EMCAL_FIRSTYEARV1: 4 SM, corresponding to the 2010 geometry
- EMCAL_COMPLETEV1: 10 SM, corresponding to the 2011 geometry
- EMCAL_COMPLETE12SMV1: 12 SM (10+2/3), corresponding to the 2012 geometry.

In this thesis, three other geometries including the DCal calorimeter (see section 4.4 for a detailed description of these implementations) have been added:

- EMCAL_COMPLETE12SMV1_DCAL: Full EMCal plus 6 DCal SM
- EMCAL_COMPLETE12SMV1_DCAL_8SM: Full EMCal plus 6 DCal SM plus 2 1/3 EMCal, geometry configuration for Run2 (years 2015-18)

- EMCAL_COMPLETE12SMV1_DCAL_DEV: Full EMCal plus 10 DCal SM (possible future configuration)

Note that other geometry definitions exist in AliRoot (EMCAL_PDC06, EMCAL_WSU, EMCAL_COMPLETE, EMCAL_FIRSTYEAR) but are not used anymore or have never been used. We do not give more details about these geometries.

By default, the EMCAL_COMPLETE12SMV1 configuration is loaded while the geometry is called in a given simulation or analysis.

Accessing the geometry and its transformations

In order to be able to work with the EMCal geometry in AliRoot, few objects have to be loaded and initialized before to start to manipulate or modify the geometry of the detector. In this sub-section, the main important lines to start with in any code development on the calorimeter are presented before to give a more detailed description of the classes that we have modified in the EMCAL module.

First of all, in order to have access to the geometry pointer, one can use two options in AliRoot working or not with an AliRunLoader.

- If working with an AliRunLoader, the galice.root file is available and the geometry can be accessed the following way:

```
1 AliRunLoader *rl = AliRunLoader::Open("galice.root",
      AliConfig::GetDefaultEventFolderName(), "read");
2 rl->LoadgAlice(); // Needed to get geometry
3 AliEMCALLoader *emcalLoader =
      dynamic_cast<AliEMCALLoader*>(rl->GetDetectorLoader("EMCAL"));
4 AliRun *alirun = rl->GetAliRun();
5 AliEMCAL *emcal = (AliEMCAL*) alirun->GetDetector("EMCAL");
6 AliEMCALGeometry *geom = emcal->GetGeometry();
```

- Otherwise, the geometry can be accessed with the following line:

```
1 AliEMCALGeometry *geom =
      AliEMCALGeometry::GetInstance("EMCAL_COMPLETE") ;
```

In this second case, while an AliEMCalGeometry object becomes available to a user, it is possible to have access to any transformation of the geometry of the

calorimeter via the file "geometry.root" which is generated during the simulation process. This file contains the transformation matrices for example to translate/rotate a given super module defined in a given geant3 volume from a local position (i.e. x=0, y=, z=0) to a global one (i.e. its exact position in the ALICE cavern) or vice-versa. This will be commented later in this section.

In order to use the geometry.root file, one has to call the following line:

```
1 TGeoManager::Import("geometry.root");
```

Note however that the transformation matrices are also stored in the Event Summary Data (ESDs) that will be more commented in section 5.1.1[7].

In order to read the parameters used for a given geometry definition of the EMCal calorimeter (cells centers, distance to IP, etc.), one has to execute the method PrintGeometry() defined in the class AliEMCALEMCGeometry accessible from an AliEMCalGeometry object with the lines below:

```
1 AliEMCALEMCGeometry* emcgeom = geom->GetEMCGeometry();
2 emcgeom->PrintGeometry();
```

Moreover, one can get any parameters (defined as data members of the classes) of the geometry via the call of the different getters of the classes.

Description of the classes used to define the EMCal geometry

The EMCAL geometry is implemented in several classes in AliRoot which have been cleaned and updated as well in order to include the DCal extension geometry definition. Below, we list the main classes used to define the geometry. It is important to note however that several other classes of the EMCAL module have been modified as well but they concern the tools used for the detector response (hit, digit,

[7]In AliRoot, the reconstructed data are stored in files containing a structure properly defined by the collaboration to store all the physical parameters needed to perform any performance or physics analysis. There are two types of files: Event Summary Data (ESDs) and Analysis Object Data (AODs). ESDs contain a large spectrum of geometrical and physical informations. An AOD is the end user, physicist data. AODs are obtained by filtering ESDs (tracks, vertices, ...) or by high level reconstruction based on ESDs or AODs (charmed hadrons, jets, photons, ...).

cluster definitions, etc.), for the trigger and not its geometry so that they are not introduced here.

- *AliEMCALGeometry*: it is the steering geometry class which allows to create an EMCal geometry object and thus to load the geometry of EMCal in a given simulation/analysis independently from any other AliRoot classes. It contains no dependencies to the STEER module or to any EMCal classes not dedicated to the geometry. This class contains as well all the tools used to manipulate (indexes, AbsId, etc.) or transform (rotate/translate/change coordinate frame/etc.) the different components of the detector (from a basic cell to a complete SM).

- *AliEMCALEMCGeometry*: this class allows to precisely initialize the geometry as it contains all the parameters defining the EMCal geometries (tower composition, size, Super Modules number, η and ϕ boundaries of SM, etc.)

- *AliEMCALGeoParams*: class containing most of the geometry constants tabulated which can then be accessed from anywhere in the EMCAL code.

- *AliEMCALShishKebabTrd1Module*: in this class, the modules are defined and the position of the modules in the local super module reference system is calculated.

- *AliEMCAL, AliEMCALv0/v1/v2*: these classes are used in the simulation process, and are at the origin of the creation of the EMCal geometry volumes and definitions in the geometry.root file. More details about how the geometry is created are given in the next section. AliEMCAL is the main steering class while the AliEMCALvX derive from it. AliEMCALv0 create the geometry: it include volume definitions and creations, creation of all materials and location of all volumes and pieces of the detector. The AliEMCALv1 class which derives from v0 is not used anymore for the simulation. AliEMCalv2 which derives from v1 does all the particle propagation in the EMCal material (it corresponds to the hit response which is simulated).

  In order to configure the EMCal geometry in a given simulation via the Config.C macro, the following line has to be called:

```
1 AliEMCAL *EMCAL = new AliEMCALv2("EMCAL", TString GeoName, Bool_t
    checkGeoRun);
```

where GeoName should be one of the geometry configurations available in AliRoot listed in sub-section 4.3.1 (in paragraph: Geometry configuration options) and checkGeoRun is a boolean that activates the geometry initialization depending on the run number.

How to build the geometry of EMCal with ROOT/AliRoot/Geant3

The basic idea which is followed to create a detector geometry with ROOT and Geant3 is the following. Before to create any physical object (a tower, a module, a SM, an aluminium plate, a Pb tile, etc.), one needs to first define a global volume filled with air (which will define the mother frame) in which all the pieces of the detector will be added step-by-step and then to define volumes (nodes) to which the physical objects will be associated. This general procedure is driven by the tools available in ROOT and Geant3 to build geometries via in particular the TGeoManager[8] and the TVirtualMC[9] classes. A given volume is defined with some typical shape, dimensions and position. Typically in ALICE, the initial position given to a volume is in the center of the apparatus: x=0, y=0 and z=0 (which also defines the center of the mother volume/frame). A given volume is then filled with the designed material before to be shifted/rotated/etc. to its exact position in the mother frame. The different volumes/nodes created and stored in the geometry.root file are declared in the AliEMCALv0 class with the following names (from the biggest objects/volumes (complete EMCal) to the smallest structures (modules, etc.)): XEN1 (name of EMCal global volume) → SMOD/DCSM/SM10/SM3rd/DCEXT (names given to the different types of Super Modules in the code, i.e. DCSM and DCEXT stand for DCal Super Modules and DCal SM extension (see section 4.4) → EMOD (name of a module) → SCX/SCMX/etc. (tower) → PBTI (Pb tiles) → etc.

Moreover, the tools available to program a detector geometry in ROOT give access to the class THGeoMatrix with which transformation matrices can be created. This object allows for example to define, fill and store the transformation matrices that can be applied to a given physical object of the EMCal geometry to change its frame reference from a local coordinate system to a global one and vice-versa. These

[8]This class is embedding all the API needed for building and tracking a geometry. It defines a global pointer (gGeoManager) in order to be fully accessible from external code. TGeoManager contains lists of media, materials, transformations, shapes and volumes.

[9]This class in ROOT provides a virtual interface to Monte Carlo and enables the user to build a virtual Monte Carlo application independent of any actual underlying Monte Carlo implementation itself.

transformation matrices are declared and filled in the AliEMCALv0 class and then used in the AliEMCALGeometry class to define several transformation functions (GetGlobal(), EtaPhiFromIndex(), etc.) which apply to cells, SMs, etc. and that can be used by any ALICE member.

While all the volumes and physical objects are created, duplicated, etc., some Ids are associated to the different objects in the global EMCal frame (absolute Id = AbsId) or in local frames (i.e. in a SM frame) in order to be able to manipulate easily these objects. Several functions are programmed in the code to play with the indexes and their relations with the physical positions in η, ϕ, x, y, z, etc. Meanwhile a set of ids (and their associated functions) is (are) also defined for the TRU used for triggering in EMCal (3 TRUs are used for each super module while 1 TRU is used for a super module extension).

4.3.2 Modifications implemented in the EMCal geometry code

Among the roughly 30 classes which have been modified for this PhD work (they are listed in the class dependency diagram presented in Fig. 4.11 in the bold rectangles, the arrows representing either a dependency in terms of inclusion or an inheritance dependency between two classes), the main changes which have been performed are the implementation of three new geometries for the system EMCal / DCal. This is explained in the next section (4.4). However, the geometry code used for EMCal itself has been a bit cleaned and optimized in order to avoid several hard-declarations of the same variables at different places in the code. For these specific variables (which were numerous), the same data member declaration (initialized only once) has been propagated through the classes. As this work is very technical, we of course do not give the detail of the modifications implemented. The different names of the geometry hard-coded as well several times in the software are from now on stored in a table of names called fEMCSMSystem which should now be called through the code. The geometry software from which we started to implement the DCal geometry was the product of several physicists who made the code evolves with time. Unfortunately, it generated a dangerous non uniformity in the way it was coded which could bring to some mistakes in the geometry definitions and which required the modifications added.

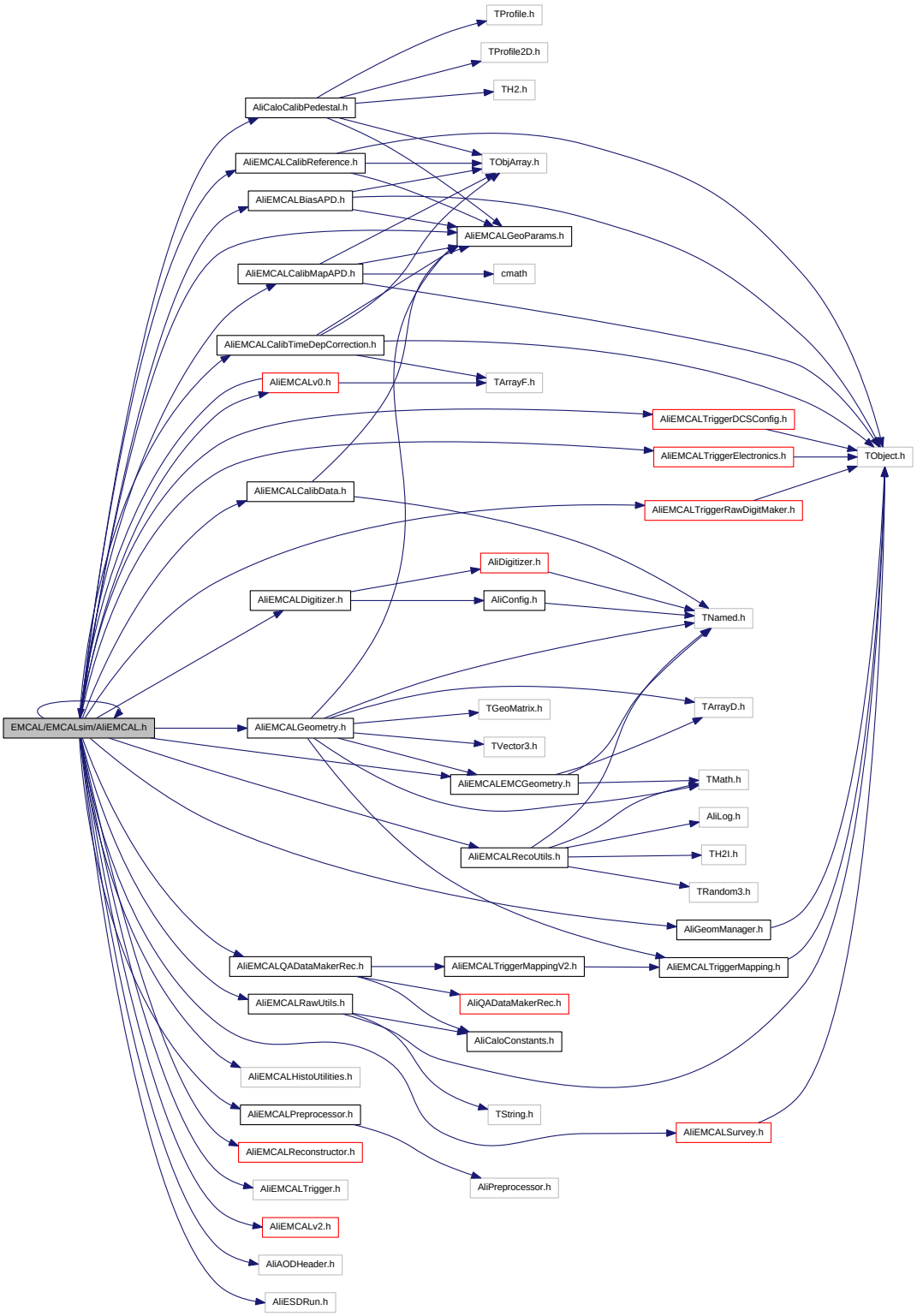

Figure 4.11: Diagram presenting the dependencies between the classes which have been modified in this PhD work. The class modified are included in bold rectangles (black and red). "Red" indicates that the corresponding box has more arrows than what is shown. The arrows represent a dependence in terms of inclusion or in terms of inheritance between two classes. This diagram has been obtained with doxygene in AliRoot [11].

4.4 The DCal calorimeter and its geometries

As previously introduced, the DCal calorimeter standing for "Di-jet Calorimeter", is a sampling electromagnetic calorimeter of same technology than the EMCal one, which has been installed in the ALICE cavern end of 2014 as an extension of the EMCal calorimeter. DCal which was designed to study back-to-back event correlations in ϕ was initially tought for historical, political and space reasons with different geometry configurations. As its final design is not yet fully decided, we have implemented 3 different versions of DCal geometry in AliRoot:

A *Geometry of its original design*: in that case, DCal contains 6 Standard DCal SM arranged in 2 arms of 3 SMs on both sides of PHOS covering a ϕ acceptance from 260° to 320° and an η coverage from 0.22 to 0.67 (0.67 being the η outer edge value of the EMCal).

B *Geometry of its current design*: it contains 6 standard DCal SM and 2 EMCal SM extension of 1/3 in ϕ. This geometry corresponds to the previous original one plus 2 SM extensions covering a region in ϕ from 320° to 327°, and $|\eta| < 0.67$ (as for EMCal). This current geometry is illustrated in Fig. 4.12.

C *Geometry of a potential future design*: it contains 10 standard DCal SM (same η acceptance as the current design but ϕ from 220° to 320°), while EMCal ϕ coverage is shifted by 40° from 80°-187° to 40°-147° in order to be exactly back-to-back in ϕ with DCal. This potential extension of DCal is still considered as some free slots are still available in the cavern on both sides of PHOS (see Fig. 4.12) and could be filled with 4 more SMs.

In order to present the work of geometry implementation done for the 3 previous geometries in the section below, the version "B" is taken as the default example, as it corresponds to the geometry of the DCal calorimeter installed so far in ALICE. The actual acceptance of DCal thus provides a 67° coverage in azimuth (260° to $\sim$ 327°) and $0.22 < |\eta| < 0.67$ in η. Together with PHOS (ochre blocks in Fig. 4.12), they provide the measurement for the electro-magnetic component of a given jet energy back-to-back to a jet measured in the EMCal.

The standard DCal SM is shorter than the EMCal ones in η. Each SM consists in 192 modules (12 (in ϕ) $\times$ 16 (in η)) against 288 for EMCal. Each DCal module is exactly the same as for EMCal, divided into 4 (2 $\times$ 2) "towers/cells". On the contrary to the standard DCal SM, the DCal SM extension is exactly the same as

the EMCal SM extension as can be seen in Fig. 4.12. In total, DCal thus counts a total of 5,376 separate elementary towers/cells.

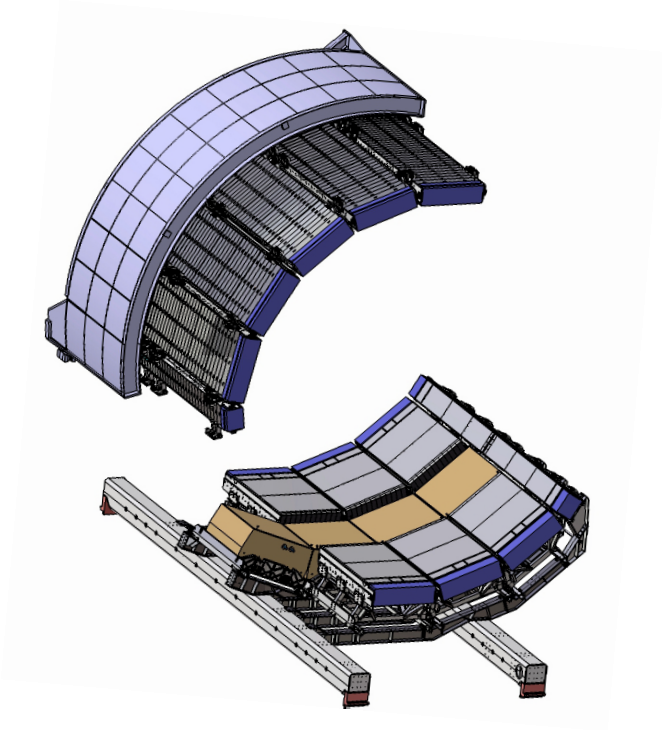

Figure 4.12: Schematic view of the calorimeter/spectrometer system: EMCal, DCal and PHOS on their respective support structures. In order to be able to see EMCal, half of its Calframe has been drawn in this picture. The ochre blocks correspond to the 4 modules of the PHOS spectrometer. The DCal calorimeter has been installed on both sides of PHOS except its extension which covers the full EMCal η acceptance. The full system allows back-to-back correlation measurements.

4.5 DCal geometry implementation in AliRoot

4.5.1 Strategy followed implementing the DCal geometry

In order to be efficient to code the DCal geometry, taking into account as well that both EMCal and DCal share a similar structure and the same physics goal, we have programmed the DCal geometry based on the EMCal one, DCal being an extension of the EMCal coverage. Below, we list the main modifications introduced in the EMCAL module in order to define DCal. As already explained, the implementation task we have performed has required modifying a bit less than 30 classes of the EMCAL module of AliRoot (Fig. 4.11). These classes concern both the simulation part of AliRoot (directly linked to the detailed geometry of the detector but

also including the detector response while a particle propagate through it) and the reconstruction one (as all the classes dedicated to the production of physics objects also needed to be modified for DCal). In this section, we explain the main modifications affecting the geometry. Details about the modifications applied for the hit production, applied in the digitizer, in the clusterizer, etc. are not given as too technical. One just needs to keep in mind that the production of hits, digits, clusters, etc. remains the same as before. We only modified the corresponding classes ensuring that they were still valid and working for DCal as well. We tested however that no bug was introduced in the edges of the detectors where the clusterization process can be affected. This is discussed in the section 4.6.2.

The different steps followed to implement the DCal geometry are listed below and discussed in more details in the sections 4.5.2, 4.5.3 and 4.5.4. In section 4.6 we then present the tests perform to validate the work performed.

- Expand the EMCal global volume declaration (XEN1) and create new DCal SM nodes (DCSM and DCEXT) in XEN1 to expand the whole Electro-Magnetic Calorimeter system. The DCal SM nodes are then positioned with respect to the EMCal SM ones taking into account the gap in ϕ between the two systems. These nodes can then be filled with a typical DCal SM geometry.

- Define the characteristics of a DCal SM from its more basic structures to its global shape in terms of volumes, size, materials, positions, etc. Note that as there is no strip module sub-structures defined in the code, the object declared allowing to build a complete standard SM is made of the association of 12 (4 for the EMCal extensions) parallel ShishKebab module lists in ϕ. A ShishKebab module list thus contains all the 24 modules present along the η direction. For DCal the standard SM (DCSM) is defined as for EMCal but the 12 lists of ShishKebab modules associated do not contain the first 8 modules starting from $\eta = 0$ as DCal SM are shorter in η.

- Give an absolute id to each DCal cells. The AbsId numbering chosen is in continuity to the EMCal one. The total number of cells increases to $17,664 = 12,288|_{EMCal} + 5,376|_{DCal} = 12,288|_{EMCal} + [6 \times (2/3) \times 1,152 + 2 \times (1/3) \times 1,152]|_{DCal}$. After modifying the functions which correlate the AbsId with the local ids of EMCal sub-systems (local id in modules, SM, etc.) and the functions which allow to define the relationship between AbsId and local or global positions (local/global transformations) make sure that they work properly for DCal and that they are still valid for EMCal.

- Increase the number of TRUs in the full EMCal/DCal system, add the corresponding mapping. After modifying the functions related to the new TRU mapping, make sure they work for DCal and are still valid for EMCal.

- Add new calibration constants corresponding to new DCal towers in both the reconstruction code and the corresponding Offline Condition Data Base (OCDB).

- Clean the EMCal code.

4.5.2 Detailed structure of a DCal SM

The details of the DCal structure are similar to the EMCal one. The main difference come from the list of "shishkebab" modules (strip modules) defined. EMCal contains a full list of 24 strip modules (index: 0 to 23); while DCal contains the last 16 strip modules of the list (index: 8 to 23) which means that the first 8 strip modules (index: 0 to 7) are removed. Figure 4.13 illustrates the different volumes (from the mother objects to the daughter objects) which have been created for the definition of a DCal SM in the geometry code starting from a full DCal SM (called DCSM) to the most basic structures: a scintillator volume called scintillator, a volume for a layer of paper called PAP and a volume for a tile of Pb plus paper called PA. In the code, each cell is defined as the superposition of 77 layers of scintillator, 76 layers of Pb and 77 layers of bound paper. This has been programmed as 77 scintillator volumes, 76 PA (PA##(01-76)) volumes and 1 PAP (PAP1) volume. This superposition of layers defines a given tower called SCMX. The association of 2 towers is called SCMY. Two SCMY volumes together form the basic module called SCM0. The complete module including the bottom and top Aluminium plates is defined as EMOD in the geometry. Finally, the modules are associated all together in a SM as can be seen in the figure based on what was already programmed for EMCal but removing the first 8 modules in the Shishkebab list, modules the closest to the $\eta = 0$ region in order to create a SM shorter in η than an EMCal one (as PHOS occupies the central region of ALICE).

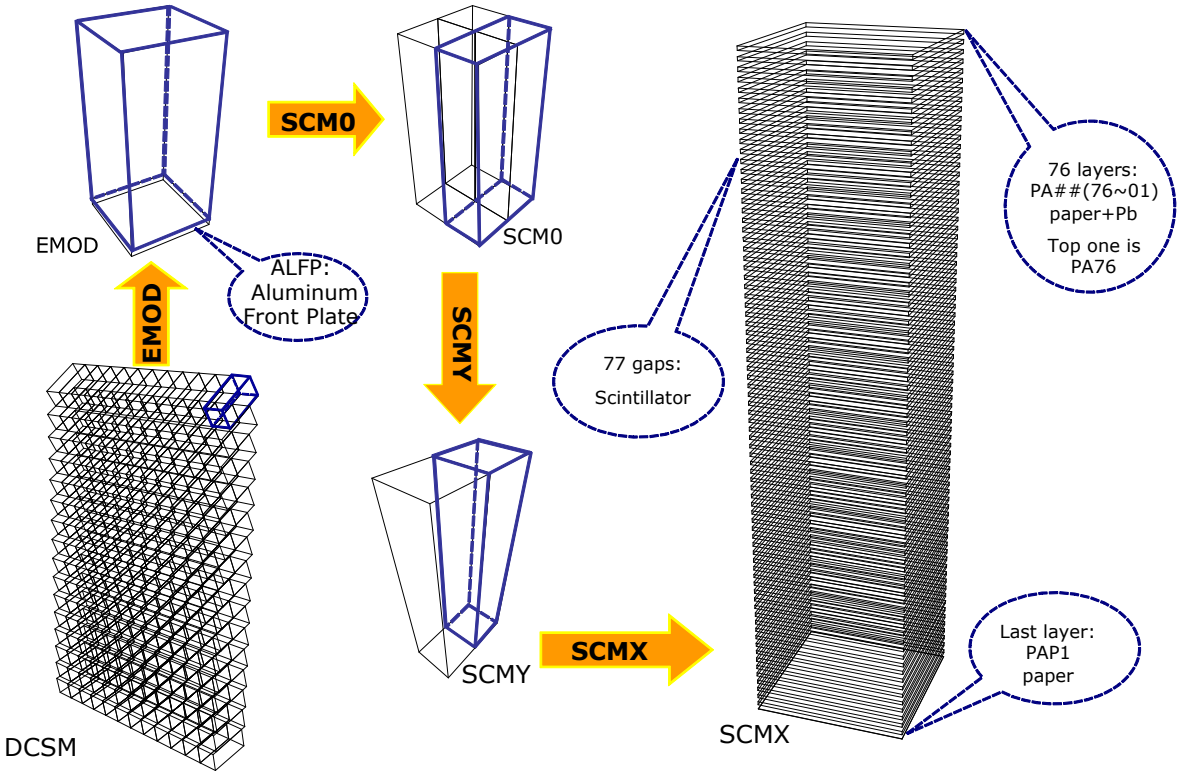

Figure 4.13: Details of the sub-structures constituting a SM from a SM to a given layer in a tower. Each sub-structure has a corresponding name in the geometry code: DCSM stands for a standard DCal SM, EMOD for a module, SCM0 for a module without aluminium plates, SCMY is half of SCM0 (it is not related to an existing part of a module as it counts two towers), SCMX defined as half of a SCMY is one tower, PAP1 and PA##(01 $\sim$ 76) represent the 77 layers of paper and the 76 layers of lead and the rest of the tower includes 77 layers of Scintillator.

4.5.3 Definitions of 3 new geometries of the system EMCal/DCal in AliRoot

A standard shorter DCal SM being defined as described in the previous section, the EMCal volume has been extended in order to add new volumes dedicated to the positioning of the new DCal ones. New transformation matrices have been defined in order to be able to create the three EMCal/DCal geometries defined in sections 4.3.1 and 4.4 C and to propagate the DCal SM from the local (0,0,0) position to their exact position relative to the EMCal. Figure 4.14 illustrates the mapping of the 3 geometries created. One can see the position of each SM on both the A and C sides of ALICE, the position of the GAP between EMCal and DCal, the region occupied by PHOS. The figure also indicates the numbering used in the code to manipulate the DCal SM which have been added in the continuity of the EMCal SM indexes.

For the standard geometry (left panel of the figure), the 6 DCal SM added are numbered from 12 to 17, for the actual geometry (right panel of the figure), the SM are numbered from 12 to 19, the indexes 18 and 19 being attributed to the 2 DCal SM extensions. The central panel of Fig. 4.14 shows the possible DCal upgrade geometry which could includes 10 SM numbered from 12 to 21.

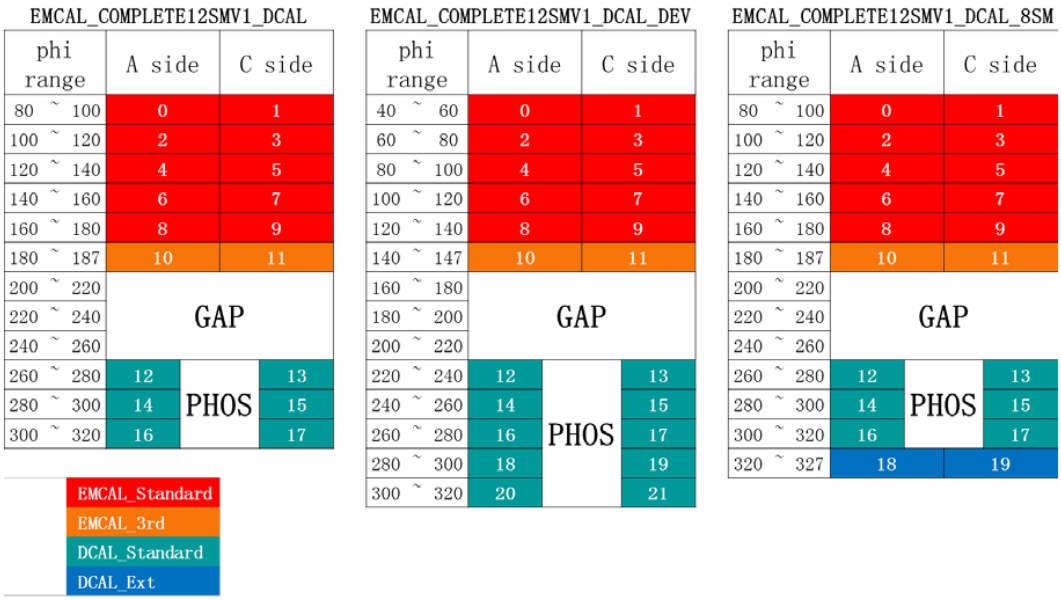

Figure 4.14: SM mapping of the 3 geometries implemented. Left: standard geometry (EMCAL_COMPLETE12SMV1_DCAL), right: actual geometry (EMCAL_COMPLETE12SMV1_DCAL_8SM) and middle: potential future geometry (EMCAL_COMPLETE12SMV1_DCAL_DEV). SM with indexes from 0 to 9 constitute EMCal, 12 to 17 or to 21 constitute DCal, 10 and 11 represent the indexes of the 2 EMCal SM extensions, 18 and 19 are the indexes of the 2 DCal SM extensions.

Eventually, the results of the three geometries implemented are illustrated in the following three figures 4.15, 4.16 and 4.17. A three dimension representation is proposed for each geometry. Three views are given on each figure in the (X,Y,Z) ALICE restframe: the 'A' panel shows a view along the Z direction (beam direction, blue axis) ; the 'B' panel shows a view along the X direction (-90° with respect to the vertical direction, red axis) and the 'C' panel shows a view along the Y direction (vertical direction, green axis).

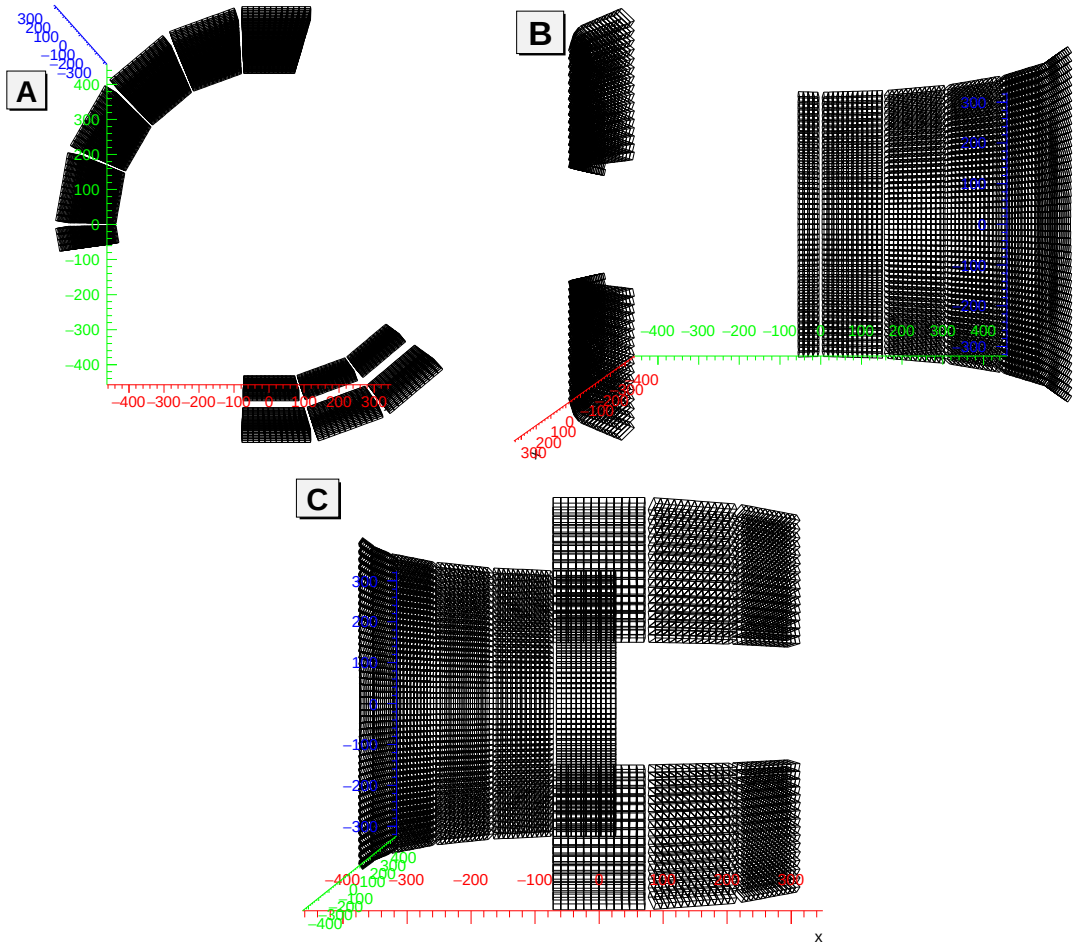

Figure 4.15: EMCAL_COMPLETE12SMV1_DCAL: geometry mapping of DCal (6 SM) + EMCal in AliRoot. The three axes show the cartesian coordinates x (in red), y (in green) and z (in blue) in cm. The figure A is the view against z axis; the figure B is the view against x axis; the figure C is the view along y axis.

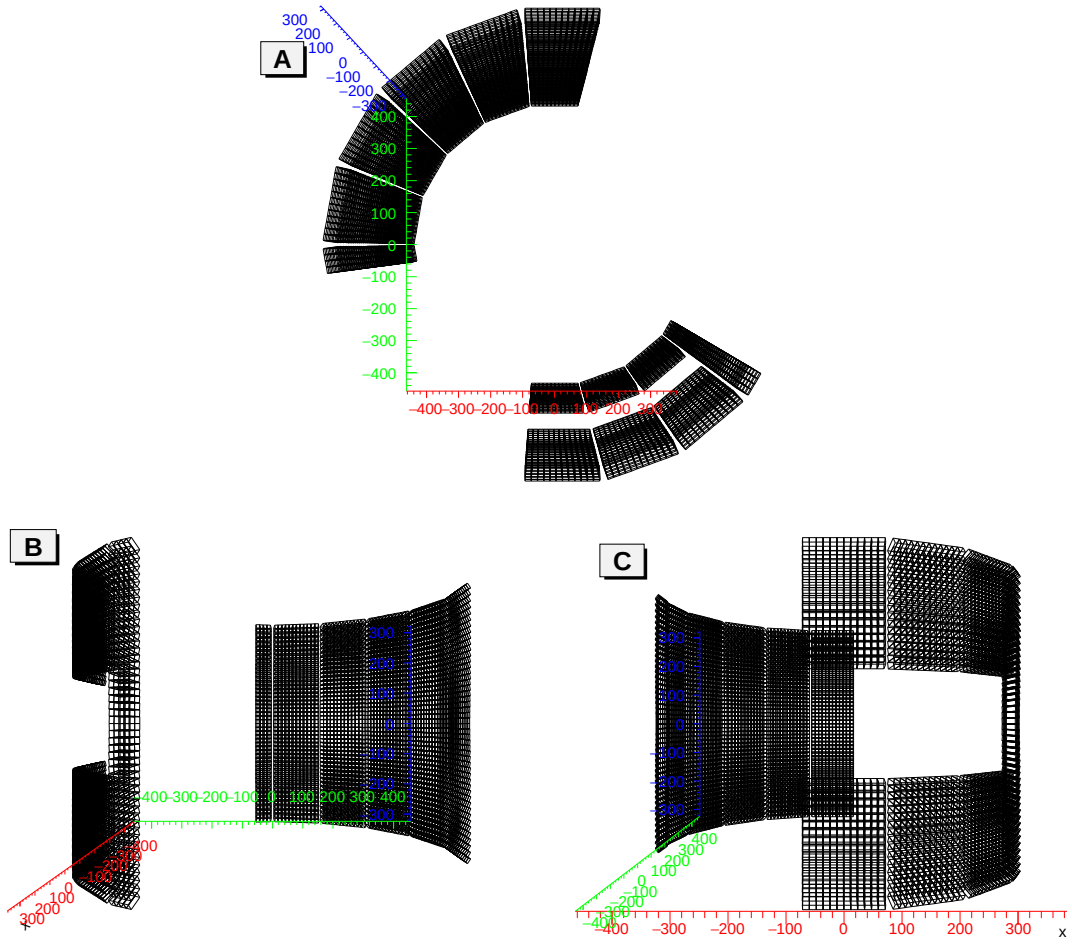

Figure 4.16: EMCAL_COMPLETE12SMV1_DCAL_8SM: geometry mapping of DCal (6+2 SM) + EMCal in AliRoot. The three axes show the cartesian coordinates x (in red), y (in green) and z (in blue) in cm. The figure A is the view against z axis; the figure B is the view against x axis; the figure C is the view along y axis.

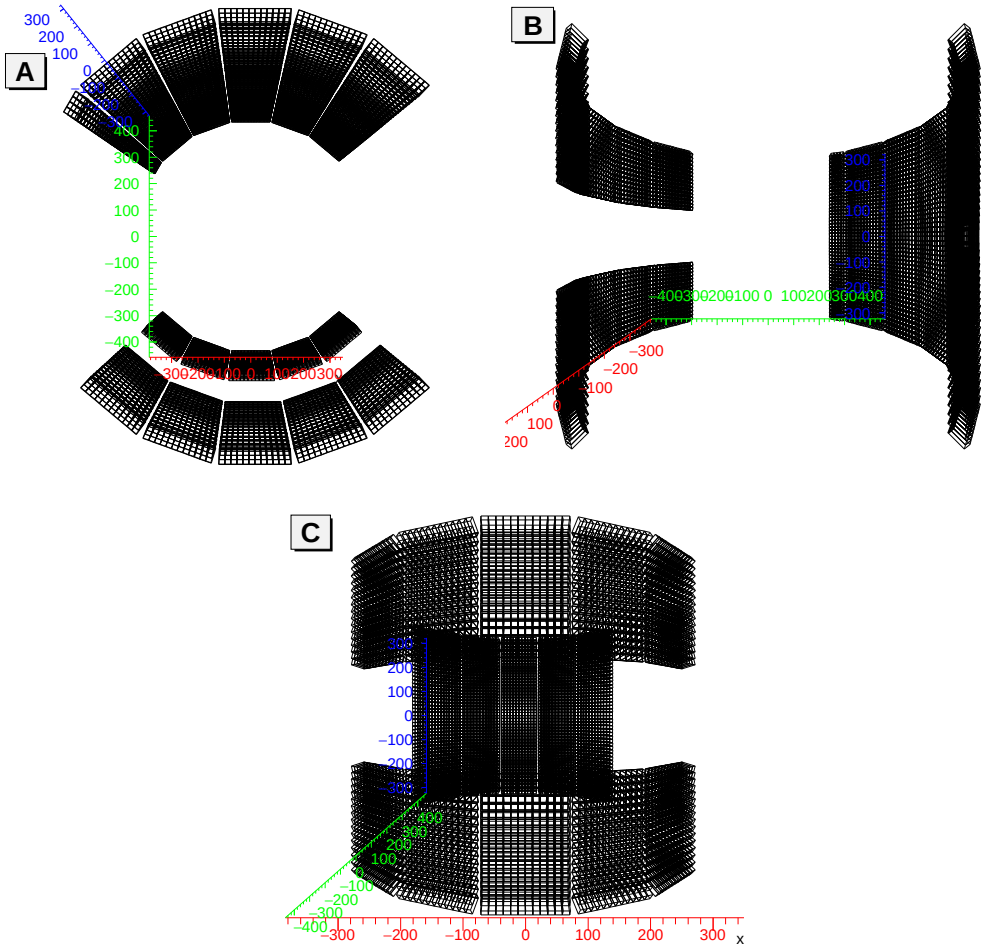

Figure 4.17: EMCAL_COMPLETE12SMV1_DCAL_DEV: geometry mapping of DCal (10 SM) + EMCal (shifted in ϕ: $(40° < \phi < 147°)$ in AliRoot. The three axes show the cartesian coordinates x (in red), y (in green) and z (in blue) in cm. The figure A is the view against z axis; the figure B is the view against x axis; the figure C is the view along y axis.

4.5.4 Indexes, positions and TRU mapping

The very thin segmentation of the detector allows to have independent capabilities to measure the energy deposition which can thus be correlated to a given position in EMCal/DCal. In order to be able to name a given module/cell in the detector, indexes in local or global frames are given to its constituting parts.

Indexes and positions

Figures 4.18, 4.20 and 4.19 illustrate the different indexes used in the EMCAL/DCAL geometry code to identify a given module or cell in a given SM (local indexes) or in the complete detector (global indexes, called for example, absolute Id for the

cells). It is indeed important to be able to name a given module or a given cell via an index. Each index, can then be associated to a position in (η,ϕ) or in (x,y,z) in the local frame of a SM or in the global frame of the full ALICE system.

Taking EMCAL as example, one can see in Fig. 4.18 the different indexes used in a SM by the collaboration.

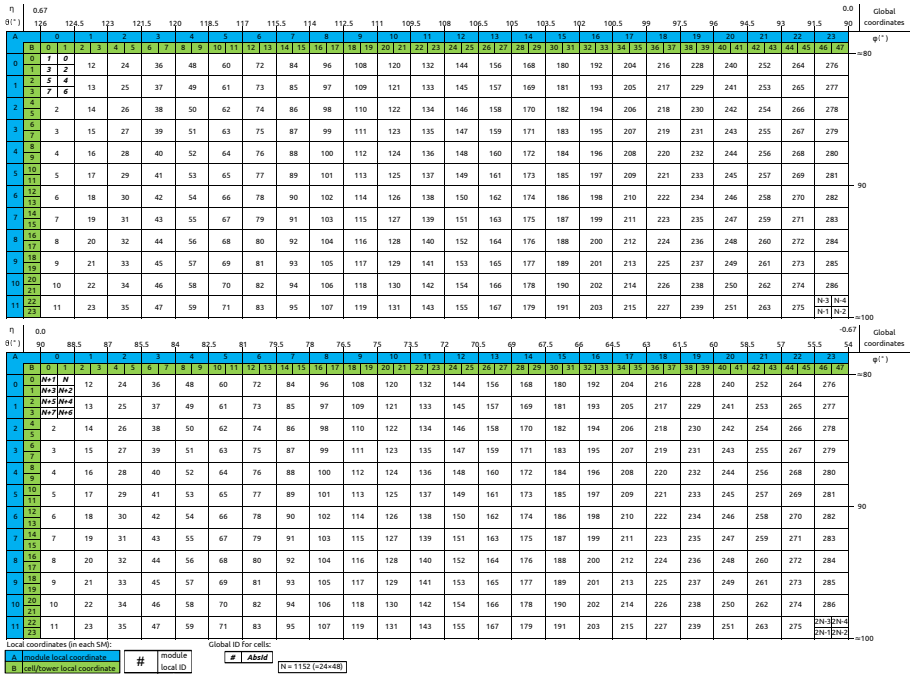

Figure 4.18: Local coordinates and global coordinates of super module in EMCal. These are from the first 2 EMCal super module (SM0 in A side and SM1 in C side). The local coordinates of modules are same in each super module, which are shown in blue background. The AbsID (are shown in only the first 2 and last modules) of cells are identical. The global coordinates are shown in the outer top (η and in ϕ) and right (in ϕ) region.

Two SM are represented in this figure. The upper one is the first EMCal SM (SM0) in the A side, while the lower one is the first EMCal SM (SM1) in the C side. Their η coverages are respectively [0.,0.67] ([90°,126°] in θ) and [-0.67,0.] ([54°,90°] in θ) for ϕ in [80°,100°]. The local indexes called *ieta* and *iphi* in η and ϕ directions (in blue in the figure) indicate the position of a given module in a local SM. *ieta* varies from 0 to 23 corresponding to the 24 stripmodules which constitute a SM while *iphi* varies from 0 to 11 corresponding to the 12 modules included in a stripmodule. In this local coordinate system, one can then associate a local Id, *iModule*, to the modules starting from the (*iphi,ieta*)=(0,0) position corresponding to *iModule*=0 to *iModule*=287 corresponding to the module at the position (*iphi,ieta*)=(11,23). Local indexes also exist for cells (in green in the figure). And the position/order of the 4

cells in each module is the same (which can refer to the first module in Fig. 4.18.

Once these local positions and indexes have been defined, each SM is then positioned in ALICE at its exact position thanks to a local to global transformation each SM carrying the indexes specified in Fig. 4.14. In this new global frame, an absolute index (*AbsId*) is then associated to all the cells/towers which constitute EMCal. The way it is distributed in modules for SM0 is illustrated in Fig. 4.18 in the first two modules and in the last one. For SM0, the *AbsId* varies from 0 to 1,151. This numbering increases continuously from one SM to the next one as shown in the figure and following the rule:

$$AbsId = N^{total}_{PreviousSM} + 4 \times iModule + iPositionIndex \tag{4.5}$$

iPositionIndex varying from 0 to 3, and $N^{total}_{PreviousSM}$, the total number of cells in the previous SM, is equal to:

$$N^{total}_{PreviousSM} = \begin{cases} 1,152 \times iSM & 0 <= iSM <= 10 \\ 11,904 & iSM = 11 \\ 11,228 + 768 \times (iSM - 12) & 12 <= iSM <= 18 \\ 16,896 & iSM = 19 \end{cases} \tag{4.6}$$

So for SM1, the *AbsId* varies from 1,152 to 2,303, for SM2 from 2,304 to 3,455, etc. This *AbsId* can give access to the exact position of a given cell in (η,ϕ) coordinates or in (x,y,z) coordinates. These Id/position transformations are all accessible to a user in the geometry code.

While implementing the DCal geometry and the new EMCal one, we have propagated these Id mapping to the complete system, taking into account the different gaps in (η,ϕ) to define the exact position of each sub-system in EMCal/DCal while keeping a continuous index numbering. Figure 4.19 is given as an example for the case of the two first SMs of DCal which come just after the EMCal SMs in the geometry numbering. One can note that *ieta* varies from 0 to 16 this time, corresponding to the 16 stripmodules which constitute a DCal SM while the number of modules in a stripmodule remains constant (same *iphi*). Note that the same kind of numbering/position has also been defined for the EMCal and DCal extensions (see Fig. 4.20 for the EMCal extensions).

All the methods allowing any transformations from local to global positions or from id to positions have been updated for the three geometries implemented.

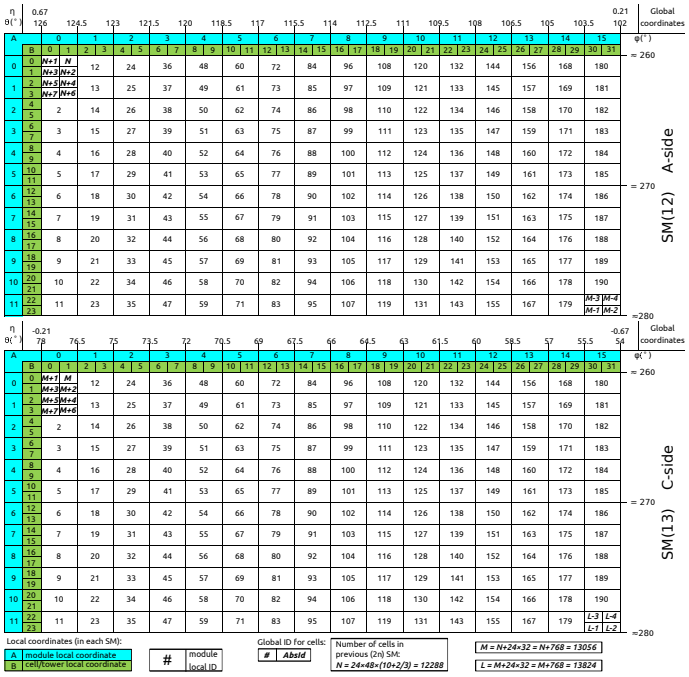

Figure 4.19: Local and global coordinates of the first 2 super modules in DCal (SM12 in A side and SM13 in C side). Same comments as for Fig. 4.18.

TRU mapping

The TRU is used to fastly process the energy deposition calculation, and give a signal to the ALICE trigger system to obtain/label the event. The SM number being increased to take into account DCal in the new calorimeter geometry, it has been necessary as well to extend the number of TRUs and their mapping. In Fig. 4.21, one can distinguish 3 horizontal zones representing the repartition of TRU per SM for the 3 implemented geometries. Each SM thus contains 3 TRUs. At the time this work has been performed, it was not decided yet how TRUs will be distributed in DCal as 1) the DCal SM are smaller in η than the EMCal ones, and 2) the electronic of the calorimeter was about to be changed based on the PHOS one.

For this work, we have thus chosen to program a default TRU mapping modeled on the EMCal one. It is illustrated in Fig. 4.21 where the distribution of TRUs and their allocated indexes can be seen. As the DCal SM are shorter in η, for each TRU used, 1/3 of the channels of a given TRU are not connected to any DCal module (this is represented as the GAP for SM number above 12 (blue regions)). For DCal, the indexes have been propagated in continuity of the EMCal indexes.

It is important to note that this TRU distribution and TRU indexes are no longer valid in ALICE as they have been modified later on based on the PHOS

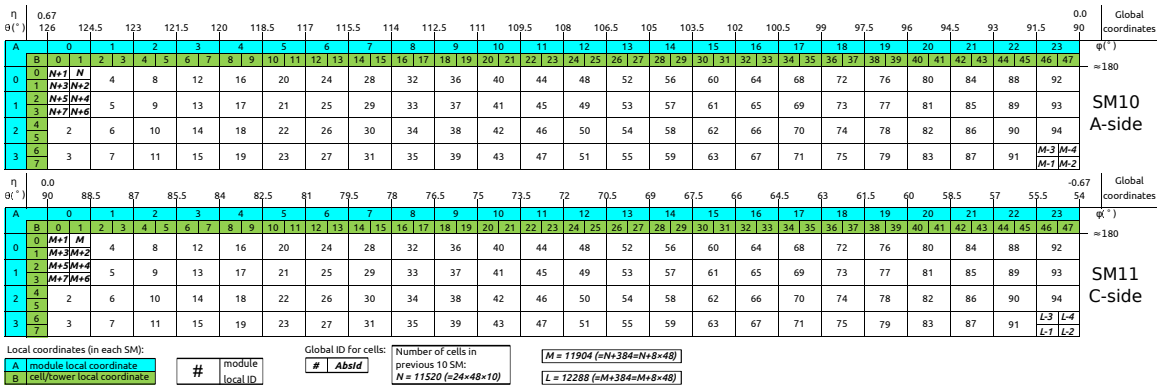

Figure 4.20: Local and global coordinates of the 2 super module extensions of EMCal (SM10 in A side and SM11 in C side). Same comments as in Fig.4.18

TRU mapping but this goes beyond the scope of our work.

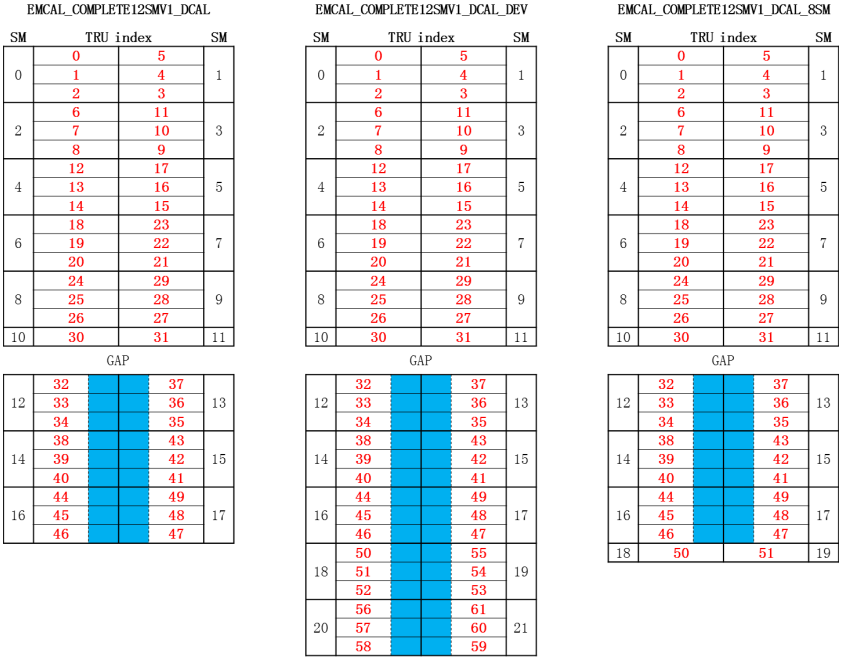

Figure 4.21: EMCal and DCal TRU mapping for different versions of geometry, the channels in blue region will not be used.

4.6 Validation tests of the DCal geometry

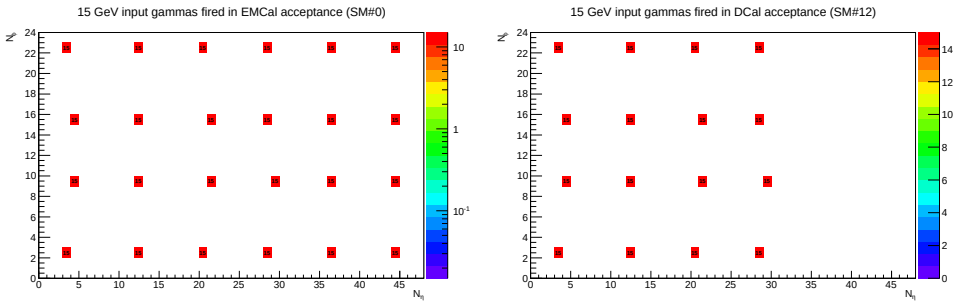

Figure 4.22: 15 GeV photons regularly simulated in SM#0 of EMCal (left) and SM#12 of DCal (right). The output of the generation process ("TParticle" or "kinematics" level) is shown before propagation in the detector. The unit of the 2 axes is the cell index in the SM.

Once the DCal geometry has been implemented in AliRoot, it has been necessary to perform a certain number of tests in order both to validate the modification added to the global EMCal software and to make sure that no bugs have been introduced in the previously programmed geometry of EMCal. Appart from checking the indexes presented in the previous section as well as the transformations via 3 dimension representations as previously shown, we have tested the different simulation/reconstruction levels of physics responses available in ALICE and this is presented in section 4.6.1. Part of the detector response concerns the most "physical" object that can be reconstructed in EMCal called a cluster. A given reconstructed cluster can be affected by the treatment of its consituting cells at the edge of a given detector. The addition of DCal in the EMCal geometry software introduced new edges which had to be taken care of in the clusterization process. In section 4.6.2, we have studied that our work did not impact the global clusterization process. In order to make sure that the physics was not affected as well by our modifications, we have studied the energy resolution of DCal and compared it to the EMCal one in section 4.6.3. Finally, a certain number of previously reconstructed runs have been reprocessed with the new EMCal geometry in order to compare them and to make sure that no specific bugs have been introduced in the EMCal geometry following our cumbersome modifications of the code (see section 4.6.4).

4.6.1 Simulation and reconstruction tests

The data processing in AliRoot generates several levels of physics responses both in the simulation and in the real data chains. As no real data were available during our PhD work as the detector was under construction and thus was not installed in ALICE, we performed some validation tests of our work based only on MC data. In the simulation chain, the AliRoot framework generates several types of files containing a physics response at different level of generation or reconstruction. The primary interactions are first simulated via generators before to be used in the transport package. The event generator produces set of "particles" (TParticle) with their momenta and their full production history. Then the transport package (GEANT3, GEANT4 or FLUKA) transports the particles through the detectors and produces hits defined as an energy deposition at a given point in the sensitive material. Each hit contains the label of the particle ("track label") that has generated it as well. Then, the digits are generated in which the detector response is taken into account. It corresponds to a "disintegrated response" of a given physics object in a detector. Two types of digits exist in ALICE: the "summable digit" and the "digits". The former uses low threshold while the latter real threshold to produce the detector response so that the result is more similar to what one would get in real data in the digits. In a digit, objects are created like in a sdigit but the energy in the cell is transformed into the ADC amplitude units and the energy threshold is of 3 ADC counts. The digits also contain the simulation of the noise.

While done with the simulation, the reconstruction can then be required to produce the "physics" objects corresponding to the detector response in terms of energy and not anymore in terms of electronic response. In case of EMCal, two types of "physics" objects can be studied: the "cells" and the "clusters". Cells and clusters are the basic information needed to perform an analysis. A cell (CaloCell) is the equivalent of a Digit but with and energy converted in eV. A cluster (CaloCluster) is a reconstructed physics object which can contains several cells and corresponds to the real physics object, in our case a reconstructed photon or a reconstructed electron which has hit the detector in several cells. These objects are reconstructed via the class AliEMCalClusterizer.

As previously written, the work performed in this PhD has affected not only the EMCal geometry classes but also all the tools available in the EMCAL package to produce an exploitable response from a simulation to a physics analysis. The

diagram presented in Fig. 4.11 already illustrated the whole classes which were impacted by our modifications. It has thus been necessary to validate them checking all the levels of simulation and reconstruction introduced above. For this purpose, we fired 15 GeV photons regularly at different (η,ϕ) positions in the SMs of DCal and EMCal. In both cases, the input γs have been generated in the full EMCal acceptance. Figure 4.22 illustrates the positions that have been fired in SM#0 of EMCal (left) and in SM#12 of DCal (right) in local coordinates. The units used in the x and y axes are the cell indexes in η and ϕ respectively. It is important to specify that the code used to simulate/reconstruct the objects in EMCal corresponds to the old one (before our modifications) in order to get a baseline previously validated by the collaboration.

One can first note that the photons simulated in DCal in the η region of EMCal where DCal does not contain modules (the DCal SMs being shorter in pseudo-rapidity) are not visible on the figure as expected. In fact, a (η,ϕ) position of simulation, corresponds to a given AbsId. In case of DCal, if this position is located outside the acceptance of the detector, the AbsId returns a -1 value which does not correspond to any local position in a given SM. It explains the absence of red squares above $N_\eta = 32$ as DCal does not have any stripmodules in this η region.

Starting from these input gammas, we then tested and validated (from the top to the bottom in Fig. 4.23): the hit generation, the sdigit production, the digit production in DCal compared to EMCal in the simulation process. We can see that all these objects are properly produced in DCal as well. The reconstruction of the cells and clusters has been tested and validated as well in the same way as illustrated in the lowest panels of Fig. 4.23.

The two lowest panels of the figure illustrates how the energy distributes in terms of cells in a given cluster. The axes are defined as $N_{\Delta\eta} = index_{cell,\eta} - index_{cluster,\eta}$ and the same in ϕ for $N_{\Delta\phi}$. The energy distribution in terms of cells in a given cluster shows nice concentration around the most energetic cell in both EMCal and DCal (note the log scale in z-axis).

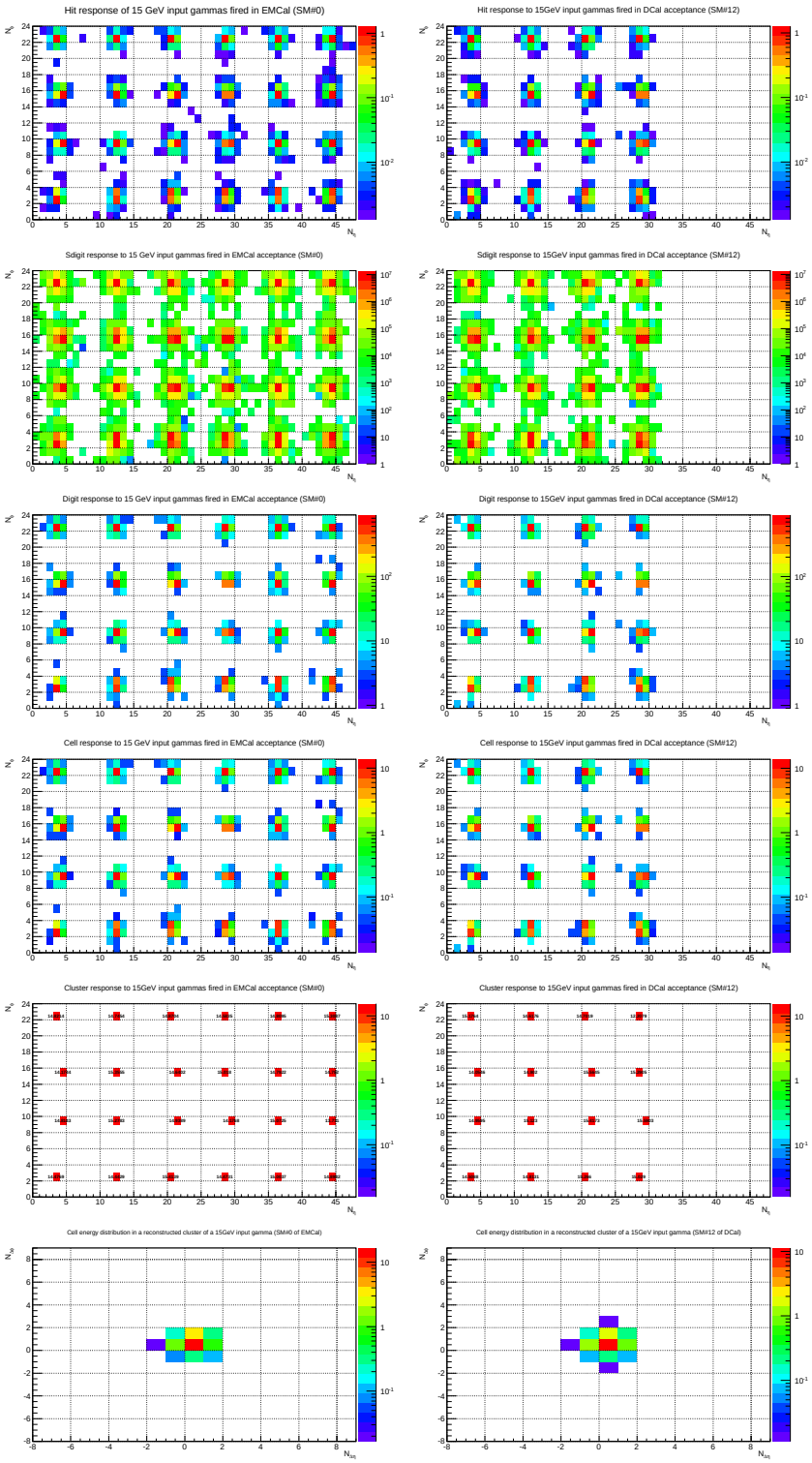

Figure 4.23: Responses of EMCal (left column) and DCal (right column) to 15 GeV photons fired in SM#0 and SM#12 respectively. The simulation and reconstruction chains have been tested at 5 levels from top to bottom: hits, sdigits, digits, cells, and clusters. The unit of the 2 axes is the cell index in the SM. The lowest panels show how the energy is distributed per cell in a given cluster.

4.6.2 Test of the inner edge effect on the clusterization

In order to properly extend the operation of the EMCal clusterizer to DCal, it has been necessary first to understand its working principle (for more details on this aspect see [96]) and then to test and modify it (if necessary) to take into account the gap in the central η region existing between the two SMs of DCal in the η^+ and η^- regions (gap which includes PHOS), gap not present in the EMCal geometry.

In order to test the clusterizer (AliEMCALClusterizerv1) which works with local coordinates, we have simulated 15 GeV photons firing EMCal in the $\eta = 0$ position and DCal at its inner edge (on the gap side, $\eta = 0.22$) in the region η positive. Our aim was to check if, in case of DCal, the corresponding reconstructed cluster will or will not propagated and thus reconstructed as well in DCal at the same ϕ position but in the region η negative (on the other side of PHOS) as the AbsId are continuous over the full DCal.

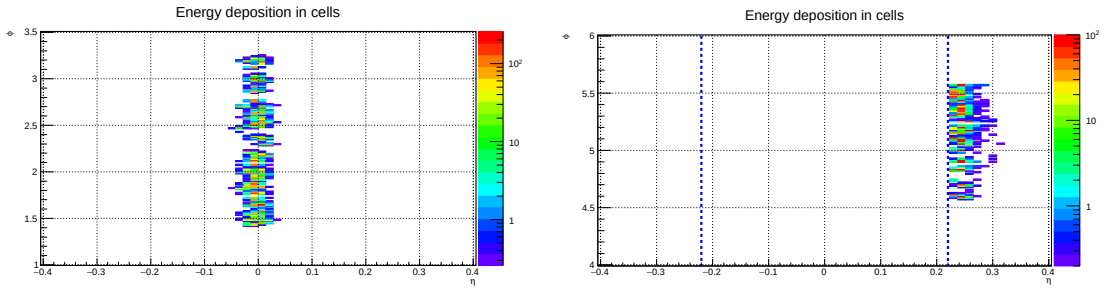

Figure 4.24: Energy deposition of the cells of the reconstructed clusters of 15 GeV γs shot in EMCal (left) and in DCal (right) acceptances. The blue dashed lines delineate the inner edges of DCal.

We have first checked how the energy of the cells in the reconstructed clusters was distributed in both cases. The result of this test is illustrated in Fig. 4.24, left panel for EMCal and right panel for DCal. We have chosen to show the results in global coordinates as it gives a direct representation of the detectors and of their physics responses. In the figure, the blue dashed line illustrate in inner edges of DCal (the gap is in between). One can clearly see that in case of EMCal, the energy is distributed around $\eta = 0$ in both the negative and positive regions. In case of DCal, the energy response of the cells in the reconstructed clusters spread in the positive η region above 0.22. Of course, no energy is measured in the gap. Moreover, no energy is visible in the negative region above -0.22 as expected for a clusterizer working properly with gaps.

We also performed a second test to check if the clusterizer would merge the

energy of photons measured on both sides of the inner edges of DCal. For that purpose, a pair of photons have been shot at a symmetric position on both sides and close to $\eta = 0$ in EMCal and near the inner edges (η positive and negative) of 2 SM at the same ϕ positions in DCal.

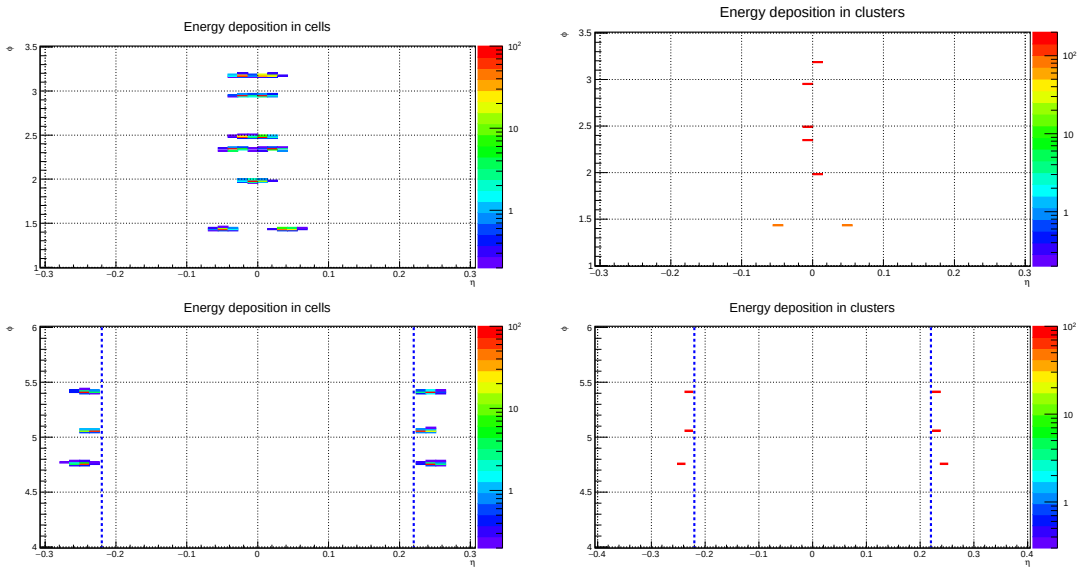

Figure 4.25: Test of the reconstruction of clusters around $\eta = 0$ in EMCal (upper row) and around $\eta = \pm 0.22$ in DCal (lower row), positions which correspond to the inner edges of this latter. Left panels illustrate the energy deposition in cells, right panels show the reconstructed clusters. The blue dashed lines delineate the inner edges of DCal.

The results are presented in Fig. 4.25, top panels for EMCal and bottom panels for DCal. The left panels illustrate how the cell energy distribute in detectors. The right panels show the positions and energies of the reconstructed clusters. In case of EMCal, the clusterizer reconstruct either one or two clusters (depending on the position of the simulated γs) with the energy $2\times E_\gamma$ or E_γ per cluster respectively as in some cases the cell energy distribute continously on both η^+ and η^- around $\eta = 0$. For DCal, the clusterizer systematically reconstruct clusters of energy $\sim E_\gamma$ in each SM of DCal on both sides of the gap.

These tests show evidence that the clusterizer works properly after the implementation of the DCal geometry. It has thus not been necessary to modify it on this aspect.

4.6.3 Energy resolution test

In order to make sure that our implementation of the DCal geometry did not affect the physics response of EMCal and DCal, we studied their energy resolution. To do so, we have computed the resolution defined as the relative difference between an input γ and its reconstructed cluster energy:

$$res = \frac{E_\gamma - E_{cluster}}{E_\gamma} \tag{4.7}$$

where the E_γ and $E_{cluster}$ are respectively the energy of the input γ and the one of the reconstructed level. Note that this resolution can directly be compared to equation 4.3 and to the results obtained previously by the ALICE EMCal collaboration (see section 4.2.5).

In this thesis, the simulation of 1 γ per event is used to calculate the resolution with only EMCal/DCal, other detectors like ITS and TPC are turned off. Input γs are simulated in an acceptance a bit larger than the acceptance of EMCAL and DCal, since γ near the detector can also have energy deposition at the edge of the detectors. In collision experiments, the physical energy distribution of γs is exponential which prevents to generate high energy photons with good statistics. In order not to be limited by the statistics, a flat distribution of γs versus P_T has been used in the simulation ($0.1 \lesssim p_T \lesssim 100$GeV/c). Meanwhile, the clusters near the edge of the detector (center at 1 or 2 cells from the edge) are removed to reject the γ which are partly in the detector

The simulation has been done for both ideal OCDB and real OCDB, OCDB meaning "Offline Condition Data Base", which contains useful information anchored to a given run. A run corresponds to a whole period of data taking after one beam injection at LHC, thus the information stored is supposed to be stable in the run. This OCDB includes general information about a run and about the detectors used during the data taking. For EMCal/DCal, it contains alignment for each SM, details about the calibration (parameters for (Summable) Digitizer in simulation/reconstruction, initial gain factors and pedestals), time information for cells and bad channels. The ideal OCDB contains the designed detector parameters while the real OCDB is obtained from real data with the run number 235840 (13 TeV *pp* collisions 2015).

The results of the resolution from the simulation for the ideal (circle) and real (triangle) OCDB cases are shown in Fig. 4.26 for EMCal and in Fig. 4.27 for DCal. The upper figures show the mean value (in percent) of the resolution distribution as

a function of the energy of the input γ while the lower figures show the corresponding RMS versus E_γ. To make the results more comparable with [94], the photons which create only 1 cluster are selected (closer to the electron case) in the simulation. But as the experiment is not done in the same condition (the results we obtain is after installtion in ALICE, while the results from [94] is tested in modules in invsetigation), the directly comparison is still not valiable.

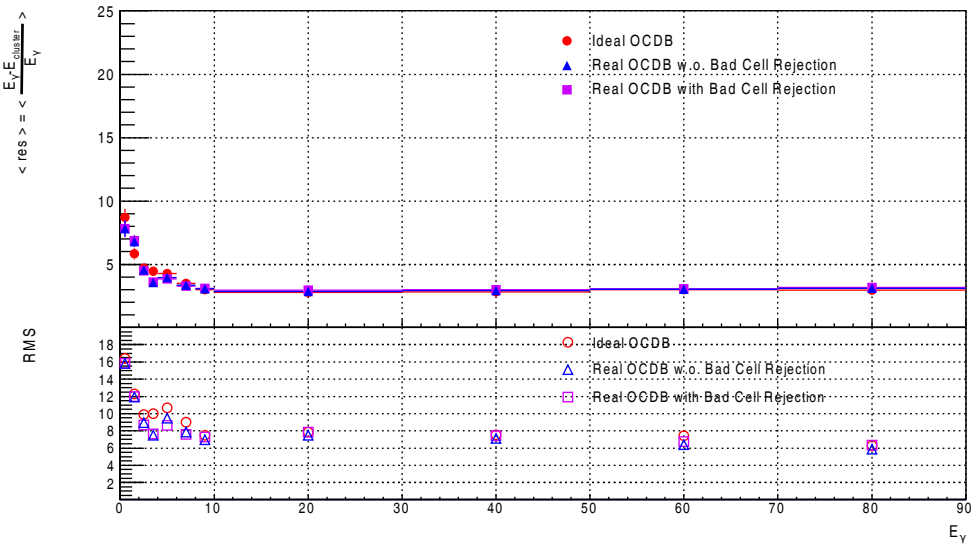

Figure 4.26: Energy resolution of EMCal defined by equation 4.7 ; mean value (upper panel) and standard deviation (lower panel) of the resolution as a function of the energy of the input γ. Three cases are compared: ideal OCDB (red circles), real OCDB without (blue triangles) or with (purple squares) bad cell rejection.

To exclude bad cell effects in the real OCDB case (red squares in Fig. 4.26 and 4.27), an event has been rejected if the γ has its energy partly deposited in the bad cell list. The results show that the performance of the EMCal is stable, and in good agreement with the ideal case as expected. The resolution of DCal in ideal OCDB is slightly worse than the EMCal. For the real OCDB, the DCal resolution is worse (higher), no matter whether the bad cells are rejected or not.

Several properties of clusters have been studied in order to find the reason. As too many figures have been produced, they will not be shown in this thesis. We only summarize the conclusions:

- We studied the potential correlation with the number of clusters created by one γ, $N_{cluster}$. This property increases with the energy of the γ, but the slope from real OCDB ($\sim$ 0.4% GeV^{-1}) is twice high as that of the ideal OCDB

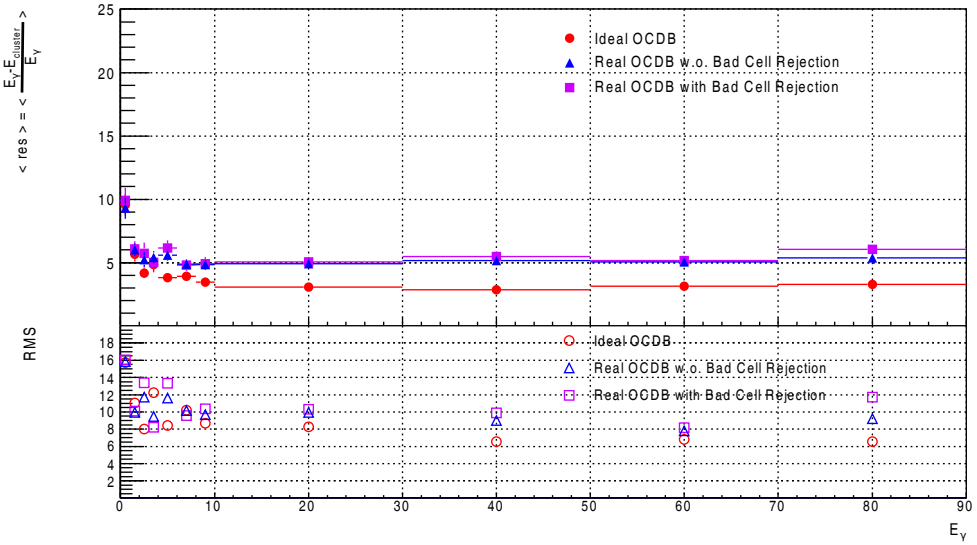

Figure 4.27: Energy resolution of DCal defined by equation 4.7 ; mean value (upper panel) and standard deviation (lower panel) of the resolution as a function of the energy of the input γ. Three cases are compared: ideal OCDB (red circles), real OCDB without (blue triangles) or with (purple squares) bad cell rejection.

($\sim 0.2\%$ GeV^{-1}). It turns back to normal if the bad cell rejection is applied. Thus this can not be the main reason of the bad resolution.

- The position resolution defined as the distance between the cluster and the input γ as been studied. The DCal in real OCDB showed a worse result ($\sim 25\%$) with/with out bad cell rejection, which coincide with the energy resolution.

- We also studied the energy distribution, defined as the weighted distance from a cell to the cluster it belongs too:

$$|\Delta\eta| = \sum \epsilon_i \cdot |\eta_i - \eta_{cluster}||\Delta\phi| = \sum \epsilon_i \cdot |\phi_i - \phi_{cluster}| \tag{4.8}$$

where i is the cell in the cluster, ϵ_i is the fraction of energy deposited by a cell in the cluster it belongs too. The results showed nice concentration and coincidence for EMCal and DCal in ideal OCDB ; while in the real OCDB, the cluster shape trend to be more elliptical for DCal ($|\Delta\eta|/|\Delta\phi| \sim 3$). These properties of clusters in DCal have also been observed in the real data.

Some issues related to the trigger in run 235840 (which is one of the first run even taken with DCAL) are likely to be responsible to the perfemences that we obtained

for the DCAL energy resolution. This test will have to be repeated with a newer run. The expected behaviour is to obtain a resolution very close to that of EMCAL.

4.6.4 EMCal reconstruction test

In order to make a complete check of the modifications introduced in the EMCal geometry code for DCal, a final sanity check has been performed on the EMCal response to make sure that the new code was fully coherent with the results of the old one concerning EMCal. For both simulated and real data, the official quality assurance plots of ALICE have been produced with the old and new EMCal codes and compared step by step.

In order to make sure that the obtained results were not impacted by the different OCDB versions used for the different produced data, several periods of production have been tested between 2010 and 2013. The simulations which have been checked on a run include LHC10d4, LHC12f2a and LHC13b2_efix without and with DCal modifications respectively which correspond to the periods 2010, 2012 and 2013. The real data tested on a run are: LHC10c, LHC11d, LHC13d and LHC13g corresponding to the periods 2010, 2011 and 2013.

Amoung the different plots compared (cell and cluster occupancies in (η,ϕ), EMCal time of flight vs energy, cell Abs Id vs the time of a cell or vs the cell energy, the number of clusters vs the number of global tracks, the sum of the cluster energies vs V0 signal (amplitude), the sum of the cell energies vs the SM number, the number of cells per cluster as a function of the energy in each SM, the π^0 mass and the π^0 mass in each SM) for both MB and EMC triggers, we have decided to show the results of the trending plots (mean and RMS) of the number of clusters per event ($N_{clusters}$/event), the average cluster energy ($<E_{cluster}>$) and the average number of cells per cluster ($<N_{cellspercluster}>$) as a function of the SM numbers for the MB and the EMC triggers obtained with the old and the new EMCal geometry code.

This is illustrated in Fig. 4.28 for the run number 1595820. In the first bin of the figure, the results obtained with the old EMCal geometry code for the different SM of EMCal as well as the average value are given. They are compared with the results obtained for exactly the same quantities and the same SM but with our new geometry code in the second bin of the figure. As can be observed, we obtained exactly the same results for EMCal before and after modifications of the code.

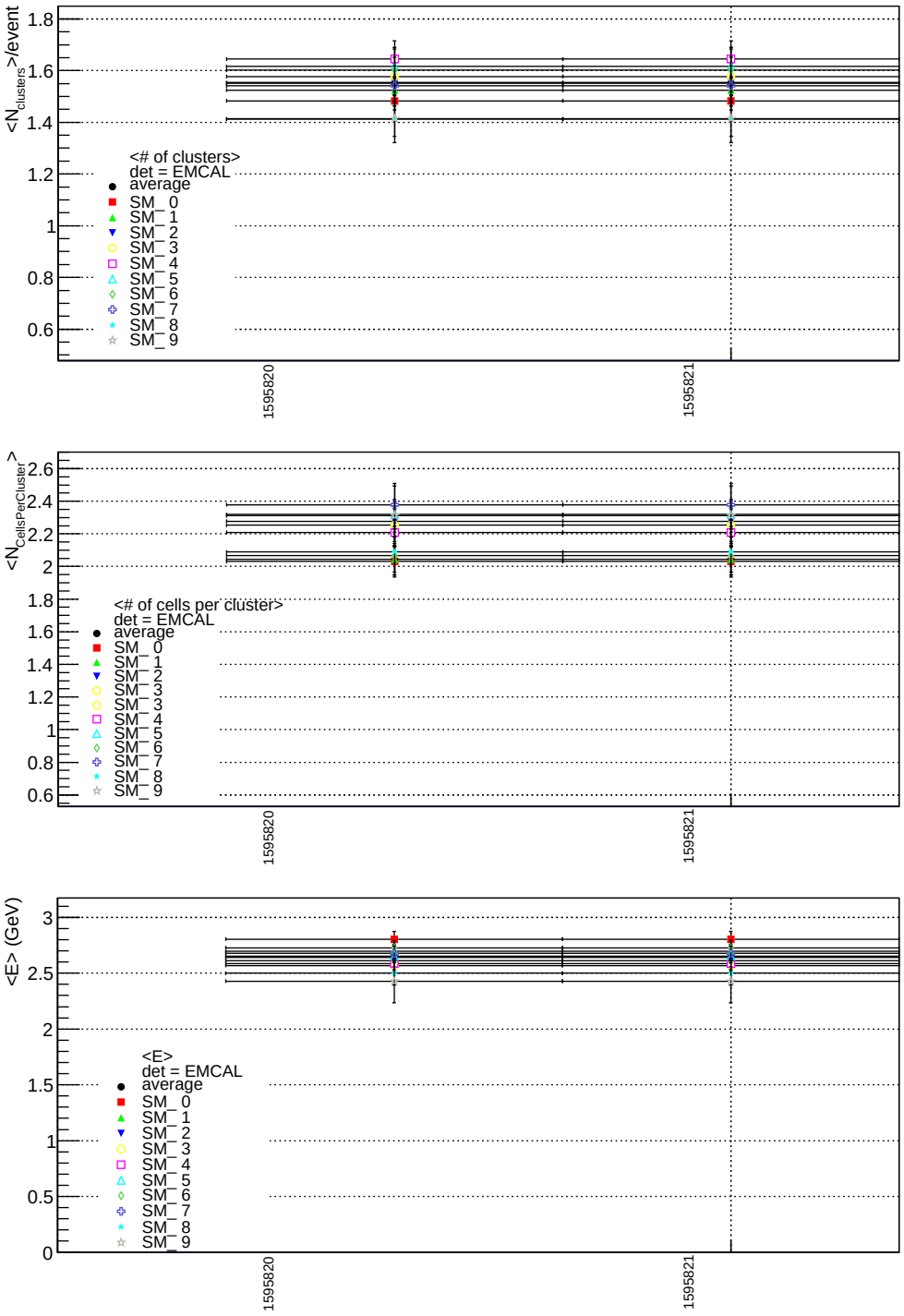

Figure 4.28: Run 1595820: Trending plots (mean and RMS) of the number of clusters per event ($N_{clusters}$/event), the average cluster energy ($<E_{cluster}>$) and the average number of cells per cluster ($<N_{cellspercluster}>$) as a function of the SM numbers for the MB and the EMC triggers obtained with the old and the new EMCal geometry code.

The trending plots which concern the π^0 QA distributions have been also com-

pared. The average π^0 mass, the sigma of the mass distribution as well as the average number of π^0 per event are represented in the different SM for the MB and EMC triggers. This is shown in Fig. 4.23 in the left column with the old EMCal code and in the right column with the new one.

As can be seen in these different figures, the distributions before and after the code modifications are fully coherent and this validates once more our work.

We would like to finish our chapter by showing performance plots produced by the collaboration [97] in order to illustrate the success of the DCal project including the work that we developed about its geometry implementation in AliRoot.

First of all, Fig. 4.29 illustrates an event display of a $Pb-Pb$ collision at $\sqrt{s_{NN}} =$ 5.5 TeV of the new data taking period which followed the LHC first long shut down after Run I. For this Run II, the DCal calorimeter which installation was fully completed in November 2014 is included in the run and works properly as can be seen in the figure. It presents a di-jet back-to-back event measured in both ALICE calorimeters. This event display uses the geometry package of AliRoot. It is one concrete direct application of the code that we have developed and presented in this PhD chapter.

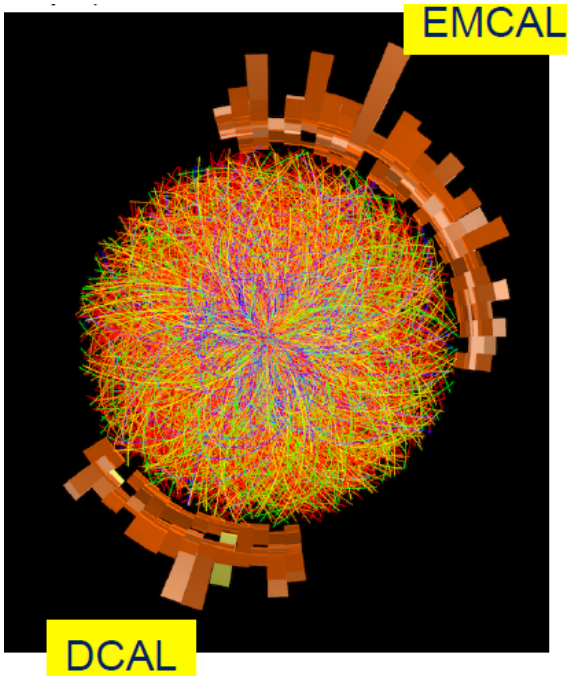

Figure 4.29: A di-jet back-to-back event display, the two jets being measured in EMCal and DCal respectively in a $Pb-Pb$ collision at $\sqrt{s_{NN}} = 5.5$ TeV.

An other measurement which has become accessible thanks to our code development is a direct measurement of the π^0 meson invariant mass not only in EMCal anymore but in DCal as well [97]. One can see the first performance result of the π^0 invariant mass reconstruction in pp collisions at $\sqrt{s} = 13$ TeV obtained using DCal (compared to EMCAL). After a fit of these distribution around the peaks with a gaussian plus a cristal ball [98], the collaboration obtained comparable mass (135-136 MeV) and resolution (10-11 MeV) with the two calorimeters after calibration as expected as they share the same technology. This measurement being the baseline of any calorimeter physics measurement, it is really promizing for the future.

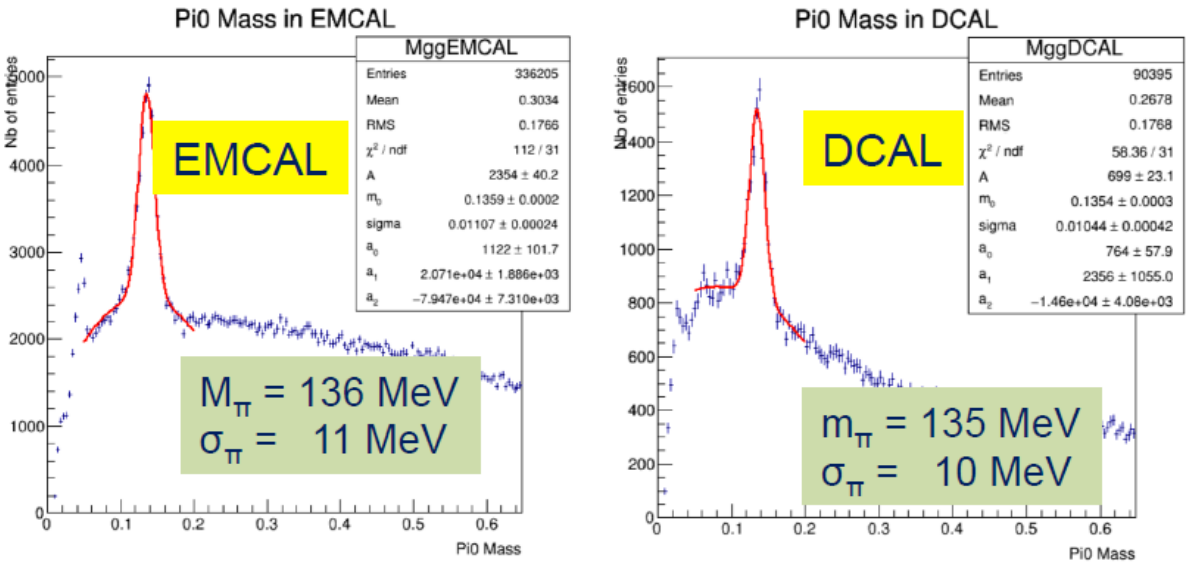

Figure 4.30: π^0 invariant mass reconstruction in pp collisions at $\sqrt{s} = 13$ TeV obtained using DCal (compared to EMCAL).

Chapter 5

Running conditions and quality check of the data

The first step to any physics analysis and in our particular case, to the extraction of the fragmentation function moments of jet is to make sure to have a good working knowledge of the running conditions (type of event selected, analysis cuts, etc.) and a good control on the quality of the data analyzed. This chapter is dedicated to the introduction of the running conditions (section 5.2) of the data which have been analyzed in this work as well as to a presentation of their quality (sections 5.3 and 5.4 for the real data and the MC respectively). But we first start by introducing the different software tools which have been used to perform our analysis in section 5.1.

5.1 Software packages and tools for analysis

5.1.1 Software packages and firmwares used for this thesis

In this section, we give a brief description of the different softwares used to compute our analysis. The main software of the ALICE collaboration is the ALICE Offline framework (ALIROOT) written in C++ which provides a set of tools that enables data processing. ALIROOT uses the ROOT system as a foundation on which the framework for simulation, reconstruction and analysis is built. In order to be able to study the response of the detectors, we used GEANT3 to perform the transport of particles through the detector and to simulate their energy deposition. The PYTHIA 6.214 event generator has been used to perform the simulation of *pp* collisions. Finally, it has been possible to process and analyze a huge amount of data thanks to the use of the Worldwide LHC Computing Grid (WLCG). In ALICE,

AliEn, a lightweight Open Source Grid Framework, is used as an interface to send data requests on the grid.

ROOT

ROOT is an Object Oriented framework written in C++ offering a large panel of tools for data analysis [95]. It is an open source project coordinated by the European Organisation for Nuclear Research, CERN in Geneva. Among other things, it provides a calculator to the user, advanced fitting options, leading-edge statistical tools as well as capabilities to plot functions, to draw histograms or graphs related to a measurement. ROOT also furnishes a programming interface to the user for any application developments (both at the interpretation and at the compilation levels) as well as a graphical user interface for interactive data analysis. In summary, ROOT is an efficient tool for heavy ion physics analyses.

GEANT3

In order to complete a complex simulation as realistic as possible in our field, it is essential first to be able to design and optimize the detector definition in the simulation and then to simulate the physics processes which take place as the particles propagate through the detector and interact with the operating materials. This is taken over thanks to the GEANT3 simulation software, acronym of "GEometry ANd Tracking". Originally developed at CERN for high energy physics experiments, it is written in FORTRAN and maintained as part of the CERNLIB. It is an open source code quite stable since 2000.

PYTHIA

The study of the feasibility of a measurement, of the performances of a detector or the correction of the data require the necessity to model or generate a physics process as close as possible to the reality. This task is carried out by event generators, family to which PYTHIA belongs. The PYTHIA program is frequently used for event generation in high-energy physics. The emphasis is put on multi-particle production in collisions between elementary particles in particular in hard interactions in e^+e^-, *pp* and *ep* colliders. The program aims at generating complete events, in as much details as possible and the closest as possible to the experiment observations, within the bounds of the current understanding of the underlying physics. For this thesis, PYTHIA 6.2 written in FORTRAN has been used for the simulation.

AliRoot

As briefly introduced above, the software environment AliRoot [99] is a complete experimental offline framework developed by the members of the ALICE collaboration. Based on ROOT and interfaced with PYTHIA and GEANT, it provides to the user all the functionalities to perform a simulation, to reconstruct MC or real data and to analyze their outputs. Written in C++, it consists of several modules (directories packaging tens of classes) dedicated to the steering of the global software, to the definition of each sub-systems of ALICE, to the simulation/reconstruction process, to data analysis, etc. We have previously described the different levels of simulation and reconstruction that can be generated with AliRoot. The main output of the global reconstruction of simulated or real data is stored in the Event Summary Data (ESD) in an output file currently named "AliESDs.root". An ESD contains all the information useful for any data analysis. The Analysis Object Data (AOD) can also be stored in ALICE in the form of an output file named "AliAOD.root". AODs contain a compact event information which derives from ESDs, usually dedicated to a specific physics analysis. These smaller size objects thus allow to increase the speed of the analysis. Today, official physics analyses in ALICE are essentially based on AODs, in which non-physical or non-useful information are rejected.

The framework is such that the same code can be run on a local workstation, or on a parallel system enabled by the "ROOT Proof" system, where different events are dispatched to different cores, or on the Grid.

Grid and AliEn

The Large Hadron Collider produces several Petabytes (PB, 10^{15} bytes) of data on annual basis. This large-scale data processing needs a cooperation across many different institutes and countries. The Grid is a parallel implementation of a computing infrastructure which makes the analysis of these data possible. A tool named AliEn (ALICE Environment) is developed by the ALICE offline collaboration to access the Grid. It provides interface including virtual file catalog and also the job management, which makes all the clusters (computing centers) on the grid connected. The data accessing, storage, processing (simulation, reconstruction and analysis) are also available for all collaborators all around the world. The jobs of processing is submitted to a central queue. The status of the connected computing centers and submitted jobs are monitored and visualized to all users through MonaLisa (MONitoring Agents using a Large Integrated Services Architecture) which is

accessible through a simple web interface [1].

5.1.2 The ALICE Analysis framework

In AliRoot, several modules have been specifically developed and written for the analysis. The way an analysis is computed in ALICE follows a well defined computing structure which allows the collaboration to run the different user's analyses at the same time in what is currently called a Lego train [100]. The ALICE analysis framework offers such functionalities providing common tools for processing data in an efficient way. The framework was designed to take advantage of the existing technologies for parallel computing and provide access to CPU and data to several concurrent analysis modules in the same time (same process).

The framework overall philosophy can be summarized the following way. Each analysis processed in a given train is independent. However, it can communicate with an other analysis by exchanging processed data via container objects, making the model data oriented. A manager class containing a list of client modules (tasks) coordinates an analysis session. All tasks in the same session share the same event loop (functionality provided by TSelector) and derive from the same base class. Tasks need to implement a set of virtual methods that are called in different stages of processing. The access to any specific simulation/reconstruction or analysis data is provided via ESD, AOD and MC event handlers.

5.2 Data selection and analysis cuts

Since 2009, the ALICE experiment has collected a substantial data set of *pp* collisions. The data analyzed in this thesis correspond to Min-Bias triggered *pp* collisions at 2.76 TeV taken in 2011 and 2013. The corresponding periods are LHC11a and LHC13g. The total number of MB collisions collected is about 40 million (M) good events.

Before to select them, events are reconstructed by combining information from the detectors that are participating in the run. A sketch of the event reconstruction procedure is shown figure 5.1. After clusterisation, the tracks are reconstructed as well as the event vertex.

[1] http://alimonitor.cern.ch/map.jsp

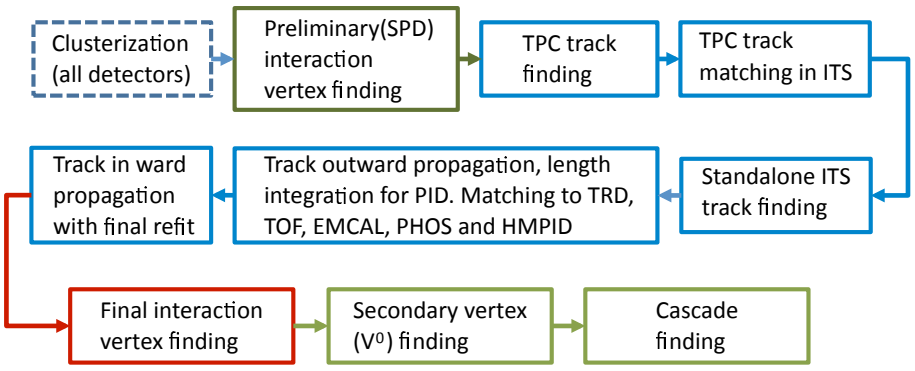

Figure 5.1: Event reconstruction flow.

The event selection criteria will be presented below, section 5.2.1.

The good run numbers of the LHC11a period are the following: 146746, 146747, 146748, 146801, 146802, 146803, 146804, 146805, 146806, 146807, 146817, 146824, 146856, 146858, 146859, 146860 For LHC13g : 197669, 197611, 197608, 197584, 197583, 197555, 197501, 197500, 197499, 197497, 197471, 197553

Min-Bias Event Trigger

Min-Bias events are selected by requiring the trigger bit AliVEvent::kMB, corresponding to an interaction trigger coded as kINT1 which requires a signal in either of V0A, V0C or SPD, in coincidence with the presence of a bunch crossing.

5.2.1 Selection criteria of the good events

Several criteria are applied to select events:

First, the hardware trigger decides if a an event is recorded or not. Only events with collision vertices that fulfill certain restrictions are used:

All selected events must have a reconstructed collision vertex. The z-position along the beam axis is only allowed to be within 10 cm of the nominal interaction point. The primary vertex must be reconstructed using data from the SPD, the radial deviation of the primary vertex is within 1 cm of the nominal interaction point. These are quality cuts to ensure that a major part of the event is contained in the acceptance.

5.2.2 Selection criteria of the tracks

Tracks are the only constituents of the charged jets that we will use for our fragmentation functions studies. For this reson, good tracks are crucial to have a good control on the corresponding jet sample.

As we have seen in the previous chapters the main detectors used for charged jet studies are the ITS and the TPC. After being reconstructed by the tracking algorithm (based on a kalman fitting procedure [101–104]), the tracks need to be selected.

In the ALICE TPC, depending on the vertex position, tracks can be reconstructed for pseudo-rapidity up to $|\eta < 1.4|$. However to insure a uniform efficiency, tracks are only accepted, if they are reconstructed with $|\eta < 0.9|$. In addition, as the single track efficiency is also rapidly falling for very low track transverse momenta, the minimum track p_T used in p_T>0.150 GeV/c.

"Hybrid" tracks

In practice, the tracks quality depends on the performance of the corresponding tracking detectors.

Some inefficiencies in η or ϕ (due for instance to cooling problems in the SPD) with result in bad quality tracks. To overcome this issue the concept of "hybrid" tracks has been introduced. The idea is to use, as tracks for our jet finding, the sum of up to 3 different set of tracks in order to obtain a uniform distribution in ϕ.

If a track does not fully meet the requirements of a high-quality track (also called global track), it is accepted as a complementary track without ITS refit or hit in the SPD,

This procedure guarantees a quite uniform track distribution, see figure 5.2.

The global track themselves are selected using several cuts:

- p_{T} dependent cut on number of TPC clusters (159 in maxim) in the first iteration: if $p_{\mathrm{T}} \leqslant$ 20 GeV/c, the maxim number of TPC clusters is $N_{max} = 70 + 30/20 * p_{\mathrm{T}}$. If $p_{\mathrm{T}} >$ 20 GeV/c, the maxim number is $N_{max} = 100$
- χ^2 per TPC cluster in first iteration < 4
- No kink daughters,
- Require TPC refit

- Fraction of shared TPC clusters < 0.4
- χ^2 between TPC constrained and global < 36
- χ^2 per ITS cluster < 36
- DCA$_{xy} < 2.4$ cm, DCA_{xy} is the distance of closest approach to the vertex in transverse plane.
- DCA$_z < 3.2$ cm, DCA_{xy} is the distance of closest approach to the vertex along beam.
- Require ITS refit
- At least one hit on SPD

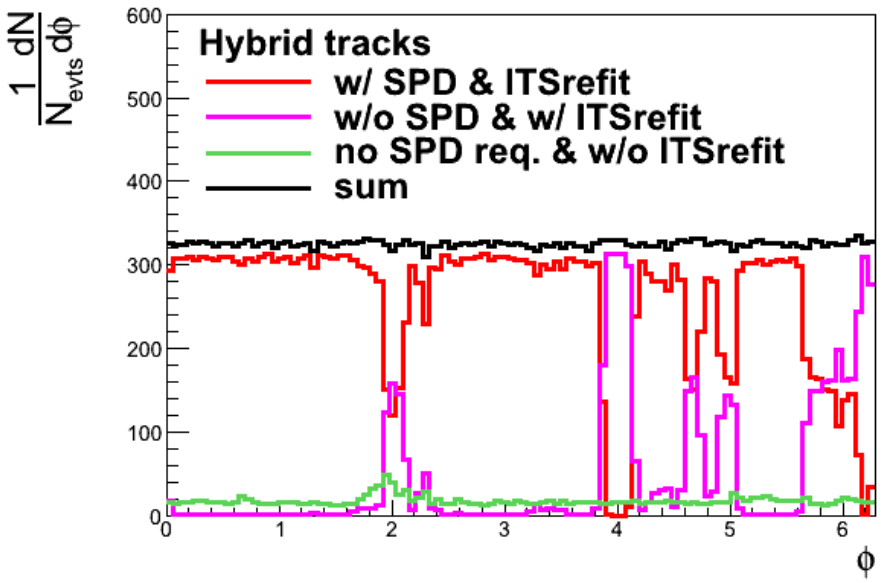

Figure 5.2: The figure shows the composition of "hybrid tracks". The line in red is with SPD & ITS refit; the purple one is without SPD clusters but with ITS refit; the green one does not require SPD clusters or ITS refit. The black line is the sum of the three.

5.2.3 Jets selection

We use massless jets which are reconstructed from tracks using the anti-kT sequential recombination algorithm. In addition we require jets with a given resolution parameter R to be with $\eta_{jet} < |\eta_{tracks}| - R$

5.3 Quality Assurance (QA) for the runs

Figure 5.3 shows the vertex and η, ϕ (which are flat as expected) and p_T distributions for tracks (LHC11a). Figure 5.4 shows corresponding distribution for R=0.4 jets.

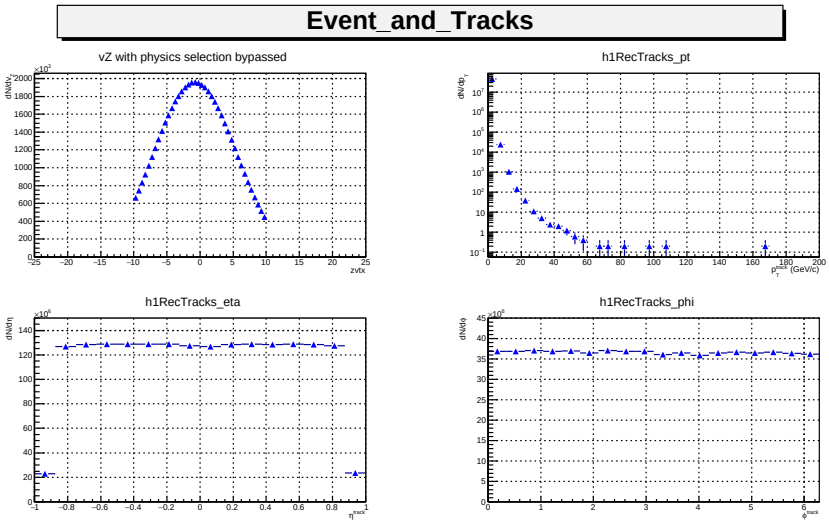

Figure 5.3: vertex and track QA distributions for LHC11a

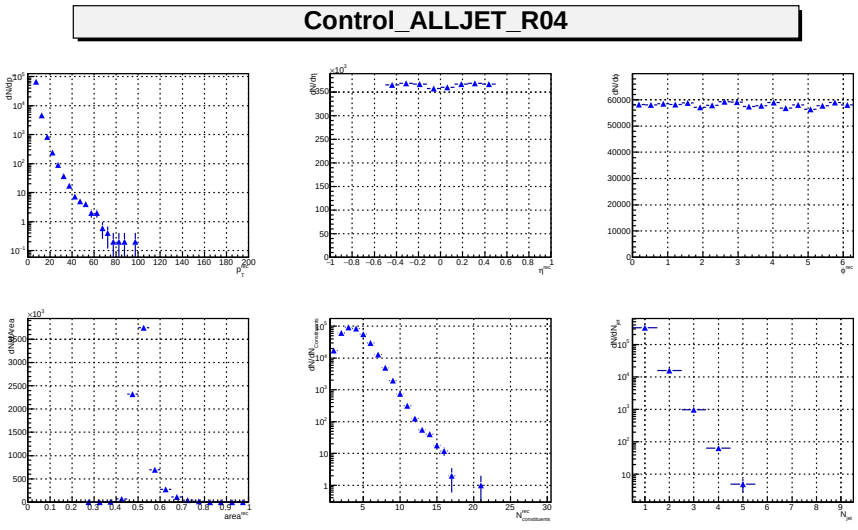

Figure 5.4: QA distributions for jets. The top row, from left to right, they are the distribution jet p_{T}, η and ϕ. The second row, from left to right, are respectively the jet area, the number of constituents in jets and the number of event with a given number of jets event.

5.4 Monte-Carlo Simulation

A full Monte-Carlo simulation is used to study the detector effect introduced by the ALICE detector. The Monte-Carlo simulation used for our analysis is named LHC12a15a, it is based ("anchored") on the real data run number 146805. The generator used in this Monte-Carlo is PYTHIA (Perugia-2011). The particle decay is also included in PYTHIA. And the transport (interaction with the detector) is made with GEANT3. The electronic response of the detectors is also simulated with AliRoot (included electronic noise,..).

This sample have been produced in 10 are different p_{T}^{hard} bins.

The scale factor used for the event weighting is:

$$w_{p_{\mathrm{T}}^{hard}} = \frac{\sigma_{p_{\mathrm{T}}^{hard}}}{N_{trials}} \tag{5.1}$$

For example, the full p_{T} spectrum can be calculated as sum of scaled p_{T} spectrum in each p_{T}^{hard} bins:

$$\frac{d\sigma}{dp_{\mathrm{T}}} = \sum_{all\ p_{\mathrm{T}}^{hard}\ bins} w_{p_{\mathrm{T}}^{hard}} \cdot \frac{dN_{p_{\mathrm{T}}^{hard}}}{dp_{\mathrm{T}}}$$

The generated p_{T}^{hard} bins are:

$$0,\ 5,\ 11,\ 21,\ 36,\ 57,\ 84,\ 117,\ 152,\ 191,\ 234,\ \infty.$$

5.4.1 Monte-Carlo QA

Similarly to real data, the MC QA distributions are used to check the quality of our simulation.

Fig 5.5 shows the track distributions and Fig 5.6 the corresponding jet distributions in MC of reconstructed level and generated level.

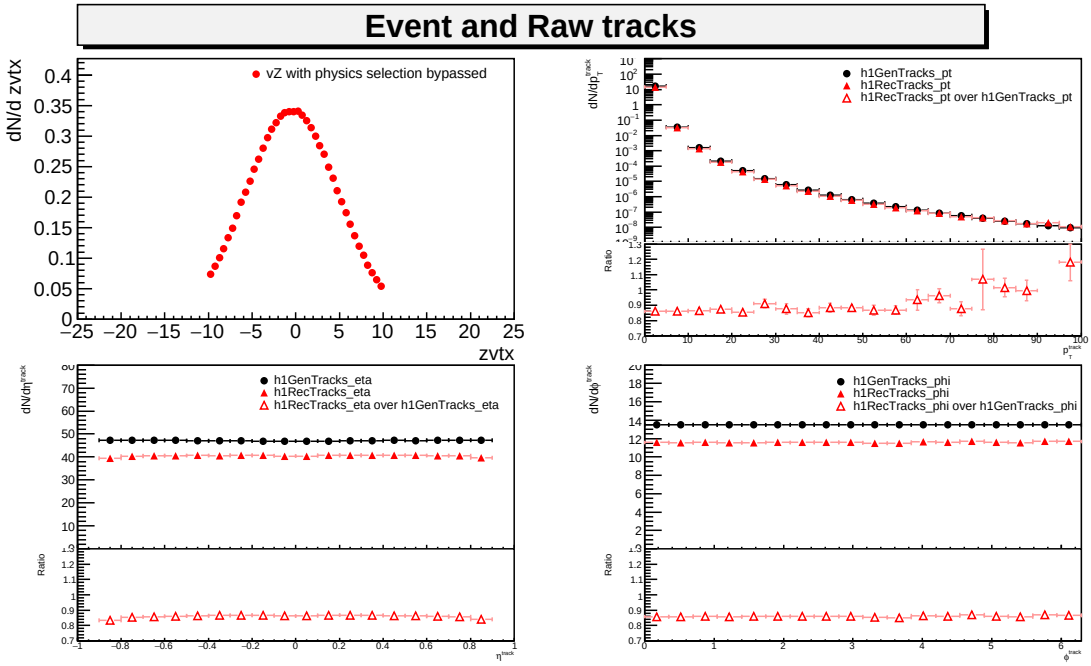

Figure 5.5: MC event and track distributions

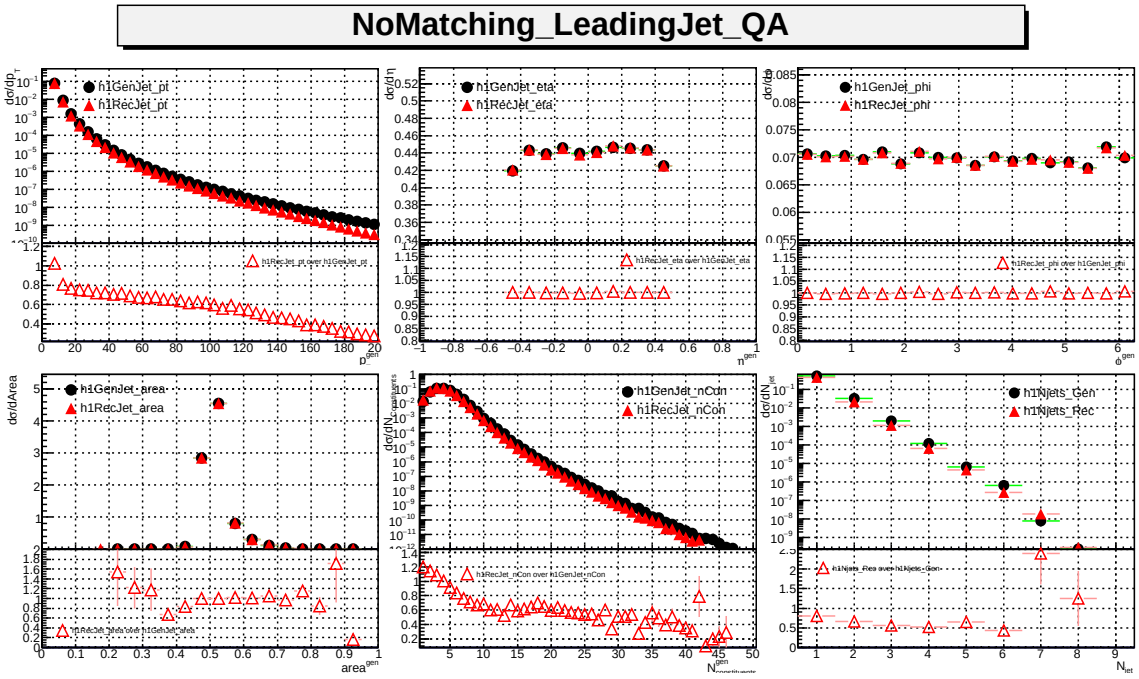

Figure 5.6: Jet QA distributions in our simulation.

Also a comparison of reconstructed distribution is done between data and MC as in Fig 5.7 shows the track distributions and Fig 5.8 the corresponding jet distributions.

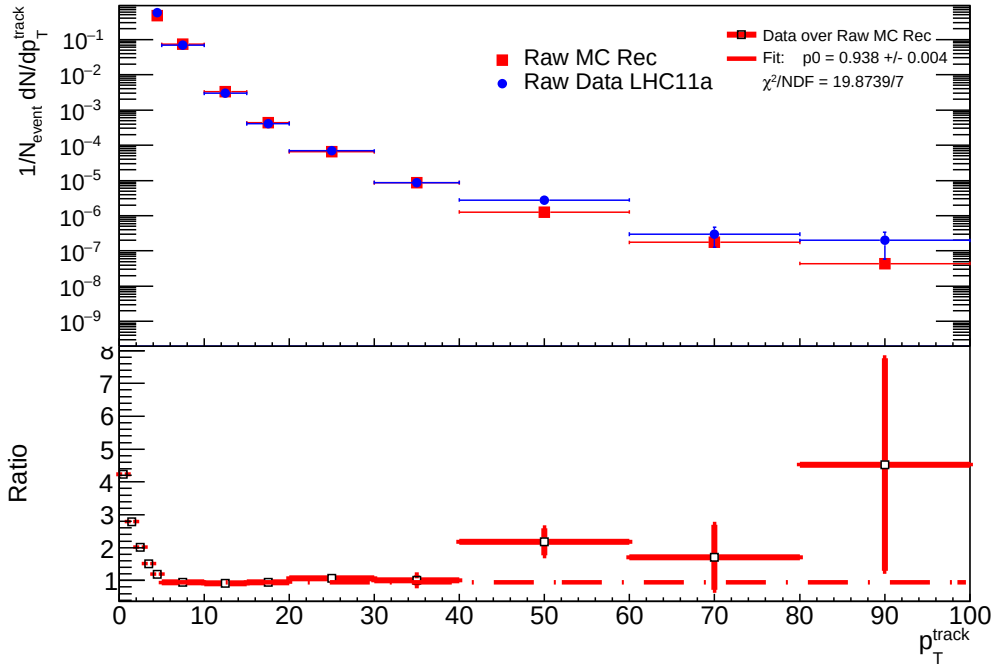

Figure 5.7: Reconstructed track p_{T} distributions from data and MC

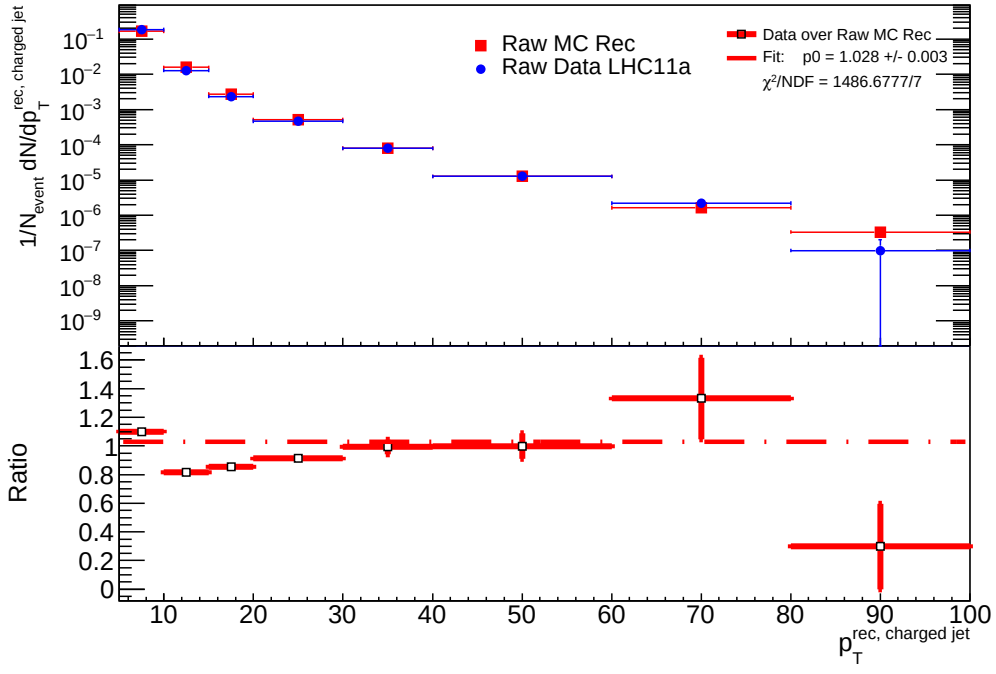

Figure 5.8: Reconstructed jet p_{T} distributions from data and MC

This MC simulation is in good agreement with 2.76 Tev *pp* data and will now be used to correct our measurement of jet fragmentation function and the one of their moments in the following two chapters.

Chapter 6

Jet fragmentation and intra-jet radiation analyses

In this chapter dedicated to the physics of jets, we concentrate on the analysis of the properties of the structure of jets, namely their fragmentation functions (FF) as well as the intra-jet radiations (IJR) (see section 2.4). Part of these observables has already been studied and published in the past for 7 TeV *pp* data (2010) by the ALICE experiment [5, 52]. In order to have a good control of the analysis we developed for the measurement of the moments of the jet fragmentation functions (FFM) (see next chapter), we measured the jet fragmentation at $\sqrt{s} = 2.76$ TeV before to move to FFM analysis. The details of the FF analysis are given in this chapter. We start by presenting the general analysis strategy followed to do the measurement in section 6.1. First raw results are shown in section 6.1.3. The MC used for the analysis and for the corrections is validated in section 6.2 before to explain the different corrections applied to our measurement in paragraph 6.3. The study of the systematic errors is developed in section 6.4. Eventually, the results are presented and discussed in the last section.

6.1 Analysis strategy

6.1.1 Generalities

The sample of *pp* collisions at $\sqrt{s} = 2.76$ TeV (LHC11a and LHC13g) analyzed has been presented in the previous chapter as well as the event selection criteria and the cuts used for the measurement at the level of tracks and jets. After physics selection and vertex cuts, we analyze 40 M good events at 2.76 TeV. In the charged

jet p_T intervals 5-10 GeV/c, 10-20 GeV/c, 20-30 GeV/c, 30-40 GeV/c, 40-60 GeV/c and 60-80 GeV/c (not used in the summary plots because of lack of statistics) are used.

Several differential observables are studied: the jet constituent transverse momentum p_T distributions, as well as the distributions of the scaled variables z = $p_T^{had}/p_T^{jet,ch}$ and $\xi = ln(1/z)$ for the leading jet in each event. These observables are associated to the jet fragmentation. We also look at how the hadrons distribute transversally in the jet and their collimation properties by looking at the density of tracks with respect to the jet axis. This can be quantified measuring their θ distribution (angle between a hadron and the jet axis) in the leading jet. The collimation can also be studied by looking at how the track p_T spread in the orthogonal plane of the jet axis. j_T is defined as $p_T^{track} \times sin(\theta) = \frac{|\vec{p^{track}} \times \vec{p^{jet}}|}{|\vec{p^{jet}}|}$. The spectra are normalized per reconstructed jet and presented in bins of jet p_T.

The software initially written for the FFM analysis, and then extended for sanity check to the FF analysis, can be found in the class called AliAnalysisTaskJetFFMoment which is stored in the directory $\$ALICE\_ROOT/PWGJE$. It is based on the ROOT and AliRoot packages introduced in section 5.1 and follows the structure imposed by the Alice analysis framework. That means that our analysis, when processed, enters the global official analysis lego train of the collaboration. It allows to run on the grid (see section 5.1) over the whole statistics available in a very short time. Our software is also based on the FASTJET package [48] not only to perform the jet reconstruction but also to compute the FFM. This point will be developed in the next chapter. We add the option to calculate the FF in the software with the aim to control the different steps we followed to compute the FFM analysis. It has thus been possible for us to control step-by-step the results obtained for the FF by comparing them with the one obtained running the AliAnalysisFragmentationFunction class, the official class for FF analysis. Validating our selection criteria and analysis cuts doing this comparison allowed to build an analysis that we could trust not only producing FF results at lower center of mass energy (2.76 TeV) but also measuring the moments of the FF (see next chapter).

6.1.2 Milestone, methods and options of the analysis

As the FF and FFM analyses require to loop several times on the list of tracks and reconstructed jets of the event, the global strategy that we followed before to start to compute anything was to fill several lists of selected tracks (either real tracks or

MC tracks) that meet definite criteria (acceptance cuts, kinetics cuts, particle type: primaries, secondaries strange or non-strange, etc.) and the same for jets. In that second case, the analysis we developed offers two options: either working with jets already reconstructed in a task upstream and stored in the working AODs, either reconstructing the jets of the event "on the fly" with the jet finders available in the FASTJET package. Two options concerning the tracks and the jets useful for the correction part of the analysis were added. In the case of tracks, we made the association (via the MC track label) of a reconstructed track to the corresponding generated tracks and we stored this information so that it could be available for the whole list of tracks in the event.

Concerning jets, we added an option which, in the same way, allows to associate a reconstructed jet to a generated one, called "jet matching" [1]. Several parameters are associated to this jet matching procedure, like the distance (in $\eta - \phi$ space) between jets on levels of generation (particle) and reconstruction (tracks), the p_{T} fraction of sum of reconstructed particles over all particles in the jet. We studied its impact on on our analysis and conclude it as negligible. This can be understood as that the jets from the level of generation and reconstruction are mostly "auto-matched", since the only leading jet is used in each level while there is limited number of jets per event in the *pp* event. See the last figure in Fig. 5.4 for data and the corresponding results in Fig 5.6 for simulation.

Having access to the lists of appropriate tracks and jets of the event, the FFs of jets can be calculated. As they correspond to the way the hadron p_T distribute in a jet one can imagine two methods to calculate them:

- With the jet constituents (the tracks which have been associated to a jet during its reconstruction). We will call them "TrackRef" as in an AliAODJet (the C++ object used in ALICE to store the properties of a reconstructed jet), the full list of the tracks belonging to a jet is not stored but a reference to those tracks.

- With the list of tracks taken in a cone of radius R centered around the jet axis. We will call them "Track Pointing".

The analysis has been performed with the two types of tracks, both at the reconstructed and the generated levels. We studied 4 different methods summarized

[1] In AliRoot, several tools have been developed for that purpose in the past. We used one of the methods available in the class AliAnalysisHelperJetTasks. Several parameters are associated to this jet matching procedure.

in table 6.1 while comparing the reconstructed and the generated data for the correction part. Moreover, we also added the possibility in the code to calculate the ξ and z variables at the function of the reconstructed p_T of the jets, or as the function of the generated jet p_T. All these cases have been compared and the associated results are shown in section 6.5.4. Note that it has been previously shown in ALICE that TrackRef and Pointing are equivalent methods with a proper treatment of the background re-scaling. For this thesis, we showed that the methods are equivalent within the error bars (see section 6.5).

Table 6.1: Methods used while comparing reconstructed (real or MC) and generated data.

	Real Data / MC rec	MC gen
Method 0	Pointing	Pointing
Method 1	TrackRef	Pointing
Method 2	TrackRef	TrackRef
Method 3	track ref	TrackRef

After having compare the different possible methods to do the analysis (details presented in section 6.5.4), Method 0 has been selected and is used to present the steps of the analysis in the following sections from the raw extraction of the FFs to their corrected values.

Note that the number of parameters of such analyses is quite large and they require a careful study. They will be commented all along the following sections as well. We have made the choice to present the results as a function of the jet resolution parameter R (R=0.2, R=0.4 and R=0.6 have been studied) and in bins of jet p_T. The jets analyzed have been reconstructed with the FASTJET anti-k_T algorithm [46] whereas the background in jets has been estimated using the k_T algorithm [47] more appropriate for a good treatment of the underlying event.

6.1.3 Raw spectra

Figure 6.1 shows the typical shapes of the raw momentum distributions of charged hadrons in jets as a function of the hadron p_T (left), ξ (middle) and z (right) variables obtained for the reconstructed jet p_T bin 20-30 GeV/c over the full real data statistics. As expected, the dN/dx (x=p_T or z) distributions are steeply falling respectively with the track p_T and z. The last p_T and z bins contain small statistics denoting a rare hard fragmentation in jets. Their values below 30 GeV/c

and 1 respectively are one indicator that our distributions are filled properly. The typical "hump-backed plateau" shape is obtained for the ξ distribution [4]. The collimated structure of jets can already be seen in the raw $\Delta\theta$ (Fig. 6.2) distribution where the density of tracks decreases going away from the jet axis.

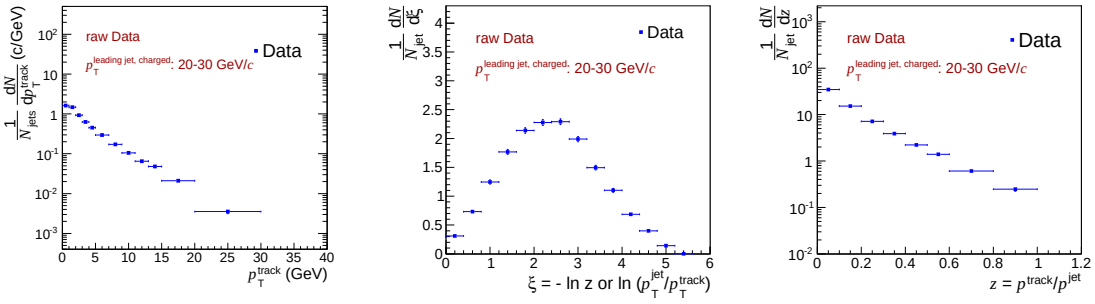

Figure 6.1: Left: p_T distribution of tracks in 20 to 30 GeV/c reconstructed jets (real data); middle: same for ξ distribution of tracks in jets; right: same for z distribution of tracks in jets.

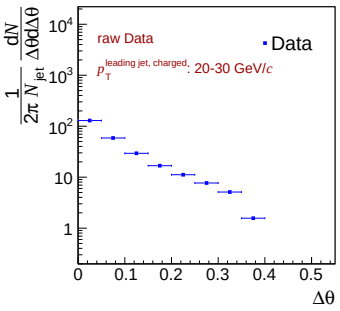

Figure 6.2: $\Delta\theta$ distribution of tracks in 20 to 30 GeV/c reconstructed jets (real data)

.

Each of these distributions have been computed as well in bins of jet p_T and with respect to R, our aim being to study (after correction) how fragmentation evolves with the energy available in the system considered and with respect to the jet axis. An example for the ξ raw spectra of real data is illustrated in Fig. 6.3 for the jet p_T dependence and for the z raw spectra in Fig. 6.4 for their variation with R. In that latter case, jets have been reconstructed in the fiducial eta regions $|\eta_{jets}| < 0.7$, $|\eta_{jets}| < 0.5$ and $|\eta_{jets}| < 0.3$ respectively for R = 0.2, 0.4 and 0.6 in order to fit the TPC acceptance. A systematic study of the fragmentation vs these physics variables has been performed and will be commented in the last section of this chapter when corrected.

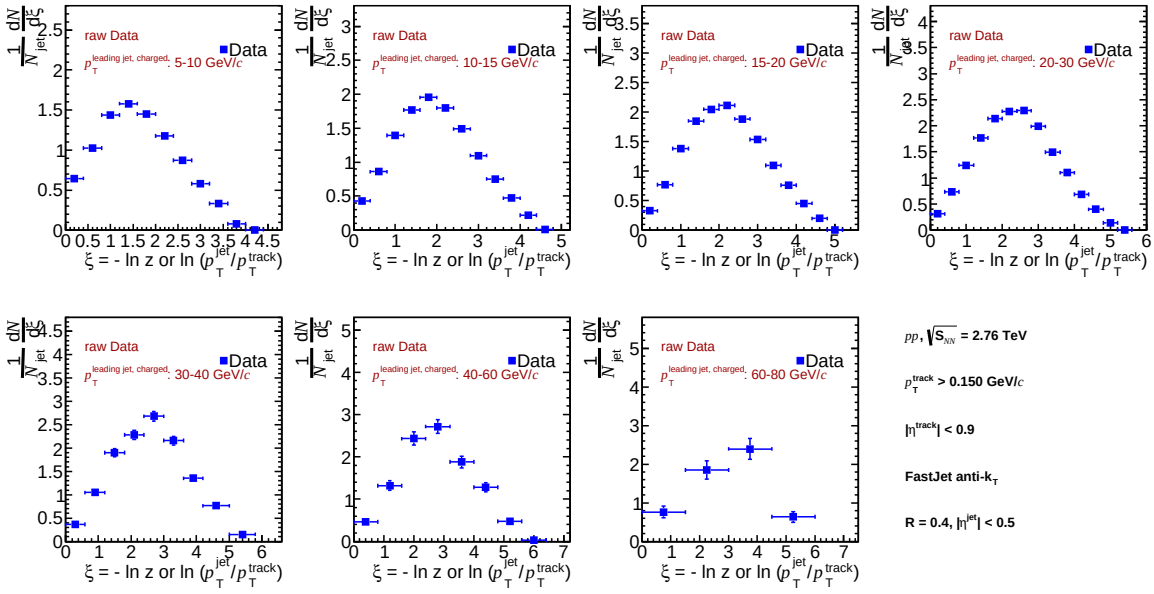

Figure 6.3: Dependence of the ξ distribution with the p_T of the reconstructed jets with R=0.4. 7 bins of jet p_T have been studied from the very low p_T 5-10 GeV/c (top left) to the 60-80 GeV/c one (bottom right).

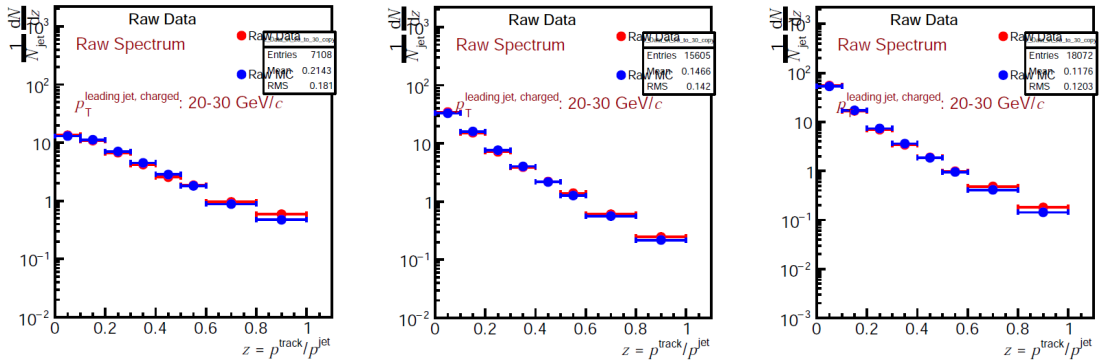

Figure 6.4: Dependence of the z distribution with the resolution parameter R. Left: R = 0.2 and $|\eta_{jets}| < 0.7$; middle: R = 0.4 and $|\eta_{jets}| < 0.5$; right: R = 0.6 and $|\eta_{jets}| < 0.3$.

6.1.4 Treatment of the background

The underlying event (UE) in single particle collisions, as already explained in section 2.3.2, can be defined as all the particles produced in a given event but the ones coming from the hard process of the event. In MC based event generators,

the UE includes initial and final[2] state radiations, multiple interactions and beam-beam remnants. The underlying event has been extensively studied in the past at lower center of mass energies [105] showing that its activity increases with $\sqrt{s}$. At LHC energies, pp collisions present a huge UE which can be identified as a strong background for the study of jets. Jet finders have to deal with its subtraction to estimate the energy of the jet produced. In the same way, studying the fragmentation inside jets, one has to subtract its contribution to the dN/dx (x=p_T^{track}, z or ξ) distributions.

One can imagine several ways to estimate the UE contribution to the FF distribution [106]. Whatever the method, the idea is to measure the particles produced in a region distinct from the reconstructed jet in the event and then to build the "background FF" or the "background transverse momentum distribution" with those particles to be re-scaled and subtracted from the measured FF. To do such measurement, we used two methods based on previous famous and extensive work on the topic [107]:

- build the background FF with the particles included in a cone of radius R perpendicular to the real jet axis keeping the same η ($\eta = \eta_{jet}$ and $\phi = \phi_{jet} + \pi/2$). Note that we ensure in this way a same dN/dη distribution of the background in the perpendicular cone and in the jet cone. This method is called bckg perp in what follows.

- build the background FF with the particles included in two cones of radius R perpendicular to the real jet axis keeping the same η ($\eta = \eta_{jet}$ and $\phi = \phi_{jet} \pm \pi/2$). This method is called bckg 2 perp below.

The background transverse momentum distribution has thus been built with the tracks reconstructed in one or two cones perpendicular to the jet axis. In the same way, the dN/dξ and dN/dz distributions have been obtained with respect to the p_T of the reconstructed reference jet. Note that the background FF should in principle be resealed as the background area of πR^2 or 2πR^2 does not exactly correspond to the jet area which is different from a circle with anti-k_T. As it has been shown that the difference is at the percent level [108], we chose not to re-scaled our background estimation.

Figure 6.5 illustrates the global shape of the background FF (blue circles) and how it contributes to the measured FF (red circles) in the transverse momentum (left

[2]For final state radiations, it can be argued as they can contribute to the fragmentation process we are interested in.

panels) and ξ (right panels) distributions. As expected, the background contribution is dominant in the low track p_T region or at high ξ. We also show how it evolves with the reconstructed jet p_T ($10 < p_T^{jet} < 15$ GeV/c (top panels) and $30 < p_T^{jet} < 40$ GeV/c (bottom panels)). As expected, the UE does not depend on the jet energy. We also observe in the dN/dp_T^{track} distributions that the background falls more rapidly at $\sqrt{s} = 2.76$ TeV compared to 7 TeV giving a different S/B ratio. Finally, the pink circles illustrate the obtained spectra after background subtraction.

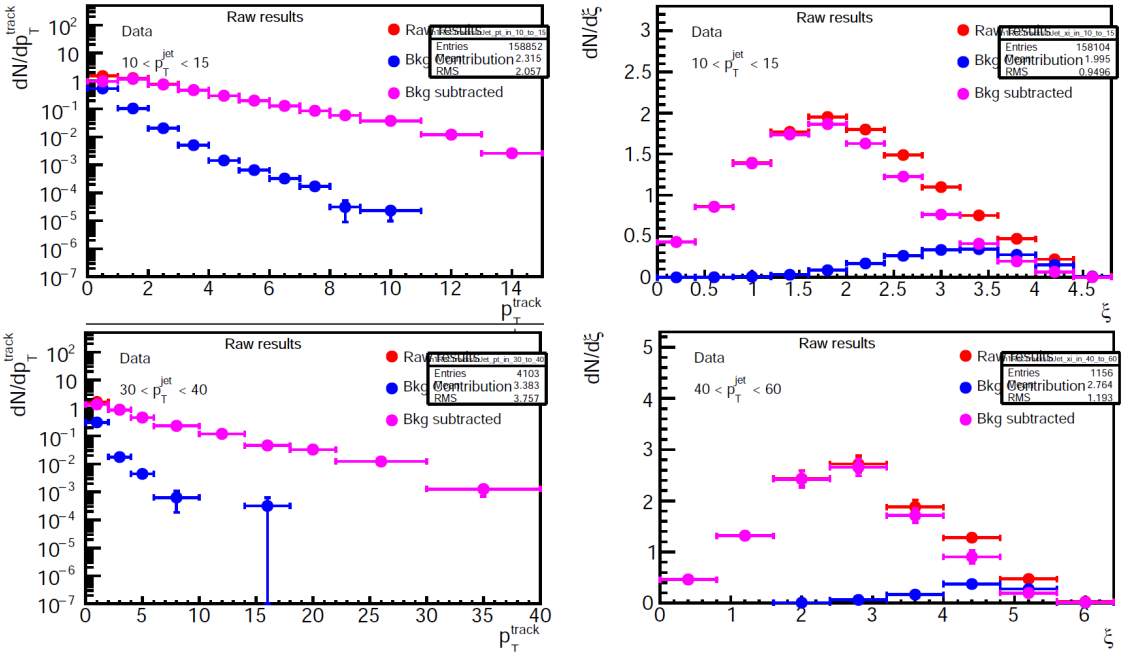

Figure 6.5: Left: dN/dp_T^{track} distributions; right: $dN/d\xi$ distributions for: top: 10 to 15 GeV/c and bottom: 20 to 30 GeV/c reconstructed jet p_T. The measured (red), background (blue) and background subtracted (pink) distributions are compared on each panel.

Within error bars, the methods are in agreement. The only difference that can be noted is in the error bars which are smaller for the 2 perp method as the probability to meet tracks in a cone perpendicular to the jet axis increases with the number of cones considered.

We also made the exercise to open the cone while building the background distributions. In Fig. 6.6, we represent the background FF obtained with R=0.2, 0.4 and 0.6 re-scaled to their respective areas. As expected, within error bars, the background FF evolves linearly with the area of the surface probed.

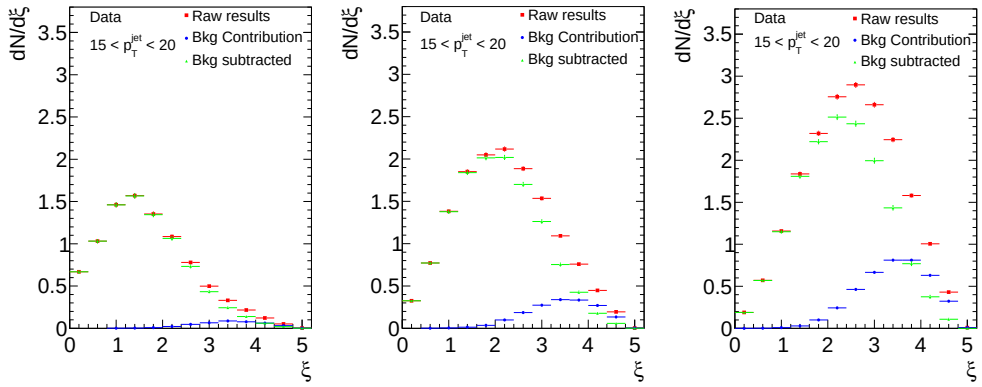

Figure 6.6: Background contributions of ξ distribution with the resolution parameter R in the jet $p_{\mathrm{T}}$of 15 $\sim$ 20 GeV/c. Left: R = 0.2 and $|\eta_{jets}| < 0.7$; middle: R = 0.4 and $|\eta_{jets}| < 0.5$; right: R = 0.6 and $|\eta_{jets}| < 0.3$.

6.2 Validation of the simulation for a Monte-Carlo based correction

Whatever the measurement performed (signal or background), it requires to be corrected. The procedure follows for both the signal and the background corrections as well as the details of the different correction factors obtained are presented in the section below.

Before, we ensure we have a good control of the simulation before to move to the correction of our data. The results of the work carried out to test the validity of our simulation are presented in this section.

To estimate the impact of the detector response on the measurement, we used the PYTHIA-Perugia2011 generated events presented in the previous chapter. To validate the quality of the MC simulation, we compare the uncorrected raw distributions in track p_T, ξ and z to the simulation at the detector level (reconstructed MC). This is respectively illustrated in Fig. 6.7, 6.8 and 6.9 for the $\mathrm{dN/d}p_T^{track}$, $\mathrm{dN/d}\xi$ and dN/dz distributions with circles for MC and squares for the data for all the jet p_T bins studied. In order to quantify the discrepancies, the ratio MC/Data is also proposed in the bottom panel of each figure and fit with a constant.

We observe a good agreement between the uncorrected data and the reconstructed MC as in [47] except for the bins of low jet p_T. The main reasons of such discrepancies could be related to the fragmentation pattern in the simulation and to the way the UE and the secondaries (see section 6.3.1) are modeled in PYTHIA [79].

Moreover, the figures demonstrate that this MC sample contains enough statis-

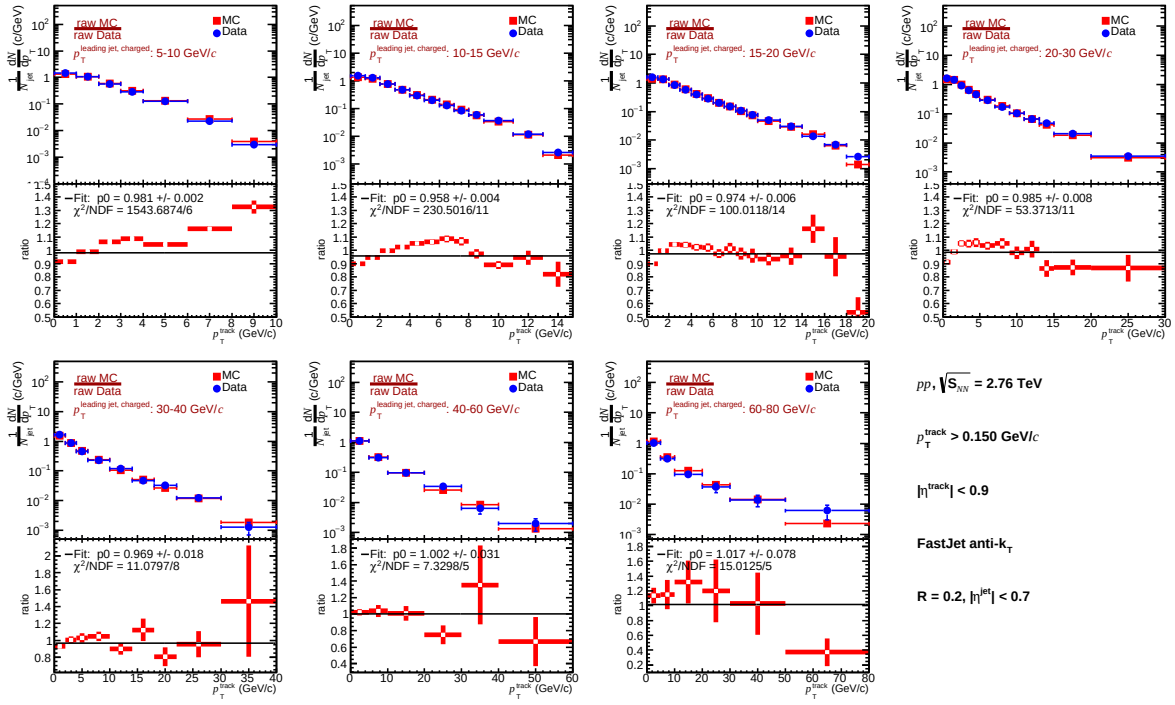

Figure 6.7: Comparison of the dN/dp_T^{track} distributions between the uncorrected spectra (squares) and the simulation at the detector level (circles) for the 7 jet p_T bin studied. The ratio MC/data is proposed in the bottom panel of each figure to quantify the discrepancies.

tics in terms of integrated cross-section compared to the data sample to guaranty small statistical uncertainties of the corrections.

6.3 Corrections

Once the simulation is validated, the last step of the analysis before to study the systematic uncertainties is to correct the obtained raw distributions for two different contributions:

1 - the detector effects including tracking efficiency and track momentum resolution, and

2 - the contamination of the measurement by secondary particles.

Monte-Carlo based corrections allow to contemplate two different strategies to correct the raw FF distributions. A '2-steps' correction can be applied to independently estimate the correction factors of the contributions 1 and 2 above. In that case, we will note the corresponding correction factors C1 and C2 respectively. But it is

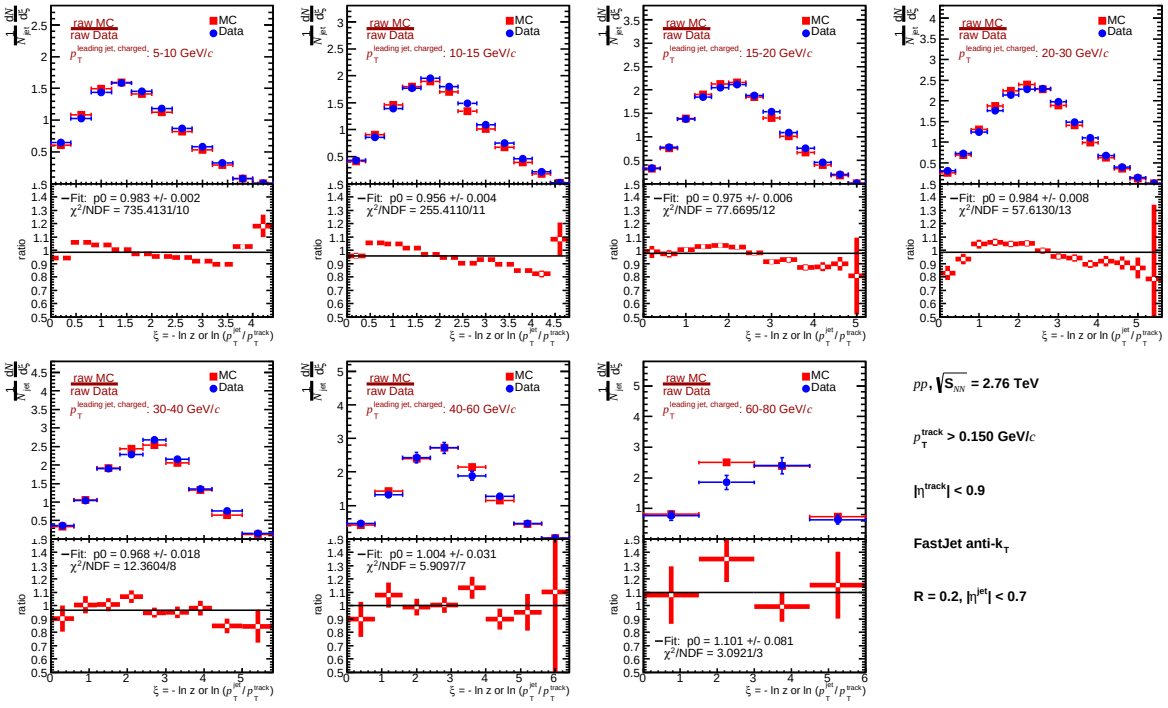

Figure 6.8: Comparison of the dN/dξ distributions between the uncorrected spectra (squares) and the simulation at the detector level (circles) for the 7 jet p_T bin studied. The ratio MC/data is proposed in the bottom panel of each figure to quantify the discrepancies.

also possible to compute a 'global' correction estimating the correction factor C according to formula 6.1.

$$C = \frac{gen}{rec} = \frac{gen}{rec\,prim + rec\,sec} \tag{6.1}$$

Taking the z distribution as example, this symbolic correction factor should be understood as:

$$C_z = \frac{dN^{gen}/dz^{gen}}{dN^{rec}/dz^{rec}} = \frac{dN^{gen}/d(p_T^{track\,gen}/p_T^{jet\,gen})}{dN^{rec}/d(p_T^{track\,rec}/p_T^{jet\,rec})} \tag{6.2}$$

In equation 6.2, rec both include primaries and secondaries.

Ensuring then that C1×C2 = C is a good way to validate our correction procedure. In what follows, the principal correction we worked on is the 2-steps one. The C factor has been quickly computed to cross-check our results but is not the correction factor we used to obtain our final corrected results. Below in sub-sections 6.3.1 and 6.3.2, the 2-steps and 1-step methods are presented and their corresponding correction factors are extracted and compared. The corrected results are shown in section 6.5.

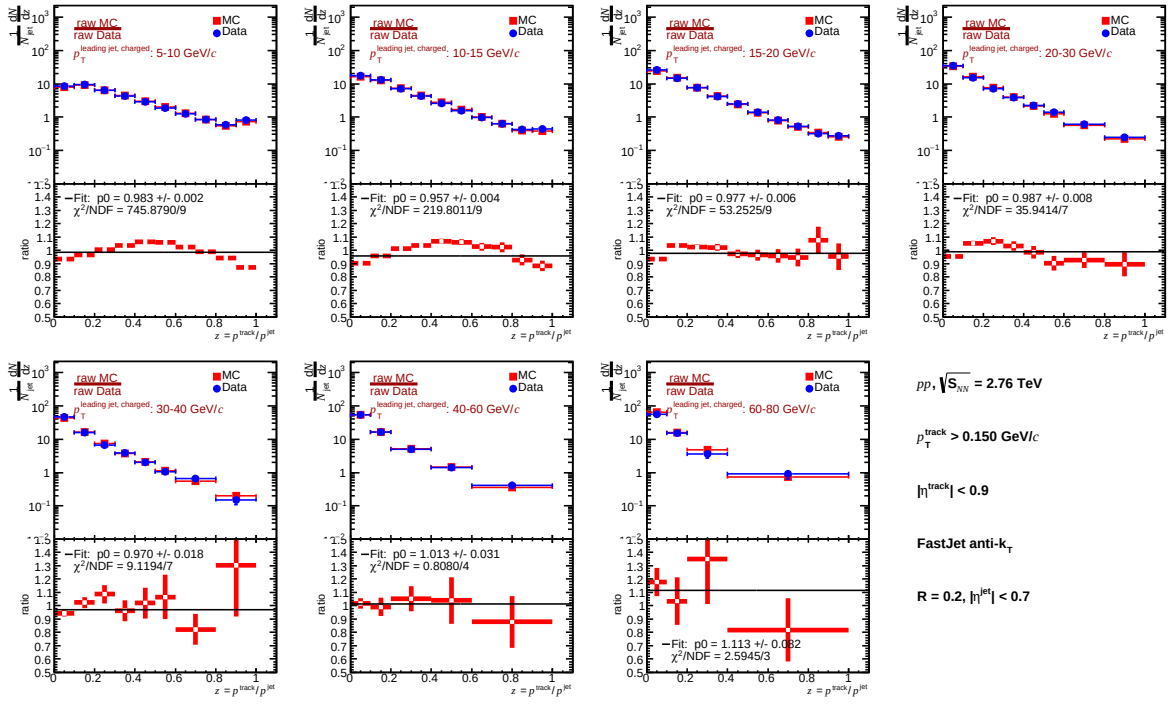

Figure 6.9: Comparison of the dN/dz distributions between the uncorrected spectra (squares) and the simulation at the detector level (circles) for the 7 jet p_T bin studied. The ratio MC/data is proposed in the bottom panel of each figure to quantify the discrepancies.

6.3.1 The '2-steps' correction method

Corrections for tracking inefficiency and finite track momentum resolution

Both track efficiency and track momentum resolution affect the momentum distribution of tracks in jets modifying the number of reconstructed tracks and their momenta with respect to an ideal detector case, but they also have an impact on the kinematics of the reconstructed jet itself (for more details, see [51]). This point is probably one of the most complicated aspect one has to deal with doing jet physics analysis. Because of the track momentum resolution and due to its steeply falling shape with jet p_T, the jet p_T spectrum is smeared with respect to its true value. Moreover, the tracking inefficiency induces a shift to the lower energies of the reconstructed jet energy as not all the produced particles have a corresponding reconstructed track in the detector [52]. So to say, a sample of charged jets stored in a given reconstructed p_T bin 30 to 40 GeV/c for example does not totally correspond to the jets generated in the p_T bin 30 to 40 GeV/c. Some of the reconstructed jets feed in or down of a given generated charged jet p_T bin. Smearing and shift thus

indirectly affect as well the FF distributions biasing the true value of the considered jet p_T in the computation of z $= p_T^{had}/p_T^{jet}$ or $\xi = ln(p_T^{jet}/p_T^{had})$.

In order to highlight these experimental issues, we have compared the track transverse momentum distributions computed at the detector (reconstructed) level to the same distribution computed at particle level (generated). The former is built with reconstructed tracks associated to physical primary particles and jet finding at the detector level, while the latter is built with generated tracks and jet finding at generator level. The result is presented in Fig. 6.11for the dN/dξ distributions.

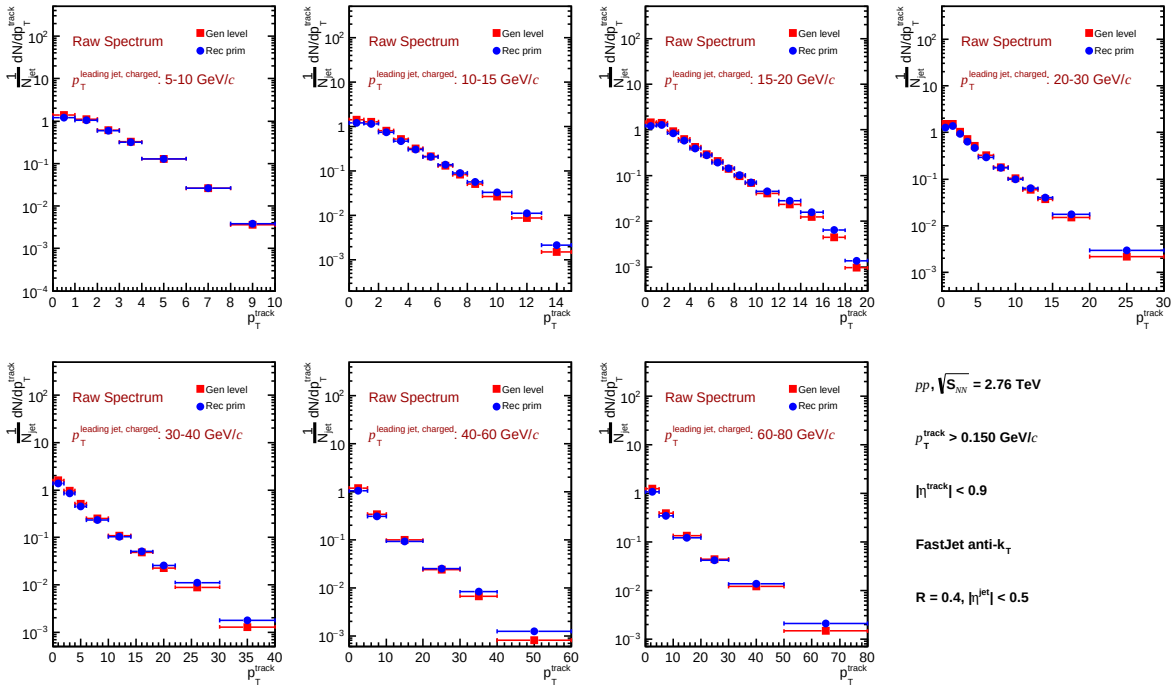

Figure 6.10: Transverse momentum (p_T) distributions on the detector (circles) and particle (squares) levels. The distributions are compared in the same nominal charged jet p_T bins.

We observe that the multiplicity (integral of the distributions) of the reconstructed jets is smaller than the generated ones. The distributions deviate from each others above $\xi = 1.5$ and a difference larger at higher ξ between reconstructed and generated. Moreover, whatever the distribution in p_T^{track} or z, the reconstructed distributions are systematically flatter than the generated one in all bins of jet p_T.

To correct the reconstructed level to the true one, bin-by-bin correction factors, C1, have been extracted for the track momentum distribution in jets and for the background FF doing the ratio of the generated distribution over the reconstructed ones from Figs. 6.10, 6.11, 6.12:

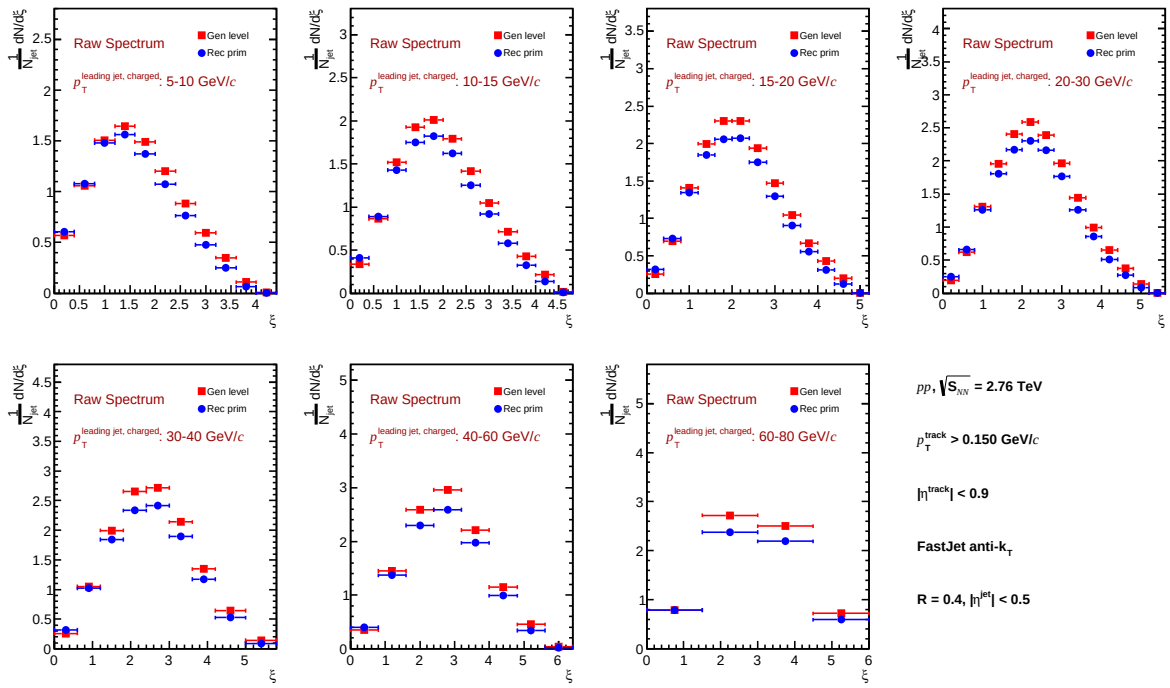

Figure 6.11: Scaled transverse momentum (ξ) distributions on the detector (circles) and particle (squares) levels. The distributions are compared in the same nominal charged jet p_T bins.

$$C1 = \frac{gen}{rec\,prim} \tag{6.3}$$

C1 should be red exactly the same as C but with a denominator including only reconstructed primaries.

The results are presented in Fig. 6.13 as a function of p_T^{track} (left), ξ (middle) and z (right) for the different bins of jet p_T. These ratios correspond to the correction factors associated to detector effects. First of all, no strong dependence with jet p_T is observed. Looking at the distributions in p_T^{track} or in z, the different ratios decrease with these variables as they are nothing but 1 over the efficiency (+ jet smearing effect especially at large p_T^{track} or z). Lower or higher particle level jets populating neighboring p_T bins implies a ratio smaller than unity (or an efficiency larger than one) in the high z region.

The signal being defined as all the tracks belonging to a jet or the jet itself and the background as the UE, one can obviously write that the composition in terms of tracks of a jet or of the background are different. In case of jet, we expect a distribution of tracks driven by angular ordering while in case of background, an isotropic distribution of tracks in azimuth can be expected. Therefore, both

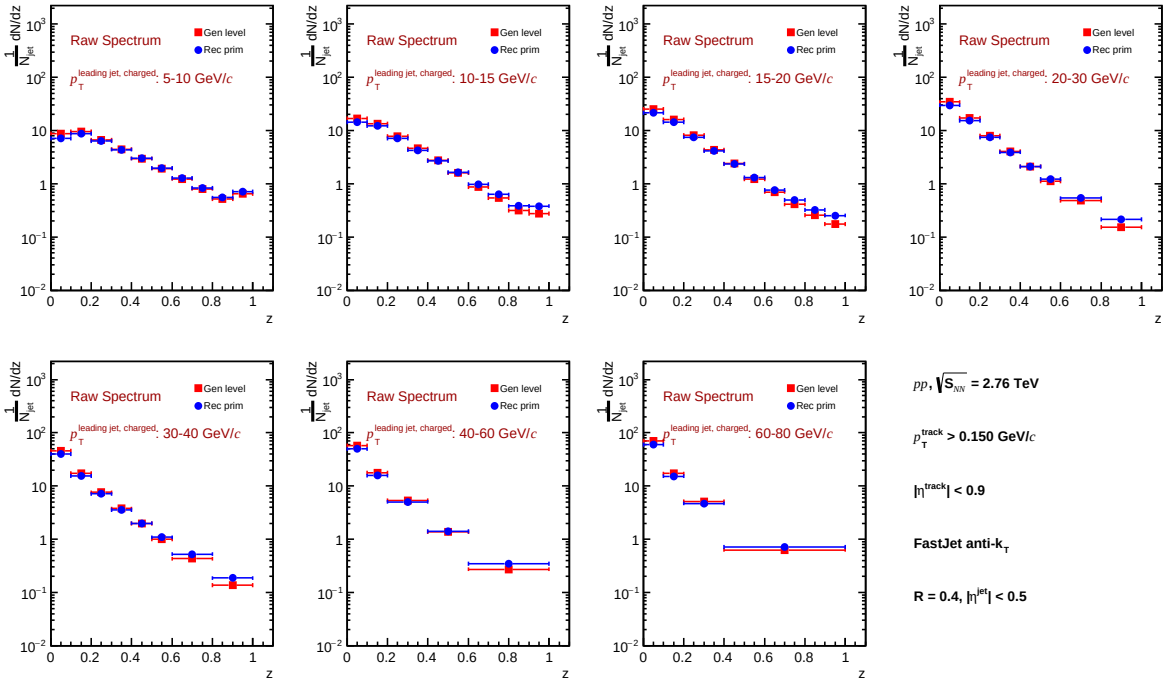

Figure 6.12: Scaled transverse momentum (z) distributions on the detector (circles) and particle (squares) levels. The distributions are compared in the same nominal charged jet p_T bins.

quantities should be corrected separately for detector effects by bin-by-bin correction before to be subtract the background corrected distribution to the corrected spectra.

In this work, we extracted the correction factor for the background jets as similar to described above. As the statistics is a lot smaller for background than for signal statistical fluctuations are frequent.

Corrections of the secondaries

Secondary particles in our study can be classified in two samples. The first family does not stem from the jet fragmentation process but can contribute to the jet energy scale. It includes photon conversions, hadronic interactions in the detector material, decay products of charged pions and weak decays of strange particles (K^0, Λ, Ξ, etc.). The second family include all neutral particles (π^0, K_s^0, Λ, etc.) produced in the fragmentation process which charged decay products are "counted" in the dN/dx (x=p_T^{track}, ξ and z) distributions whereas they should not be. These decay products should be considered as a contamination for our study.

However, in the analysis procedure, one of the track cuts applied, the DCA, allows to select primary particles leaving over a small amount of secondaries that

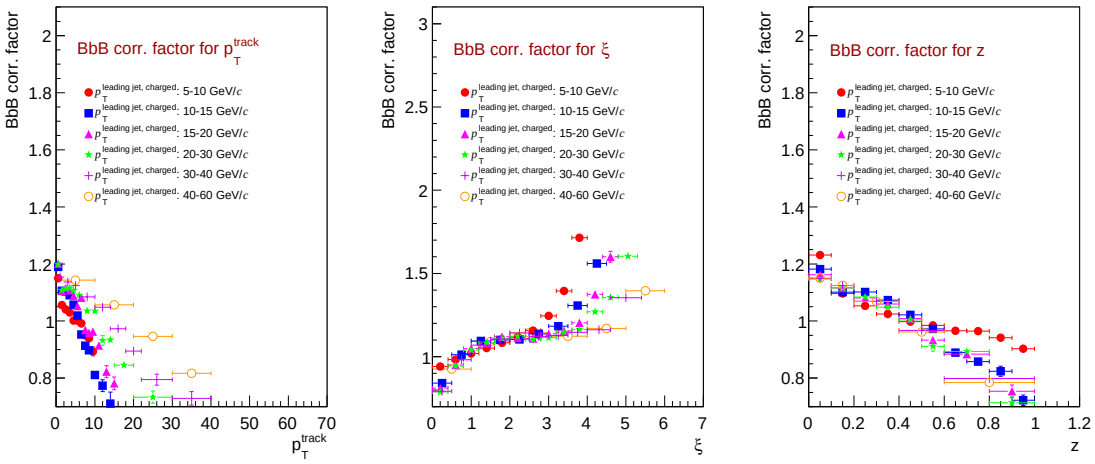

Figure 6.13: Bin-by-bin correction factors as a function of the track p_T in jets (left), ξ (middle) and z (right) for 6 jet p_T bins.

still need to be corrected for. Concerning first the jet energy scale, as in the jet reconstruction process in MC only physical primaries are kept, the secondary contamination is implicitly corrected for bin-by-bin. This has been already discussed in the previous section. Concerning secondaries in the fragmentation distributions in p_T^{track}, ξ and z, their contribution has been estimated for each bin of jet p_T based on MC simulations. Their correction factor is estimated as the fraction of secondary particles, differentially in the fragmentation variable, in bins of reconstructed jet p_T as given equation 6.4 and 6.5 as an example in the ξ variable.

$$C2 = \frac{rec\,prim}{rec\,prim + rec\,sec} \tag{6.4}$$

$$\begin{aligned} C2_\xi &= \frac{dN^{rec\,prim}/d\xi^{rec\,prim}}{dN^{rec\,prim+sec}/d\xi^{rec\,prim+sec}} \\ &= \frac{dN^{rec\,prim}/ln(p_T^{rec\,jet}/p_T^{rec\,prim})}{dN^{rec\,prim}/dln(p_T^{rec\,jet}/p_T^{rec\,prim}) + dN^{rec\,sec}/dln(p_T^{rec\,jet}/p_T^{rec\,sec})} \end{aligned} \tag{6.5}$$

The results obtained for both jets (full triangles) and the UE (open symbols) are presented in Fig. 6.14 for the 7 bins of jet p_T studied in the ξ variable. For the background cases, the two methods investigated and discussed in section 6.1.4 are compared. In the last panel of the figure, we put all the figures on top of each others for comparison vs jet p_T. Note that the same distributions in the p_T^{track} and z variables have been computed and used for the correction, but are not shown in the chapter.

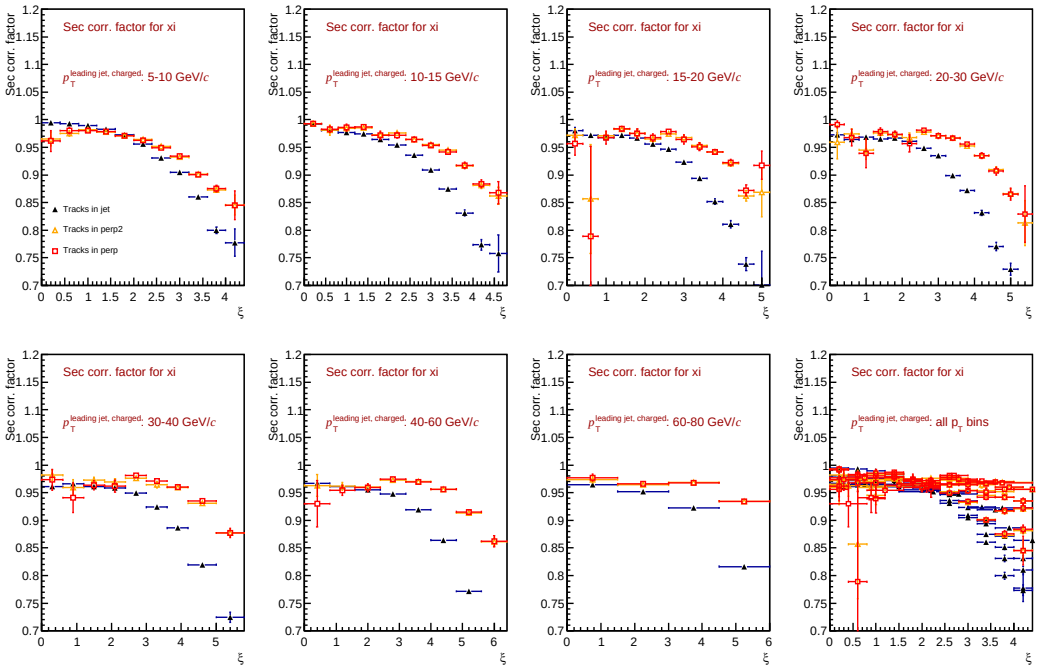

Figure 6.14: Secondaries correction factors as a function of ξ for the jets (full triangles) and the background (perp method: open squares, perp2 method: open triangles) for the 7 jet p_T bins studied.

The distributions for the signal and the background are slightly different but the global behavior is equivalent. For the jets, at high ξ, the correction is the largest and riches 25-30% while in the low ξ region, the correction factor is small (few percents). In the region where the dN/dξ is maximum, the correction is of the order of 5%. These figures show that the contribution of secondaries in the jets are a bit higher than in the transverse regions (where the background is calculated). Thus, the amplitude of the correction for the background is smaller. It riches at maximum 15% in the high ξ region. Note that the correction factors obtained for the 2 methods of background extraction are equivalent.

6.3.2 The '1-step' correction method

In order to cross-check our results on the correction factors presented above, we compute the global correction factor in 1 step as defined by equation 6.6. The way our analysis software was programmed prevented us to use the trackref in jets to perform a 2-steps correction in an acceptable analysis time. However, trackref can be used to evaluate the 1-step correction and we used them. Using MC, we computed the ratio of the reconstructed particle momentum distribution (detector level) to

the generated one (particle level) using trackrefs in both cases (cf. Method2 in table 6.1). This ratio has then been compared to the product C1 × C2 as illustrated in Fig. 6.15 with both Method0 and Method1. In the figure, the relative difference (C1×C2 (Method0 or 1)-C'(Method2))/C'(Method2) is shown for Method0 (red squares) and Method 1 (blue dots) (see section 6.5.4) as a function of z for the 7 bins of jet p_T studied.

$$C' = \frac{gen}{rec\,prim + rec\,sec} \tag{6.6}$$

We obtain a very good agreement between the two corrections and we also see that the correction factors obtained with Method0 or Method1 used to build the FF are equivalent within the error bars.

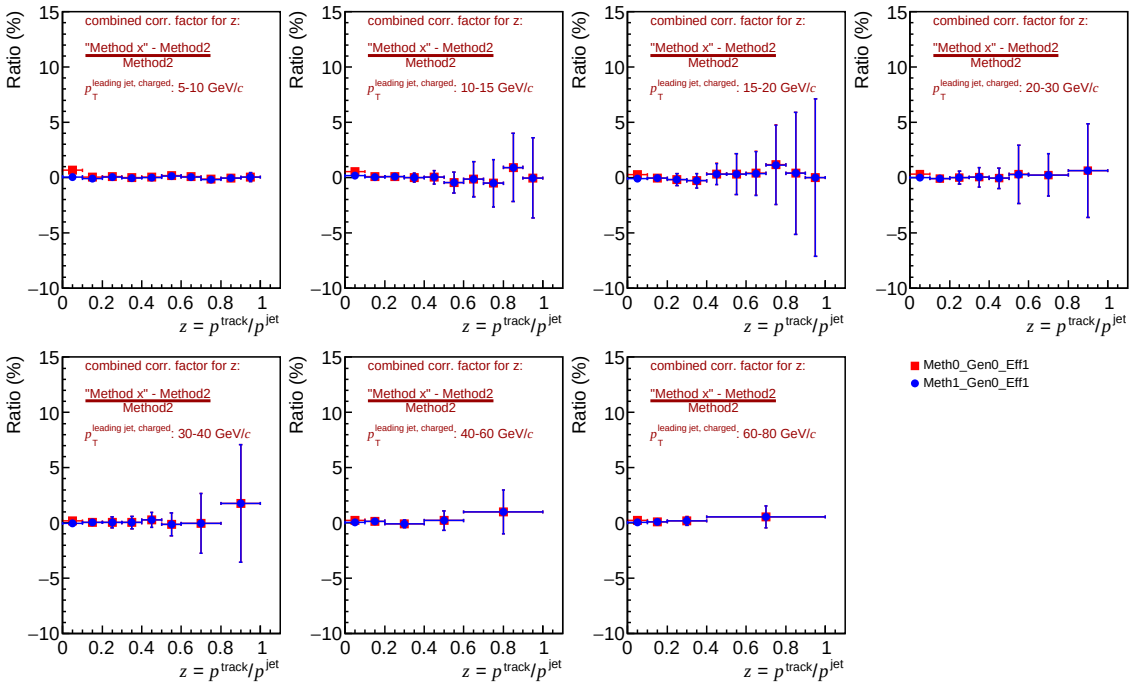

Figure 6.15: Relative difference (C=C1×C2 (Method0 or 1)-C'(Method2))/C'(Method2)

6.4 Systematic errors

The last step of the analysis developed consist in evaluation the systematic errors associated to the measurement. Before discussing in more details each contribution, we start by showing summary plots (Fig. 6.16, 6.17 and 6.18) of the relative contributions to the total systematic error (quadratic sum of all the components).

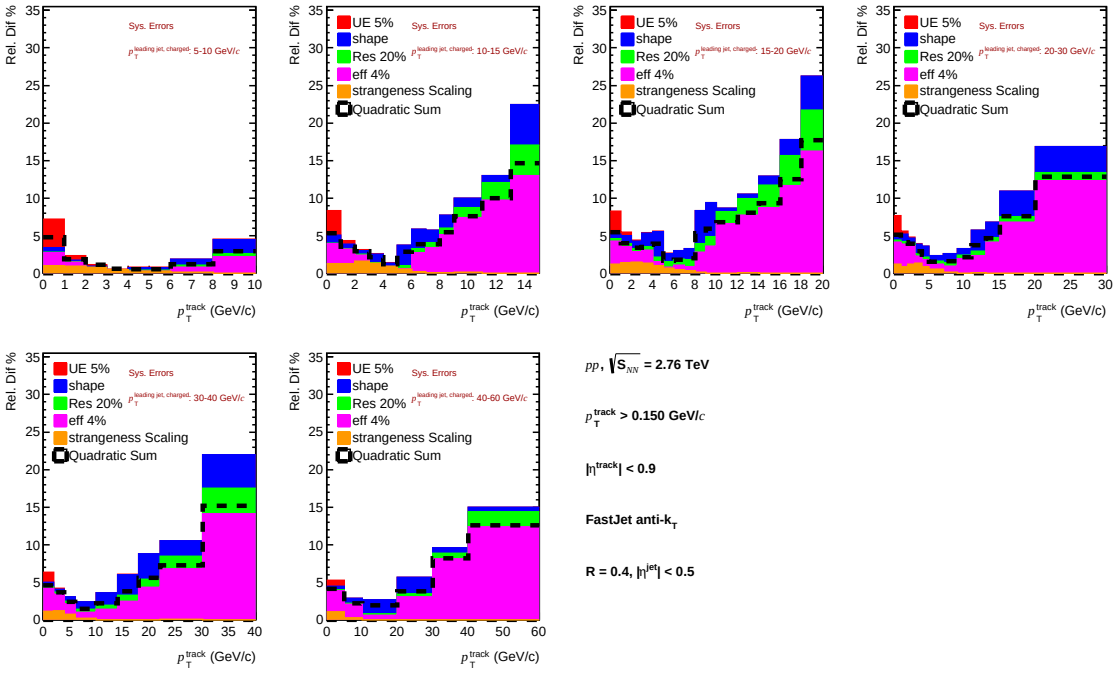

Figure 6.16: Summary of the systematic errors contribution together with their quadratic sum (dashed line) as a function of the track p_T in jets for 6 jet p_T bins

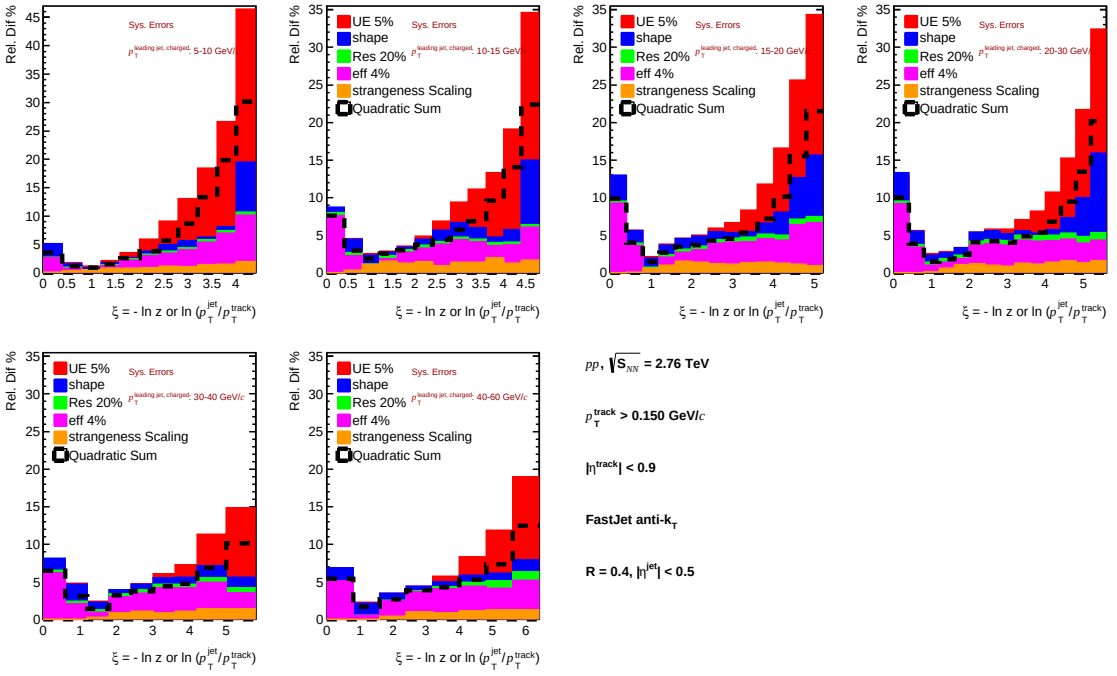

Figure 6.17: Summary of the systematic errors contribution together with their quadratic sum (dashed line) as a function of ξ for 6 jet p_T bins

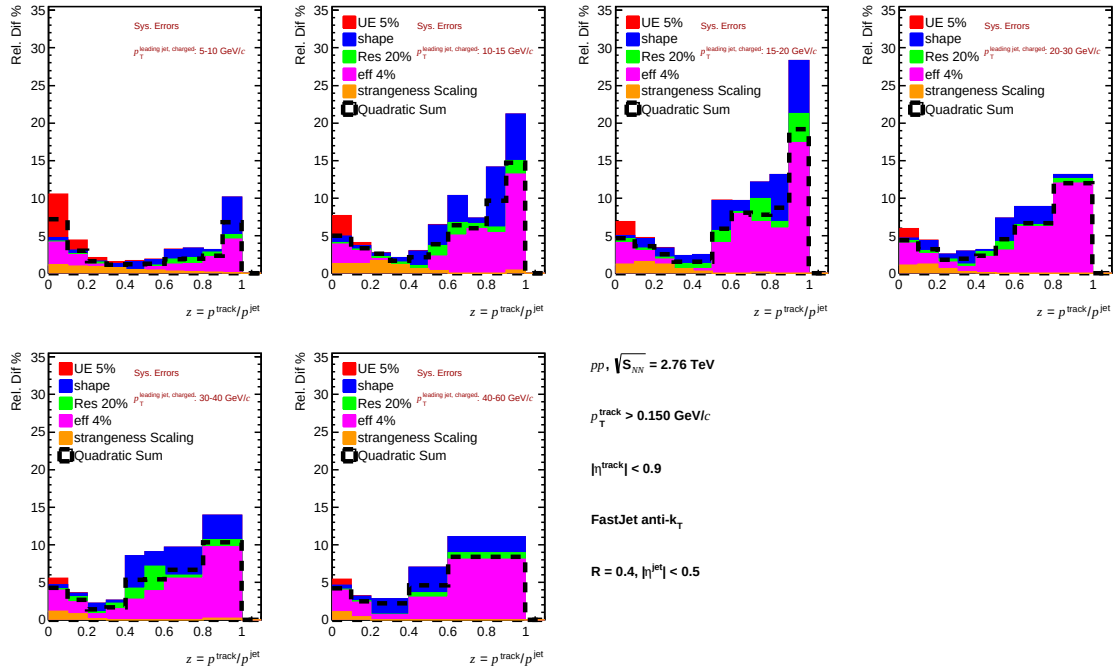

Figure 6.18: Summary of the systematic errors contribution together with their quadratic sum (dashed line) as a function of the track z in jets for 6 jet p_T bins

We will now discuss the contributions that we have considered.

6.4.1 Scaling of strange particles

The corrections discussed 6.3.1 have been driven a step further in order to better simulate the strangeness yields too low in the MC (Perugia-0). As a part of the systematic uncertainties, our correction factor have been multiplied by a data-driven correction based on measurements made by the CMS collaboration of strange particle production in non-single-diffractive events at $\sqrt{s} = 7TeV$ [] []. The strangeness decay products in PYTHIA tune Perugia0 have been compared to the CMS measurement by looking at the ratio of the K_s^0 (not feed-down corrected), Λ (not feed-down corrected) and Ξ spectra simulated and measured at 7 TeV. These ratios act as p_T dependent scale factors to be applied track-by-track to the strangeness decay daughters in our analysis. Note that we used the ratio obtained at 7 TeV for our measurement at $\sqrt{s} = 2.76$ TeV. The corresponding measurements and comparison to MC at 900 GeV and 7 TeV by the CMS experiment are presented in Fig. 6.19. One can see that the correction to consider for strangeness should be in between the 2 energies. Taking 7 TeV data instead of 2.76 TeV does not really change the strangeness correction factors (the point to point variation of the correction fac-

tors is at most 20% between 900 GeV and 7 TeV (a lot smaller than that for most points).. Of course a measurement of those correction factors (MC/DATA) at 2.76 TeV would be prefered but to our knowledge, such measurement is not available. The impact of such strangeness scaling is illustrated in Fig. 6.20 and 6.21 which

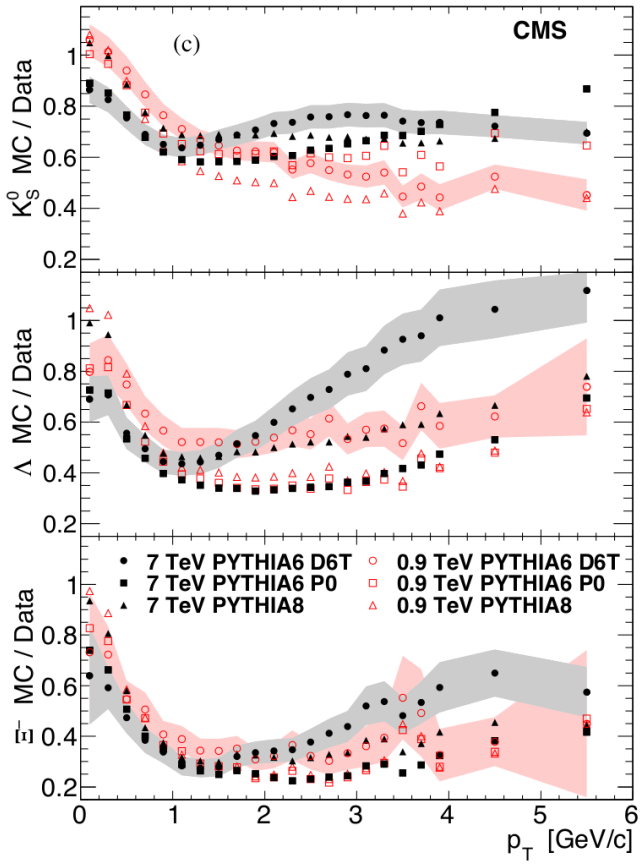

Figure 6.19: Ratios of MC/Data for the strange particles K^0_s (top), Λ (middle) and Ξ^- (bottom) measured by the CMS collaboration at $\sqrt{s}$ =900 GeV (open symbol) and 7 TeV (full symbol. Three different PYTHIA tuning are compared: PYTHIA6 D6T, PYTHIA6 P0 and PYTHIA8.

show how the correction factor for secondaries changes with the strangeness rescaling. In Fig. 6.20 we see the comparison of the correction factors with and without rescaling in the top panels of each figure and the ratio MC/MC scaled in the bottom panels. It is fit by a constant. Figures 6.21, 6.22 and 6.23 illustrates the relative difference (strangeness scaling - no strangeness scaling)/no strangeness scaling for the charged particle p_T spectra (left, (middle: dN/dξ, right: dN/dz) for the usual jet p_T bins, reconstructed with R=0.4. The strangeness rescaling implies a slightly larger correction for secondaries. The difference in the corrections is of the order of 1-2%.

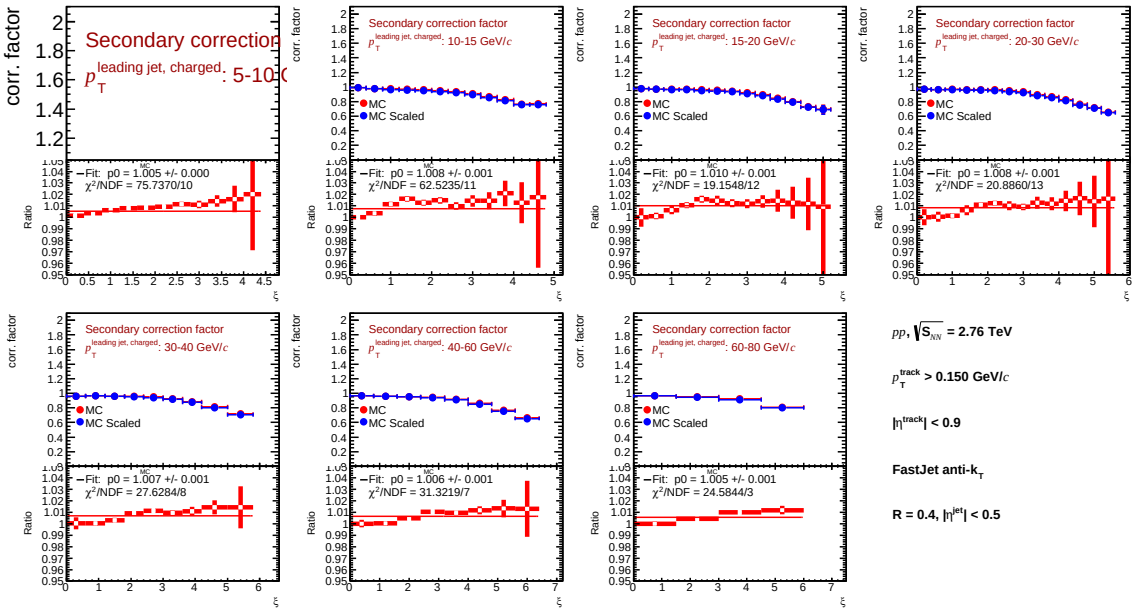

Figure 6.20: Comparison of the correction factors for the secondaries contamination with (blue) and without (red) strangeness rescaling for the 7 jet p_T bins studied. The ratio MC/MC scaled is also shown in the bottom panel of each figure as well as its fit by a constant.

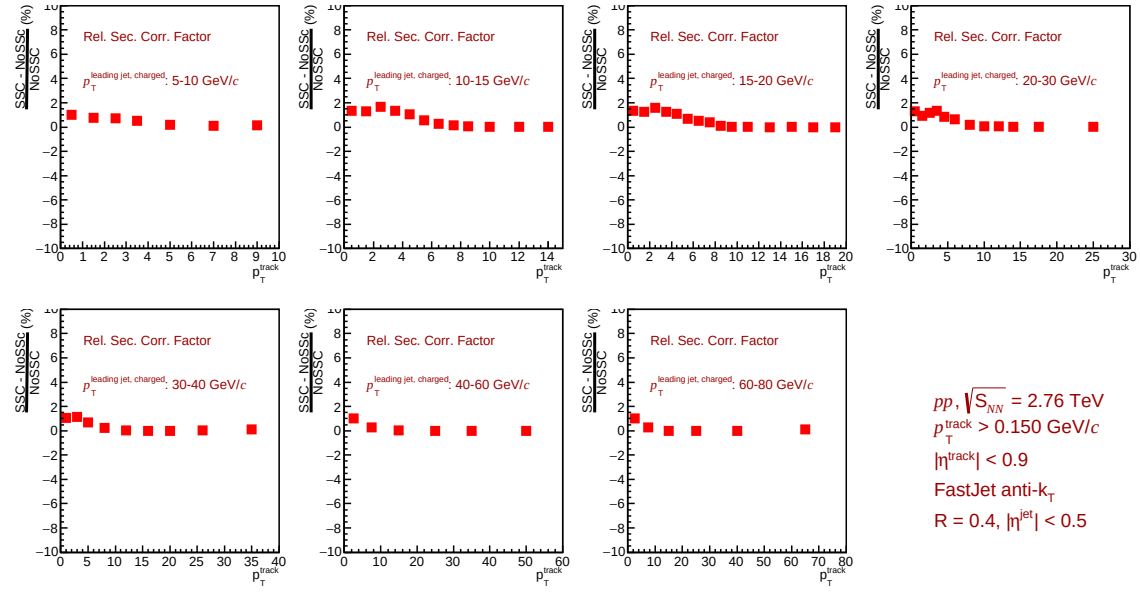

Figure 6.21: Relative difference with and without strangeness rescaling of the correction factors taking into account secondaries contamination as a function of charged jet p_T as a function of p_T^{track}.

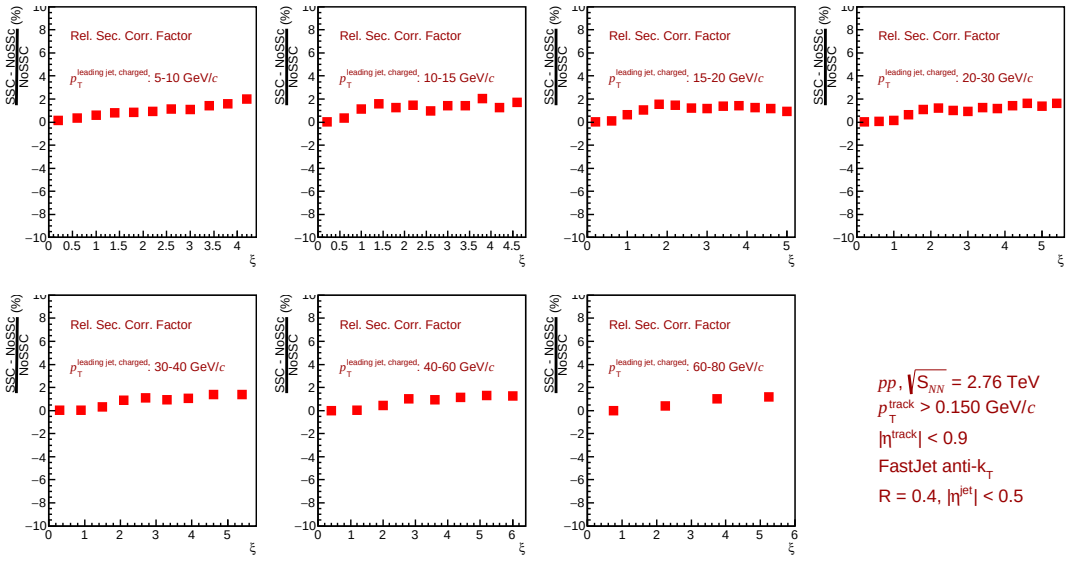

Figure 6.22: Relative difference with and without strangeness rescaling of the correction factors taking into account secondaries contamination as a function of charged jet p_T as a function of ξ.

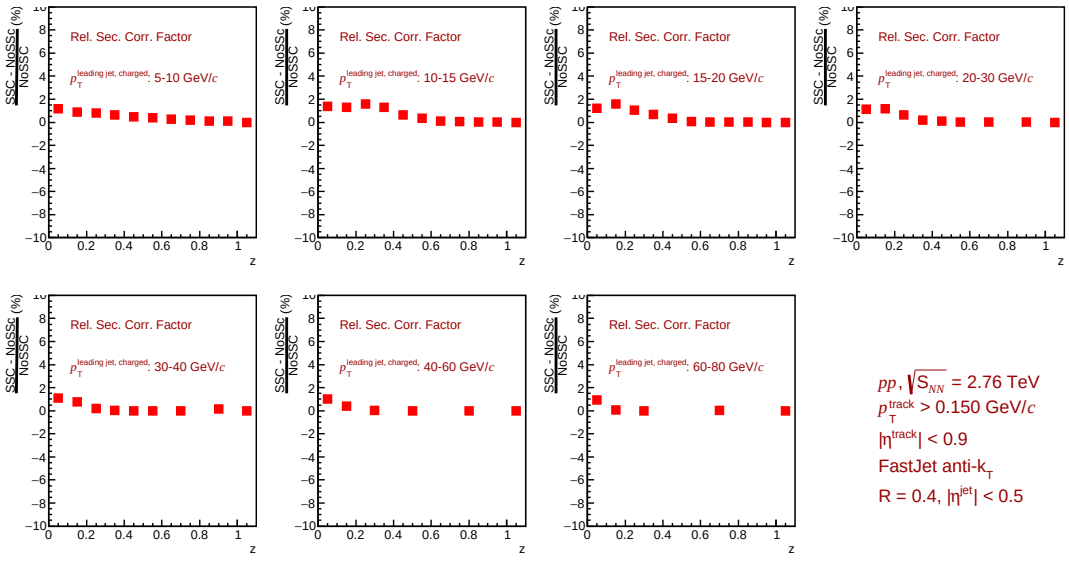

Figure 6.23: Relative difference with and without strangeness rescaling of the correction factors taking into account secondaries contamination as a function of charged jet p_T as a function of z.

6.4.2 Systematic variation of the UE contribution

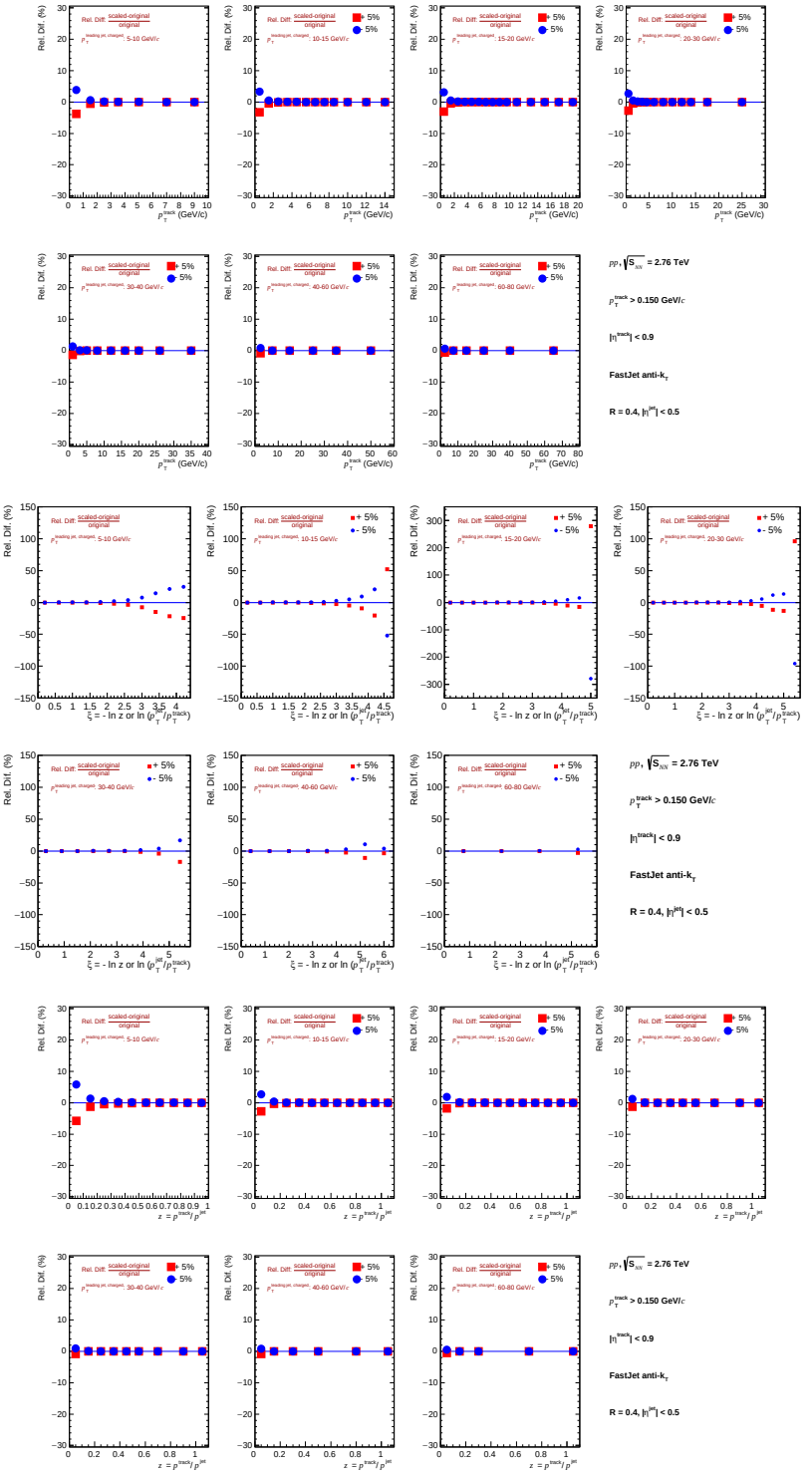

Figure 6.24: Relative difference of the UE variations (positive or negative) for charged jet p_T as a function of p_T^{track}, ξ and z.

To estimate the corresponding systematic uncertainty, the UE distribution is scaled up or down (by $\pm 5\%$) and then subtracted from the the signal distribution.

For ξ to avoid statistical fluctuations on the systematic errors (especially in the last bin where statistics is very low), we then used a fit by a polynomial.

The resulting systematic errors (shown Fig. 6.24) are $< 2-3\%$ for p_T and z but can be as high as $\sim 20-25\%$ at high ξ.

6.4.3 Detector response

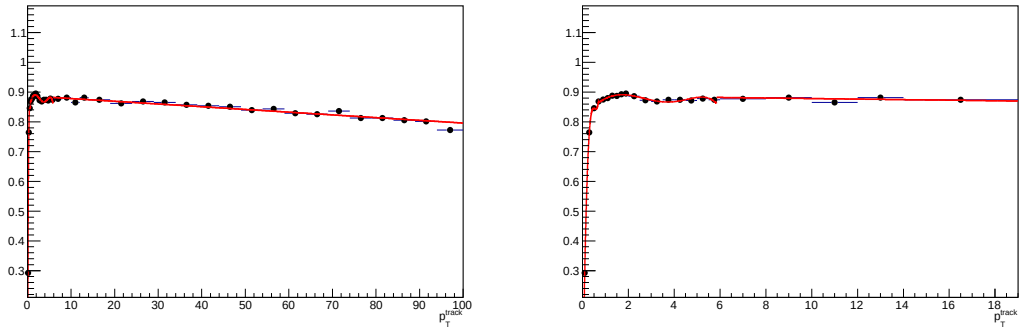

Figure 6.25: Pasteurization of the single track efficiency. At zoom at low p_T is also show (right figure).

The Single track efficiency estimated for the full detector simulation (that was used to correct the data) is parametrized (see Fig. 6.25). A smearing of the inverse of the tracks transverse momentum using a gaussian (extracted from the same full simulation) is also used to simulate the momentum resolution.

A fast simulation (toy-model) using some kinematics events as input is then used. The input charged particles are accepted or discarded randomly based using the parametrisation of the single track efficiency.

Their momentum is also smeared based on the parametrisation of the detector (the ALICE TPC) resolution. As for the full simulation, the FastJet anti-k_T algorithm is then used to reconstruct jets from those tracks. This is done twice is parallel: using directly the particles from the input PYTHIA event and also using them after applying the parametried efficiency and resolution. Both sets of jets are then used, as it was the case with the full simulation to calculate the bin-by-bin correction factors.

The Fig. 6.26 shows that the Fast sim, full sim (at the reconstructed level) and the data are in fair agreement.

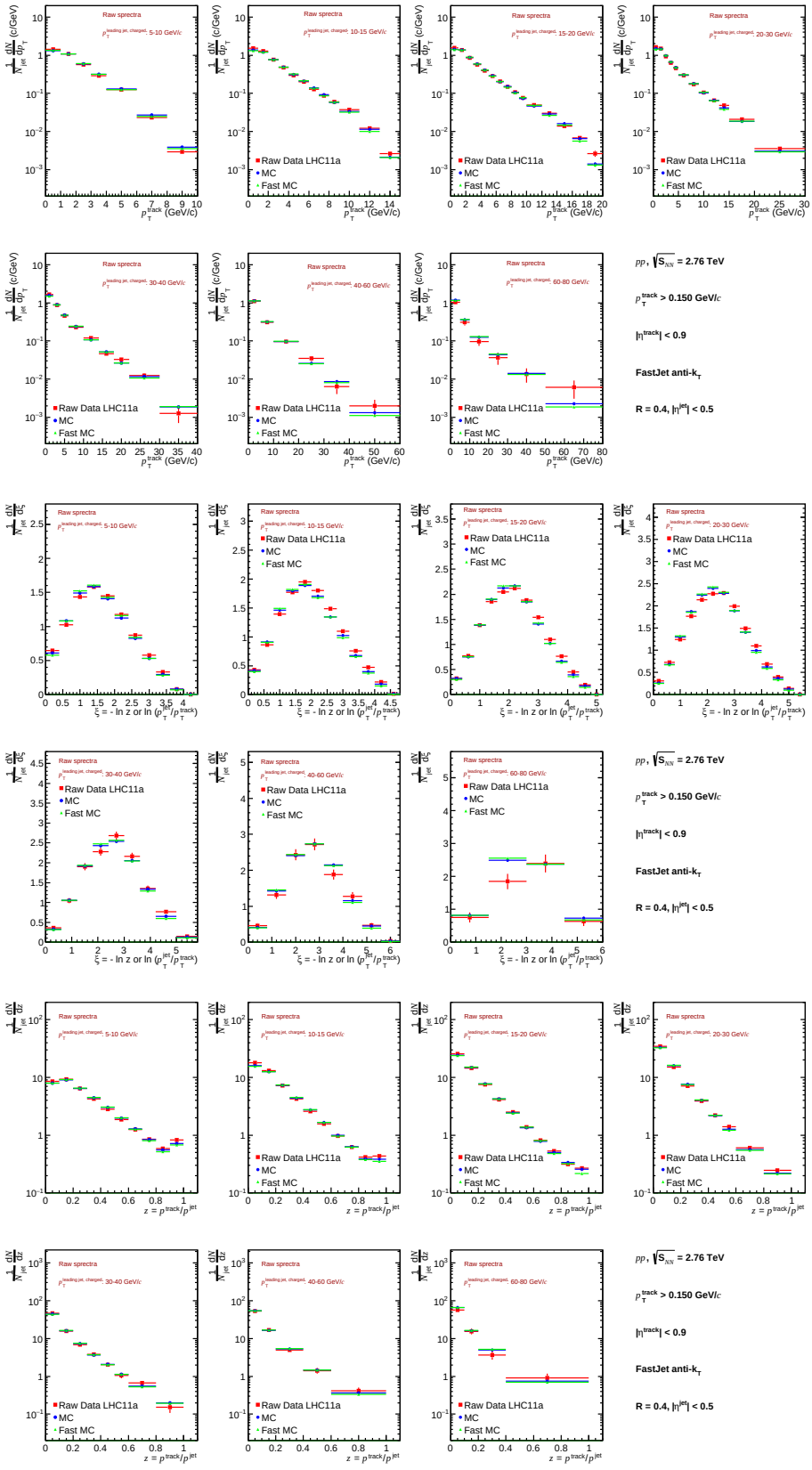

Figure 6.26: Comparison between raw data (LHC11a), fast sim, and full simulation, for p_T^{track}, ξ and z.

The fast simulation allows us to systematically vary detector efficiency and resolution within the systematic uncertainties (which are ±4% for the track efficiency and ±20% for the momentum resolution) and to propagate these to the systematic uncertainties on the bin-by-bin correction factors.

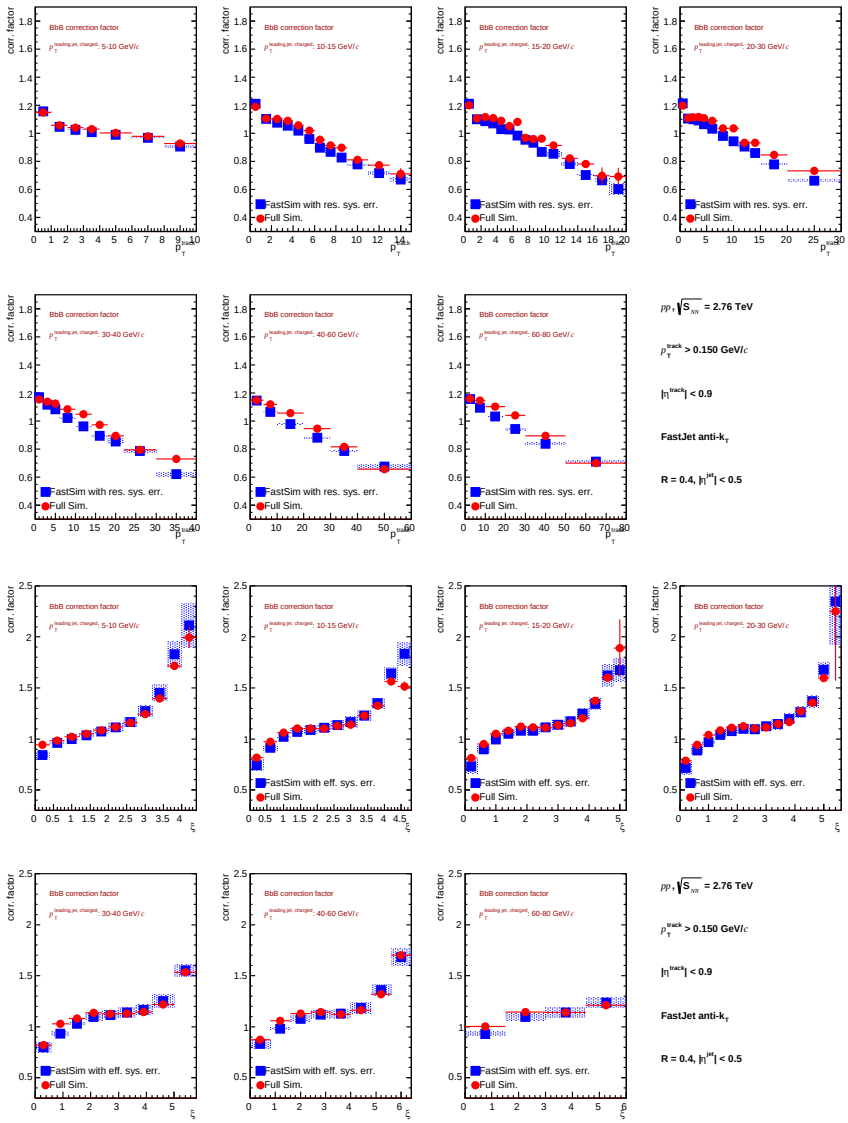

Figure 6.27: Comparison between the bin-by-bin correction factors between full simulation (red) and the fast sim (blue). The shaded bands are showing the effect of the variation of the efficiency (±4%) or resolution (±20%).

Fig.6.27 shows the comparisons between the correction factors obtained using the full simulation in red and for the fast simulation in blue. The effect of varying the efficiency (by ±4%) and the momentum resolution (by ±20%) are shown using

a shaded box.

The resulting systematic uncertainties are shown Fig. 6.16, 6.17 and 6.18. The variation of the efficiency is the biggest source of systematics. Varying the resolution has a small effect (few percents) depending on the variable and the jet p_T bin considered.

6.4.4 The event generator dependence (or shape dependence)

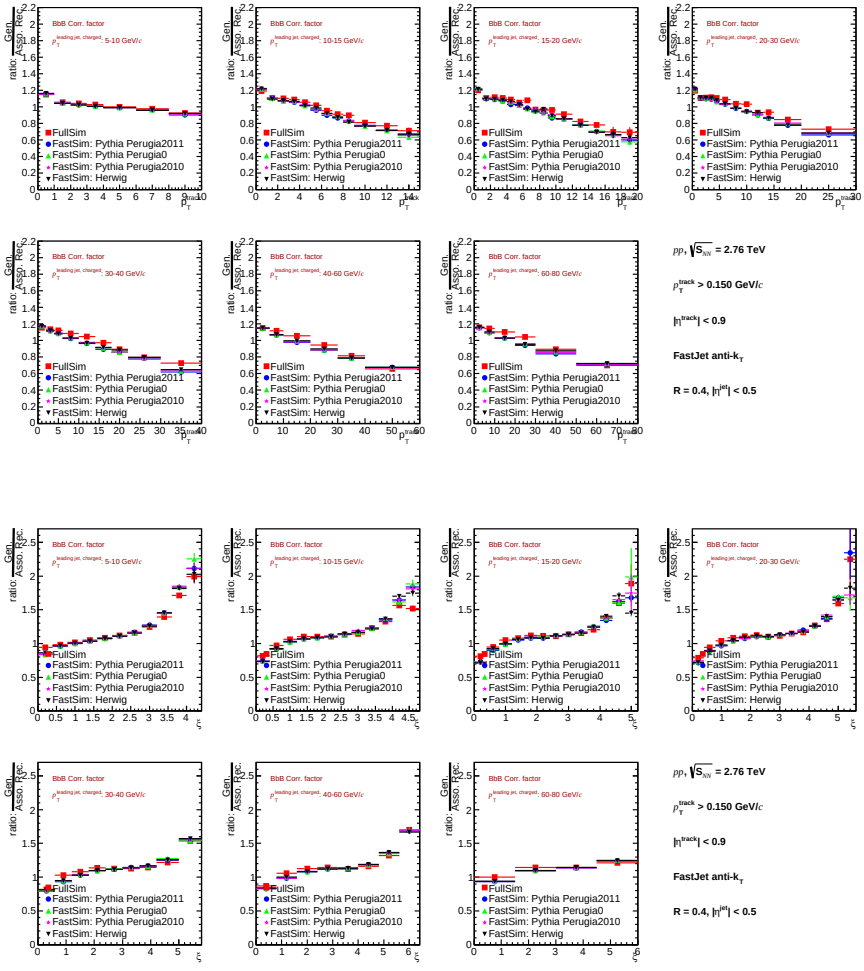

Figure 6.28: Comparison between the bin-by-bin correction factors between full simulation (red) and the fast sim using several event generators

The same procedure is used but using different MC event generators as input of the toy model. The detector effect are in this case simulated using the nominal single track efficiency and momentum resolution (parametrised from the full simulation).

Fig. 6.28 shows the correction factors obtained for each of the MC generators considered (PYTHIA 6 Perugia 0, 2010, 2011 as well as HEARWIG 6 [109]) compared to the full simulation

The relative differences between the standard fast sim tune and the others are used as systematic error (which is typically of a few percents, as shown Fig. 6.16, 6.17 and 6.18).

6.4.5 Secondary particle contamination

By varying the track cuts, it was shown at 7 TeV that the resulting variation of the secondaries is $\Delta Sec/Sec \sim 20\%$.. As the fraction of secondary particles is small the resulting systematics is very small and has not yet been taken into account in our analysis.

6.5 Results and discussion

6.5.1 Constituents in jets

The Figs. 6.29,6.30, 6.31 6.32 and 6.33 present the measured p_T spectra dN/dp_T and scaled p_T spectra $dN/d\xi$ and dN/dz of charged particles in leading charged jets reconstructed with a resolution parameter R = 0.4. The data have been corrected for underlying event background (except Fig 6.30 and 6.33), detector effects and contamination from secondary particles. On the presented distribution, only statistical error bars are included so far, the systematic errors being under study (see the previous 6.4). The two set of data studied corresponding to the periods LHC11a (top) and LHC13g (bottom) have been represented and corrected separately. In the future, these two measurements will be merged to improve the statistic of the final combined results.

In the following, dN/dp_T, $dN/d\xi$ and dN/dz will respectively be called F^{p_T}, F^{ξ} and F^{z} as in the 7 TeV publication to simplify the notation.

The particle momentum distribution F^{p_T}, F^{ξ} and F^{z} have been evaluated after correction for six bins in jet transverse momentum: 5-10 (inverse triangles), 10-15 (circles), 15-20 (squares), 20-30 (triangles), 30-40 (stars) and 40-60 (crosses) GeV/c. Note that the last 60-80 GeV/c bin has not been included in the final result for lack of statistics. It will probably be in the future when combining the two samples of data. In order to improve the clarity of the representations of F^{p_T} and F^{z}, the

different distributions in jet p_T bins but the 5-10 GeV/c have been scaled by 10, 100, 1000, 1e4 and 1e5 respectively. For F^{ξ}, the distributions have been represented in different unscaled panels from the bin 5-10 GeV/c in the bottom to the 40-60 GeV/c in the top of the figure. Moreover, the three corrected distributions are compared to the simulated PYTHIA-Perugia2011 data obtained in the same analysis conditions. In the following subsections, the dependence versus jet p_T (6.5.2) and resolution parameter R (6.5.3) of these particle momentum distributions are discussed. We also compare the corrected distributions with the simulated ones by studying the evolution of the ratio MC/Data vs p_T^{track}, ξ and z respectively in subsection 6.5.4. So far, a good agreement is obtained between corrected data and MC.

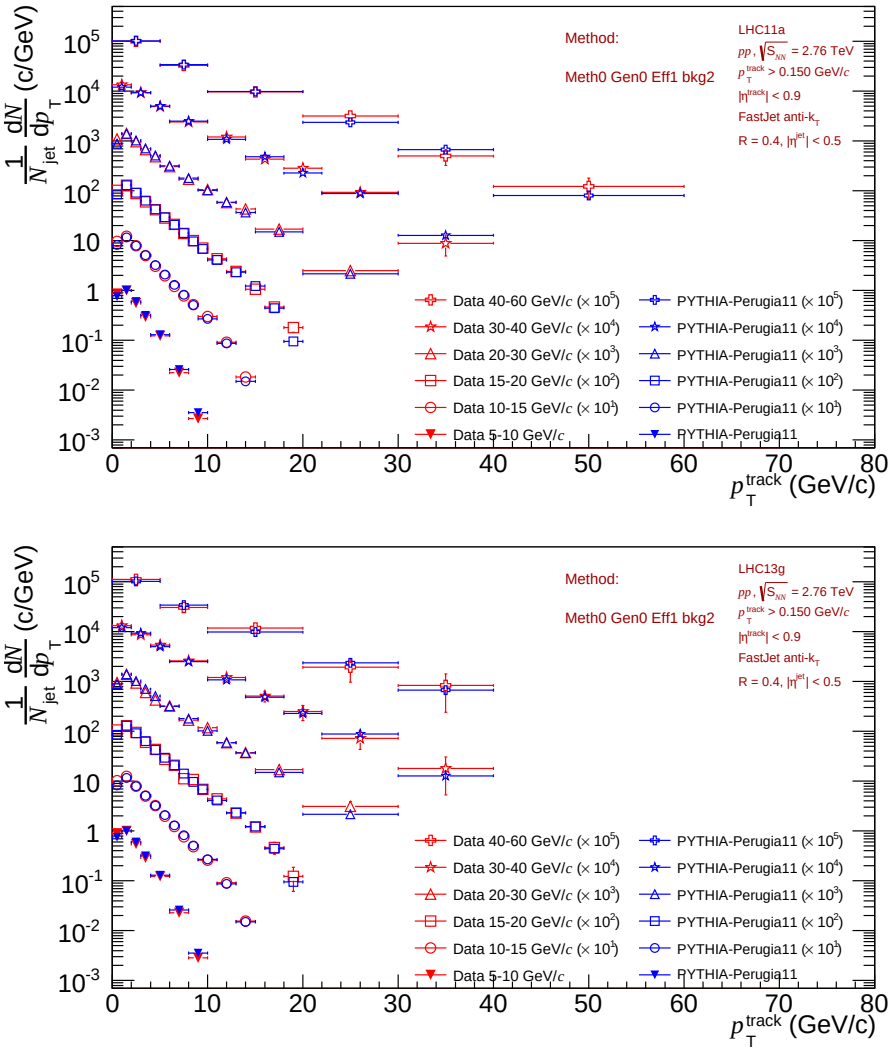

Figure 6.29: Charged particle p_T spectra dN/dp_T in leading jets for different bins in jet transverse momentum compared to simulation. For simulations and data, the UE contribution is subtracted. Top: LHC11a ; bottom: LHC13g.

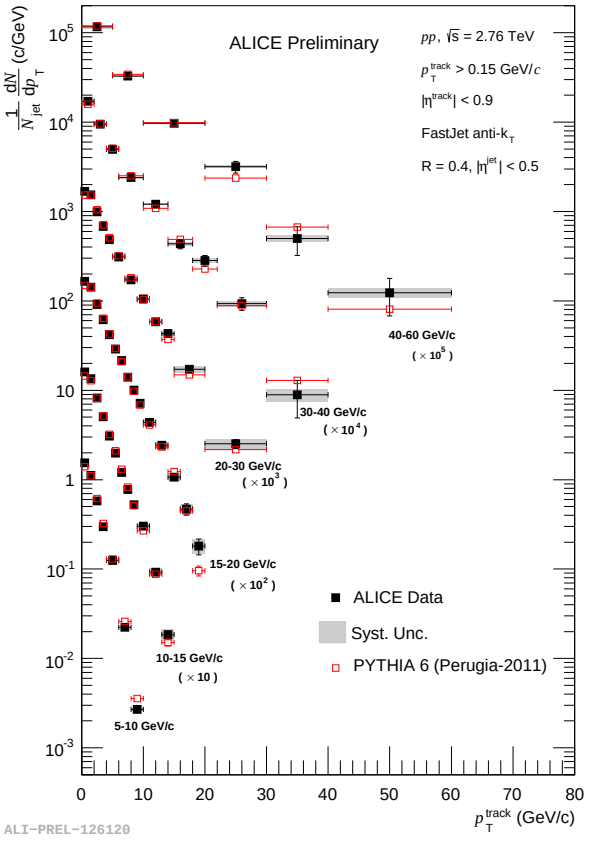

Figure 6.30: Charged particle p_T spectra dN/dp_T in leading jets ($R = 0.4$) for 6 jet p_T bins (LHC11a) compared to Pythia Perugia2011. The UE contribution is not subtracted.

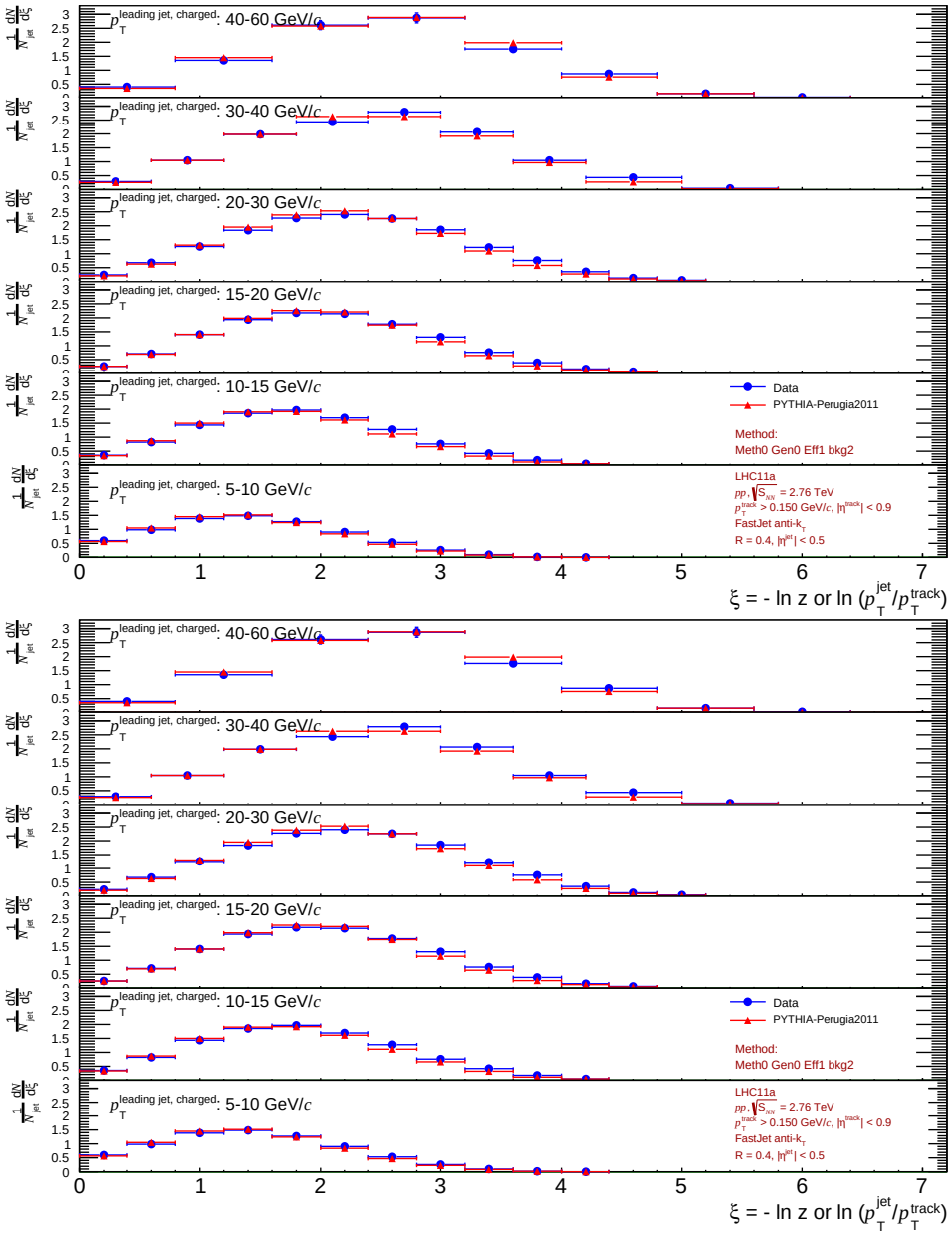

Figure 6.31: Charged particle scaled p_T spectra $dN/d\xi$ in leading jets for different bins in jet transverse momentum compared to simulation. For simulations and data, the UE contribution is subtracted. Top: LHC11a ; bottom: LHC13g.

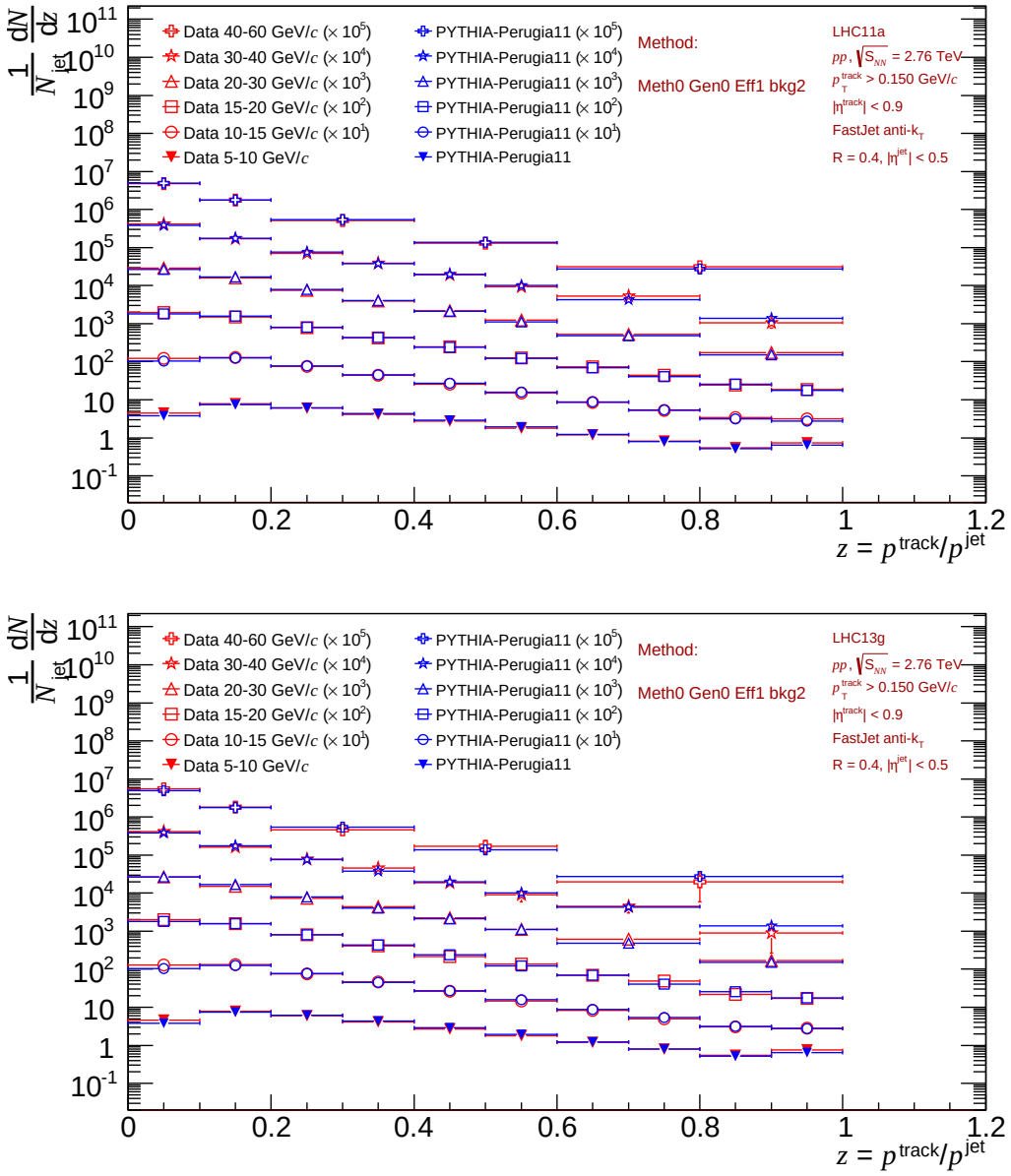

Figure 6.32: Charged particle scaled p_T spectra dN/dz in leading jets for different bins in jet transverse momentum compared to simulation. For simulations and data, the UE contribution is subtracted. Top: LHC11a ; bottom: LHC13g.

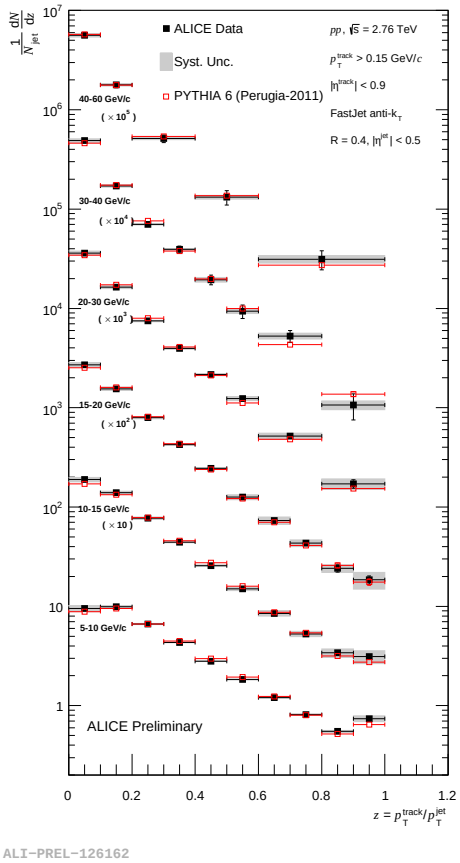

Figure 6.33: Charged particle z spectra dN/dp_T in leading jets ($R = 0.4$) for 6 jet p_T bins (LHC11a) compared to Pythia Perugia2011. The UE contribution is not subtracted.

6.5.2 Dependence with the jet p_T

In this subsection, we comment how the particle momentum distributions evolve with the jet p_T.

Concerning the F^{p_T} distributions first, we can note that the p_T spectra of jet constituents span 2 to 3 orders of magnitude. The slopes are more abrupt for the smallest jet p_T and progressively flatter with increasing jet p_T. One can conclude that the more energy available in the system, the harder the fragmentation reached. The fragmentation seems to be driven by the jet energy scale and this can be seen rescaling the p_T distributions by the jet p_T. The F^z gives such a representation. As can be seen in Fig. 6.34 and 6.35 (no UE subtraction) in z representation in the high z region (z $>$ 0.1) or in Fig. 6.37 (or 6.36 with no UE subtraction) in ξ representation, in the low ξ region, apart from the lowest jet p_T bin (5-10 GeV/c), all the distributions are on top on each others within uncertainties consistently with the jet p_T scale dependence.

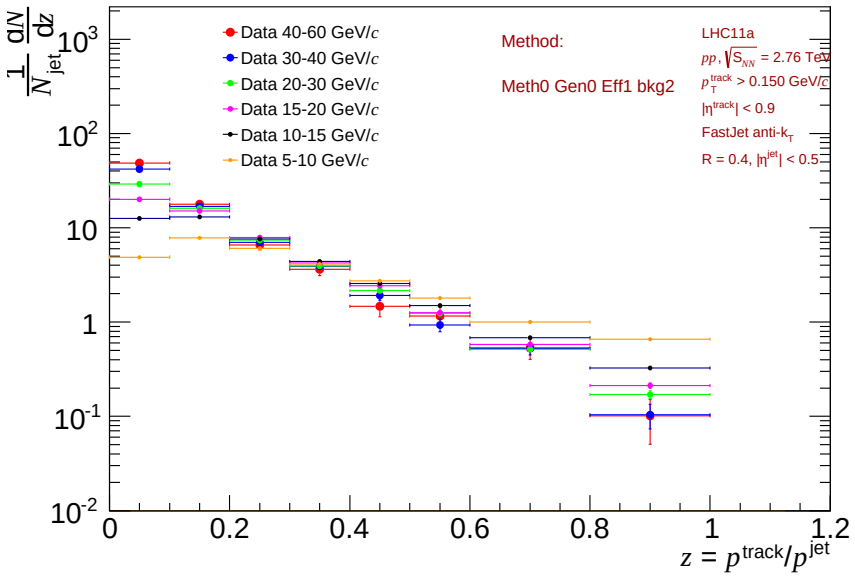

Figure 6.34: Charged particle scaled p_T spectra dN/dz in leading jets for different bins in jet transverse momentum.

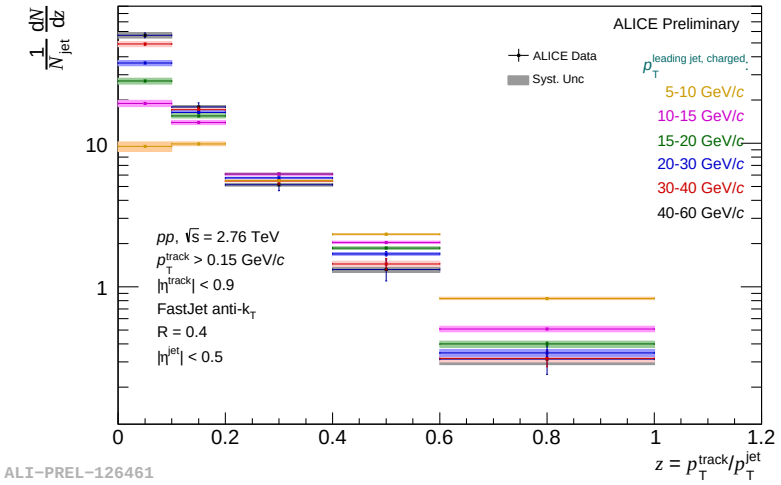

Figure 6.35: Charged particle z spectra in leading jets of $R = 0.4$ for 6 jet p_T bins (LHC11a). The UE contribution is not subtracted.

Concerning the evolution of the distribution in the low p_T (z) region, it is more instructive to change the representation and to move to the F^{ξ} distributions plotting the jet p_T representations on top of each others. First, apart from the lowest jet p_T bin, the typical "hump-backed" plateau is observed reaching a maximum (ξ_{max}) and going down at larger ξ. This behavior comes from the coherence effect of QCD. Going from low ξ to high ξ, the more energy available in the system, the more I have energy to radiate gluons in the shower in a given θ angle (in our case, R). At

some point, because of angular ordering and because of limited R, I can not radiate anymore above a given angle and the radiation stops (drop of the distribution at high ξ). Note that the maximum of the distributions shifts to higher values of ξ with increasing jet p_T. The radiation stops on average "later" in most energetic jets as there is more energy available to radiate. The distributions we observe are qualitatively comparable to the modified leading log approximation calculation (MLLA) [78] which shows exactly the same behavior. Unfortunately, we can not directly quantitatively compare them as the jet p_T which enters the computation of ξ is not the parton momentum as in the QCD based calculation. In the same way, it is important to specify that the position of ξ_{max} can not be used to estimate α_s as we are working with a different definition of ξ than in QCD

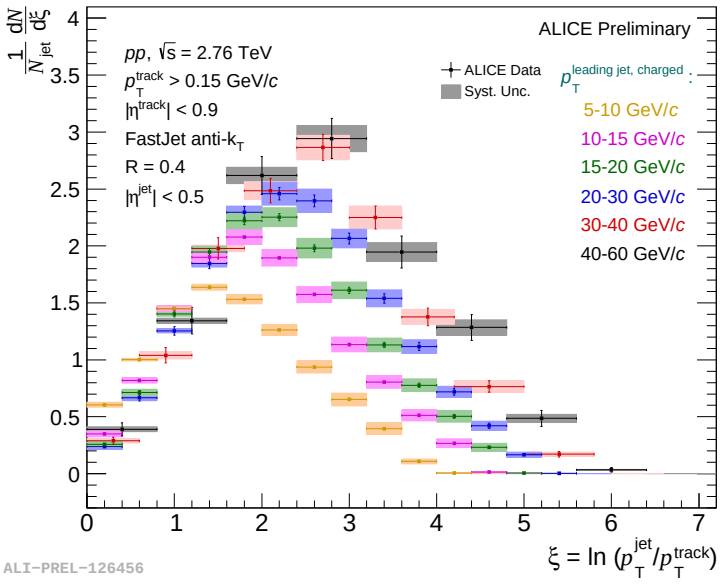

Figure 6.36: Charged particle ξ spectra in leading jets of $R = 0.4$ for 6 jet p_T bins (LHC11a). The UE contribution is not subtracted.

6.5.3 Dependence with the jet resolution parameter R

Increasing the jet resolution parameter is nothing but increasing the θ angle which defines the jet "size". In a manner of speaking, it increases the phase-space available for the gluon radiations inside a jet. One would thus expect to see an increase of the F^{ξ} distributions at high ξ (and a shift of ξ_{max} to higher values) or an increase of F^{z} at low z.

This is what has been studied in this section and what is shown in Fig. 6.38 which illustrates how F^{p_T}, F^{ξ} and F^{z} behave with three different jet resolution

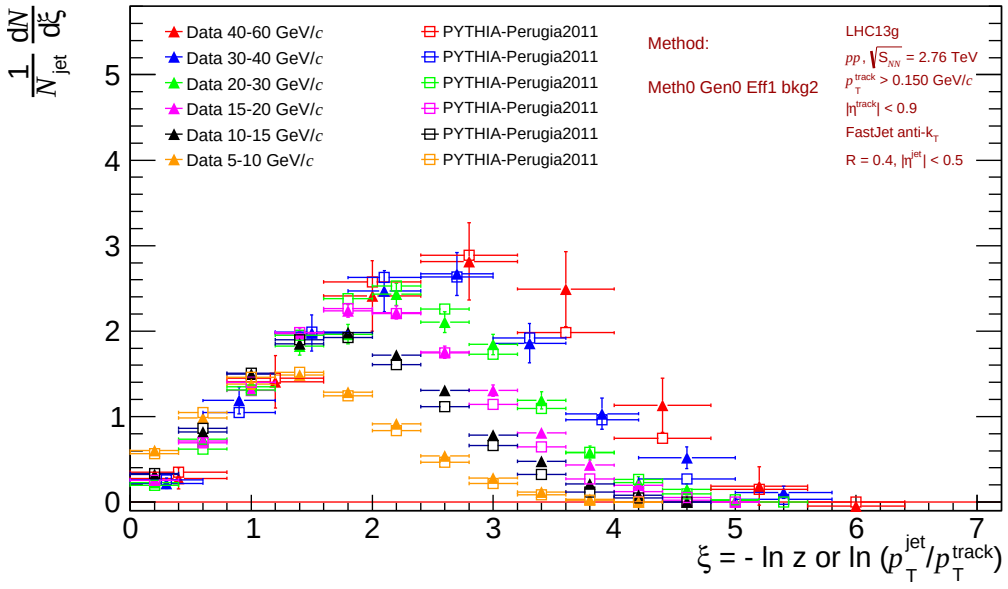

Figure 6.37: Charged particle scaled p_T spectra $dN/d\xi$ in leading jets for different bins in jet transverse momentum.

parameter R=0.2, R=0.4 and R=0.6 for the two bins of jet p_T 15-20 GeV/c and 30-40 GeV/cc. Note that we put the full spectra of F^{p_T}, F^{ξ} and F^{z} obtained for the sample LHC11a with R=0.2, R=0.4 and R=0.6, but not showing in this thesis and will be combined as results in the ALICE group.

6.5.4 Comparison to the simulation

Eventually, in order to better compare the corrected results we obtained with calculations from event generator, we looked at the ratio of the simulated PYTHIA-Perugia2011 spectra F^{x}_{MC} (x=p_T^{track}, ξ or z) over the corresponding corrected data (F^{s}_{Data}) both already compared at the spectra level in Fig. 6.29, 6.31 and 6.32. The ratio obtained with Method0 and Method1 are shown in Fig. 6.39 and 6.40 for the 7 bins of jet p_T studied. Both data and MC have been subtracted for the UE contribution.

Except for the two lowest jet p_T bins where the data is systematically lower than the simulation at both low and high p_T or z from 10-20 (low p_T) to 30% (high p_T), at high particle transverse momenta and high z, the data and the simulations agree within uncertainties (deviation $<$ 5%).

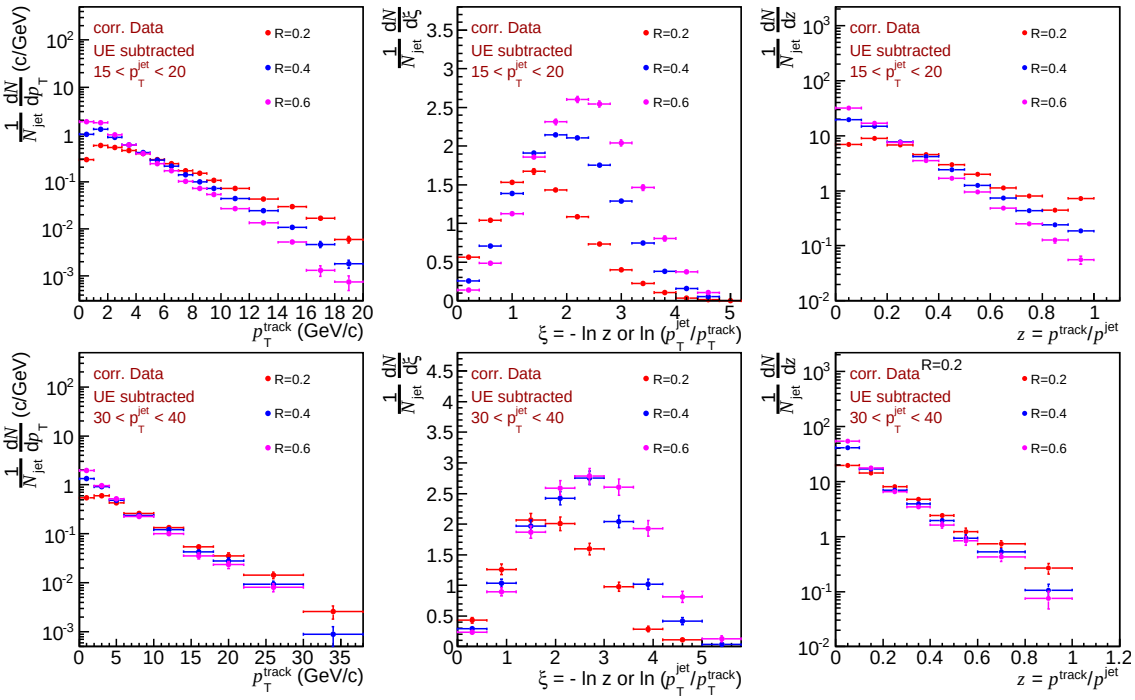

Figure 6.38: F^{p_T} (left), F^{ξ} (middle) and F^{z} (right) dependence with the jet resolution parameter R for $15 < p_T^{jet} < 20$ GeV/c (top) and $30 < p_T^{jet} < 40$ GeV/c (bottom).

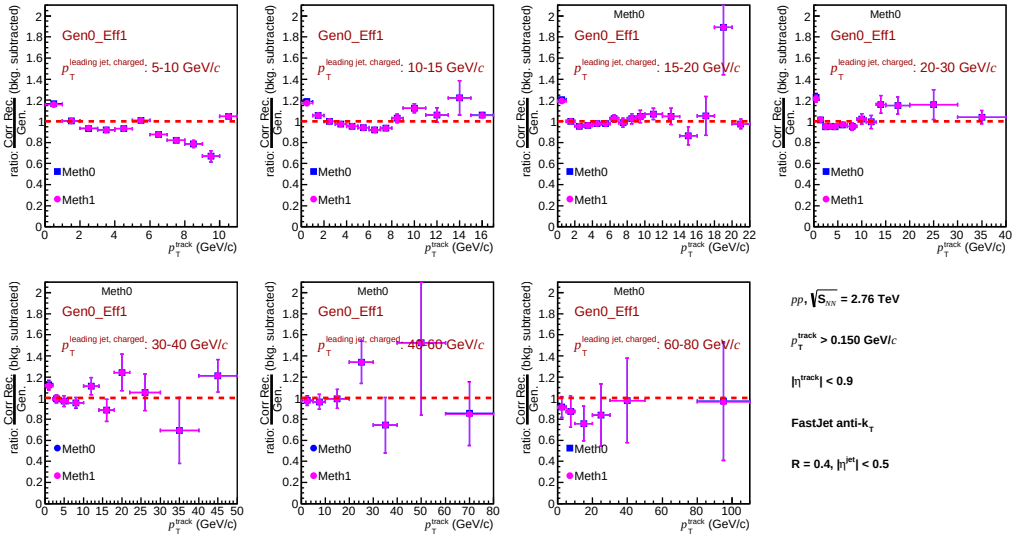

Figure 6.39: Ratio of simulations to data of the F^{ξ} distributions. The UE contributions are subtracted from both data and simulations.

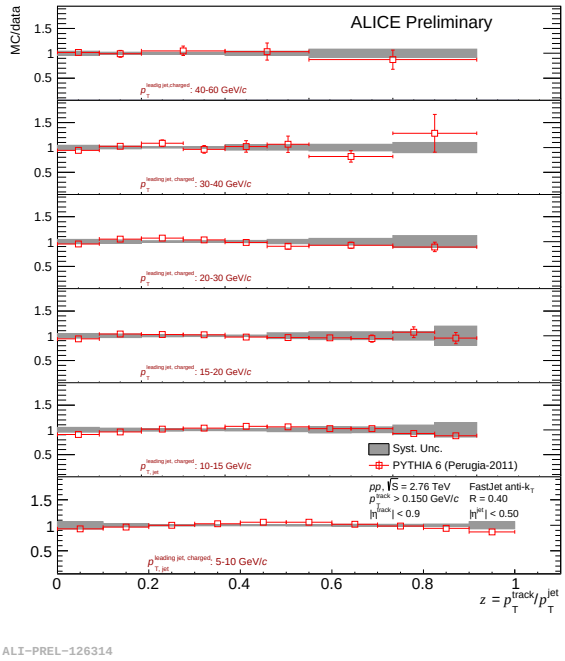

Figure 6.40: Ratio of simulations to data of the F^z distributions for a jet resolution parameter R = 0.4. The UE contributions are not subtracted from data or simulations.

6.5.5 Jet collimation

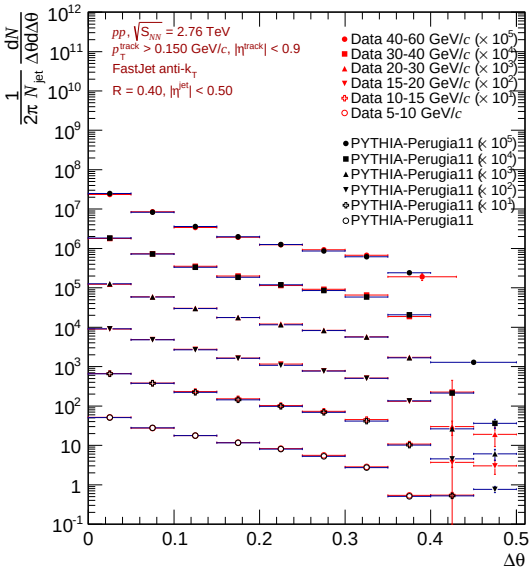

Figure 6.41: $\Delta\theta$ distribution of corrrected data compared to MC for R=0.4.

Besides the fragmentation functions for the energy distribution in the jet, the collimation of jets have also been studied as the $\Delta\theta$, which is defined as the angles between the constituents and the jet axis. The Fig. 6.41 showed the density of the tracks in the $\eta - \phi$ cone for different jet p_{T}. All of which are decreasing as the increasing of the $\Delta\theta$, the central region around the jet axis is dominated as expected, shows a good collimation. This collimation also increase as the jet p_{T} as expected in QCD.

This $\Delta\theta$ distribution is a density shows the spreading of tracks. The collimation of jets can also be studied in the spreading of the energy in the orthogonal plane of the jet axis, which the definition is j_T:

$$j_T \equiv \frac{|\vec{p}_{track} \times \vec{p}_{jet}|}{|\vec{p}_{jet}|} \tag{6.7}$$

the distribution of $ln(j_T)$ is shown in Fig. 6.42, which reveal the similar behavior of collimation in jets as the $\Delta\theta$ does. As the ln in front of j_T, the equal bin width in distribution showed in fact a meticulous in small j_T, which also shows nice collimation in jet as the $\Delta\theta$ does.

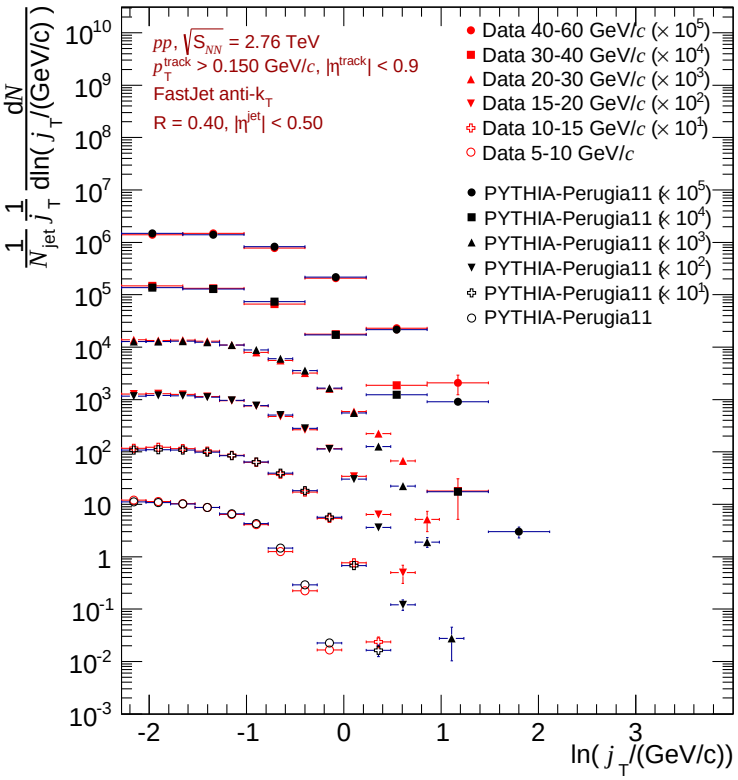

Figure 6.42: Corrected j_T distribution compared to MC for R=0.4.

Chapter 7

Analysis of the Fragmentation Function Moments of jets

This final chapter is dedicated to the first measurement of the moments of the jet fragmentation function in pp collisions at $\sqrt{s}$ =2.76 TeV in the ALICE experiment. The different steps of the analysis described in the previous chapter are applied to the FFM computation from the raw results to the correction factors to be applied. The corrected results are presented before to be discussed.

7.1 Measurement of the FFM: analysis steps

7.1.1 Calculation of the fragmentation function moments

The FFM analysis has been written and developed in the AliAnalysisTaskJetFF-Moment class introduced in the previous chapter section 6.1.1. The fragmentation function moments defined as the moments of the fragmentation functions studied in the previous chapter, can be expressed as in equation 7.1 [1].

$$M_N = \frac{1}{N_{jets}} \int_0^1 z^N \frac{dN_{hadron}}{dz} dz, z = \frac{p_T^{hadron}}{p_T^{jet}} \tag{7.1}$$

In practice it can be computed following the formula 7.2:

$$M_N = \sum\nolimits_{i \in jet} z_i^N = \frac{\sum_{i \in jet} p_{T,i}^N}{p_{T,jet}^N} = \frac{\sum_{i \in jet} p_{T,i}^N}{(\sum_{i \in jet} p_{T,i})^N},$$

The process to get the fragmentation function moments as described in [1] is the following: for a fixed N, a histogram of the M_N for all the jets stored in an

input list (for real data, in a given jet p_T range or, for MC in a given p_T^{hard} bin) as explained in the previous chapter is filled. An example of typical M_N distribution obtained following this procedure is shown in Fig 7.1 where $N = -0.25$ and the sample of jets considered corresponds the jets in p_T^{hard} bin #5: [57, 84] GeV/c. Note that the authors of the publication who proposed to study this observable represent the product $[(N+1)/2]^\alpha \times M_N$ instead of M_N (with α varying from 2 to 4) in order to visualize clearly the full range of interest versus N as it increases fast with N.

The mean value (2.583) and the standard deviation σ (1.059) of the distribution in Fig. 7.1 (left) are extracted and will correspond to 1 N bin in the FFM final distribution. As this is showed in histogram, the precision is restricted by the bin width, which will especially affect the high N region. Thus, in the real calculation, the precise values from all jets are used to calculate the mean and the error (using standard deviation, σ). Once the whole mean values and errors (computed as $RMS/\sqrt{N}$ are extracted from these distributions for different N, the fragmentation function moments distribution versus N is filled as illustrated by Fig. 7.1 (right). Note that for the rest of the thesis, we will write M_N instead of the mean value $< M_N >$ for simplicity.

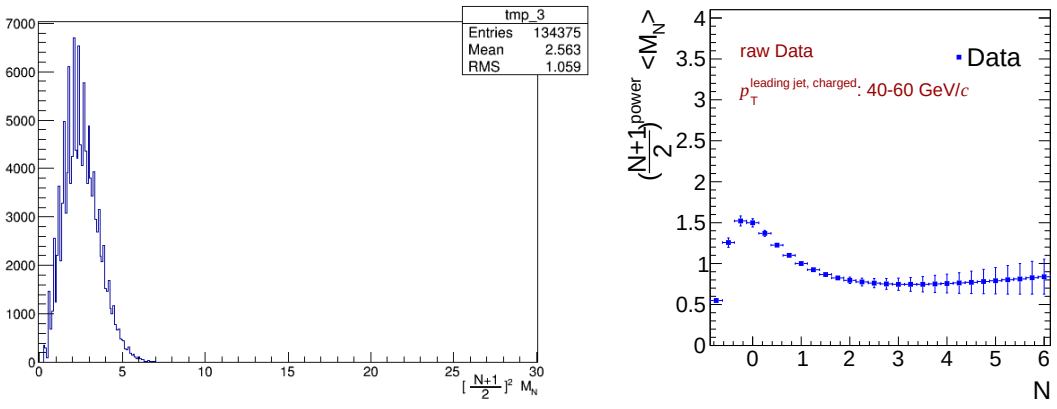

Figure 7.1: Left: example of fragmentation function moments distribution obtained for $N = -0.25$, the X-axis is the scaled M_N, the Y-axis is the number of jets. Right: example of fragmentation function moments distribution as a function of N. Here, the scaling power α is equal to 2.5.

7.1.2 Tuning of the scaling power α

As briefly introduced in the previous section, a scaling factor $[(N+1)/2]^\alpha$ is used to improve the visualization of the distribution in a reasonable Y scale. In the publication, a α power of 4 is used to show the FFM obtained under ATLAS

running conditions for 100 and 200 GeV/c jets. This power is not at all adapted to ALICE where the p_T region of jets probed is below 80 GeV/c. Because the corresponding jets contain less constituents, it strongly modifies the global shape of the distribution with respect to the ATLAS one. To illustrate this, Fig. 7.2 shows how the 2-Dimension FFM(N) raw modifies for 20-30 GeV/c jets with $\alpha = 2$ (left) and 4 (right). In both figures, the contents for each different bin of X-axis (N) will give us a slice of different distribution similar to 7.1. We clearly see that moving from 2 to 4 completely squeeze the points in a narrow low value region in the low N region (where we expect to see some modification in the presence of quenching in heavy ion collisions) whereas the large N region spread well above the Y range of the figure introducing an artificial bias in the average representation (see below). In that specific example, $\alpha = 2$ should be preferred to keep the precision both at low and high N without running out of acceptance.

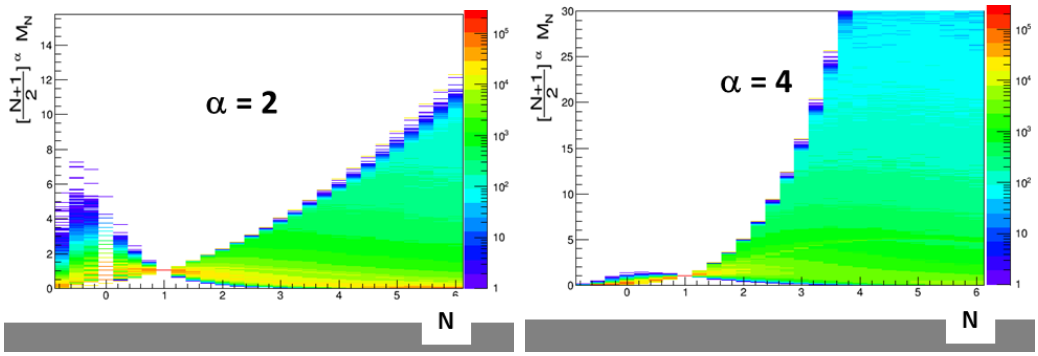

Figure 7.2: Comparison of the impact of the scaling power α on the 2-Dimension FFM (R=0.4, Data). Left: $\alpha = 2$; right: $\alpha = 4$.

The comparison of the 1-Dimension fragmentation function moments with different powers α are shown in Fig. 7.3. The spectra in black dot, red triangle and blue triangle are respectively for the fragmentation function moments built with power $\alpha = 2,\ 3$ and 4. These spectra are directly extracted from the 2-D histogram shown in Fig. 7.2. Going to larger α clearly biases the representation at large N as some of the points of the distribution are out of the range in this region as long as we want to keep a reasonable scale of representation in the Y-axis. This does not happen in a real calculation, as we will use the precise value (stored in a TProfile) instead of the 2-D histograms but the really big tail at high N is not convenient to have good precision on FFM over the full N region. Again, in the figure, a scaling power of $\alpha = 2$ should be preferred for ALICE to keep the mean value of FFM in each bin of N in a similar range from negative N to N = 6.

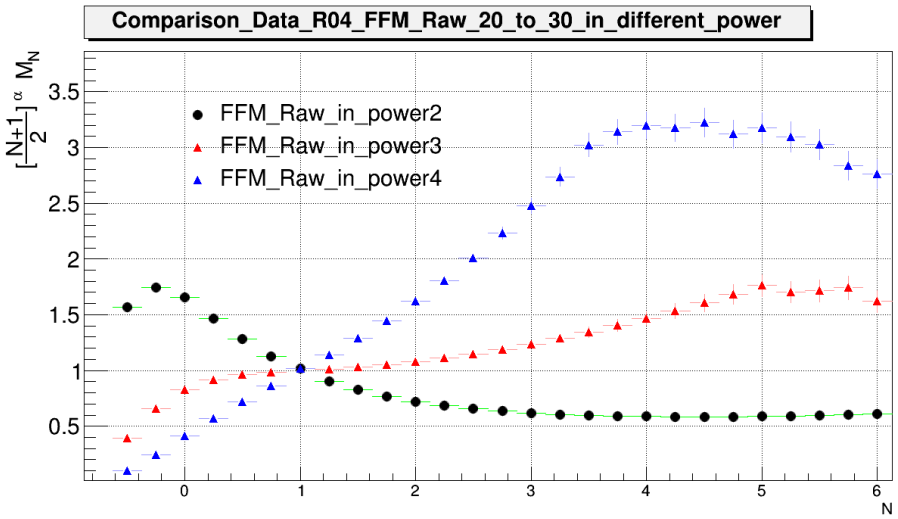

Figure 7.3: Comparison of scaling power α for fragmentation function moments in real data. The spectra are abstract from the 2-D histograms in Fig. 7.2 (the spectra of $\alpha = 3$ is not showed). The black dot, red triangle and blue triangle are receptively for the fragmentation function moments with power $\alpha = 2,\ 3$ and 4 for real data.

Dependence with jet p_T

The previous discussion has been driven with 20-30 GeV/c jets. We performed a systematic study of α varying the jet p_T under ALICE running conditions in pp collisions at 2.76 TeV. In Fig. 7.4, the left plot shows how the FFMs vary increasing α for 15-20 GeV/c jets, while the right plot shows the same comparison for 30-40 GeV/c jets. First, we clearly exclude the case $\alpha = 4$ as it completely modifies the global shape of the distribution versus N whatever the jet p_T of our studies. Going to smaller α values extend the shape of the distribution in the low N region which could be interesting to highlight quenching effects in heavy ion collisions. However, working with a too small α value tends to squeeze the FFM distributions at large N versus the jet p_T preventing to see differences between jet p_T at large N. This is illustrated in Fig. 7.5 where the evolution of the FFM versus jet p_T are shown for $\alpha = 2$ (left), $\alpha = 2.5$ (middle) and $\alpha = 3$ (right). If one is interesting to see FFM behavior at large N for harder fragmentation, he could be tempt to work with $\alpha = 3$. In our case, we have decided to work with a power 2.5 which seems to be a good compromise to exploit both the low and high N regions considering the bins of jet p_T covered.

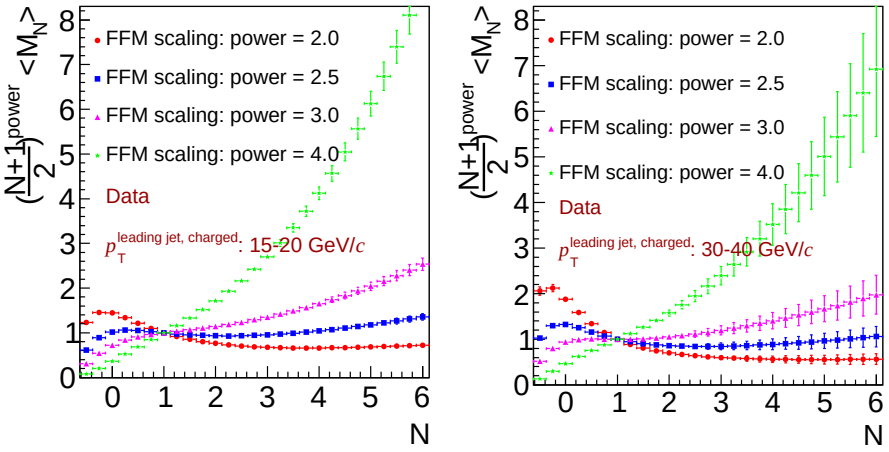

Figure 7.4: Comparison of scaling power α for fragmentation function moments in real data for two jet p_T bins: 15-20 GeV/c (left) and 30-40 GeV/c (right). Four α values are compared: $\alpha = 2$ (dot), 2.5 (square), 3 (triangle) and 4 (star).

7.2 Raw results of fragmentation function moments

Raw distributions and dependence with jet p_T

After having discussed technicalities on the fragmentation function moments, their raw spectra are presented and discussed in this section. Figure 7.6 shows the raw fragmentation function moments obtained for 5 bins of jet p_T. The different symbols: star, inverse triangle, triangle, square and circle are respectively for jets in $5 < p_{\mathrm{T}} < 10$, $10 < p_{\mathrm{T}} < 15$, $15 < p_{\mathrm{T}} < 20$, $20 < p_{\mathrm{T}} < 30$ and $30 < p_{\mathrm{T}} < 40$(GeV/c). The Y-axis is the scaled fragmentation function moments: $((N+1)/2)^{2.5}\ M_N$; the X-axis is the order of the moment (power of z in the definition): N. These spectra exhibit the same trend as in the publication [1].

According to the definition, the distribution can be divided in two regions on either sides of $N = 1$, where by definition the FFM(1) equals unity:

$$\left[\frac{N+1}{2}\right]^2 \cdot M_N\Big|_{N=1} = \left[\frac{1+1}{2}\right]^2 \cdot \left(\sum_i z_i^1\right) = 1 \cdot 1 = 1$$

where $\sum_i z_i = 1$, due to track momentum conservation in the jet (all the constituents are used to define the jet p_T). Before $N = 1$, the fragmentation function moments increase with the jet p_{T} (from black stars to orange circles), whereas above $N = 1$, the fragmentation function moments decrease with the jet p_{T} increasing. Another

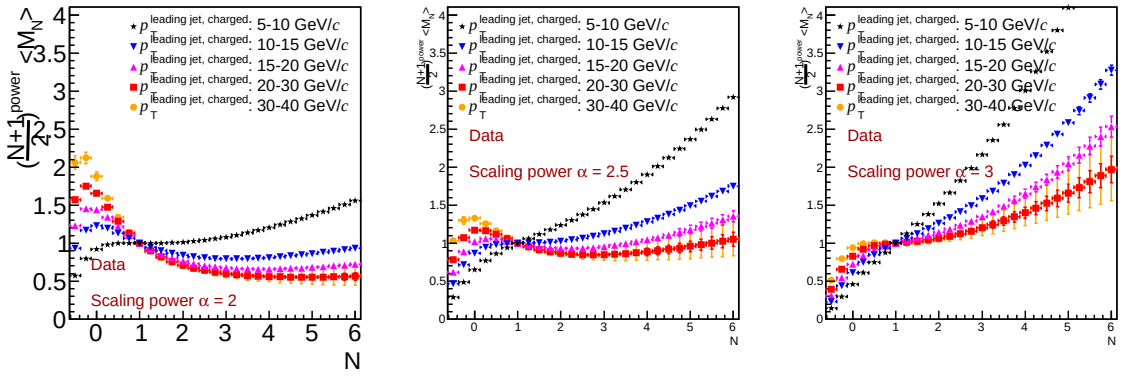

Figure 7.5: Comparison of the fragmentation function moments in real data as a function of the jet p_T. The distributions have been calculated with $\alpha = 2$ in the left panel, $\alpha = 2.5$ in the middle and $\alpha = 3$ in the right one.

important point in the distribution can be extracted for N = 0:

$$\left[\frac{N+1}{2}\right]^2 \cdot M_N\Big|_{N=1} = \left[\frac{0+1}{2}\right]^2 \cdot (\sum_i z_i^0) = \frac{1}{4}\, N_{constituents}.$$

This value is proportional to the number of charged particles/tracks in the jet (the number of constituents), which increases with the jet p_{T} increasing, as more fragmentation is expected with higher energy available in the system. In the contrary, above N = 1, an increase of the jet multiplicity with the jet p_T translates into a decrease of the distribution from pure mathematical considerations: more "fragments" are expected with increasing jet p_T, the effect from the higher order of N will make the distribution decrease faster than the increase of the number of constituents.

In the following sections, we review the results obtained for the different steps of analysis already presented in the previous chapter for the FF studies. We followed exactly the same logic to extract the corrected FFMs.

7.3 The background subtraction procedure

The same procedure (background tracks measured in a cone perpendicular to the jet axis in ϕ) as the one used for FF background subtraction has been applied to the FFM. The result is presented in Fig. 7.7. A specific procedure to subtract the background contribution to the FFM has been proposed by the authors of the publication. This method is based on the calculation of a background density in

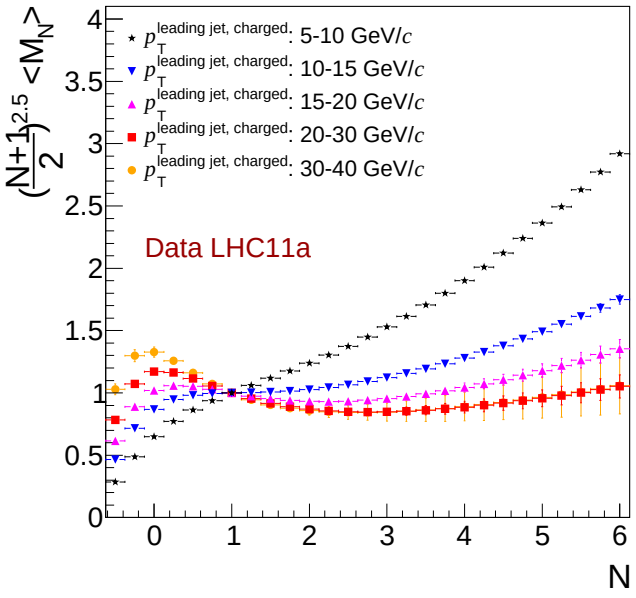

Figure 7.6: Spectra of fragmentation function moments distribution for real data. Five bins of jet p_T are compared: $5 < p_{\mathrm{T}} < 10$ (star), $10 < p_{\mathrm{T}} < 15$ (inverse triangle), $15 < p_{\mathrm{T}} < 20$ (triangle), $20 < p_{\mathrm{T}} < 30$ and $30 < p_{\mathrm{T}} < 40$ (GeV/c).

moment space $\rho_N = \text{median}(\sum_i p_{T,i}^N / A^{jet})$. The key for this method (as well as for any method reacquiring to compute a background density (even the standard background density ρ) to work, is to find and then use a "good" region to estimate this background density. The authors of the publication are proposing to use a doughnut around a given signal jet. However to be able to do so, a detector with a large acceptance like ATLAS is needed. In the case of ALICE we do not have enough acceptance to do the same thing. In our case, we however implemented a fastjet::Selector (called SelectorPerp and deriving from fastjet::SelectorWorker) that calculates the background density in a cone perpendicular to the jet axis (jet by jet) ie in the same way as we do for our fragmentation functions but using a background density. We tried to use this selector however as the background is very small in pp, the background density ρ_N calculated this way is null in most cases. Resulting in a background subtracted fragmentation function moments distribution which looks almost identical to the signal distribution...This is under investigation. Consequently for the time being we decided not to subtract the UE on the corrected results yet.

In the high multiplicity environment of heavy ion collisions, taking into account the large fluctuations of the background, it is essential to apply the improved method

for background subtraction explained in the publication and available to the users in the Fastjet/FFMoment package but we did not use it in our study as we worked with elementary pp collisions. That said, we note that as this improved subtraction is based on the assumption of small background fluctuations (as it's based on some analytical unfolding in moment space). Given the magnitude of the background fluctuations (quantified in chapter 2) that we get in the jet p_T range accessible with ALICE, that may imply that this background subtraction method would only be reliable at high or very high jet p_T (>150 GeV/c) that will only be accessible in the future (in the case of ALICE).

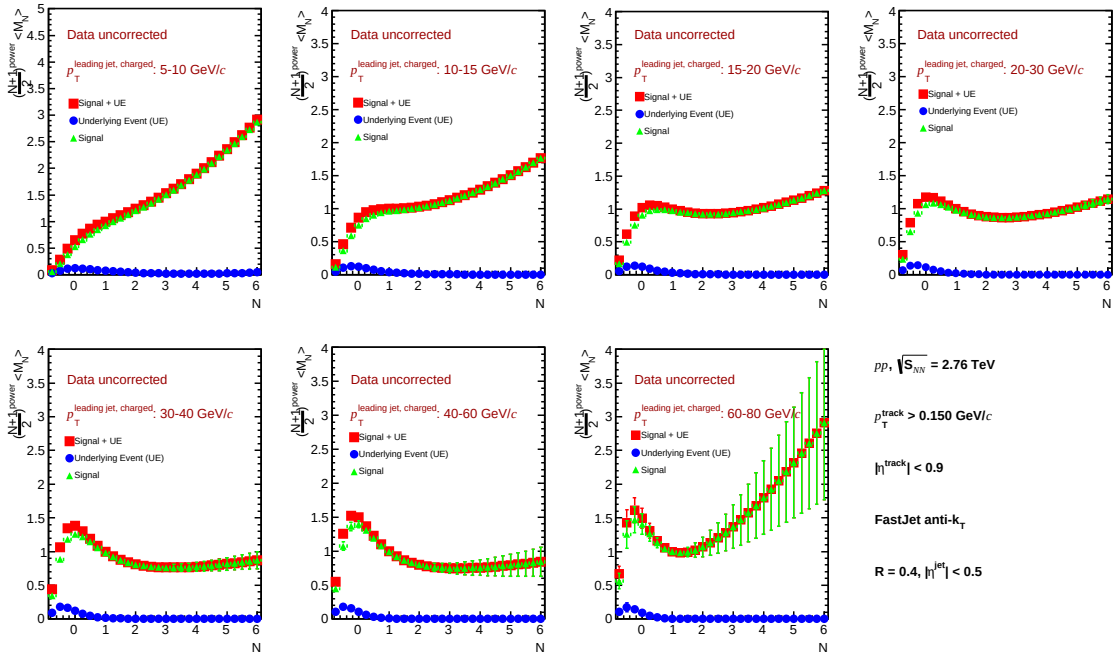

Figure 7.7: Background contribution in fragmentation function momentscalculated using the same way as for fragmentation functions (i.e not using ρ_N).

7.4 MC validation

Before to correct our data, the MC sample has been validated by comparing the reconstructed simulation to our raw results. This is presented in Fig. 7.8 for the seven bins of jet p_T studied. The agreement over the full N range is quite good. The simulation is systematically a bit smaller than the real data. It is mostly better than 5% except in the very low or very high N regions where the discrepancies can reach 10% in some cases. Apart from the very low jet p_T (they should probably be

studied more carrefully independantly), 2 bins of jet p_T (20-30 and 60-80 GeV/c) show differencies between raw and MC larger than 10% especially at large N.

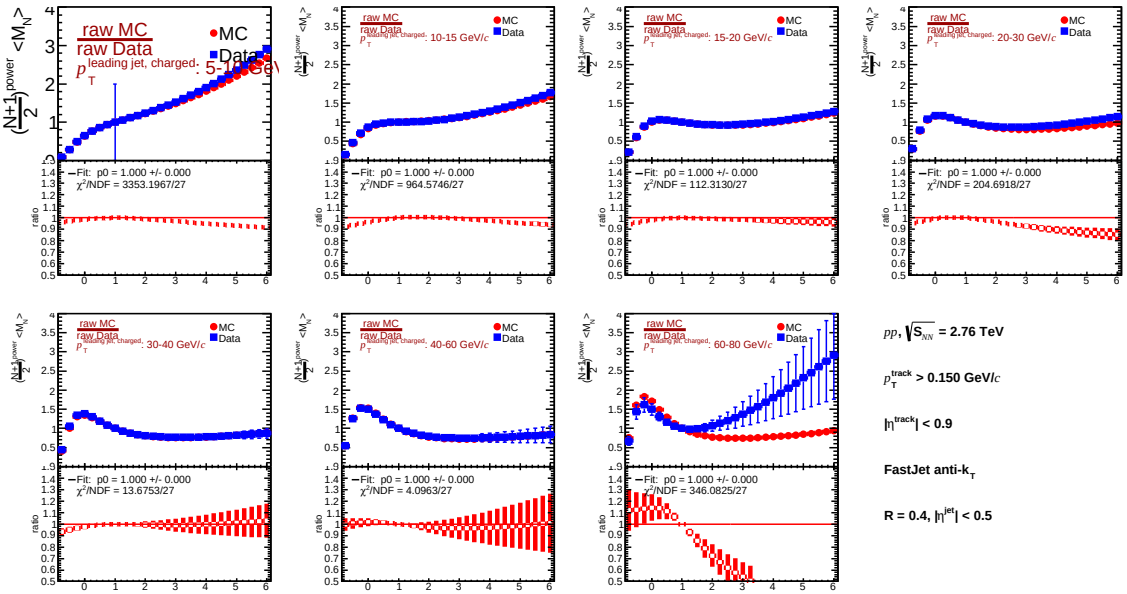

Figure 7.8: FFM comparison between the simulation (circle) and the raw data (square) for seven bins of jet p_T.

The poor statistics achievable in real data for the bin 60-80 GeV/c can explain the differences observed between raw and MC data. However, we don't have specific argument to justify the differences observed in the 20-30 GeV/c bin of jet p_T. We reach 15% of differences at large N.

However, we consider this comparison study good enough to validate the MC sample and to use it for the correction.

7.5 Corrections

The FFM distributions have been corrected exactly the same way as the FF. In this section, we present the correction factors extracted for both the detector effects and the contamination by the secondaries. However, before to do that, we tried to evaluate how the smearing effect at the level of the reconstructed jet p_T compared to the generated one affected the fragmentation function moments.

Feed-in / feed-out

In order to estimate how jet smearing modifies the fragmentation function, we tried to calculate the fragmentation function momentsdistributions for all the reconstructed jets which populate a given jet p_T bin lower or higher than the bin it would have populated as generated jet. In Fig. 7.9, we first tried to count (top right panel) from a sample of 20-40 GeV/c generated jets how many are reconstructed in the corresponding reconstructed jet p_T bins, how many reconstructed jets populate a smaller/larger p_T bin (feed-out). Over the full statistics, we see that we have more than 3 orders of magnitude between reconstructed jets which have been effectively reconstructed in the same p_T range than the generated one and the jets which feeded-in or out of the range. We can conclude that a really small statistics contributed to the feed-in/out of reconstructed jets with respect to generated jets. The different distributions of Fig. 7.9 illustrate of the different types of jet affect the FFM. For the jet reconstructed "out of range", we see that we measure deviation of 4 to 15% but the really low statistics does not really affect the FFM measurement as can be seen in the bottom left (jets for which we have rec region = gen region) and the top middle (the whole jets of the sample) distributions which are comparable. From this study, we concluded that a bin-by-bin correction was application for the correction in our study.

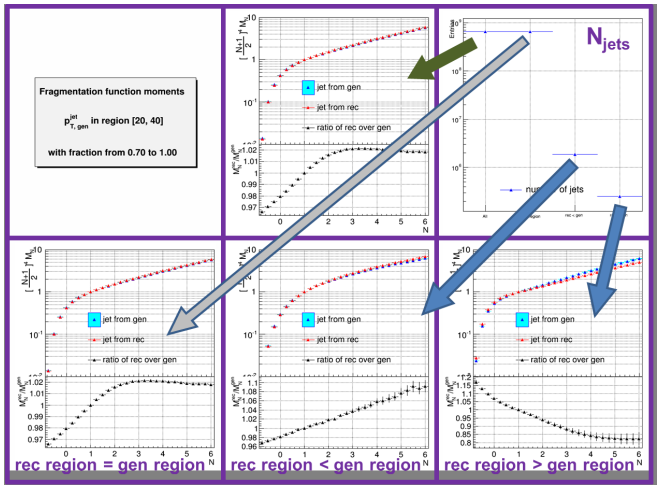

Figure 7.9: For jet pt in [20, 40] GeV/c, the upper middle plot show the overall results of FFM from rec and gen and the ratio of rec/gen which is in 3%. The number of the contribution of the jet from different pt region are showed in the plot upper right. The lower plots from left to right are the corresponding results as the overall from different regions: rec region =- gen region, rec region $<$ gen region, rec region $>$ gen region. The results from different region gives negligible contribution, Bin-by-Bin correction could be applied.

7.5.1 Bin-by-bin correction

The bin-by-bin correction method presented in the previous section has been applied to correct our FFM measurement. The correction factors estimated for 6 jet p_T bins are presented (method 1) in Fig. 7.10.

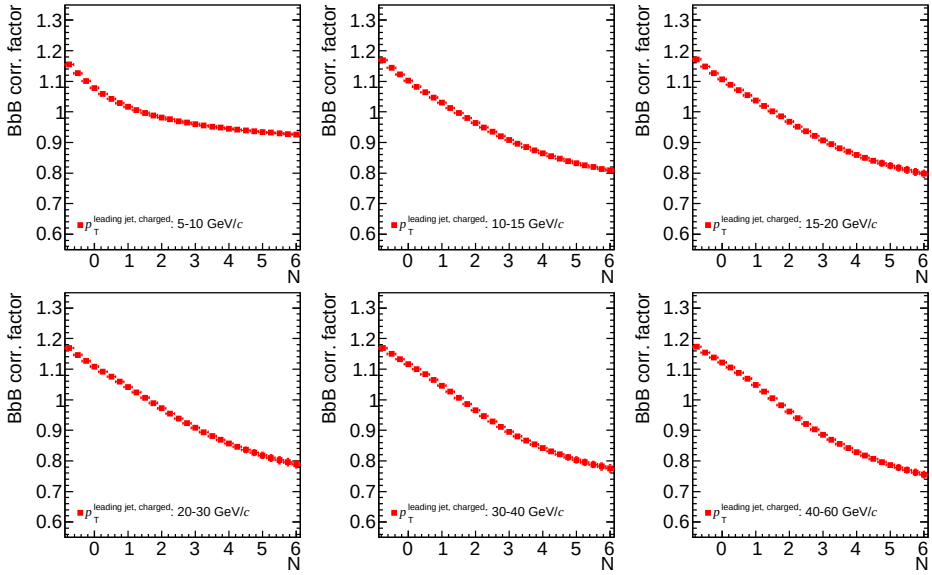

Figure 7.10: Bin-by-bin correction factors obtained for 6 bins of jet p_T and with method1.

7.5.2 Contamination by the secondaries

Just as for the FF, we have extracted the correction factors for the contamination from secondaries. The result is illustrated in Fig. 7.11

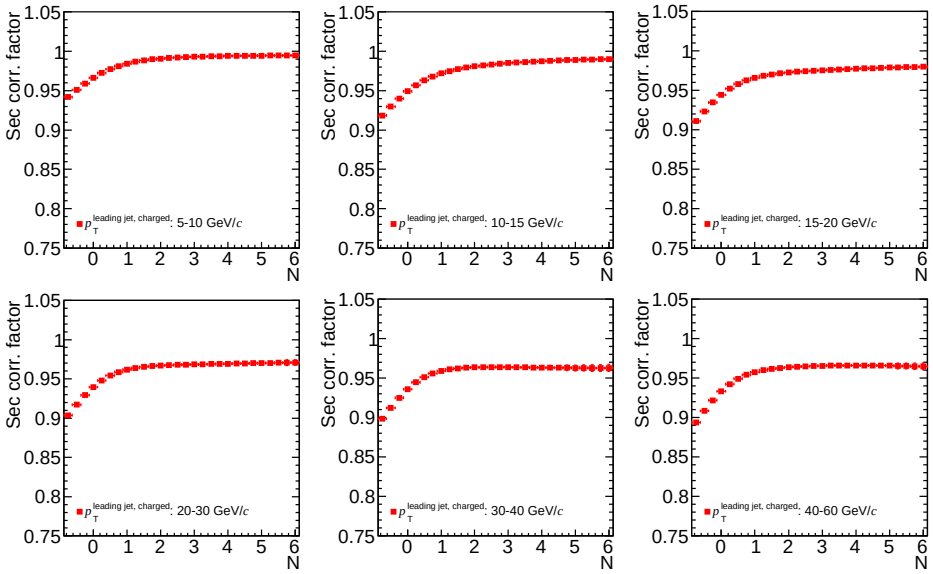

Figure 7.11: Correction factors for secondary contamination obtained for 6 bins of jet p_T with method1.

7.6 Systematic Errors

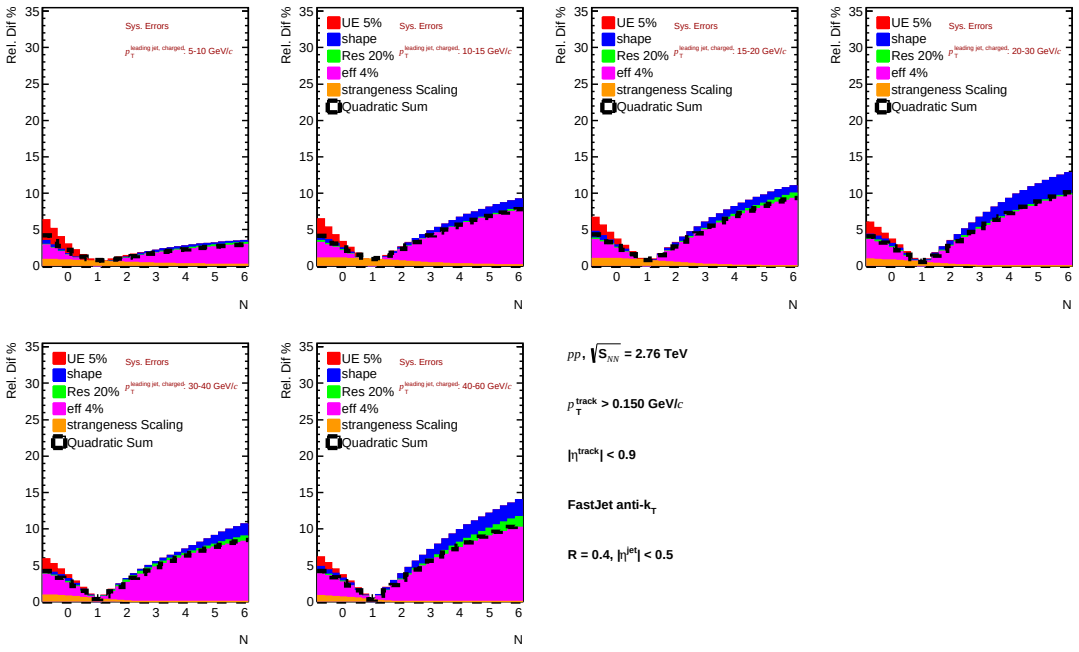

Figure 7.12: Summary of the systematic errors contribution together with their quadratic sum (dashed line)

Before discussing in more details each contribution, we start by showing summary plots (Fig. 7.12) of the relative contributions of the different contributions to the total systematic error.

The same sources (see previous chapter) of systematic errors as for fragmentation functions have been studied for the fragmentation function moments.

As the methods are exactly the same as in the previous chapter, only the corresponding plots for Fragmentation Function Momentswill follow without discussing them again.

7.6.1 Scaling of strange particles

The same study as in the previous chapter has been done for Fragmentation Function Moments. Figures 7.13, illustrates the relative difference (strangeness scaling - no strangeness scaling)/no strangeness scaling for Fragmentation Function Momentsdistributions, for the usual jet p_T bins, reconstructed with R=0.4. The strangeness rescaling implies a slightly larger correction for secondaries. The difference in the corrections is of the order of 1-2%.

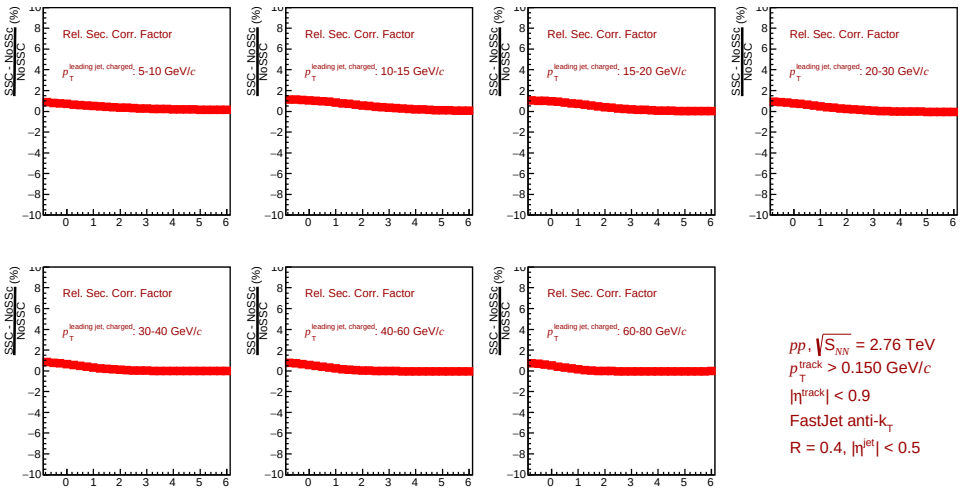

Figure 7.13: Relative difference with and without strangeness rescaling of the correction factors taking into account secondaries contamination as a function of charged jet p_T for FFM (R=0.4).

7.6.2 Systematics on the UE contribution

To estimate the corresponding systematic uncertainty, the UE distribution (obtained using the Perp method) is scaled up or down (by ±5%) and then subtracted

from the the signal distribution.

The corresponding systematics is shown Fig. 7.14 and is $< 2\%$.

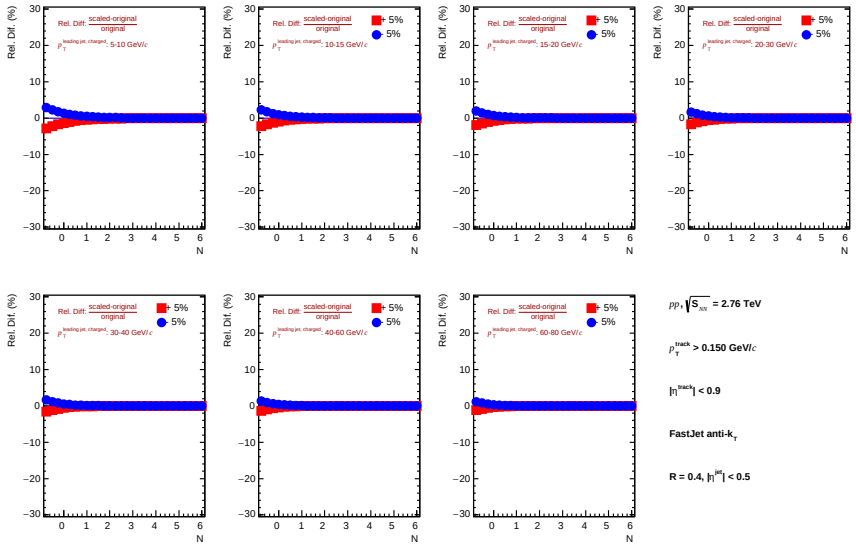

Figure 7.14: Relative difference of the UE variations a for charged jet for Fragmentation Function Moments.

7.6.3 Detector response

As in the previous chapter, the fast and full simulations are in good agreement with the data as shown figure 7.15.

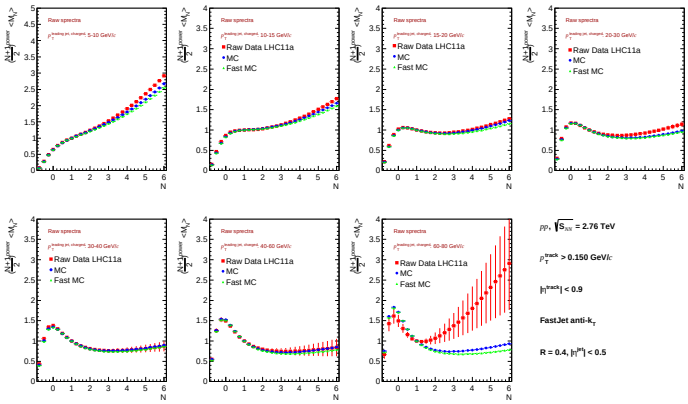

Figure 7.15: Comparison between raw data (LHC11a), fast sim, and full simulation, for Fragmentation Function Moments

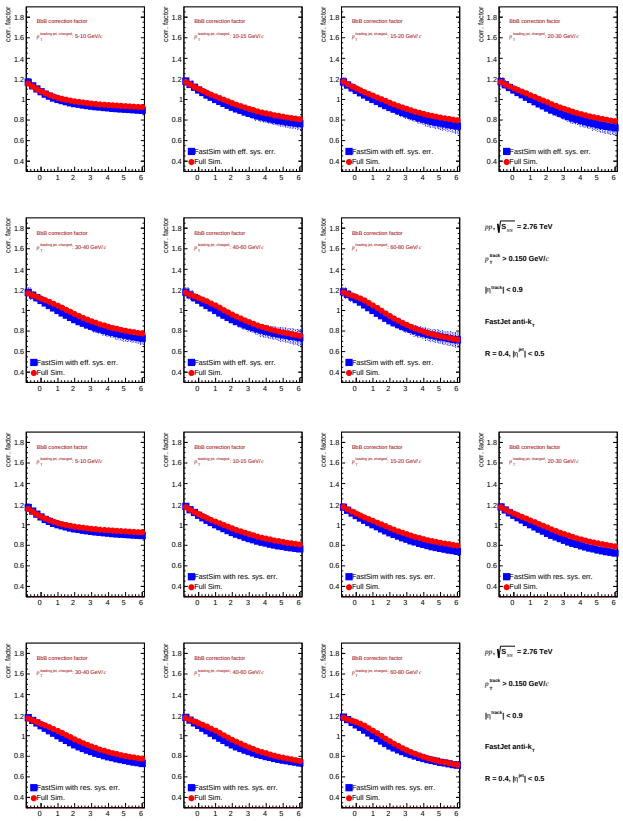

Figure 7.16: Comparison between the bin-by-bin correction factors between full simulation (red) and the fast sim (blue). The shaded bands are showing the effect of the variation of the efficiency (±4%) or resolution (±20%).

As in the previous chapter, the efficiency and resolutions are varied. The comparison of the resulting correction factors are shown figure 7.16. Once again, the variation of the efficiency is the biggest source of systematics (see figure 7.12).

7.6.4 The event generator dependence (or shape dependence)

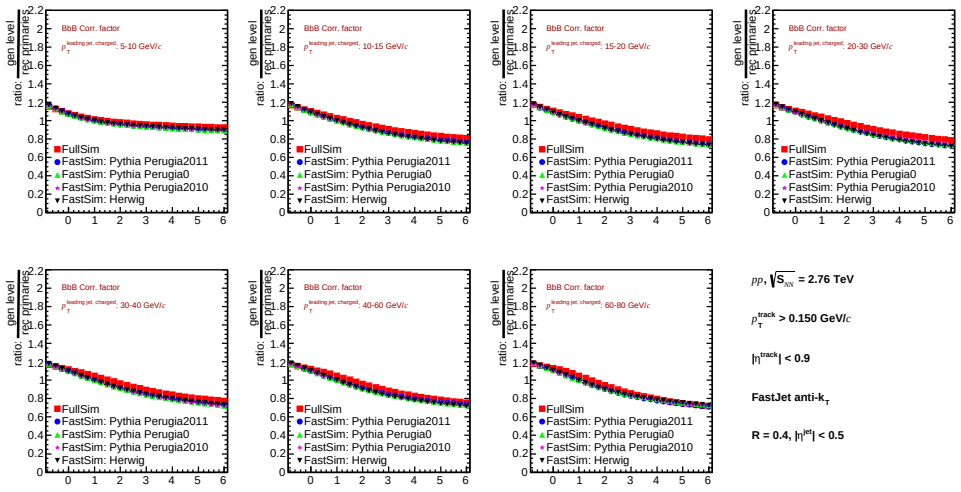

Figure 7.17: Comparison between the bin-by-bin correction factors between full simulation (red) and the fast sim using several event generators

As in the previous chapter, comparisons correction factors obtained using several PYTHIA tunes (Perugia0, 2010, 2011) as well as Herwig are shown figure 7.17, the resulting systematics is shown on figure 7.12.

7.7 Corrected Results and discussion

The Figs. 7.20, 7.21 and 7.22 present the measured of leading charged jet fragmentation function moments (using a scaling power of 2.5 and method 1) reconstructed with a resolution parameter R = 0.2, 0.4 and 0.6. The data have been corrected for detector effects and contamination from secondary particles. On the presented distribution, only statistical error bars are included so far, the systematic errors being under study (see the previous section 7.6). The two set of data studied corresponding to the periods LHC11a and LHC13g Those corrected distributions are shown for six bins in (mini)-jet transverse momentum: 5-10 (inverse triangles), 10-15 (circles), 15-20 (squares), 20-30 (triangles), 30-40 (stars) and 40-60 (crosses) GeV/c. Note that the last 60-80 GeV/c bin has not been included in the final result for lack of statistics. It will probably be in the future when combining the two samples of data. For sake of clarity, let us discuss separately the evolution with jet p_T at a fixed R, and then

the evolution with R.

7.7.1 Dependence with jet p_T

The corrected distribution behave the same what as we described in the case of raw data (see section 7.2. As we already mentioned (when discussing about raw data), the value at N = 0 is proportional to the number of charged particles/tracks in the jet (the number of constituents), which increases with the jet p_{T} increasing, as more fragmentation is expected with higher energy available in the system. In the contrary, above N = 1, an increase of the jet multiplicity with the jet p_T translates into a decrease of the distribution from pure mathematical considerations: more "fragments" are expected with increasing jet p_T, the effect from the higher order of N will make the distribution decrease faster than the increase of the number of constituents.

7.7.2 Dependence with the jet resolution parameter R

he fragmentation function moments have also been systematically studied with respect to the jet resolution parameter R (0.2, O.4 and 0.6). In order to have a clear view of the R dependence (at fixed jet p_T), Fig. 7.18 and Fig. 7.19 can be used.

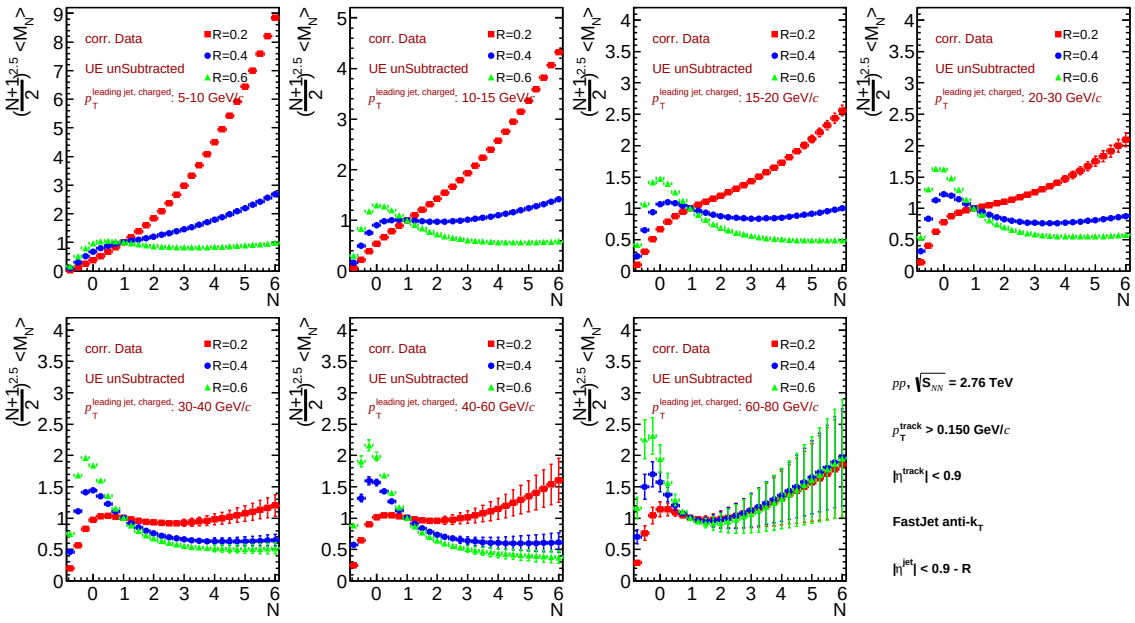

Figure 7.18: Dependence of the fragmentation function moments with the jet resolution parameter R. Three values of R are compared (R=0.2,0.4 and 0.6) in 15-20 (left), 40-60 (middle) and 60-80 GeV/cc jets. The data on these distributions have been corrected and include a treatment of the background which is subtracted.

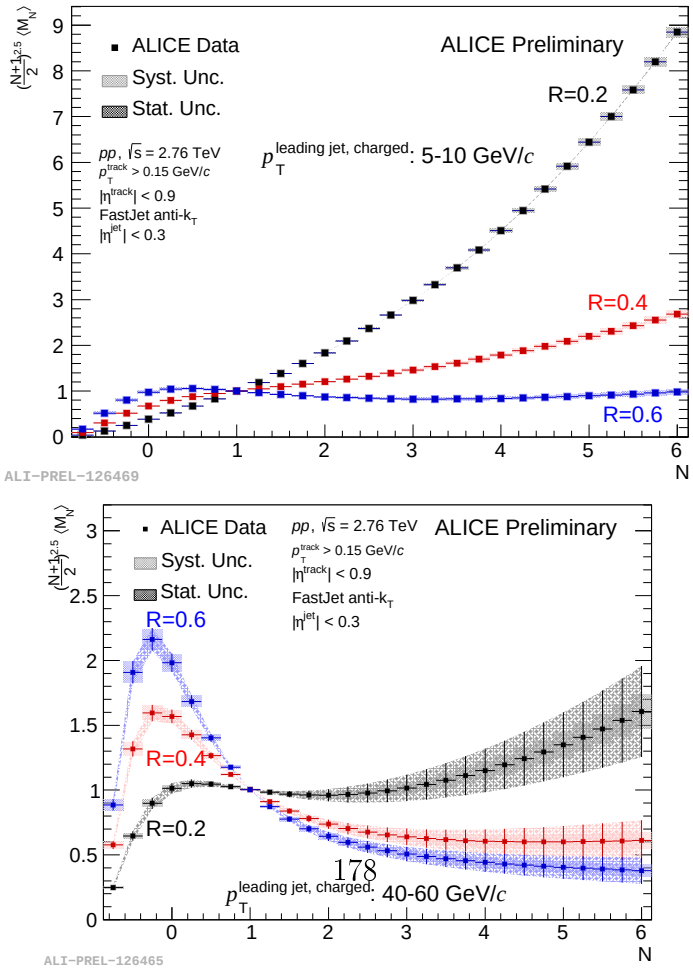

Figure 7.19: fragmentation function moments distributions comparison between $R = 0.2$, $R = 0.4$

We first observe that the smaller R, the smaller the jet multiplicity in the given opening angle (red distribution above the blue and the green ones above N=1). We also observe that the discrepancies between the distributions for different R decrease with the jet p_T increasing suggesting that higher p_T jets are more collimated. Indeed, whatever the opening angle, the multiplicity of the jet does not change much as the three distributions for 60-80 GeV/c jets are close to be on top of each others. Looking at the bin 40-60 GeV/c, we see that it does not change much to open the cone from R=0.4 to R=0.6 to recover the jet constituents.

7.7.3 Comparison with PYTHIA Perugia2011

The results from Figs. 7.23, 7.24 and 7.25 are shown together with the corresponding MC curve (at generator level). Those distributions are in fair agreement with the data. The ratio Data/MC obtained are shown in Fig. 7.26, 7.27 and 7.28 for the 6 bins of jet p_T studied. Both data and MC have not been subtracted for the UE contribution. We observe that depending R, jet p_T and value of N, the deviation varies from less than 2% to as much as about 15% (withing uncertainties).

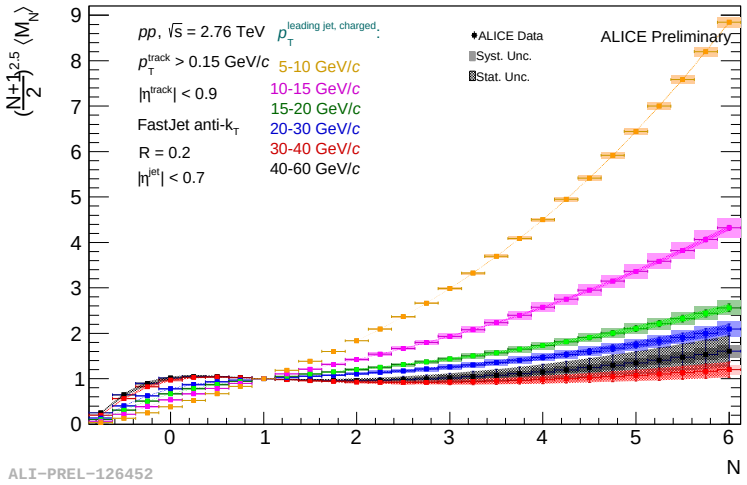

Figure 7.20: Corrected fragmentation function moments distribution for $R = 0.2$ for 6 jet p_T bins (LHC11a). The systematic uncertenties are shown using boxes. A color band is used to indicate that the stat errors are correlated.

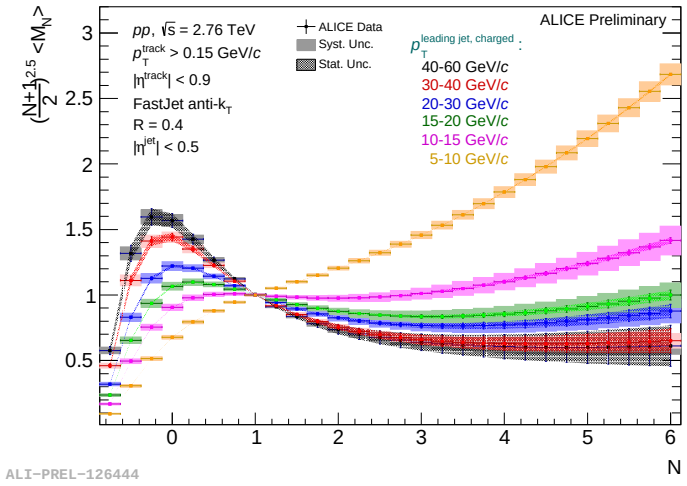

Figure 7.21: Corrected fragmentation function moments distribution for $R = 0.4$ for 6 jet p_T bins (LHC11a). The systematic uncertenties are shown using boxes. A color band is used to indicate that the stat errors are correlated.

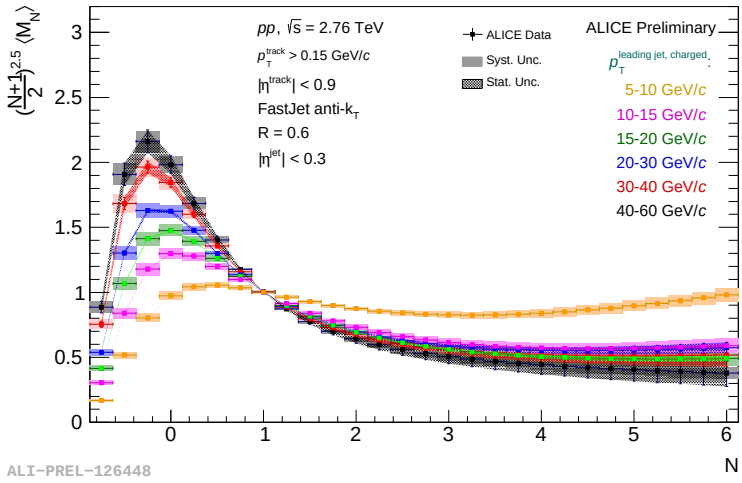

Figure 7.22: Corrected fragmentation function moments distribution for $R = 0.6$ for 6 jet p_T bins (LHC11a). The systematic uncertenties are shown using boxes. A color band is used to indicate that the stat errors are correlated.

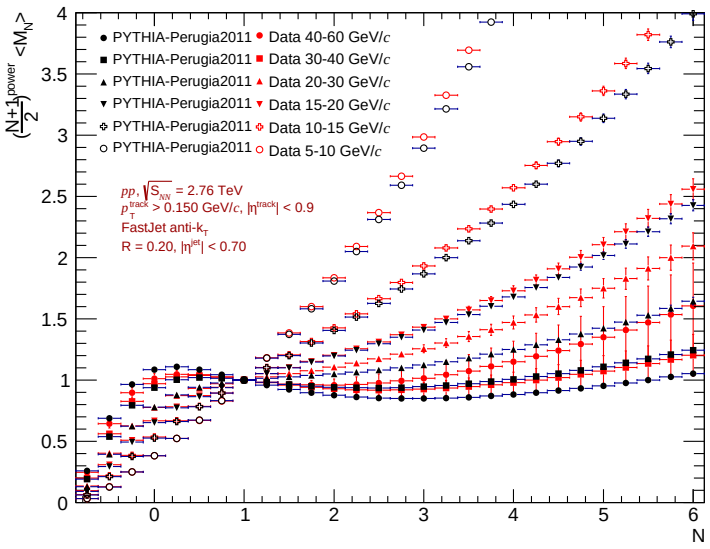

Figure 7.23: Corrected FFM obtained with jet resolution parameter R = 0.2. (compared to PYTHIA Perugia2011).

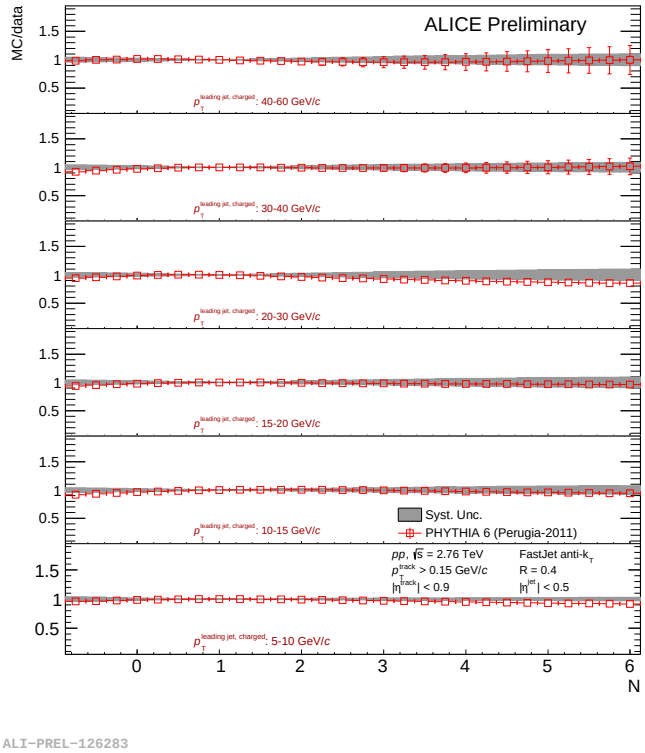

Figure 7.27: Ratio of simulations to data of the fragmentation function momentsdistributions for a jet resolution parameter R = 0.4. The UE contributions are not subtracted from data or simulations.

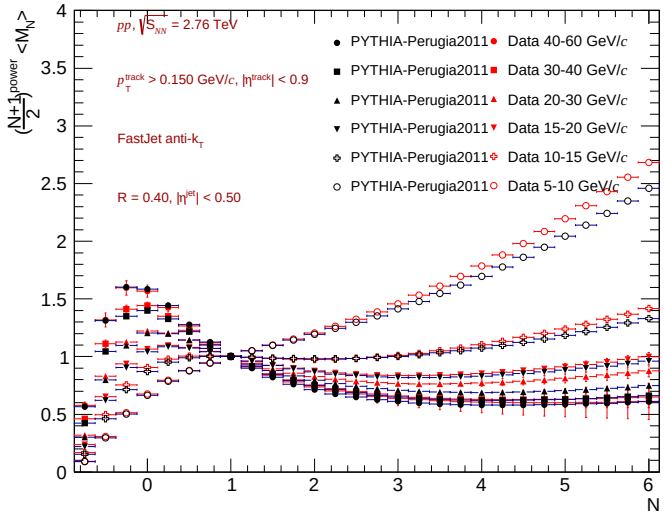

Figure 7.24: Corrected FFM obtained with jet resolution parameter R = 0.4 (compared to PYTHIA Perugia2011).

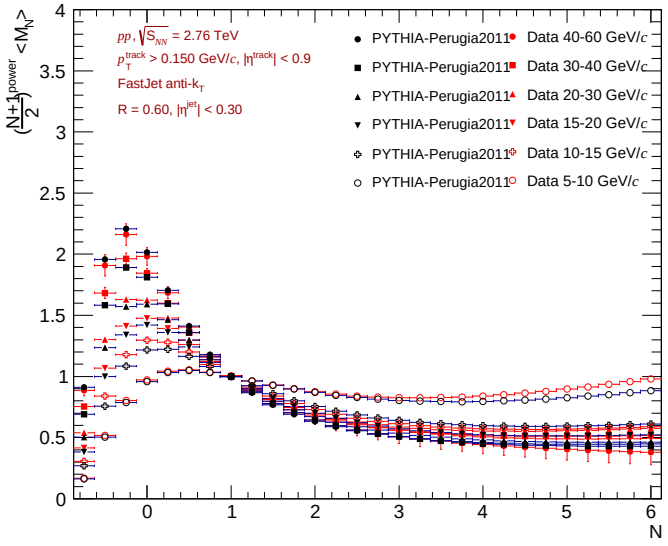

Figure 7.25: Corrected FFM obtained with jet resolution parameter R = 0.6 (compared to PYTHIA Perugia2011).

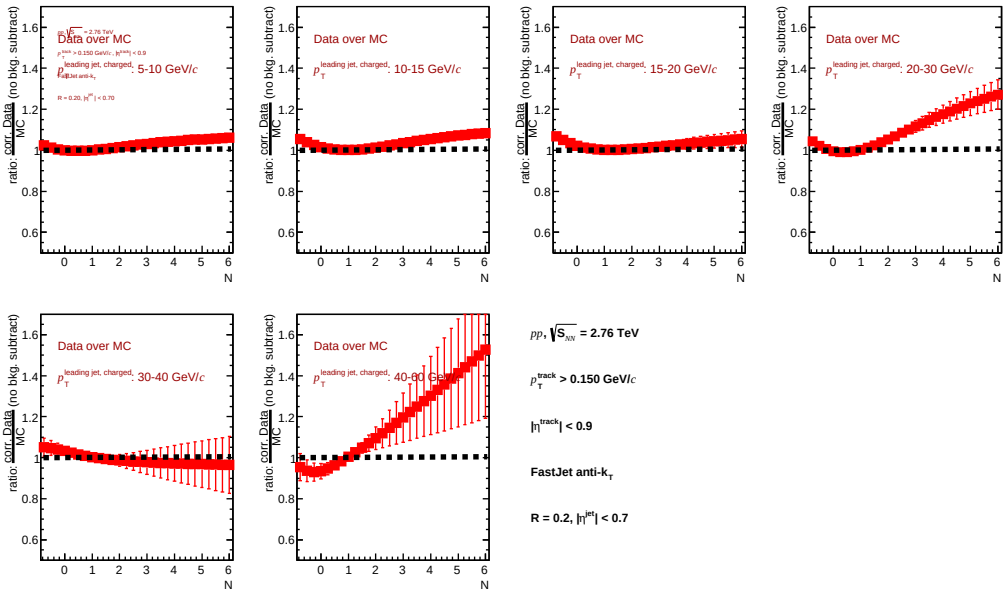

Figure 7.26: Ratio of simulations to data of the fragmentation function momentsdistributions for a jet resolution parameter R = 0.2. The UE contributions are not subtracted from data or simulations.

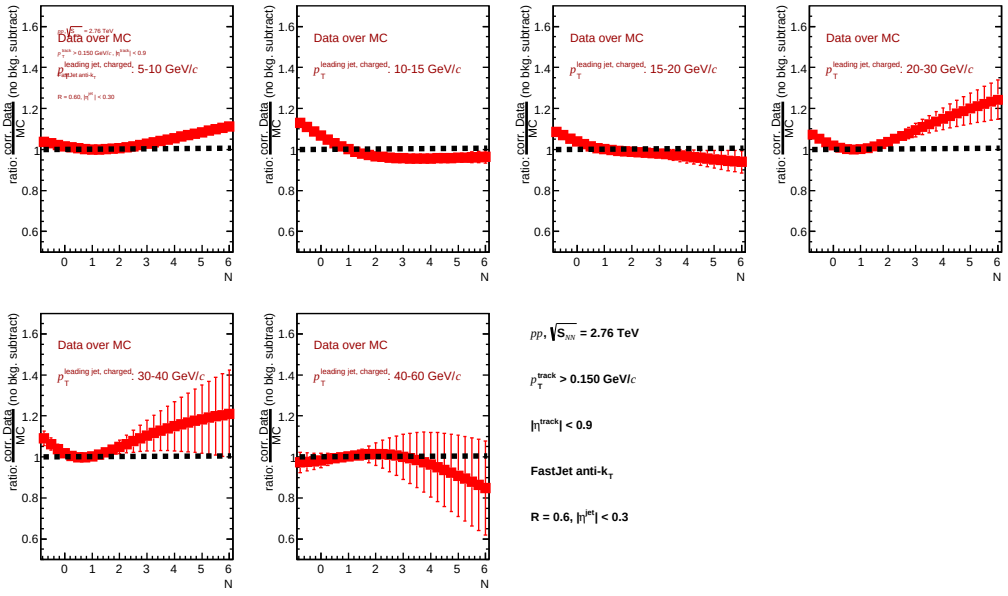

Figure 7.28: Ratio of simulations to data of the fragmentation function momentsdistributions for jet resolution parameter R = 0.6 The UE contributions are not subtracted from data or simulations.

Summary

In this thesis we started by giving a general physics introduction. We breifly introduced the basics of QCD and of the standard model before focussing more on the "phase transition" of nuclear matter. We saw that a cross-over between ordinary nuclear matter and a state of deconfined quarks and gluons, the Quark Gluon Plasma (QGP), is predicted by lattice QCD calculations at low chemical potential and high temperature in the nuclear phase diagram. We also introduced how ultra-relativistic heavy ion collisions are used to produce and to study the hot and dense QGP medium. We finished by describing a few aspects of experimental heavy ion physics.

In chapter two, dedicated to several aspects of jet physics, we started by introducing jet production in binary nucleon-nucleon collisions. After discussing how a jet can be theoretically defined, we saw how the jet production cross section can by prediced by pQCD calculations using the factorisation theorem and we defined the so called underlying event (UE). We then moved to the experiemntal definitions of a jet and to the measurment of its cross-section (which is in good agreement with NLO pQCD) before foccusing on reviewing jet measurements with the ALICE detector. After defining the two types of jets "charged" and "full" that are used in ALICE, we discussed about the contamination caused by the jet background in both pp and A-A collisions where it is one of the main experimental difficulties for measuring jets. In both cases we explained how the background contribution could be quantified and then subtracted. We saw that A-A collisions suffer from a very big background affected by large event-by-event fluctuations and we reviewed how those fluctuations have been quantified by the ALICE collaboration. We then discussed about the jet nuclear modification factors. We saw that in p-A collision, the jet R_{pA} is found to be consistant with binary scaling indicating that cold nuclear effects at LHC are very small (if not null) compared what was measured at lower energies at RHIC. Jets are strongly suppressed in Pb-Pb collisions. However, jet R_{AA} measurements sufer from several experimental biases (such as leading track p_T cut, which

biases the jet fragmentation, out-of-cone fuctuations and surface biases) which prevent to give a direct physics interpretation of the suppression. We then presented the measurements of "recoil-jets" and we saw that this observable can be seen as a "solution" to background effects, allowing to measure jets with larger resolution parameters. Finally we finished by introducing and by motivating the main topic of this thesis: the measurement of jet fragmentation functions (our measurment is presented chapter 6), which are also affected by the large and fluctuating heavy ion background in A-A colisions. For this reason, the study of fragmentation function moments has been proposed as a way to overcome this limitation. We also performed the measurment of this observable in pp collisions with ALICE. This work is presented in chapter 7.

In chapter 3, we first introduced the LHC. We presented the pp beam characteristics togeather with how its luminosity is defined. We also took the exemple of the ALICE case during run I to discuss the LHC running conditions. We then presented its main experiments focussing on their main physics goals related to heavy ion physics. ATLAS and CMS were introduced before to focuss mainely on ALICE. Its experimental apparatus (different sub-systems) was presented. We then focussed mainly on the detectors that are used for event and centrality selections as well as the ones used for our jet studies. The main ones being the ITS which provides a precise event vertex and tracking togeather with the TPC. They allows to precisely measure jets using charged tracks down to very low momenta (150 MeV/c). Adding the electro-magnetic calorimeters EMCAL, DCAL and PHOS allows to measure "full jets", and to trigger on them. For Run II an evaluation of the jet background density using their combined trigger system is currently under study.

The chapter 4 is dedicated to the ALICE electro-magnetic calorimeters EMCAL and its extension DCAL. After reviewing the basic principles of electromagnetic calorimeters, we presented the structure, readout and triggering system, as well as the performences of EMCAL. We then presented the offline implementaton of its geometry in the ALICE offline framework ALIROOT. We then introduced DCAL. Based on the EMCAL geometry, we discussed how we modified it and how we implemented 3 versions of the geometry of the new DCAL calorimeter. Our Strategy as well as the steps that we followed to create those geometries (as well as to update all other related classes) were extensively described. After presenting the geometries that we implemented we presented the steps we followed in order to validate and to test our work. We first made some reconstruction tests to verify that the response of EMCAL and DCAL were consistant at all levels (hits, sdigits, digits, cells, and

clusters). After that, we checked the behaviour of the clusterizer on the inner eges of DCal (close to PHOS) and confirmed that it was behaving as expected. To check and compare the performences of EMCAL and DCAL we also studied their respective energy resolution. After finishing those tests (needed to validate our implementation), we also compared (real data or simulation) results obtained with our updated code to the same results (same data or simulation) produced using the original EMCAL code (before our modifications), in order to make sure that our modifications did not break backward compatibility with existing EMCAL data and simulations. Once this was successful, the code was finally committed in AliRoot. This work has also been validated as a service task for the ALICE collaboration. Such service works are now mandatory for all PhD students in the collaboration. The resulting code is now used for all simulation or real data reconstruction using EMCAL/DCAL in ALICE. At the end of the chapter we presented the first results obtained using DCal showing its performences in data. Those results are promising for the futur. EMCAL, DCAL and PHOS will be used for photon, elecron, jet (and their correlations) physics measurments in the comming years.

In chapter 5, the different tools software tools that we used for our physics analyses were presented (ROOT, ALIROOT, Pythia, Geant as well as the ALICE analysis framework and the Grid tools). After that, we focussed on presenting the dataset and the corresponding (trigger, event vertex, track, jet) selections that we used for our analyses. We then breifely presented some QA distributions for both tracks and jets in order to show that the quality of the data, as well as the one of the Monte-Carlo simulation, that we used to correct the data, togeather with the selections that we made are good and/or under control. We finished by comparing the various distributions (at the event, track as well as jet level) obtained from real data compared to the corresponding MC distributions. This confirmed that our full MC simulation could be used to correct our measurements.

In chapter 6, we presented our measurement of charged jet Fragmentation Functions in pp collision at $\sqrt{s} = 2.76$ TeV with ALICE. After presenting our analysis strategy, we introduced the tools that we developped, optimized and then used for our analysis. We then showed the raw data distributions for both "signal" and backgroud before discussing how we subtracted the UE. After that we showed how our MC simulation was validated and then we focussed on the correction procedure that we developped and followed: Our data were corrected by applying several correction factors (bin-by-bin, secondary particle corrections as well as UE subraction). After presenting and defining each of those correction factors we discussed

their effect. After that we presented the different sources of systematic uncertenties associated to our measurement. We finished by presenting our results which were compared to Pythia Perugia-2011 distributions. We obtained fully corrected and UE subtracted distributions for 5 variables (jet constituent p_T, z, ξ, j_T and $\Delta\theta$) for 3 jet radii (R=0.2, R=0.4 and R=0.6). Those distributions have been studied in 6 (mini)-jet p_T bins (from 5-10 GeV/c up to 40-60 GeV/c) using about 40M event from LHC11a and LHC13g datasets. Our results are in good agreement with expectations for QCD angular ordering as well as with Pythia Perugia-2011 and with previous ALICE results at 7 TeV.

The last chapter of this thesis is dedicated to our measurement of charged jet Fragmentation Function Moments in pp collision at $\sqrt{s} = 2.76$ TeV with ALICE. The chapter is organised in the same way as the previous one. After introducing this new observable, a study of one of its parameter (the scaling power α) is presented. The correction strategy that we applied is the same as the one we used for our FF measurement. We obtained fully corrected jet Fragmentation Function moments distributions for 3 jet radii (R=0.2, R=0.4 and R=0.6). Those distributions have been studied in 6 (mini)-jet p_T bins (from 5-10 GeV/c up to 40-60 GeV/c) using about 40M event from LHC11a and LHC13g datasets. Our results (first experimental study of jet Fragmentation Function Moment distributions) are in fair agreament with Pythia Perugia-2011.

Our study of jet Fragmentation Function Moments has shown that this observable could be measured in pp collisions with ALICE. It can also be seen as a first step for a futur study of jet Fragmentation Function moments in A-A collisions. At this occasion, the proposed improved background subtraction method will be tested experimentally.

Our work on the DCal callorimeter will also allow futur measurements of electrons, photons as well as jet observables (togeather with their corelations) in the comming years.

Appendix A

Additional summary plots

In this appendix, additional results are shown All results are shown in 6 different jet p_{T} bins: [5,10], [10-15], [15-20], [20-30], [30-40] and [40-60] (GeV/c).

A.1 Fragmentation Functions: R comparisons

The following figures (A.1 to A.9) show comparsons between LHC11a data and Pythia Perugia 2011.

A.1.1 Charged particle p_T spectra dN/dp_T in leading jets

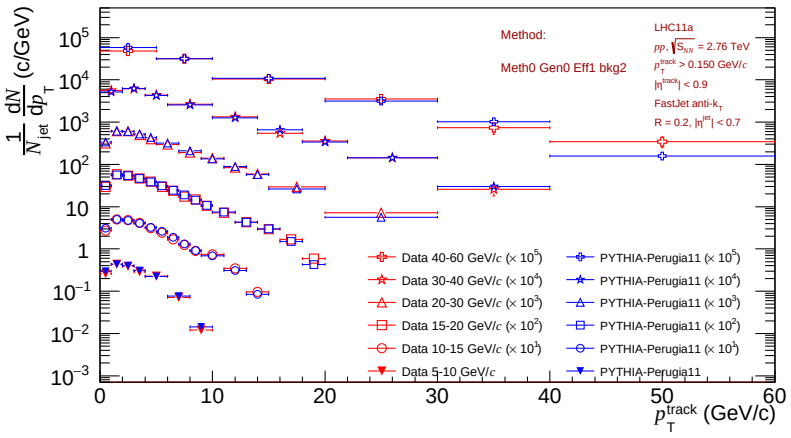

Figure A.1: Charged particle p_T spectra dN/dp_T in leading jets ($R = 0.2$) for 6 jet p_T bins (LHC11a) compared to Pythia Perugia2011. The UE contribution is subtracted.

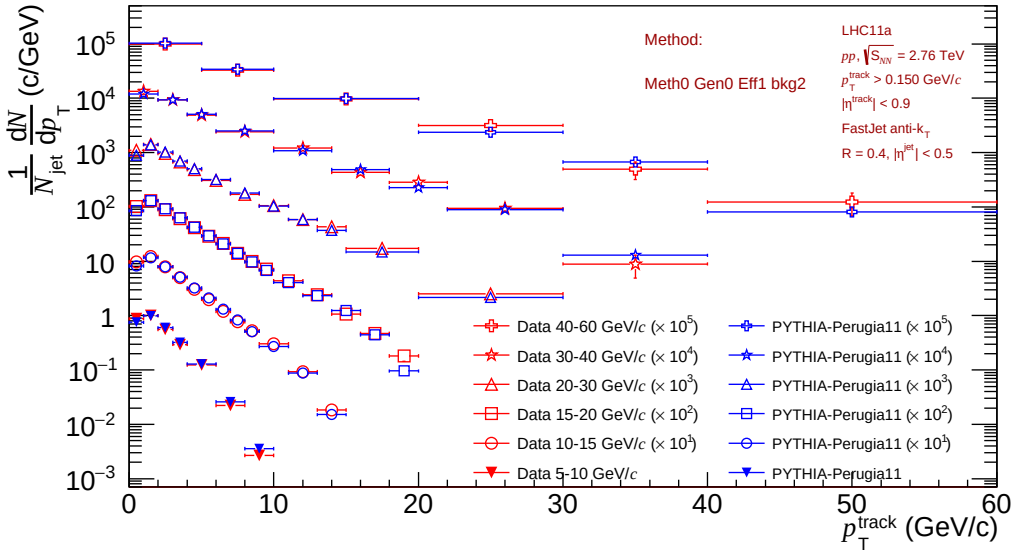

Figure A.2: Charged particle p_T spectra dN/dp_T in leading jets of ($R = 0.4$) for 6 jet p_T bins (LHC11a) compared to Pythia Perugia2011. The UE contribution is subtracted.

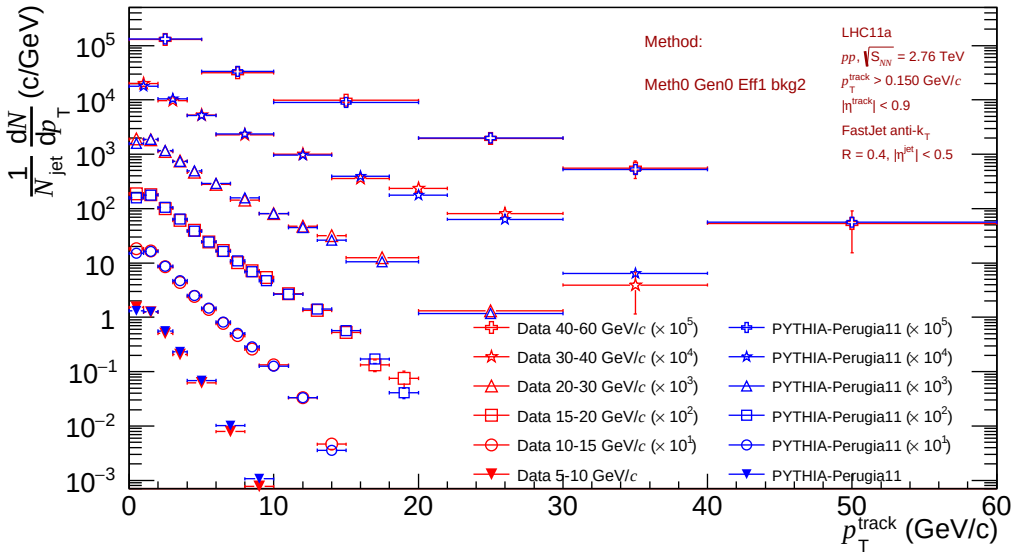

Figure A.3: Charged particle p_T spectra dN/dp_T in leading jets ($R = 0.6$) for 6 jet p_T bins (LHC11a) compared to Pythia Perugia2011. The UE contribution is subtracted.

A.1.2 ξ

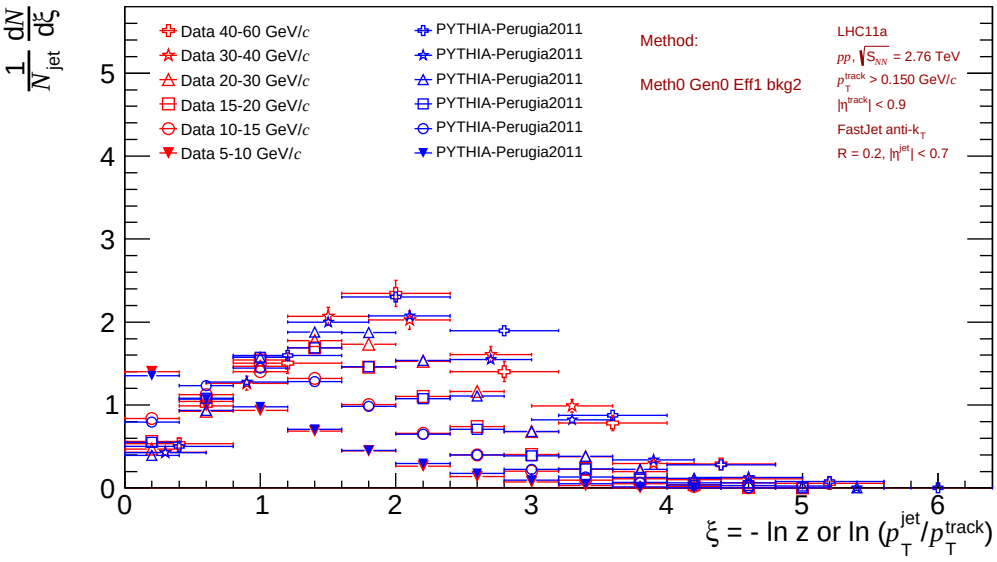

Figure A.4: Charged particle ξ spectra $dN/d\xi$ in leading jets ($R = 0.2$) for 6 jet p_T bins (LHC11a) compared to Pythia Perugia2011. The UE contribution is subtracted.

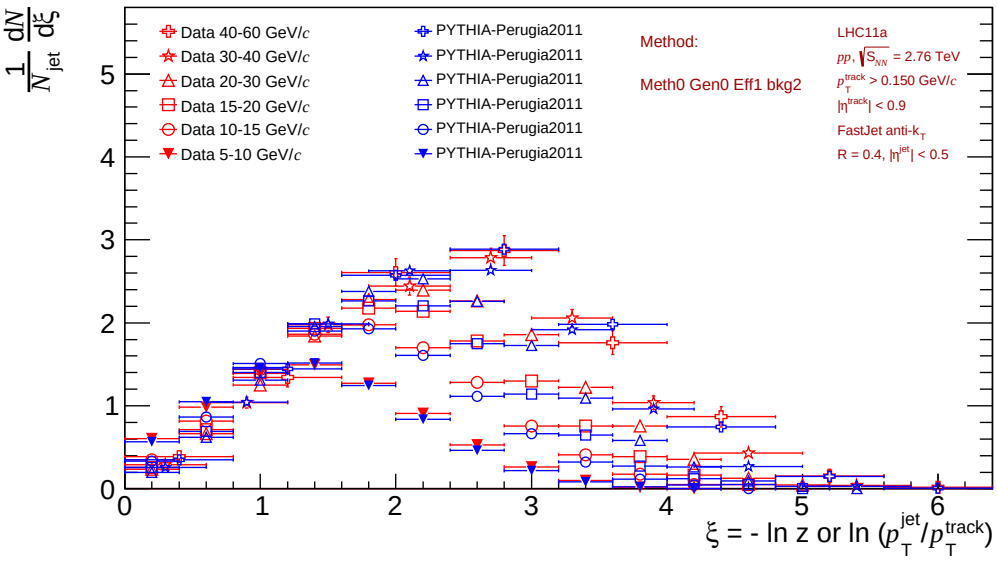

Figure A.5: Charged particle ξ spectra $dN/d\xi$ in leading jets ($R = 0.4$) for 6 jet p_T bins (LHC11a) compared to Pythia Perugia2011. The UE contribution is subtracted.

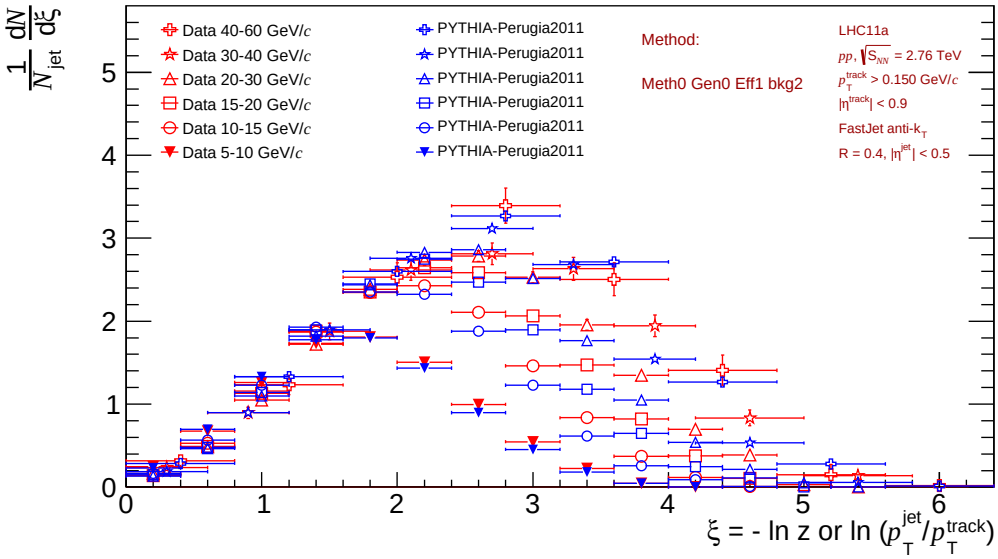

Figure A.6: Charged particle ξ spectra $dN/d\xi$ in leading jets ($R = 0.6$) for 6 jet p_T bins (LHC11a) compared to Pythia Perugia2011. The UE contribution is subtracted.

A.1.3 z

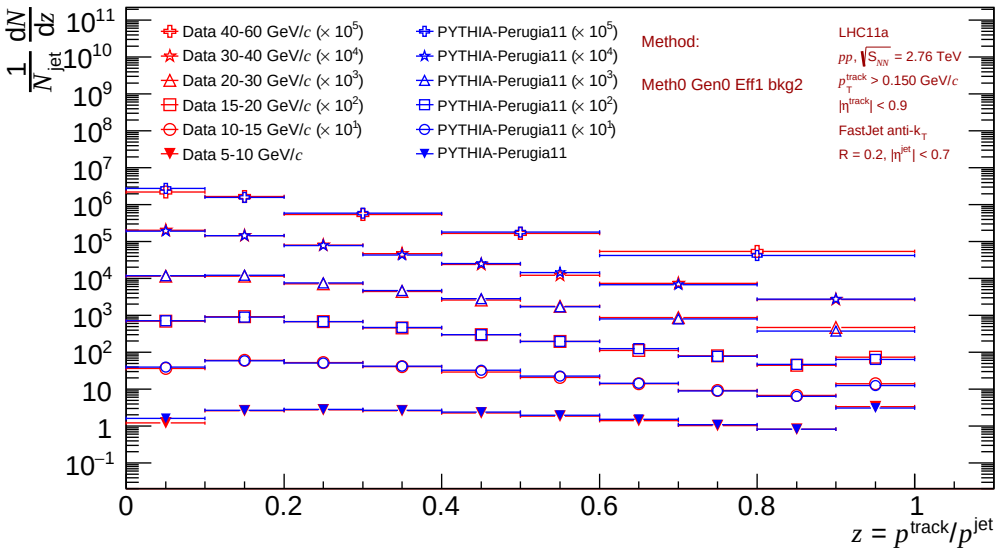

Figure A.7: Charged particle z spectra dN/dz in leading jets ($R = 0.2$) for 6 jet p_T bins (LHC11a) compared to Pythia Perugia2011. The UE contribution is subtracted.

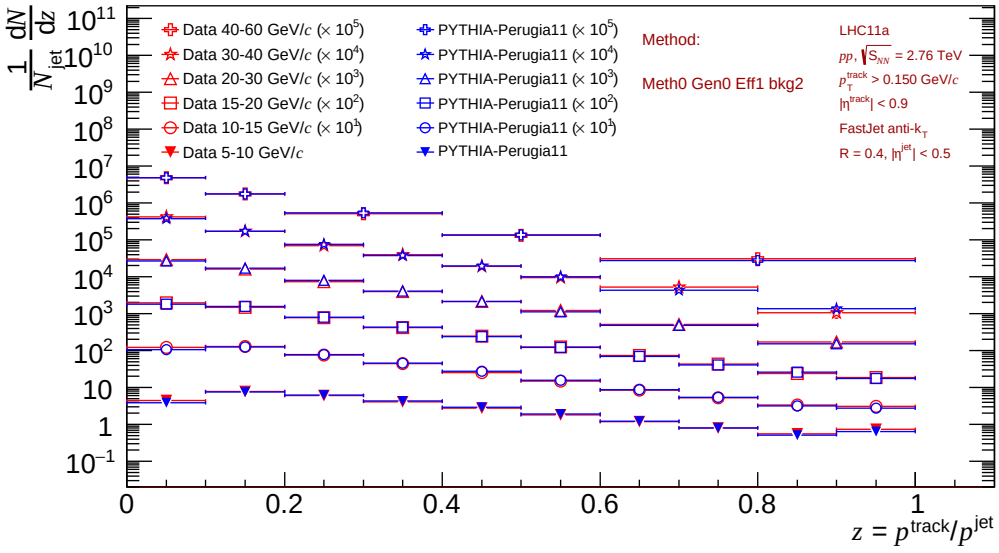

Figure A.8: Charged particle z spectra dN/dz in leading jets ($R = 0.2$) for 6 jet p_T bins (LHC11a) compared to Pythia Perugia2011. The UE contribution is subtracted.

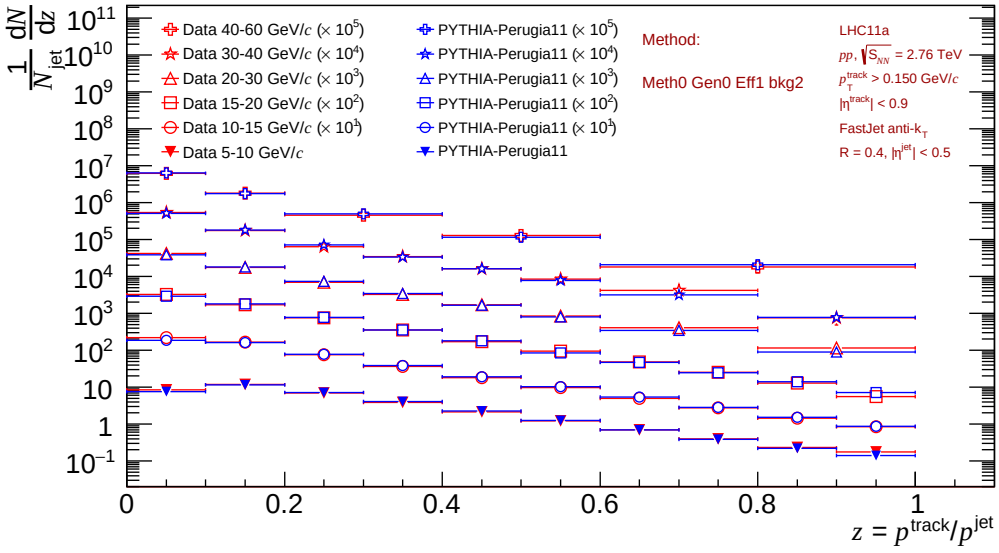

Figure A.9: Charged particle z spectra dN/dz in leading jets of $R = 0.6$ in leading jets ($R = 0.2$) for 6 jet p_T bins (LHC11a) compared to Pythia Perugia2011. The UE contribution is subtracted.

A.2 Fragmentation Function Moments scale power comparison

In this sections results (LHC11a, compared to Pythia Perugia2011) are commpared for two values of the scelling power. The standard value that we chose (2.5) is compared to $\alpha = 2$.

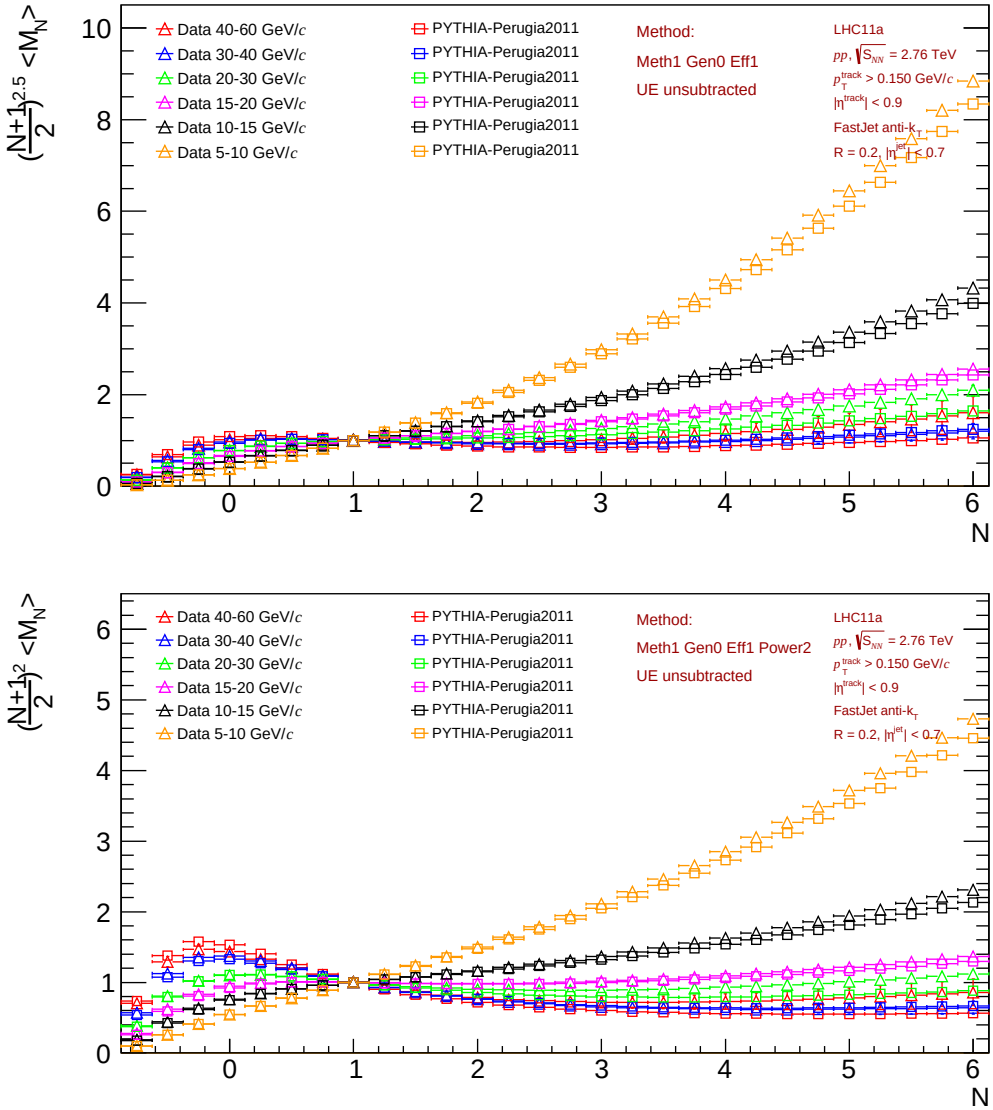

Figure A.10: fragmentation function moments distribution using $R = 0.2$ for 6 jet p_T bins (LHC11a) compared to Pythia Perugia2011. The UE contribution have not been subtracted. The upper figure $alpha = 2.5$, lower figure is using $alpha = 2$.

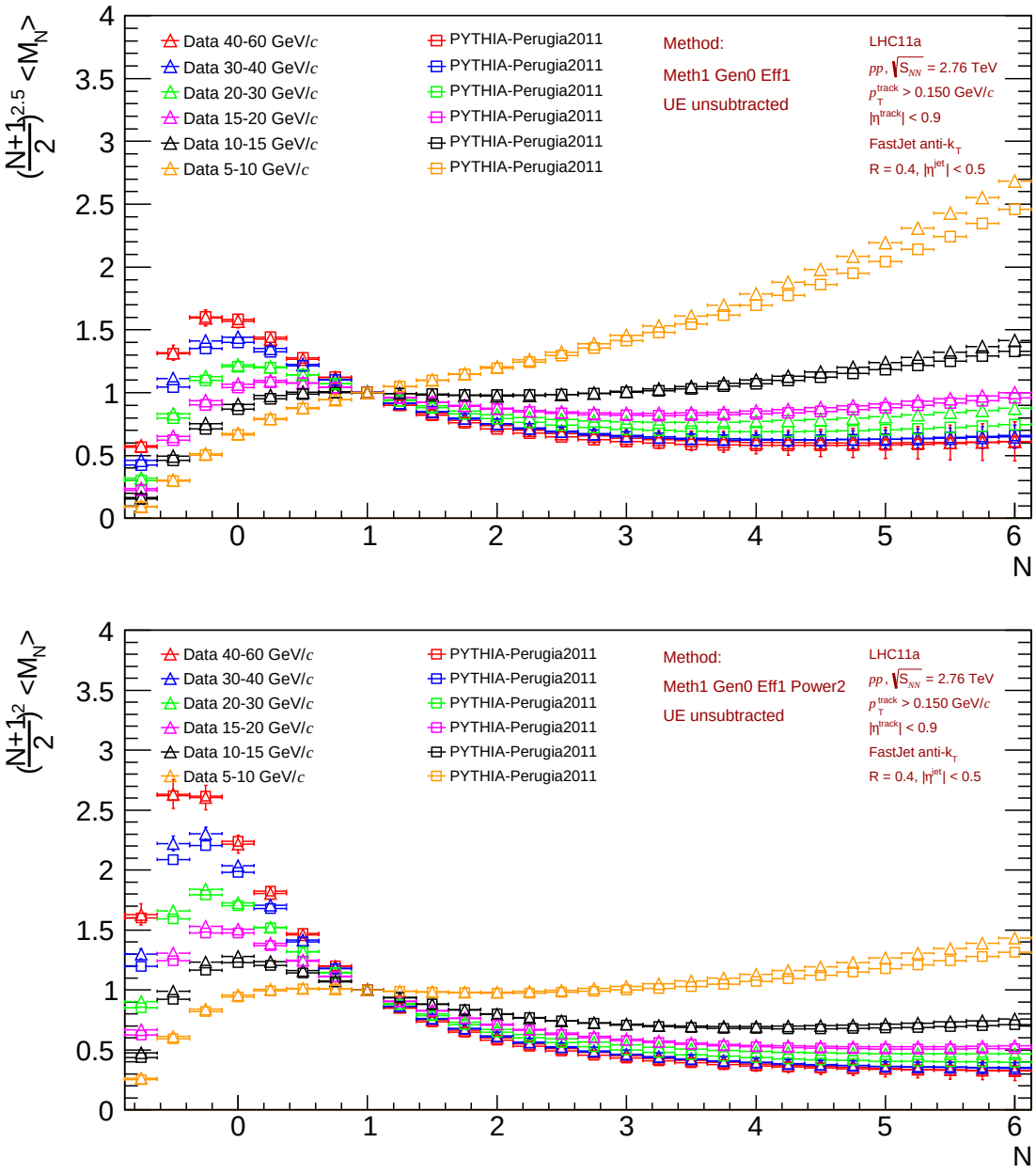

Figure A.11: fragmentation function moments distribution using $R = 0.4$ for 6 jet p_T bins (LHC11a) compared to Pythia Perugia2011. The UE contribution have not been subtracted. The upper figure $alpha = 2.5$, lower figure is using $alpha = 2$.

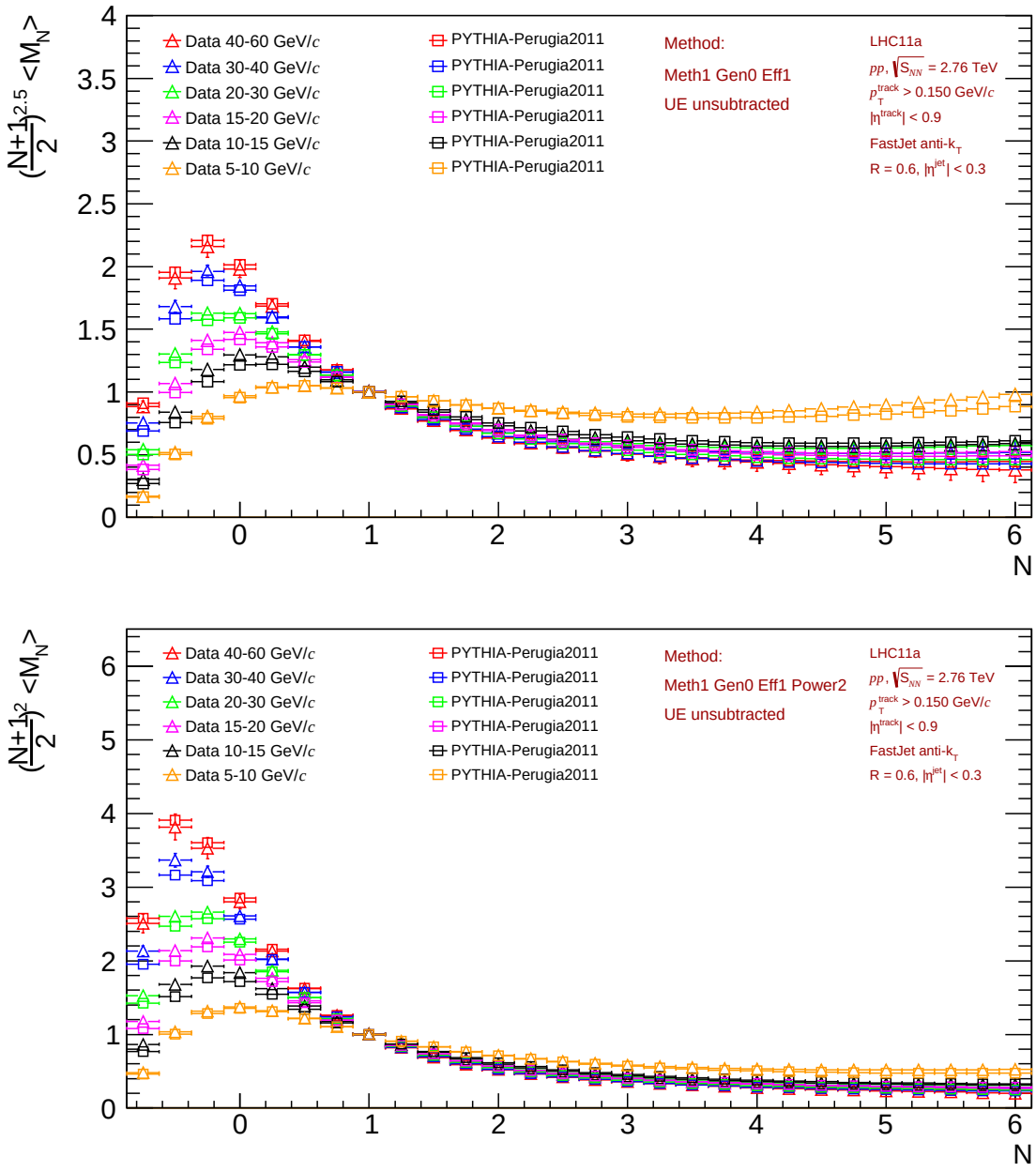

Figure A.12: fragmentation function moments distribution using $R = 0.6$ for 6 jet p_T bins (LHC11a) compared to Pythia Perugia2011. The UE contribution have not been subtracted. The upper figure $alpha = 2.5$, lower figure is using $alpha = 2$.

A.3 Preliminary plots

A.3.1 Fragmentation Function Moments

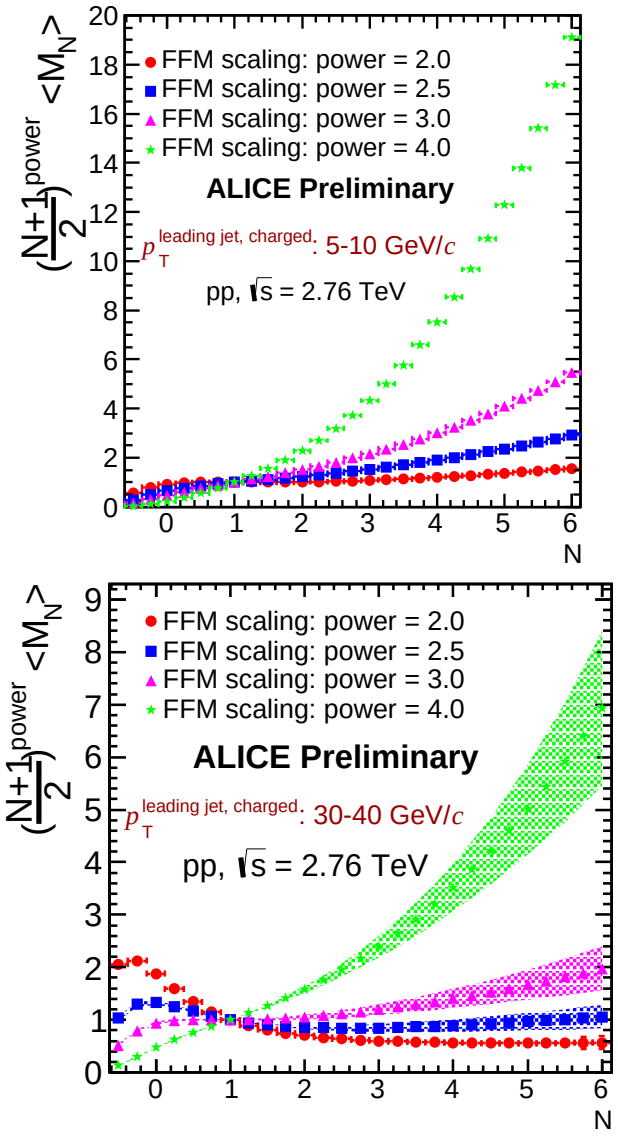

Figure A.13: Comparison of scaling power α for fragmentation function moments in real data for two jet p_T bins: 5-10 GeV/c (left) and 30-40 GeV/c (right). Four α values are compared: $\alpha = 2$ (dot), 2.5 (square), 3 (triangle) and 4 (star).

Bibliography

[1] M. Cacciari, P. Quiroga-Arias, G. P. Salam, and G. Soyez, "Jet Fragmentation Function Moments in Heavy Ion Collisions," *Eur. Phys. J.*, vol. C73, no. 3, p. 2319, 2013.

[2] J. Beringer *et al.*, "Review of Particle Physics (RPP)," *Phys. Rev.*, vol. D86, p. 010001, 2012.

[3] K. Aamodt *et al.*, "Elliptic flow of charged particles in Pb-Pb collisions at 2.76 TeV," *Phys. Rev. Lett.*, vol. 105, p. 252302, 2010.

[4] D. Acosta *et al.*, "Momentum distribution of charged particles in jets in dijet events in $p\bar{p}$ collisions at $\sqrt{s} = 1.8$ TeV and comparisons to perturbative QCD predictions," *Phys. Rev.*, vol. D68, p. 012003, 2003.

[5] B. B. Abelev *et al.*, "Charged jet cross sections and properties in proton-proton collisions at $\sqrt{s} = 7$ TeV," *Phys. Rev.*, vol. D91, no. 11, p. 112012, 2015.

[6] D. G. d'Enterria, "Forward Physics at the LHC," in *Proceedings, 15th International Workshop on Deep-inelastic scattering and related subjects (DIS 2007). Vol. 1 and 2: Munich, Germany, April 16-20, 2007*, pp. 1141–1152, 2007.

[7] P. G. Kuijer, "Commissioning and Prospects for Early Physics with ALICE," *Nucl. Phys.*, vol. A830, pp. 81C–88C, 2009.

[8] P. Cortese *et al.*, "ALICE: Physics performance report, volume I," *J. Phys.*, vol. G30, pp. 1517–1763, 2004.

[9] C. Patrignani *et al.*, "Review of Particle Physics," *Chin. Phys.*, vol. C40, no. 10, p. 100001, 2016.

[10] C. W. Fabjan, "Detectors for high energy nuclear collisions," *Nucl. Phys.*, vol. A461, pp. 371–374, 1987.

[11] "Doxygen project webpages." http://www.stack.nl/~dimitri/doxygen/index.html, 2016. Accessed: 2016-11-30.

[12] G. Aad *et al.*, "Observation of a new particle in the search for the Standard Model Higgs boson with the ATLAS detector at the LHC," *Phys. Lett.*, vol. B716, pp. 1–29, 2012.

[13] S. Chatrchyan *et al.*, "Observation of a new boson at a mass of 125 GeV with the CMS experiment at the LHC," *Phys. Lett.*, vol. B716, pp. 30–61, 2012.

[14] K. Nakamura *et al.*, "Review of particle physics," *J. Phys.*, vol. G37, p. 075021, 2010.

[15] G. 't Hooft, "A Planar Diagram Theory for Strong Interactions," *Nucl. Phys.*, vol. B72, p. 461, 1974.

[16] D. J. Gross and F. Wilczek, "Ultraviolet Behavior of Nonabelian Gauge Theories," *Phys. Rev. Lett.*, vol. 30, pp. 1343–1346, 1973.

[17] H. D. Politzer, "Reliable Perturbative Results for Strong Interactions?," *Phys. Rev. Lett.*, vol. 30, pp. 1346–1349, 1973.

[18] K. G. Wilson, "Confinement of Quarks," *Phys. Rev.*, vol. D10, pp. 2445–2459, 1974.

[19] E. V. Shuryak, "Quantum Chromodynamics and the Theory of Superdense Matter," *Phys. Rept.*, vol. 61, pp. 71–158, 1980.

[20] F. Karsch, "Lattice QCD at high temperature and density," *Lect. Notes Phys.*, vol. 583, pp. 209–249, 2002.

[21] F. Karsch, E. Laermann, and A. Peikert, "The Pressure in two flavor, (2+1)-flavor and three flavor QCD," *Phys. Lett.*, vol. B478, pp. 447–455, 2000.

[22] G. Altarelli and G. Parisi, "Asymptotic Freedom in Parton Language," *Nucl. Phys.*, vol. B126, pp. 298–318, 1977.

[23] F. Gelis, E. Iancu, J. Jalilian-Marian, and R. Venugopalan, "The Color Glass Condensate," *Ann. Rev. Nucl. Part. Sci.*, vol. 60, pp. 463–489, 2010.

[24] M. A. Stephanov, "QCD phase diagram: An Overview," *PoS*, vol. LAT2006, p. 024, 2006.

[25] Y. Aoki, G. Endrodi, Z. Fodor, S. D. Katz, and K. K. Szabo, "The Order of the quantum chromodynamics transition predicted by the standard model of particle physics," *Nature*, vol. 443, pp. 675–678, 2006.

[26] J. M. Lattimer and M. Prakash, "Neutron Star Observations: Prognosis for Equation of State Constraints," *Phys. Rept.*, vol. 442, pp. 109–165, 2007.

[27] S. B. Ruester, V. Werth, M. Buballa, I. A. Shovkovy, and D. H. Rischke, "The Phase diagram of neutral quark matter: Self-consistent treatment of quark masses," *Phys. Rev.*, vol. D72, p. 034004, 2005.

[28] N. Armesto, "Nuclear shadowing," *J. Phys.*, vol. G32, pp. R367–R394, 2006.

[29] K. J. Eskola, H. Paukkunen, and C. A. Salgado, "An Improved global analysis of nuclear parton distribution functions including RHIC data," *JHEP*, vol. 07, p. 102, 2008.

[30] K. J. Eskola, H. Paukkunen, and C. A. Salgado, "EPS09: A New Generation of NLO and LO Nuclear Parton Distribution Functions," *JHEP*, vol. 04, p. 065, 2009.

[31] I. Vitev, "Initial state parton broadening and energy loss probed in d + Au at RHIC," *Phys. Lett.*, vol. B562, pp. 36–44, 2003.

[32] C. Shen, U. Heinz, P. Huovinen, and H. Song, "Radial and elliptic flow in Pb+Pb collisions at the Large Hadron Collider from viscous hydrodynamic," *Phys. Rev.*, vol. C84, p. 044903, 2011.

[33] B. B. Abelev *et al.*, "Elliptic flow of identified hadrons in Pb-Pb collisions at $\sqrt{s_{\rm NN}} = 2.76$ TeV," *JHEP*, vol. 06, p. 190, 2015.

[34] A. H. Mueller, "On the Multiplicity of Hadrons in QCD Jets," *Phys. Lett.*, vol. B104, pp. 161–164, 1981.

[35] A. D. Martin, W. J. Stirling, R. S. Thorne, and G. Watt, "Parton distributions for the LHC," *Eur. Phys. J.*, vol. C63, pp. 189–285, 2009.

[36] J. Pumplin, D. R. Stump, J. Huston, H. L. Lai, P. M. Nadolsky, and W. K. Tung, "New generation of parton distributions with uncertainties from global QCD analysis," *JHEP*, vol. 07, p. 012, 2002.

[37] R. D. Ball *et al.*, "Parton distributions with LHC data," *Nucl. Phys.*, vol. B867, pp. 244–289, 2013.

[38] V. N. Gribov and L. N. Lipatov, "Deep inelastic e p scattering in perturbation theory," *Sov. J. Nucl. Phys.*, vol. 15, pp. 438–450, 1972. [Yad. Fiz.15,781(1972)].

[39] Y. L. Dokshitzer, "Calculation of the Structure Functions for Deep Inelastic Scattering and e+ e- Annihilation by Perturbation Theory in Quantum Chromodynamics.," *Sov. Phys. JETP*, vol. 46, pp. 641–653, 1977. [Zh. Eksp. Teor. Fiz.73,1216(1977)].

[40] G. F. Sterman and S. Weinberg, "Jets from Quantum Chromodynamics," *Phys. Rev. Lett.*, vol. 39, p. 1436, 1977.

[41] S. Moretti, L. Lonnblad, and T. Sjostrand, "New and old jet clustering algorithms for electron - positron events," *JHEP*, vol. 08, p. 001, 1998.

[42] G. C. Blazey *et al.*, "Run II jet physics," in *QCD and weak boson physics in Run II. Proceedings, Batavia, USA, March 4-6, June 3-4, November 4-6, 1999*, pp. 47–77, 2000.

[43] S. D. Ellis, J. Huston, K. Hatakeyama, P. Loch, and M. Tonnesmann, "Jets in hadron-hadron collisions," *Prog. Part. Nucl. Phys.*, vol. 60, pp. 484–551, 2008.

[44] G. P. Salam, "Towards Jetography," *Eur. Phys. J.*, vol. C67, pp. 637–686, 2010.

[45] A. Ali and G. Kramer, "Jets and QCD: A Historical Review of the Discovery of the Quark and Gluon Jets and its Impact on QCD," *Eur. Phys. J.*, vol. H36, pp. 245–326, 2011.

[46] M. Cacciari, G. P. Salam, and G. Soyez, "The Anti-k(t) jet clustering algorithm," *JHEP*, vol. 04, p. 063, 2008.

[47] M. Cacciari and G. P. Salam, "Pileup subtraction using jet areas," *Phys. Lett.*, vol. B659, pp. 119–126, 2008.

[48] M. Cacciari, G. P. Salam, and G. Soyez, "FastJet User Manual," *Eur. Phys. J.*, vol. C72, p. 1896, 2012.

[49] T. Affolder *et al.*, "Measurement of the inclusive jet cross section in $\bar{p}p$ collisions at $\sqrt{s} = 1.8$ TeV," *Phys. Rev.*, vol. D64, p. 032001, 2001. [Erratum: Phys. Rev.D65,039903(2002)].

[50] S.-L. Blyth *et al.*, "A Cone jet-finding algorithm for heavy-ion collisions at LHC energies," *J. Phys.*, vol. G34, pp. 271–281, 2007.

[51] P. Cortese *et al.*, "ALICE: Physics performance report, volume II," *J. Phys.*, vol. G32, pp. 1295–2040, 2006.

[52] S. Jangal, *Study of jet production in ALICE experiment at LHC collider*. PhD thesis, Strasbourg U., 2012.

[53] A. Hocker and V. Kartvelishvili, "SVD approach to data unfolding," *Nucl. Instrum. Meth.*, vol. A372, pp. 469–481, 1996.

[54] T. Adye, "Unfolding algorithms and tests using RooUnfold," in *Proceedings, PHYSTAT 2011 Workshop on Statistical Issues Related to Discovery Claims in Search Experiments and Unfolding, CERN,Geneva, Switzerland 17-20 January 2011*, (Geneva), pp. 313–318, CERN, CERN, 2011.

[55] V. Blobel, "An Unfolding method for high-energy physics experiments," in *Advanced Statistical Techniques in Particle Physics. Proceedings, Conference, Durham, UK, March 18-22, 2002*, pp. 258–267, 2002.

[56] G. D'Agostini, "Bayesian inference in processing experimental data: Principles and basic applications," *Rept. Prog. Phys.*, vol. 66, pp. 1383–1420, 2003.

[57] K. Aamodt *et al.*, "Centrality dependence of the charged-particle multiplicity density at mid-rapidity in Pb-Pb collisions at $\sqrt{s_{NN}} = 2.76$ TeV," *Phys. Rev. Lett.*, vol. 106, p. 032301, 2011.

[58] R. Field and R. C. Group, "PYTHIA tune A, HERWIG, and JIMMY in Run 2 at CDF," 2005.

[59] B. Abelev *et al.*, "Measurement of the inclusive differential jet cross section in pp collisions at $\sqrt{s} = 2.76$ TeV," *Phys. Lett.*, vol. B722, pp. 262–272, 2013.

[60] B. Abelev *et al.*, "Measurement of Event Background Fluctuations for Charged Particle Jet Reconstruction in Pb-Pb collisions at $\sqrt{s_{NN}} = 2.76$ TeV," *JHEP*, vol. 03, p. 053, 2012.

[61] R. J. Reed, "Inclusive jet spectra in 2.76 TeV collisions from ALICE," *Nucl. Phys.*, vol. A904-905, pp. 721c–724c, 2013.

[62] M. Cacciari, J. Rojo, G. P. Salam, and G. Soyez, "Jet Reconstruction in Heavy Ion Collisions," *Eur. Phys. J.*, vol. C71, p. 1539, 2011.

[63] P. M. Jacobs, "Background Fluctuations in Heavy Ion Jet Reconstruction," *Nucl. Phys.*, vol. A855, p. 299, 2011.

[64] B. Abelev *et al.*, "Measurement of charged jet suppression in Pb-Pb collisions at $\sqrt{s_{NN}} = 2.76$ TeV," *JHEP*, vol. 03, p. 013, 2014.

[65] J. Adam *et al.*, "Measurement of jet quenching with semi-inclusive hadron-jet distributions in central Pb-Pb collisions at $\sqrt{s_{\rm NN}} = 2.76$ TeV," *JHEP*, vol. 09, p. 170, 2015.

[66] S. S. Adler *et al.*, "High p_T charged hadron suppression in Au + Au collisions at $\sqrt{s}_{NN} = 200$ GeV," *Phys. Rev.*, vol. C69, p. 034910, 2004.

[67] S. S. Adler *et al.*, "Suppressed π^0production at large transverse momentum in central Au+ Au collisions at $\sqrt{s}_{NN} = 200$ GeV," *Phys. Rev. Lett.*, vol. 91, p. 072301, 2003.

[68] J. Adams *et al.*, "Evidence from d + Au measurements for final state suppression of high p(T) hadrons in Au+Au collisions at RHIC," *Phys. Rev. Lett.*, vol. 91, p. 072304, 2003.

[69] J. Adam *et al.*, "Measurement of charged jet production cross sections and nuclear modification in p-Pb collisions at $\sqrt{s_{\rm NN}} = 5.02$ TeV," *Phys. Lett.*, vol. B749, pp. 68–81, 2015.

[70] M. Shao, "Cronin effect at RHIC," *AIP Conf. Proc.*, vol. 828, pp. 49–54, 2006. [,49(2006)].

[71] B. B. Abelev *et al.*, "Transverse momentum dependence of inclusive primary charged-particle production in p-Pb collisions at $\sqrt{s_{\rm NN}} = 5.02$ TeV," *Eur. Phys. J.*, vol. C74, no. 9, p. 3054, 2014.

[72] K. C. Zapp, "Geometrical aspects of jet quenching in JEWEL," *Phys. Lett.*, vol. B735, pp. 157–163, 2014.

[73] T. Renk, "Physics probed by the P_T dependence of the nuclear suppression factor," *Phys. Rev.*, vol. C88, no. 1, p. 014905, 2013.

[74] T. A. collaboration, "Measurement of W boson production and the lepton charge asymmetry in PbPb collisions at $\sqrt{sNN = 2.76TeV}$ with the ATLAS detector," 2014.

[75] E. Chapon, "W and Z bosons with CMS in pp, pPb and PbPb collisions," *Nucl. Phys.*, vol. A956, pp. 441–444, 2016.

[76] H. Zhang, J. F. Owens, E. Wang, and X.-N. Wang, "Dihadron tomography of high-energy nuclear collisions in NLO pQCD," *Phys. Rev. Lett.*, vol. 98, p. 212301, 2007.

[77] K. J. Eskola, H. Honkanen, C. A. Salgado, and U. A. Wiedemann, "The Fragility of high-p(T) hadron spectra as a hard probe," *Nucl. Phys.*, vol. A747, pp. 511–529, 2005.

[78] Y. I. Azimov, Y. L. Dokshitzer, V. A. Khoze, and S. I. Troyan, "Humpbacked QCD Plateau in Hadron Spectra," *Z. Phys.*, vol. C31, p. 213, 1986.

[79] T. Sjostrand, S. Mrenna, and P. Z. Skands, "PYTHIA 6.4 Physics and Manual," *JHEP*, vol. 05, p. 026, 2006.

[80] I. P. Lokhtin and A. M. Snigirev, "A Model of jet quenching in ultrarelativistic heavy ion collisions and high-p(T) hadron spectra at RHIC," *Eur. Phys. J.*, vol. C45, pp. 211–217, 2006.

[81] I. P. Lokhtin, A. V. Belyaev, L. V. Malinina, S. V. Petrushanko, E. P. Rogochaya, and A. M. Snigirev, "Hadron spectra, flow and correlations in PbPb collisions at the LHC: interplay between soft and hard physics," *Eur. Phys. J.*, vol. C72, p. 2045, 2012.

[82] R. Ostojic and S. Weisz, "Proposed Systems Layout of the Low beta Insertions for the LHC Experiments," *Conf. Proc.*, vol. C970512, p. 3696, 1997.

[83] K. Potter, "Luminosity measurements and calculations," in *CERN Accelerator School: Course on General Accelerator Physics Jyvaskyla, Finland, September 7-18, 1992*, pp. 117–129, 1992.

[84] B. B. Abelev *et al.*, "Measurement of visible cross sections in proton-lead collisions at $\sqrt{s_{\rm NN}} = 5.02$ TeV in van der Meer scans with the ALICE detector," *JINST*, vol. 9, no. 11, p. P11003, 2014.

[85] S. Chatrchyan *et al.*, "Studies of jet quenching using isolated-photon+jet correlations in PbPb and *pp* collisions at $\sqrt{s_{NN}} = 2.76$ TeV," *Phys. Lett.*, vol. B718, pp. 773–794, 2013.

[86] J. A. Robles, "Measurement of b-jet to inclusive jet ratio in PbPb and pp collisions at $\sqrt{s} = 2.76$ TeV with the CMS detector," *Nucl. Phys.*, vol. A904-905, pp. 1011c–1014c, 2013.

[87] K. Aamodt *et al.*, "The ALICE experiment at the CERN LHC," *JINST*, vol. 3, p. S08002, 2008.

[88] G. Dellacasa *et al.*, "ALICE technical design report of the inner tracking system (ITS)," 1999.

[89] G. Dellacasa *et al.*, "ALICE: Technical design report of the time projection chamber," 2000.

[90] G. Dellacasa *et al.*, "ALICE technical design report of the zero degree calorimeter (ZDC)," 1999.

[91] P. Cortese *et al.*, "ALICE electromagnetic calorimeter technical design report," 2008.

[92] O. Bourrion, R. Guernane, B. Boyer, J. L. Bouly, and G. Marcotte, "Level-1 jet trigger hardware for the ALICE electromagnetic calorimeter at LHC," *JINST*, vol. 5, p. C12048, 2010.

[93] J. Allen and M. e. a. Wang, "ALICE DCal: An Addendum to the EMCal Technical Design Report Di-Jet and Hadron-Jet correlation measurements in ALICE," Tech. Rep. CERN-LHCC-2010-011. ALICE-TDR-14-add-1, Jun 2010.

[94] J. Allen *et al.*, "Performance of prototypes for the ALICE electromagnetic calorimeter," *Nucl. Instrum. Meth.*, vol. A615, pp. 6–13, 2010.

[95] R. Brun and F. Rademakers, "ROOT: An object oriented data analysis framework," *Nucl. Instrum. Meth.*, vol. A389, pp. 81–86, 1997.

[96] A. E. collaboration, "Emcal offline documentation in aliroot: Emcal/doc/emcaldocumentation.pdf," 2013.

[97] G. Conesa Balbastre. private communication, 2016.

[98] T. Skwarnicki, *A study of the radiative CASCADE transitions between the Upsilon-Prime and Upsilon resonances, PhD thesis, Cracow, INP, 1986.* PhD thesis.

[99] "Aliroot documentation | alice offline pages." http://aliweb.cern.ch/Offline/AliRoot/Manual.html, 2011. Accessed: 2015-09-30.

[100] M. Zimmermann, "The ALICE analysis train system," *J. Phys. Conf. Ser.*, vol. 608, no. 1, p. 012019, 2015.

[101] P. Billoir, "Track Fitting With Multiple Scattering: A New Method," *Nucl. Instrum. Meth.*, vol. A225, pp. 352–366, 1984.

[102] P. Billoir, R. Fruhwirth, and M. Regler, "TRACK ELEMENT MERGING STRATEGY AND VERTEX FITTING IN COMPLEX MODULAR DETECTORS," *Nucl. Instrum. Meth.*, vol. A241, pp. 115–131, 1985.

[103] R. Fruhwirth, "Application of Kalman filtering to track and vertex fitting," *Nucl. Instrum. Meth.*, vol. A262, pp. 444–450, 1987.

[104] P. Billoir, "Progressive track recognition with a Kalman like fitting procedure," *Comput. Phys. Commun.*, vol. 57, pp. 390–394, 1989.

[105] J. Bielcikova, "Jet reconstruction and underlying event studies in p+p and d+Au collisions from STAR," *J. Phys. Conf. Ser.*, vol. 316, p. 012013, 2011.

[106] O. B. M. Estienne, "Alianalysistaskjetfragmentationfunction analalysis task," 2013.

[107] M. Estienne, "Jet fragmentation Monte Carlo study in vacuum and in medium in the ALICE experiment at the LHC," *Nuovo Cim.*, vol. C034N2, pp. 49–55, 2011.

[108] O. Busch, "Charged particle momentum distribution in jets." Analysis Note, 2012-2014.

[109] G. Corcella, I. G. Knowles, G. Marchesini, S. Moretti, K. Odagiri, P. Richardson, M. H. Seymour, and B. R. Webber, "HERWIG 6.5 release note," 2002.

Acknowledgments

This thesis could be understood as a summary of all my studies in China and France, including the pre-foundation work in CCNU and the main work which is done with in SUBATECH. These years will be unforgettable through all my life. Here, I really want to express my appreciation and gratitude to all the people with in the journey with my limited words.

First of all, I am deeply indebted to two of my supervisors, Alexandre SHABETAI and Magali ESTIENNE, who gave the most detailed guides and discussion during the research around my Ph.D. topic. I have benefitted from their creativity, enthusiasm and amazing energy. I feel fortunate to work under their strict and patient guidance, and also the support and friendship over the last four years. And I will never forget those precious memories of our discussions. This thesis would be just illusory without their help. Meanwhile, I appreciate to my supervisor, Sonia KABANA. From her, I get great encouragement and all wholehearted supports to my defense. I will also thank my colleges in Nantes, Marco BREGANT, Alexis MAS, Javier MARTIN, Lucile RONFLETTE... I really appreciate for your help on the research of discussion and daily life. And also I would like to thank Jianhui, Xin, Xiao and all my Chinese friends, for the good time we sharing in Nantes.

Secondly, I sincerely thank my supervisor Daicui ZHOU and together with prof. Zhongbao YIN, who led me to the fascinating world of high energy particle experiments. With their kind guidance and support, I get the opportunity to take part in the international collabotarion research, and have a whole new horizon on physics and the world. I also thanks to Prof. Daicui Zhou to give a lot of strong supports on my works and life. And he set me a super example in pursuing a career with his powerful persistence and enthusiasm in working. I also would like to thank the professors in Institutes of Particle Physics for the guide and teaching. For the members who are/were in Wuhan Group during the long period: Wenchang XIANG, Yaping WANG, Xianbao YUAN, Yaxian MAO, Renzhuo WAN, Xiaoming ZHANG, Dong WANG, Fang ZHANG, Ping YANG, Changzhou XIANG, Jianlin

ZHU, Fengchu ZHOU, Shuang LI, Xuan YIN, Jiebin LUO, Haitao ZHANG, Jianhui ZHU, Hongsheng ZHU, Yonghong ZHANG, Yang ZHAN, Zuman ZHANG, Wenzhao LUO, Xinye PENG and Kai WANG, many thanks to their useful discussions and kind help, the perpetual friendships will be shining forever in my future.

I am grateful to Prof. Xu CAI, Prof. Nu XU, Prof. Xinnian WANG, Prof. Enke WANG, Prof. Yadong YANG, Prof. Chunbin YANG, Prof. Feng LIU, Prof. Benwei ZHANG, Prof. Fuming LIU, Mrs. Yanming GAO, Mr. Haitao LIU and Mr. Chao LIU, *et al* from IOPP for providing us a strong academic atmosphere and their teaching.

Last but not the least, I deeply thank my parents. Only with their understanding and emotionally support, I get the chance to chasing my dream; and fortunately meet my lifetime companion, Ruina. With her love, great comprehension, warm support, kind tolerance have supported me all the time. With deeply loves and dedication from you, I have conquered all the hard time. My apologies to all of the people I may have forgotten!

Words cannot expressing my gratitude! To all of you,

Thank you!

Mengliang WANG

Wuhan

December 17, 2016

UNIVERSITE BRETAGNE LOIRE

UNIVERSITÉ DE NANTES

Thèse de Doctorat

Mengliang WANG

Mesure des fonctions de fragmentation des jets et de leurs moments dans les collisions pp à √s = 2.76 TeV avec ALICE au LHC.

Measurement of jet fragmentation functions and of their moments in pp collisions at √s=2.76 TeV with ALICE at the LHC.

Résumé

Un cross-over entre la matière nucléaire ordinaire et le plasma de quarks et gluons (PQG) est prédit par la QCD sur réseau à bas μ_B et haute température. Expérimentalement les collisions d'ions lourds ultra-relativistes sont utilisées pour étudier cet état dense et chaud. Produits lors d'un processus dur en début de collision, un parton de grande énergie en perd dans le milieu avant de fragmenter en une gerbe de hadrons appelée jet. Une étude de la modification de la structure et de la fragmentation du jet dans le milieu par rapport au vide permet d'améliorer notre connaissance du PQG. Les fonctions de fragmentation (FF) d'un jet décrivent les distributions en impulsion des hadrons dans ce dernier. Dans les collisions proton-proton (pp), leur mesure est importante pour comprendre les mécanismes de fragmentation de partons. Dans les collisions noyau-noyau, elle permet d'étudier les mécanismes de perte d'énergie. Cependant, la présence d'un important bruit de fond qui fluctue rend la mesure complexe. Il a alors été suggéré de mesurer les moments des FF qui y seraient moins sensibles. Le détecteur ALICE au LHC a des capacités de trajectométrie uniques permettant la mesure des particules chargées jusqu'à des impulsions de 150 MeV/c rendant possible une étude fine de la structure du jet et de ses FF. Les calorimètres électromagnétiques (EMCal et DCal) peuvent aussi être utilisés pour améliorer la mesure de l'énergie du jet. Nous présentons les mesures des FF des jets chargés et les premières études des moments des FF dans les collisions pp à √s=2.76 TeV dans ALICE. Une partie du travail est aussi dédiée à l'implémentation de la géométrie de DCal dans le logiciel d'analyse.

Mots clés :
collisions pp, collisions d'ions lourds ultra-relativistes, PQG, ALICE, Jets, (moments des) fonctions de fragmentation, Calorimètres électromagnétiques, DCal

Abstract

A cross-over between ordinary nuclear matter and a state of deconfined quarks and gluons, the Quark Gluon Plasma (QGP), is predicted by lattice QCD at low μ_B and high temperature. Experimentally, ultra-relativistic heavy ion collisions are used to produce and to study the hot and dense QGP medium. Produced in a hard scattering at the early stage of the collision a highly energetic parton is expected to lose energy in the medium before fragmenting into a spray of hadrons called jet. A study of the modification of the jet structure and of its fragmentation pattern in medium compared to the vacuum case should provide insights into the QGP properties. The jet fragmentation functions (FF) describe the momentum distribution of hadrons inside a jet. In proton-proton (pp) collisions their measurement is important for understanding the mechanisms of parton fragmentation while it can shed light on the energy loss mechanisms in nucleus-nucleus (AA) collisions. However, the presence of a large fluctuating background in AA makes the measurement a challenging task. The use of FF moments has been proposed to overcome this difficulty. The ALICE detector at the LHC has unique tracking capabilities enabling to measure charged particles down to transverse momenta of 150 MeV/c. This allows assessing possible modifications of the jet structure and FF. The electromagnetic calorimeters (EMCal and DCal) can also be used to improve the measurement of the jet energy. We present the measurements of charged-jet FF and the first studies of FF moments in pp collisions at √s=2.76 TeV in ALICE. Part of the work is also dedicated to the implementation of the DCal geometry in the ALICE offline software.

Key Words:
pp collisions, ultra-relativistic heavy-ion collisions, QGP, ALICE, Jets, fragmentation functions (moments), electromagnetic calorimeters**,** DCal